AN INVESTIGATION OF MICROSCOPIC PHASES IN THE BON ACCORD NI-OXIDE BODY, BARBERTON REGION, SOUTH AFRICA

By

Antje Wildau

Dissertation submitted in fulfillment of the requirements for the degree of

MASTER OF SCIENCE

In the
Faculty of Science
University of the Free State
Bloemfontein, South Africa

2012

Supervisor: Professor Marian Tredoux

Declaration of Independence

Herewith I declare that I wrote this thesis self-independent and that I did not use other literature and media as those, which I denoted. All places in this thesis, which are taken from publications literally or analogously or from ulterior foreign utterances, are identified as such.

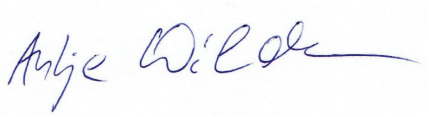

Antje Wildau 10th of January 2012

I. Abstract

The 3.5 Ga aged Bon Accord Ni-oxide deposit is hosted by strongly serpentinized meta-peridotites in the Barberton greenstone belt, South Africa. This small-sized deposit (6 m x 3 m x 0.35 m) graded about 36 % NiO and is mined out since the 1960s. It is highly unusual in its mineralogy (Ni-oxides, Ni-spinels, Ni-silicates) and in its depletion in S and Cu, as well as in its enrichment in platinum group elements. Due to its occurrence within the Jamestown ophiolite complex as well as its highly unusual mineralogy it has been suggested in the past to regard the Bon Accord as a new rock type and to name it jamestownite. The formation of this deposit, to be either an altered product of a palaeometeorite respectively to represent an oxidized body of Ni-Fe, derived from the Earth's core, is still controversial. The earliest assemblage of the Bon Accord has been suggested to have been either trevorite, liebenbergite, bonaccordite and Fe-rich bunsenite, respectively liebenbergite, Ni-Co-spinel and bunsenite.

Within the scope of this study, the microscopic phases, their textures and fabrics as well as the mineral chemistry are detailed investigated, to contribute to a better understanding about unusual occurrences like this. Though several minerals have been described as new species between 1960 and 1980, there were still gaps in the detailed microscopic description of all minerals as well as in the mineral chemistry, which are closed with this study. For this, optical microscopy, EPMA and μPIXE have been used intensely; also XRF-data from literature are included in this study.

The observation of bonaccordite, bunsenite, cochromite, liebenbergite, népouite, nimite, trevorite and willemseite is in agreement with previous documentations, but gaspéite, reevesite and nichromite are not observed. In addition to the already described new mineral species on the Bon Accord, six further new minerals are discovered: $Ni_3(As,Sb)$, Ni_3Sb, Ni_3Sb_2, $(Ni,Fe)_3As_2$, Ni_7AsS_5 and $Ni^{2+}(Ni^{3+},Fe^{3+})_2O_4$. The latter represents the missing link between $NiFe_2O_4$ (trevorite) and $NiNi_2O_4$, which is not known to reported to occur in nature. Also $Ni^{2+}(Fe^{3+},Ni^{3+})_2O_4$ is observed and represents the ferroan variety of $Ni^{2+}(Ni^{3+},Fe^{3+})_2O_4$. Furthermore two generations of trevorite are observed which differ in their phenotype and chemically. Xenomorphic trevorite is Ge-depleted and Sb-enriched, whereas lath-shaped trevorite is Ge-depleted and Sb-enriched. Also two bunsenite generations are observed that differ only in their texture but not chemically as documented in the past. The early bunsenite generation is replaced by xenomorphic trevorite, whereas the late bunsenite generation replaces the xenomorphic trevorite.

Detailed analysis of the mineral relations reveals a magmatic high-temperature and a hydrothermal low-temperature formation step. The primary assemblage consisted of liebenbergite and Ni-Co-spinel, including possibly the early generation of bunsenite, which is the magmatic high-temperature step. During the hydrothermal low-temperature formation step liebenbergite became altered to its serpentine and further to its talc, forming thereby the lath-shaped trevorite as by-product. Nimite formed during the hydrothermal conditions as well as the xenomorphic trevorite, bonaccordite and the second generation of bunsenite. Sulphides, sulphosalts and pure Sb and Cu formed at least contemporaneously with the xenomorphic trevorite. Considering Ni-Co-spinel and liebenbergite (roughly calculated to have been about 50 % prior to alteration) as the primary assemblage, the parent rock is suggested to have been a Ni-rich spinel-peridotite. The compositional variation of the Ni-silicates, Ni-spinels and Ni-Co-spinels shows the decrease in alteration from samples with

the Ni-poorest minerals to those with the Ni-richest minerals, which is in good accordance to the degree of deformation. Some open gaps in the understanding of the Bon Accord occurrence could be closed within this study, though the source of the high Ni remains controversial.

II. Table of Content

III. List of Figures

IV. List of Tables

V. Abbreviations

Å	Angstrom
a.d.	above detection limit
b.d.	below detection limit
BA	Bon Accord
Bon	bonaccordite
Bun	bunsenite
Cc	chalcocite
Ch	chert
Chr	chromite
Clc	clinochlore
CoChr	cochromite
Cp	chalcopyrite
Cu	copper
EDS	energy-dispersive spectroscopy / energy-dispersive spectrometer
EPMA	electron probe micro-analyzer
Fer	feruvite
FTrv	ferroan trevorite
Goe	goethite
Hem	hematite
HM body	hematite-magentite body
Hzl	heazlewoodite
Ilm	ilmenite
IMA	International Mineralogical Association
Lb	liebenbergite
LOI	loss on ignition
LREE	light rare earth elements
Mhb	magnesio-hornblende
Mlr	millerite
MORB	mid ocean ridge basalt
Mr	marcasite
Mt	magnetite
n	number (of)
n.d.	not detected
Nep	népouite
Nim	nimite
NiMt	nickeloan magnetite

Nis	nisbite
PGE	platinum group elements
Qtz	quartz
R	reflectivity
SACS	South African Committee for Stratigraphy
Sb	antimony
SEM	scanning electron microscope
Sul	sulphides / sulphosalts
Trv	trevorite
UFS	University of the Free State
Ukn	unknown
USil	unidentified silicate
VHMS	volcanic-hosted massive sulphide deposits
Wa	wairauite
WD-XRF	wavelength-dispersive X-ray fluorescence
WDS	wavelength-dispersive spectroscopy or Wavelength-dispersive spectrometer
Will	willemseite
wt%	weight percent
Wus	wustite
XRF	X-ray fluorescence
µPIXE	proton-Induced X-Ray Emision (on micro scale)

1. Introduction

1.1 Introduction into the geology of the Bon Accord Ni-oxide body

The Bon Accord body was a lens-shaped Ni deposit that contained about 20 t of ore containing approximately 36 % NiO (De Waal, 1986). Since the early 1930s it has been mined out, leaving a pit measuring 6 m x 3 m x 0.35 m. The ore material was regarded as a mixture of Ni silicate and magnetite by Major Tudor Gruffydd Trevor who first reported about this occurrence in the metaperidotites of the Barberton greenstone belt in 1920 (De Waal, 1977). Figure 1.1 shows the pit as it appeared in January 2010: the length has diminished somewhat, probably as a result of slumping, and has deepened to approximately 2 m.

Figure 1.1 The Bon Accord pit, 2010.

The Bon Accord Ni-oxide body is located on the Bon Accord Stock Farm, 2.8 km northwest of Sheba Siding and 20 km northeast of Barberton, Mpumalanga, South Africa. Barberton is situated in the De Kaap Valley and is fringed by the Mkhonjwa mountains. It is 43 km south of Nelspruit and 360 km to the east of Johannesburg (figures 1.2 and 1.3). The position of the Bon Accord deposit is marked in figure 1.3 with a black square.

Figure 1.2 Map of South Africa and the surrounding countries (modified after Manor, 2008).

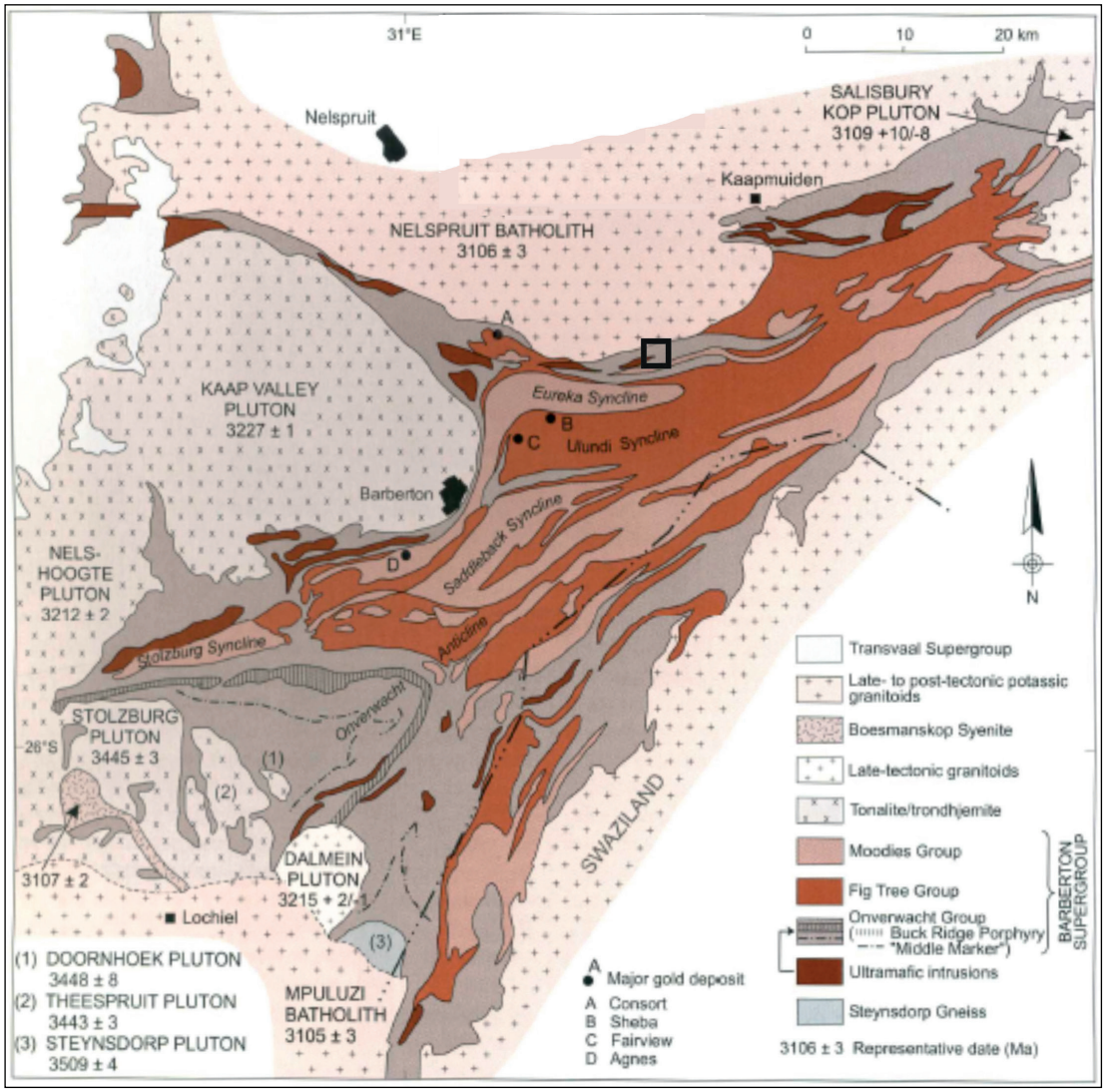

Figure 1.3 Stratigraphic map of the Barberton greenstone belt and the surrounding intrusions. The black square marks the position of Bon Accord Ni-oxide body (modified after Brandl et al., 2006).

1.1.1 The Kaapvaal craton

The Archaean Kaapvaal craton has an age of 3.7 Ga (De Wit *et al.*, 1992) and is part of an ancient crystalline shield. According to De Wit *et al.* (1992), it took a span of about 1 Ga for the formation of the Kaapvaal craton up to its stabilization at 2.6 Ga. This period is subdivided into two periods. Within the first one (3.7 Ga to 3.1 Ga), initial separation of the continental lithosphere of the craton from the mantle took place. Polyphase plate tectonic processes in shallow water depths occurred. The second period captured intra-continental and continental-margin processes, mainly the combination of tectonic accretion of crustal fragments and subduction-related igneous processes, which allowed continental growth. The processes are similar to those that occur nowadays at mid-ocean-ridges, ocean subduction zones and continental margins *(ibid.)*.

Most of the Kaapvaal craton is covered by Neoarchaean to Palaeoproterozoic volcano-sedimentary sequences. The Barberton greenstone belt is one of the best exposed areas of pre-Neoarchaean rocks in this craton, and indeed in the whole world. As presented in figure 1.4, there are greenstone complexes of different age in the Kaapvaal craton.

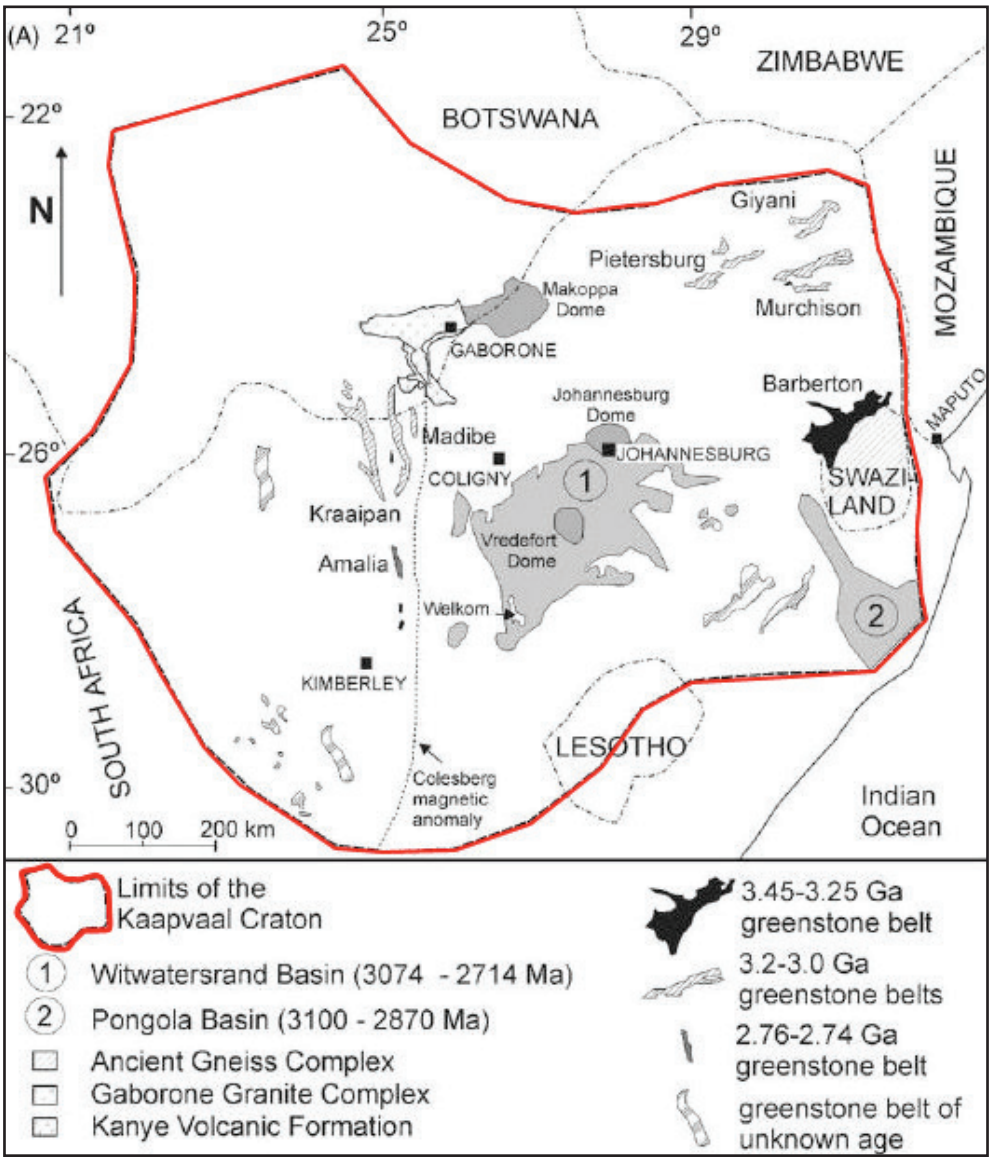

Figure 1.4 Simplified outline of the Kaapvaal craton. This formation includes parts of South Africa, Lesotho, Swaziland in total, and Botswana. The black unit marks the Barberton greenstone belt. The other greenstone belts occur mainly in South Africa and are younger (modified after Poujol, 2003).

1.1.2 The Barberton greenstone belt

The Barberton greenstone belt is a granite-greenstone terrain; with its age of 3.5 Ga it belongs to one of the three oldest known greenstone belts on Earth. It is part of the Barberton mountain land, occupies an area of 120 km x 50 km and is situated close to Nelspruit and at the western border of Swaziland (see figure 1.3). In contrast to all of the Earth's greenstone belts, this one and the northwestern Pilbara craton in Australia are the only regions left that have a substantial portion of more or less pristine mid-Archaean rocks. The belt itself has a shallow, broadly tabular structure and is surrounded by a variety of intrusions. According to De Wit *et al.* (1987), there are in total 27, that have caused strong metamorphism and folding, which resulted in an east-northeast trend.

The origin of the Barberton greenstone belt is controversial and various interpretations exist. As summarized by Lowe (1994), this greenstone belt has been interpreted by Anhaeusser (1973) in terms of vertical tectonics, by Condie and Hunter (1976) in terms of plate-related continental rifts, by De Wit *et al.* (1987) in terms of oceanic

spreading centres, by De Wit *et al.* (1992) in terms of accretionary complexes, as well as by De Ronde and De Wit (1994) as an accretionary belt, being composed of two major terrains, which include early komatiitic and basaltic units that resemble mid-ocean ridge rocks, as well as later felsic volcanic units that formed along one or more convergent margins. According to Anhaeusser (1973), the early crust in the south of Africa resembled the today's abyssal regions of the oceans. After progressive thickening, the early Earth's crust stabilized about 3.0 Ga ago, followed by the development of the first interior or cratonic-type sedimentary basins. The structure of the greenstone belt and its sediments is extensively affected by a multiplicity of diapiric intrusions, as for instance the Nelspruit batholith *(op. cit.)*. In contrast to this, Condie and Hunter (1976) suggested a plume model, which can account for the episodisity of magmatism as it is observed in the Barberton region. Assuming a sialic crust approximately 3.5 Ga in age developed during earlier magmatic periods as well as a geothermal gradient that is similar to the present-day one close to average ocean basin or cratonic crust, a mantle plume is suggested to have ascended 3.5 Ga ago. This plume is suggested to have ascended to the lithosphere's base that might have spread laterally, accompanied by the development of an overlying rift system, which contained ultramafic and mafic magmas of the Onverwacht Group, derived from the plume's upper part. Furthermore at this time, ultramafic and mafic magmas may well have intruded the lithosphere. The sinking of the rift zone, flank erosion as well as erosion of exposed parts of the Onverwacht Group could have happened due to the cooling and sinking of the plume. Condie and Hunter (1976) suggested that these events have led to the rise of the Moodies and Fig Tree sediments. Deformation of the rift-zone rocks might have happened due to gravitational sinking of the crust. The repetition of partial melting and renewed plume activity were suggested to have developed the Barberton greenstone belt. The east-northeast trend in the belt is explained with the assumption of a megarift zone involving a series of interconnected rift zones, having developed due to a southwest-trending linear array of mantle plume *(op. cit.)*. De Wit *et al.* (1987) suggested that the Barberton greenstone belt represents oceanic crust. Based on field observations, an integral section through the belt consists of a lower peridotitic tectonite zone, overlain by a complex array zone of vertical magma conduits, that intrude into a substantial carapace of pillow lavas as well as thin cherts, which cover the conduits. De Wit *et al.* (1987, page 718) tentatively classified this sequence "as an ophiolite *sensu stricto* as in the Steinmann Trinity and the Penrose Conference definition" and proposed to call it the Jamestown ophiolite complex, though there are in general conspicuous differences with Phanerozoic ophiolites. These are, for instance, the different proportions of the rock types, but especially the much greater regional extent of hydration and metasomatic alteration that has affected the rocks of the Barberton greenstone belt. De Wit *et al.* (1987) concluded that equilibrium conditions have been reached during the simatic metasomatism. This leads to the suggestion of thinner and more permeable simatic lithosphere than in later eras, irrespective of the upper crustal component's age. The pervasiveness of the simatic metasomatism has been interpreted to reflect very close spacing or merging of hydrothermally active centres over a large area, implying the representation of a thin Archaean crust, e.g. the Jamestown ophiolite complex *(op. cit.)*. As the author of the present study regards the observations and interpretations of De Wit *et al.* (1987) as most convincing, the suggestion that the Barberton greenstone belt represents simatic crust is favored. De Ronde and De Wit (1994) outlined three major deformation events. The first event has been manifested differently in the northern and southern part of the belt. Thereby the greywackes in the north experienced the emplacement of slivers of the underlying chert and ultramafic rocks, and in the south, components of the Onverwacht Group became involved in tectonic imbrication. The second deformation event caused isoclinal

folds with northeast – southwest or eastwest-trending axes. During the third event, the southern part of the greenstone belt became subdivided into different structural domains. De Ronde and De Wit (1994) concluded that in the time span from 3.2 Ga to 3.0 Ga, regional accretion as well as the assembly of the Kaapvaal craton in the greenstone belt began, followed by the second and third deformation event between 3.2 Ga and 3.0 Ga, which in turn was followed by the formation of arc and trench blocks as well as calc-alkaline rocks at about 3.2 Ga *(op. cit.)*.

A dominant feature in greenstone belts is the cyclical nature of volcanism and sedimentary successions (Anhaeusser, 1976). Ultramafic rocks are present in the lower formations and decrease in the upper formations, whereas the presence of felsic volcanic rocks increases in the upper parts. As shown in figure 1.3, plutonism and volcanism had been very active between 3.5 and 3.2 Ga around the Barberton greenstone belt. Table 1.1 gives an overview of the plutons and batholiths; U-Pb and Pb-Pb zircon dating were used to establish the ages. The oldest sediments in this greenstone belt have an estimated age of about 3.4 to 3.5 Ga and were deposited on oceanic-like crust; subsequently, they were affected by tectonic events (De Wit, 1991). According to De Wit (1991), sedimentation occurred predominantly in subaqueous environments, from just below the photic zone to tidal flats and deltaic plains. The Barberton greenstone belt itself has been subdivided into a northern and a southern part. The boundary zone is tectonic and characterized by thrust and strike-slip faults. These two zones are part of a fold-and-thrust belt, containing 450 Ma old rocks of complex tectonothermal events.

Table 1.1 Simplified outline of the Kaapvaal craton. This formation includes parts of South Africa, Lesotho, Swaziland in total, and Botswana. The black unit marks the Barberton greenstone belt. The other greenstone belts occur mainly in South Africa and are younger (modified after Poujol, 2003).

Formation	Age	Rock type
Steynsdorp pluton	3.5Ga	Gneiss[1]
Stolzburg pluton	3.4Ga	Gneiss[2]
Doornhoek pluton	3.4Ga	Trondhjemite gneiss[2]
Kaap Valley pluton	3.3Ga	Hornblende tonalitic gneiss[4]
Ancient gneiss complex	3.3Ga	Hornblende tonalitic gneiss[3]
Middle marker	3.3Ga	Laminated sediments[5]
Theespruit pluton	3.2Ga	Biotite tonalitic gneiss[4]
Dalmein pluton	3.2Ga	Coarse-grained porphyritic granodiorite[4]
Nelshoogte pluton	3.2Ga	Biotite tonalite / trondhjemite gneiss[4]
Stentor pluton	3.1Ga	Granite[2]
Nelspruit batholith	3.1Ga	Gneiss[4]
Mpuluzi batholith	3.1Ga	Granite sheets[6]
Salisburykop pluton	3.0Ga	Coarse-grained granodiorite[4]

Hydrothermal overprinting, associated with SiO_2 and MgO metasomatism apparently related to banded iron formations and Fe-rich black-smoker-like mineralisation, took place at about 3.5 Ga (De Wit and Hart, 1993). In addition to the ancient gneiss complex in the south of the belt, both parts of the Barberton greenstone belt belong to the core region of the Kaapvaal craton. Ultramafic rocks outcrop generally around the margin of the belt; the sediments form the core, but are probably underlain by ultramafic rocks of the same age as those around the margins. For simplification the volcanic, igneous and sedimentary rock-types of the Barberton

greenstone belt have been grouped into the Swazian Era or Barberton Supergroup (SACS, 2006) (figure 1.5). These rocks show greenschist-facies assemblages but locally, in proximity to the granitoid intrusions, they reach amphibolite facies (Hofman and Harris, 2008). De Wit (1982), Lamb (1984), Paris *et al.* (1985) and De Ronde (1991) stated that seafloor-related metasomatism occurred contemporaneously with large-scale deformation, sedimentation and volcanism, preceding the granitoid intrusions around the belt. According to De Wit (1991, page 57), "Complementary work has verified that these rocks were formed in some type of mid-oceanic-ridge environment because they are associated with extensive seafloor-type metamorphism, metasomatism, and black-smoker-type mineralisation". The chert units, which are intercalated within the Onverwacht and Fig Tree Group, were regarded by Paris *et al.* (1985) to be replacement products of pyroclastic deposits, pillow lavas and sedimentary deposits. This process is suggested to have been driven by convection of seawater.

According to Byerly and Palmer (1991), the Barberton greenstone belt with its altered Archaean rocks shows as additional unusual aspect locally pervasive boron metasomatism. Though tourmaline-bearing rocks are only a minor component, they are nevertheless ubiquitous *(op. cit.)*. The tourmaline-rich rocks are common in the low-grade, interior areas. The altered basaltic and komatiitic lavas as well as the overlying shallow marine sediments contain up to 50 % tourmaline *(op. cit.)*. Furthermore, Byerly and Palmer (1991) concluded that the

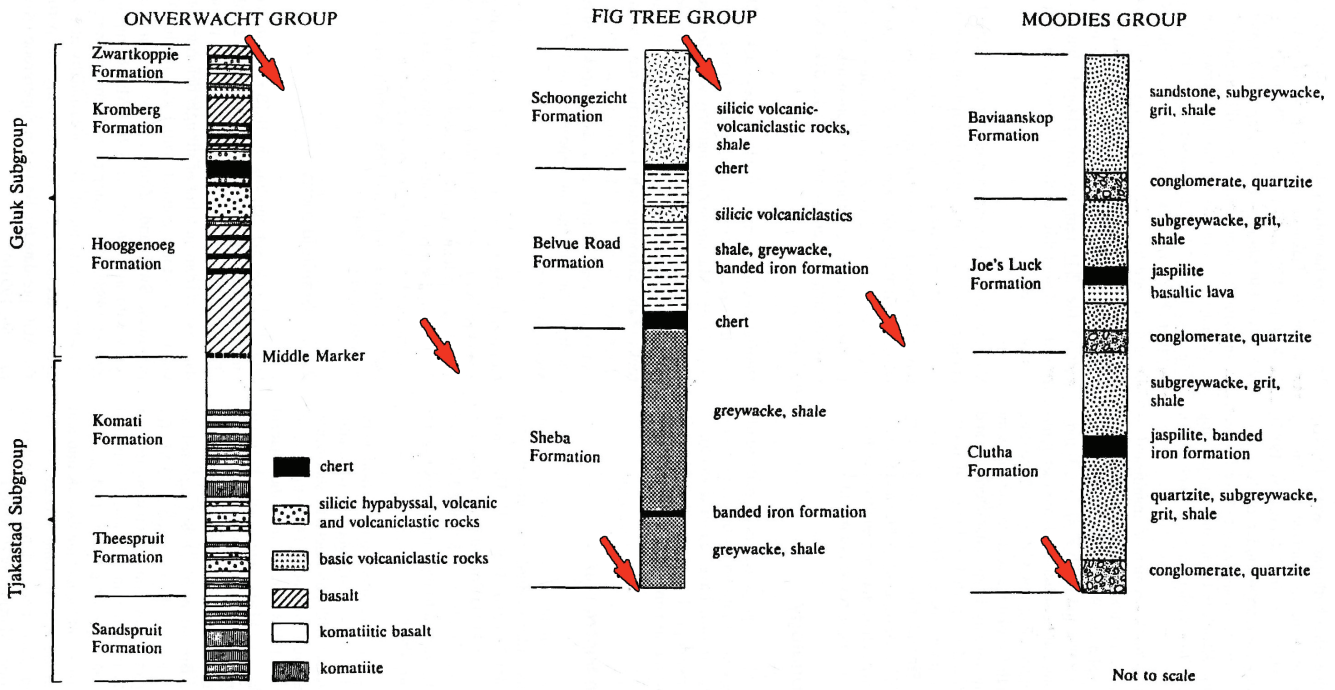

Figure 1.5 Stratigraphic overview of the Barberton Supergroup, subdivided into the Onverwacht, Fig Tree and Moodies groups (modified after Kohler, 2003).

occurrence of boron mineralisation at low temperature is a surficial process due to (for example) the presence of tourmaline-bearing rip-up clasts, tourmaline-coated grains and intraformational tourmalinite pebbles. They grouped basalts, komatiites, evaporite-bearing sediments, stromatolitic sediments and quartz veins as the five tourmaline-bearing lithologies, with stratiform tourmalinite units. These units apparently are unrelated to the granites and occur at a distance of 10 km to the margins of the greenstone belt, but always in alteration zones at the tops of mafic to ultramafic lava flows which are associated with the above-mentioned sediments. Furthermore, they reported the common association of the tourmalinites with stratiform base-metal and gold

deposits (e.g., the New Consort gold mine). The plutonic felsic rocks around the margins of the Barberton greenstone belt clearly postdate the tourmaline mineralisation: Byerly and Palmer (1991) showed evidence of tourmalinization of the lower stratigraphic units prior to consolidation of the sediments and also before the onset of felsic magmatism, suggesting a two-stage model for hydrothermal mineralisation and metasomatism. Kohler (2003) reported the presence of tourmaline-bearing quartz veins, best developed along the Stentor pluton contact, lying within the foliation. The presence of enclosing, silicified and tourmalinized schists has been explained by silica and boron metasomatism that might have accompanied the intrusion of the Stentor pluton, which contradicts the observations of Byerly and Palmer (1991).

The Barberton greenstone belt is also characterized by the paucity of Cu-Zn and Cu-Zn-Pb VHMS ore deposits, whereas for instance the Archaean greenstone terraines in the Superior Province of Canada contain several well-developed VHMS orebodies. Only one noteworthy but subeconomic deposit of this type is known southeast of the Stentor pluton (Kohler, 2003).

1.1.3 The Barberton Supergroup

The Barberton Supergroup comprises the Onverwacht Group, the overlying Fig Tree Group and on top the Moodies Group (figure 1.5). Their distribution in the Barberton greenstone belt is shown in figure 1.6.

The Onverwacht Group, the lowermost unit, formed between 3.55 to 3.3 Ga, has an estimated thickness of 15 km. It is subdivided into the Tjakastad and overlying Geluk subgroups. The Tjakastad Subgroup contains the Sandspruit, Theespruit and Komati formations; the Geluk Subgroup contains the Hooggenoeg, Kromberg and Zwartkoppie Formations. The Tjakastad and Geluk Subgroups are separated by the Middle Marker, a chertified sedimentary horizon (table 1.2) (Anhaeusser, 1973). The Tjakastad Subgroup consists of ultramafic, mafic and volcanic rocks (komatiites, komatiitic basalts and basalts). There are minor amounts of dacitic volcanic and sedimentary rocks. The lower ultramafic unit contains three formations with a high MgO content, a high Ca/Al ratio and low alkalis including potassium. Sills of dunite, peridotite, pyroxenite, harzburgite, gabbro, anorthosite and norite are present *(op. cit.)*. This unit consists of rare-earth-element depleted, carbonatized peridotitic tectonites. These are covered by complex magma chambers and conduits, which in turn are overlain by a considerably carapace of pillow lavas and thin cherts and shales. The cherts contain the middle marker, which is subdivided into three subunits. The uppermost of these units includes a large variety of volcanic and

Table 1.2 Rock types of the Subgroups of the Onverwacht Group (Kohler, 2003).

Subgroup	Formation	Rock types
Tjakastad	Sandspruit	Dominated by komatiite
	Theespruit	Mainly basalts and komatiitic basalts; subordinate intercalated silicic pyroclastic and epiclastic rocks
	Komati	Komatiite, komatiitic basalt; several layered ultrabasic sills
Geluk	Hooggenoeg	Distinct cyclic nature - pillowed and massive tholeiitic and komatiitic basalt, chert, dacitic to rhyodacitic intrusions and extrusions
	Kromberg	Dominated by tholeiitic basalt lavas and pyroclastic rocks with minor chert
	Zwartkoppie	Ultrabasic, basic and silicic schists, banded cherty sedimentary rocks

pyroclastic rocks; rhyolitic lavas are capped by chert and ferrous chert horizons. All these rocks have formed in a deep to shallow marine environment (Hofman and Harris, 2008). According to De Wit (1991) and Kohler (2003), the rocks within the Onverwacht and Fig Tree Groups experienced synvolcanic and seafloor alteration. Burial metamorphism is implicated. Kohler (2003) stated that investigations by Cloete (1990, 1991, 1994) in the Komati Formation (Onverwacht Group) showed an increasing grade of metamorphism within this unit with stratigraphic depth. Also, contact metamorphism is indicated by supracrustal rocks in close proximity to the intrusive granitoids; alteration reached the amphibolite facies, being usually characterized by an initial period of prograde metamorphism, followed by post-tectonic recrystallization and, in the waning stages, partial retrogression (Kohler, 2003).

The Fig Tree Group, having a maximum thickness of about 2.1 km, is a succession with an estimated age of 3.2 Ga. It consists of fine-grained argillaceous sediments, predominantly detrital sediments, containing subordinate volcanic and pyroclastic rocks (pelitic sediments containing banded ferrous cherts, locally banded iron formations, greywackes). This group is in turn subdivided into the Sheba, the Belvue road and the Schoongezicht Formation (table 1.3) (Anhaeusser, 1973). The Fig Tree Group has the earliest recognizable detrital sediments in this area (Kohler, 2003). The Inyoka fault separates the southern shallow-water facies from the northern, deep-water facies. Condie *et al.* (1970) gave evidence of enrichment of the Fig Tree greywackes in Mg and Ni in contrast to most other greywackes and Ca-rich granites. The greywackes of the lower Fig Tree Group are depleted in Al, Na and K. Danchin (1967) reported exceptionally high Ni and Cr contents in the Fig Tree shales.

Table 1.3 Rock types of the formations of the Fig Tree Group (Condie et al. 1970; Lowe, 1991).

Formation	Rock types
Sheba	Interbedded fine-to medium-grained turbiditic lithic greywacke, shale, siltstone, banded iron formation
Belvue Road	Shale, turbiditic siltstone and greywacke, chert, tuff, banded iron formation
Schoongezicht	Coarse, felsic, volcaniclastic sandstone

The Moodies Group overlies the Fig Tree Group; it has an estimated age of 3.2 Ga and a maximum thickness of about 3 km. The Fig Tree Group consists of coarse-grained arenaceous sediments in the form of a series of structurally isolated blocks and erosional remnants. This unit is the youngest and uppermost lithostratigraphic unit of the Barberton Supergroup, forming the high ground in the Barberton mountain land. It comprises the Clutha, Joe's Luck and Baviaanskop formations. As shown in table 1.4, clastic sedimentary sequences appear cyclically (Anhaeusser, 1976; Kohler, 2003), whereas De Ronde and De Wit (1994) interpreted the development of the Barberton greenstone belt and its successions as indicative of tectonic repetition.

Table 1.4 Rock types of the formations of the Moodies Group (Kohler, 2003).

Formation	Rock types
Clutha	Conglomerate, grit, sandstone, subgreywacke, siltstone, jaspilitic chert, banded iron formation
Joe's Luck	Conglomerate, grit, sandstone, subgreywacke, siltstone, jaspilitic chert, banded iron formation
Baviaankop	Conglomerate, grit, sandstone, subgreywacke, siltstone, jaspilitic chert, banded iron formation

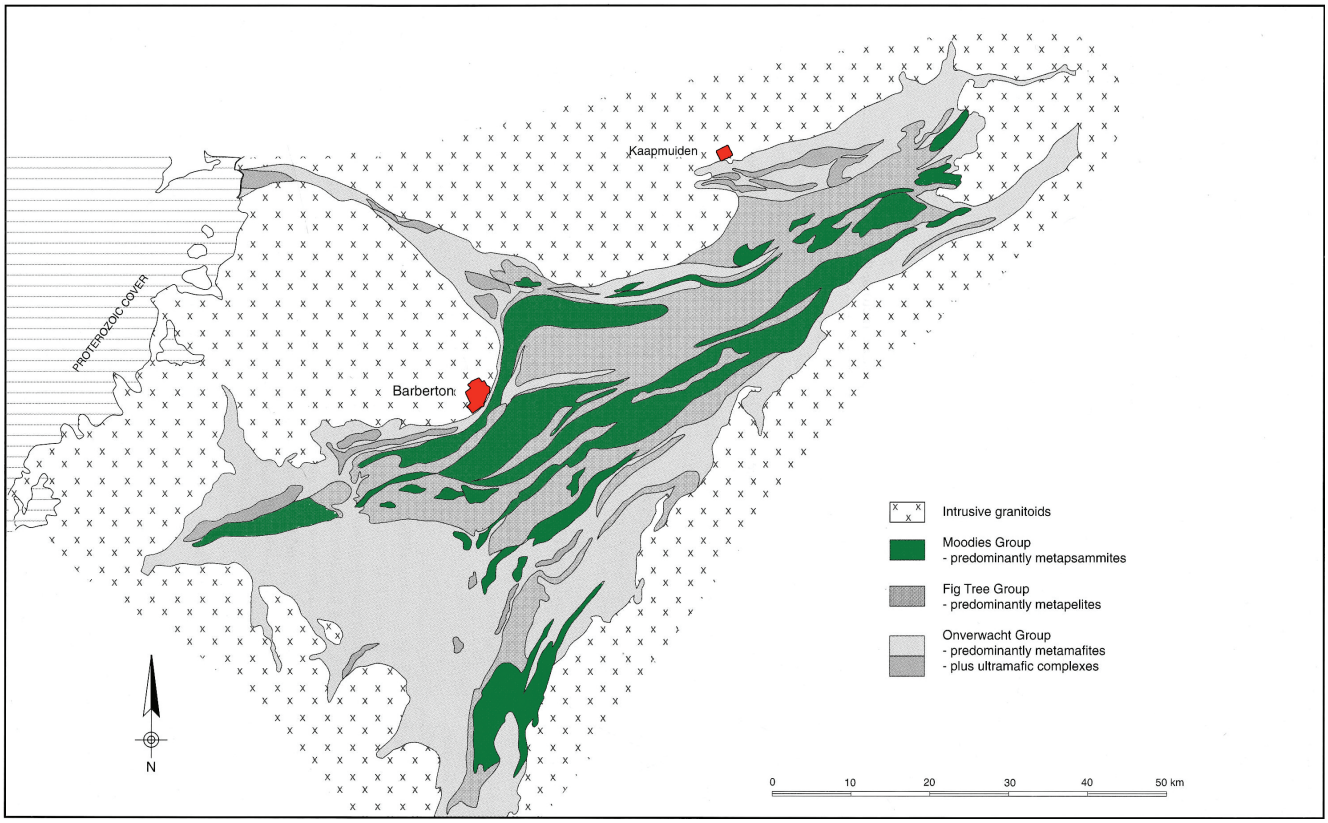

Figure 1.6 Distribution of the sediments of the Onverwacht, Fig Tree and Moodies groups in the Barberton greenstone belt (modified after Kohler, 2003).

1.1.4 Ore deposits in the Barberton greenstone belt

The Barberton greenstone belt is very rich in ore deposits, such as gold, chrysotile and others. Figure 1.7 gives an overview about their diversity and distribution.

The Au deposits are spread over the whole belt, occur in the Barberton Supergroup, but most of them appear in the aureoles of intrusions. Their origin is hydrothermal.

The barite deposits occur in the aureole of the Steynsdorp pluton and in the middle of the belt. Its host rocks are the lower Onverwacht Group to the Fig Tree Group. Their origin is pre-tectonic; they formed by sedimentary-exhalative processes being associated with the venting of hot springs on the sea floor.

"Verdite" and "buddstone" are both trade names for ornamental stone. Whilst verdite is the name for relatively monomineralic microcrystalline "fuchsite", buddstone stands for banded and contorted fuchsitic cherty rock. They occur as lenses in serpentinites of the Onverwacht Group, developed along transgressive fractures in the west of the Nelspruit batholith. Their origin is attributed to some kind of metasomatic process, representing a precursor of secondary (also hydrothermal) origin. In view of the occurrence of verdite and buddstone along the shear zones in the Nelspruit batholith they are seen to postdate the batholith.

Mercury occurs as cinnabar in just a few minor deposits along the southeastern margin of the greenstone belt; the rest of the belt is nearly devoid of any cinnabar mineralisation. Their host rocks are the folded Moodies Group quartzites. The deposits are considered to be of epithermal origin, late tectonic in timing.

Zinc deposits are very rare in the belt and only of minor prominence, showing polymetallic Zn-Ag-Au-(Cu-Pb-Sb-As-Ba) character. They are hosted by the sediments of the Onverwacht Group and considered to have an origin in a comparatively deep-water environment for the mineralisation, resulting from precipitation which

follows hydrothermal exhalation on the sea floor.

The chrysotile deposits are distributed in the northeast of the greenstone belt, in the aureole of the Kaap Valley pluton and in the south. They are hosted in serpentinized layered sill-like ultramafic rocks associated with ultramafic lavas of the Onverwacht Group. The ultramafic host-bodies appear to have been derived from parental magmas of komatiitic composition.

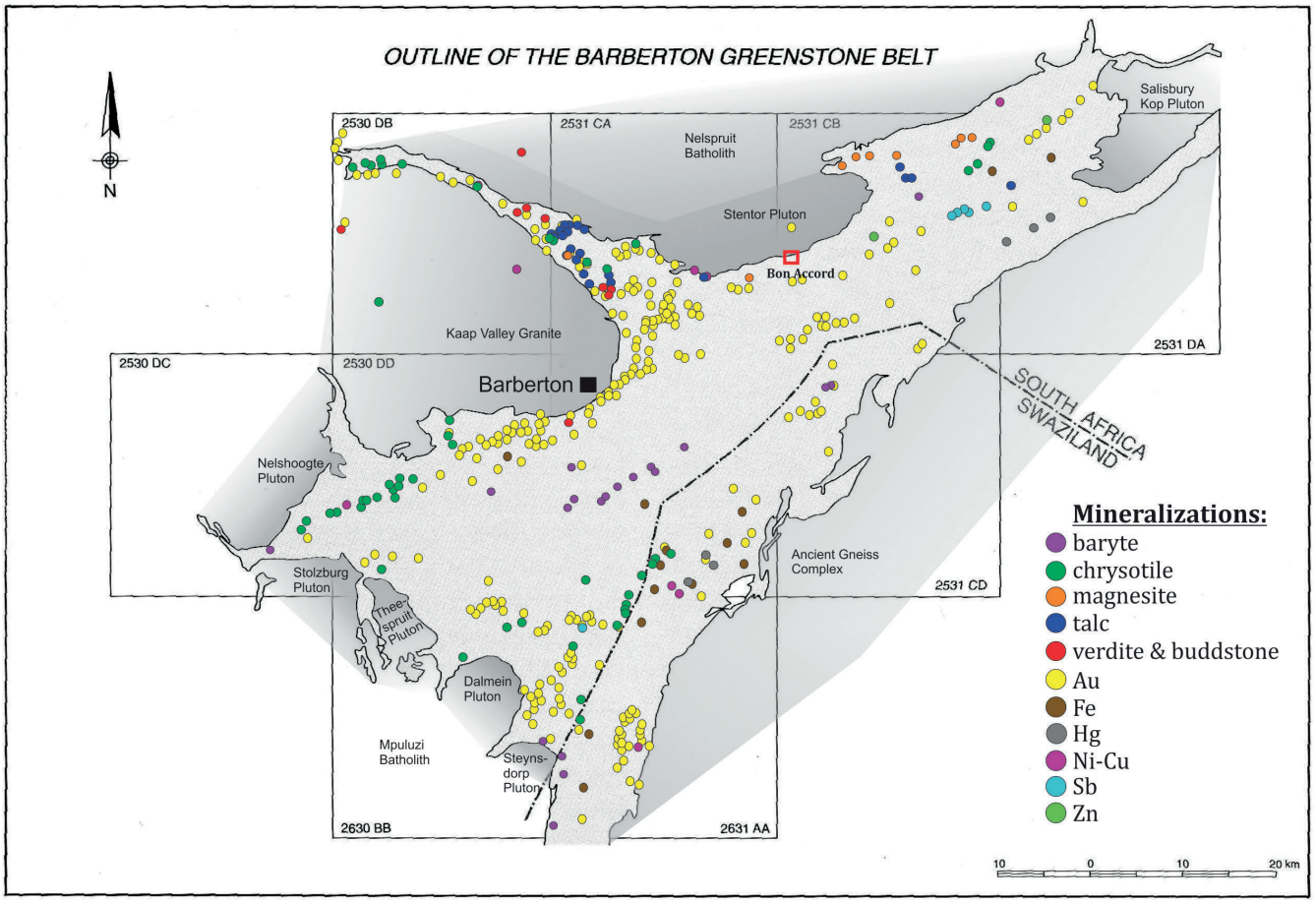

Figure 1.7 Outline of the Barberton greenstone belt and most of the surrounding intrusions and the distribution of the barite, chrysotile, magnesite, talc, verdite and buddstone, Au, Fe, Hg, Ni-Cu, Sb and Zn, which are marked with coloured points, the red square shows the position of Bon Accord (modified after Ward, 1999).

Magnesite deposits occur on the northern flank of the greenstone belt in the aureole of the Nelspruit batholith. They are hosted in sill-like, layered ultramafic bodies within the Onverwacht Group, derived from original olivine cumulates. The origin of these deposits is considered to be carbonate metasomatism, resulting from hydrothermal CO_2-bearing solutions. The formation of the deposits is seen to be a result of near-surface epithermal processes.

The talc deposits are also present on the northern flank of the belt, also in the aureole of the Nelspruit batholith. Hosted in altered ultramafic rocks of the Onverwacht Group, their formation results from the "steatitization" or hydrothermal alteration of serpentinites.

The Fe deposits occur as banded iron formations of the Algomatype in the Onverwacht and Fig Tree Group. It is supposed that their formation resulted from Fe- and Si-bearing submarine hydrothermal exhalation and chemical and biogenic precipitation of the Fe and Si to form banded rhythmites.

Nickel-Copper deposits are very rare in the Barberton greenstone belt, though it includes the type locality

for komatiites. The few deposits invariably appear at the rim of the belt in the quartz veins of the Onverwacht Group, except from one deposit which is located in the Kaap Valley granite.

The Antimony deposits occur in the chlorite-talc-carbonate schists, "fuchsite"-white mica-quartz schists and massive greenishgrey banded cherts of the Onverwacht Group. The mineralised quartz-carbonate rocks are an alteration product of komatiites, with subsequent, epigenetic, Sb-sulphide mineralisation (Ward, 1999).

1.1.5 The Bon Accord Ni-oxide body, the Bon Accord Ni-sulphide body and the hematite-magnetite body

The Bon Accord Ni-oxide body is one of the few Ni-deposits in the Barberton greenstone belt. It is very special owing its extreme Ni-enrichment, approximately 36 % NiO, but also because of its unusual mineralogy (De Waal, 1986). The depletion of S and Cu is unusual as well (Tredoux *et al.*, 1989). The Al-depleted older komatiites of the Barbertontype, with an age of >3.3 Ga, are known to generally not host Ni-Cu sulphide ore deposits (Ward, 1999). Relative to the host rocks, the Bon Accord Ni-oxide body is enriched in Co and PGE, very enriched in Fe, and shows also an extreme enrichment in As and Sb (Tredoux *et al.*, 1989). Its special mineralogy is expressed in the Ni-analogues of more common silicate minerals, for instance magnetite, olivine, chromite and chlorite, which are trevorite, liebenbergite, nichromite and nimite in the Bon Accord Ni-oxide body (subsection 1.2).

When originally discovered, Bon Accord had a lens shape with the dimensions 6 m x 3 m x 0.35 m, perhaps forming a structural boudin, and protruded from the contact schist into the talc-serpentinite footwall, in a narrow zone of chlorite-magnetite schist below a mylonitized chert horizon, close to the boundary between the Barberton greenstone belt and the Stentor pluton. The rock sequence around the Bon Accord deposit shows the same dip as the thrust slice complex containing the Barberton greenstone belt – Stentor gneisses; it is between 20° and 40° south. The upper and lower contacts of the ultramafic sheets which host Bon Accord are tectonic and bound by cherty to siliceous mylonitic layers of 10 m thickness. The ultramafic rocks are observed to be completely serpentinized. The serpentinites and also talc-carbonate schists are found along the contacts of the Bon Accord and the mylonites. Tredoux *et al.* (1989) stated that, owing to preserved relic textures in the serpentinites, the precursor was a coarse-grained dunite with minor pyroxenite, whereas Keenan (1986) argued that the paucity of Cu is typical for komatiite-related Ni mineralisation. Furthermore, the grade of metamorphism in proximity of the Bon Accord body is estimated to be of albite-epidote and hornblende-hornfels facies, implying formation temperatures of 800 K to 900 K and a low-pressure regime (De Waal, 1978; Tredoux *et al.*, 1989; Anhaeusser, 1964). Stratigraphically, Bon Accord overlies the quartzite.

Just about 1.5 km further east is the Bon Accord Ni-sulphide mineralisation located close to the Scotia Talc mine, occurring in a similar sequence of serpentinized ultramafic rocks as the Bon Accord (Tredoux *et al.*, 1989); Bon Accord is also close to the hanging-wall horizon of hornblende-tourmaline schist (figure 1.8). The Scotia Talc mine, Bon Accord and the Bon Accord Ni-sulphide body were interpreted to fall well within the metamorphic aureole of the Nelspruit batholith (Ward, 1999; De Waal, 1979) as well as within the metamorphic aureole of the Stentor pluton (Tredoux *et al.*, 1989). But to date there is no proof about a genetic relation. The formation of the Bon Accord deposit is still very controversial. There are two main hypotheses, which are mutually exlusive. De Waal (1977) suggested that Bon Accord is the product of metamorphism of a palaeometeorite, whereas Tredoux *et al.* (1989) suggested that Bon Accord is a tectonically emplaced

siderophile segregation of mantle origin. Both hypotheses are discussed in subsection 1.3.

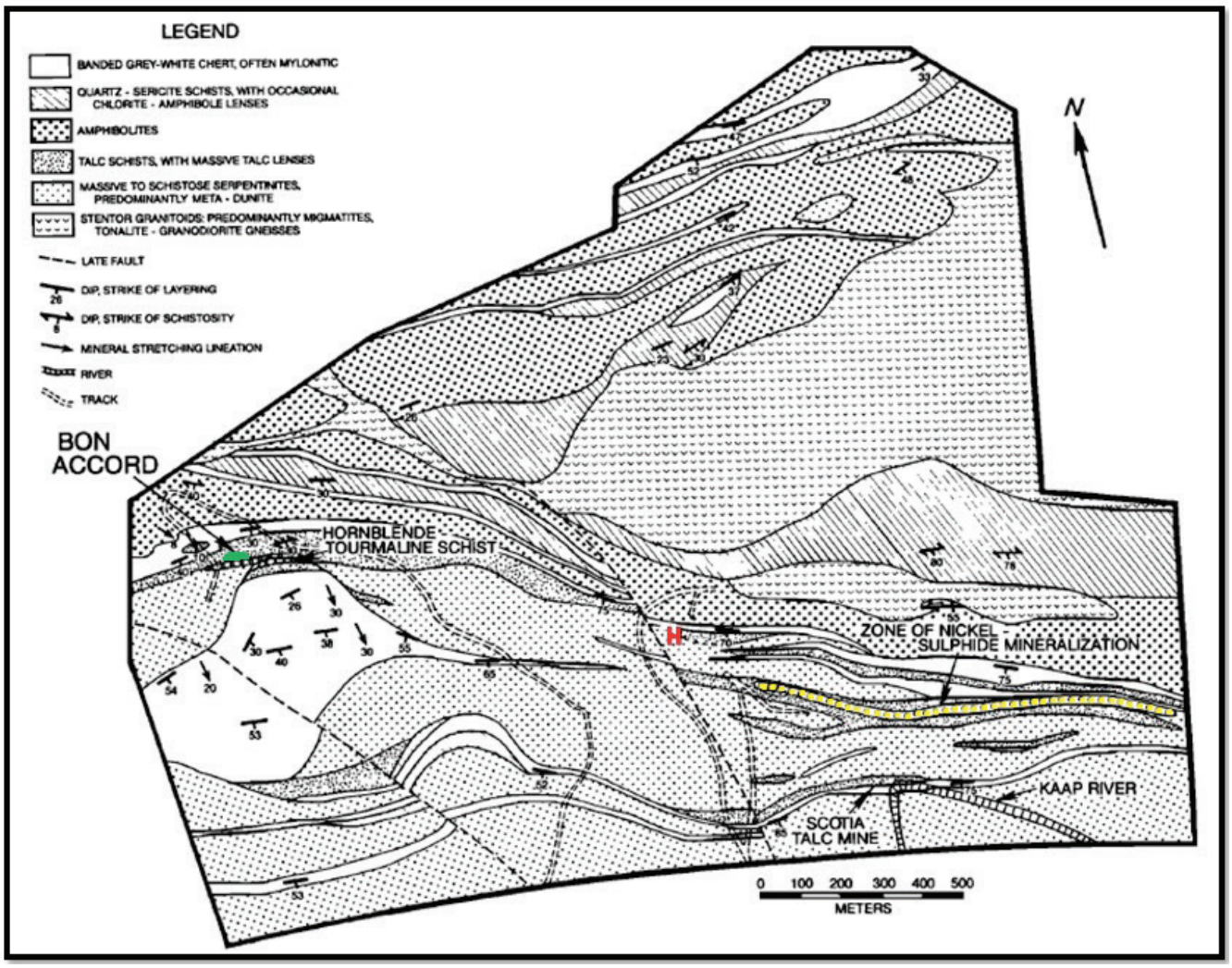

Figure 1.8 Geological map showing the position of Bon Accord (green), the hematite-magnetite body (marked with H) and the Bon Accord Ni-sulphide body (yellow) (modified after Tredoux et al., 1989).

The Bon Accord Ni-sulphide mineralisation is located on the Bon Accord stock farm 282 JU, southeast of Bon Accord. In addition to Bon Accord, this deposit also is not typical of known Archaean Ni deposits, for instance in view of the occurrence of Ni within cherty rocks. The widespread presence of "fuchsite" and chromian spinel in the quartz-muscovite schists led Keenan (1986) to suggest that the host rocks are silicified and sheared sulphide-bearing komatiites, or that the Ni-sulphides from the komatiites could have preferentially accumulated in semi-consolidated, inter-flow cherty material. A succession of east-west-striking mafic and felsic schists plus cherty and ultramafic rocks of the Theespruit Formation underlie the Bon Accord farm. The metamorphic grade is upper greenschist facies, with evidence of retrograde metamorphism to lower-temperature assemblages. The northern part of the farm the deposit is underlain by tonalite gneiss, and in the southern part, there is a large body of talc-bearing serpentinite and talc schist. Within the ultramafic rocks, there are chloritic lenses, possibly carrying minor disseminated Ni-sulphides, as at the Scotia talc mine. In the latter, the whole-rock Ni values range between 0.1 % and 2 % Ni (Tredoux *et al.*, 1989), and at the Bon Accord Ni-sulphide deposit, the value is about 1.23 % Ni, being concentrated in the siliceous rocks, but at varying stratigraphic positions and controlled by the schistosity, forming a series of overlapping sulphide lenses. The

western part of this mineralisation, the upper chert horizon, interfingers with a nickeliferous magnetite-chlorite rock (Keenan, 1986). These rocks consist of up to 70 % magnetite and were assumed by Keenan (1986) to be of similar mineralogy as the Bon Accord body. Locally, there are high concentrations of As in the Ni-sulphide body.

According to De Wit *et al.* (1987), the Barberton greenstone belt can be regarded as a remnant of the Jamestown ophiolite complex. According to Tredoux *et al.* (2010), the lowermost part of the Jamestown ophiolite complex is exposed on the Bon Accord stock farm, at the position of the Bon Accord Ni-oxide body. Owing to the highly unusual mineral paragenesis and to the deep mantle origin suggested by Tredoux *et al.* (1989), Tredoux *et al.* (2010) suggested to regard the Bon Accord Ni-oxide body as a new rock type named jamestownite.

The hematite-magnetite body shows a similar mineralogy as the Bon Accord Ni-oxide body, only that Fe plays the role of Ni. One can observe hematite and magnetite, and talc and chlorite are the hydrous minerals. In contrast to the Bon Accord Ni-oxide body, chromian spinel forms an intrinsic part of the deposit's mineralogy. In comparison to the Bon Accord Ni-oxide body, the hematite-magnetite body is depleted in Ni and enriched in Cr, As and Fe (Tredoux *et al.*, 1989). As this deposit became buried in the 1980s as a result of a tropical storm, it is difficult to locate samples for further detailed investigations about possible relations to the Bon Accord Ni-oxide body.

1.2 Mineralogy of the Bon Accord

The Bon Accord is composed of rare minerals; a number of them were described at this locality for the first time (De Waal, 1969, 1970a, 1970b, 1972; De Waal and Viljoen, 1971; De Waal and Calk, 1973; De Waal *et al.*, 1974). Besides the unusually high Ni values, the paragenesis itself is uncommon as well. This subsection gives an overview of the minerals occurring there and their known properties, sorted according to the Nickel-Strunz classification.

1.2.1 Silicates

Liebenbergite Ni_2SiO_4

According to the Nickel-Strunz classification, liebenbergite belongs to the nesosilicates without additional anions, and according to the Dana classification, it is the Ni-analogue of the olivine group $(Ni,Mg,Fe^{2+},Mn)_2SiO_4$ (Barthelmy, 2010). Table 1.5 gives the general chemical composition of liebenbergite. Its crystal system is orthorhombic, the cell parameters are a = 4.727 Å, b = 10.191 Å and c = 5.955 Å. This transparent to translucent mineral's colour in hand specimen is yellowish green with a vitreous to greasy luster; it has a white streak, a Mohs hardness of 6, and a calculated density of 4.6 g/cm³. The optical character is biaxial negative *(op.cit.)*.

Table 1.5 General chemical composition of liebenbergite in wt% (Barthelmy, 2010).

Mg	6.32
Si	14.61
Ni	45.79
O	33.29

Examined under the microscope in transmitted light, with uncrossed polarizers, liebenbergite was described to appear colourless to pale green to greenish yellow with clear pleochroism (Anthony *et al.*, 1995). De Waal and Calk (1973) reported that this mineral fills the interstices between the trevorite grains and to be almost

completely replaced by népouite.

In addition to this locality, liebenbergite has been found in the melt sheet of the Morokweng impact crater in South Africa (Andreoli *et al.*, 2008). A solid solution of synthetic liebenbergite toward synthetic forsterite was observed by Akimoto *et al.* (1976). The IMA accepted it as a new mineral species in 1973 (Barthelmy, 2010).

Népouite $Ni_3Si_2O_5(OH)_4$

According to the Nickel-Strunz classification, népouite belongs to the phyllosilicates with a kaolinite-like layer, and according to the Dana classification, it is the Ni-analogue of the serpentine-group $(Ni,Mg,Fe)_3Si_2O_5(OH)_4$ (Barthelmy, 2010). Table 1.6 gives the general chemical composition of népouite. Its crystal system is orthorhombic, the cell parameters are a = 5.27 Å, b = 9.14 Å and c = 7.24 Å. This semitransparent mineral's colour in hand specimen is intense pale green to deep green with a vitreous to pearly luster; it has a greenish white streak, a Mohs hardness of 2.5, and a calculated density of 3.2 g/cm³. The optical character is biaxial negative.

Table 1.6 General chemical composition of népouite in wt% (Barthelmy, 2010).

Si	14.77
Ni	46.30
H	1.06
O	37.87

Examined under the microscope in transmitted light, with uncrossed polarizers, népouite was described to appear colourless to dark green to yellow-green with weak pleochroism (Anthony *et al.*, 1995). De Waal and Calk (1973) described this mineral to result from the secondary replacement of liebenbergite.

Anthony *et al.* (1995) reported further occurrences of népouite from Népoui in New Caledonia, from a nickel mine in the Widgiemooltha district in Western Australia, from Pavlos in Greece, several nickel laterites, and others. In 1906 it has been accepted by the Pre-IMA as a new mineral species (Barthelmy, 2010).

Nimite $Ni_5Al(Si_3Al)O_{10}(OH)_8$

According to the Nickel-Strunz classification, nimite is a phyllosilicate with mica-like sheets, composed of tetrahedral and octahedral nets, and according to the Dana classification, it is the Ni-analogue of the chlorite group $(Al,Fe^{2+},Fe^{3+},Li,Mg,Mn,Ni)_{4\text{-}6}(Al,B,Fe^{3+},Si)_4O_{10}(OH,O)_8$ (Barthelmy, 2010). Table 1.7 gives the general chemical composition of nimite. Its crystal system is monoclinic, the cell parameters are a = 5.32 Å, b = 9.214 Å and c = 14.302 Å. This transparent to translucent mineral's colour in hand specimen is intense yellowish green with a pearly luster, having a white streak; it has a Mohs hardness of 3, and a calculated density of 3.1 g/cm³. The optical character is biaxial negative.

Table 1.7 General chemical composition of nimite in wt% (Barthelmy, 2010).

Mg	6.19
Al	8.09
Fe	5.86
Si	12.63
Ni	22.88
H	1.16
O	43.18

Examined under the microscope in transmitted light, with uncrossed polarizers, nimite appears yellow-green to apple green with faint pleochroism (Anthony *et al.*, 1995). De Waal (1970a) reported this mineral to form irregular veins in the willemseite and trevorite.

Nimite is not known to occur elsewhere in nature. The IMA accepted it to be a new mineral species in 1968 (Barthelmy, 2010).

Willemseite $Ni_3Si_4O_{10}(OH)_2$

According to the Nickel-Strunz classification, willemseite belongs to the phyllosilicates with mica-sheets, composed of tetrahedral and octahedral nets, and according to the Dana classification, it is the Ni-analogue

of the pyrophyllite-talc group $(Al_2,Mg_3,Fe^{2+}_3,Ni_3)Si_4O_{10}(OH)_2$ (Barthelmy, 2010). Table 1.8 gives the general chemical composition of willemseite. Its crystal system is monoclinic, the cell parameters are a = 5.316 Å, b = 9.149 Å and c = 18.994 Å. This translucent mineral's colour in hand specimen is pale green with a greenish white streak; it has a Mohs hardness of 2, and a calculated density of 3.3 g/cm³. The optical character is biaxial negative.

Table 1.8 General chemical composition of willemseite in wt% (Barthelmy, 2010).

Mg	3.99
Si	24.60
Ni	28.92
H	0.44
O	42.05

Examined under the microscope in transmitted light, with uncrossed polarizers, willemseite was described to appear colourless without pleochroism (Anthony *et al.*, 1995).

Willemseite is also reported from the Morokweng impact crater in South Africa. The IMA accepted it to be a new mineral species in 1970 (Barthelmy, 2010).

1.2.2 Oxides

Bunsenite NiO

According to the Nickel-Strunz classification, bunsenite belongs to the oxides with the metal:oxygen ratio 1:1, with small to medium-size cations only, and according to the Dana classification it is the Ni-analogue of the periclase group (Mg,Cd,Fe,Mn,Ni)O (Barthelmy, 2010). Table 1.9 gives the general chemical composition of bunsenite. Its crystal system is cubic, the cell parameter is a = 4.1769 Å. Anthony *et al.* (1997) described this transparent mineral's colour in hand specimen as pistachio green with a vitreous luster; it has a brownish-black streak, a Mohs hardness of 5.5, and a calculated density of 6.8 g/cm³. The optical character is isotropic.

Table 1.9 General chemical composition of bunsenite in wt% (Barthelmy, 2010).

Ni	78.58
O	21.42

Examined under the microscope in transmitted light, with uncrossed polarizers, bunsenite was described to appear pistachio-green with pleochroism to pale yellowish green. The crystals were described by Anthony *et al.* (1997) as minute octahedra which may be modified by the cube or dodecahedron faces.

Prior to its first discovery in nature, Professor Robert William Eberhard Bunsen (1811 – 1899) observed artificial bunsenite in his studies. Besides Bon Accord, bunsenite is observed to occur also in a Ni-U vein in Johanngeorgenstadt in Germany, also in the Morokweng impact crater in South Africa (Andreoli *et al.*, 2008), and in pressurized water reactors, together with trevorite and bonaccordite (Henshaw et al., 2006, Sawicki, 2008). The IMA accepted it as a grandfathered mineral species (Barthelmy, 2010).

Cochromite $(Co, Ni,Fe^{2+})(Cr,Al)_2O_4$ and Nichromite $(Ni,Co,Fe^{2+})(Cr,Fe^{3+},Al)_2O_4$

According to the Nickel-Strunz classification, cochromite and nichromite both belong to the oxides with the metal:oxygen ratio 3:4, with only medium-sized cations, and according to the Dana classification, cochromite is the Co-analogue and nichromite the Ni-analogue of the spinel group $(Co,Cu,Fe^{2+},Ge,Mg,Mn,Ni,Ti,Zn)(Al,Cr,Fe^{2+},Fe^{3+},Mg,Mn,Ti,V)_2O_4$ (Barthelmy, 2010).

Table 1.10 gives the general chemical composition for both minerals. The crystal system is cubic, the cell parameter is a = 8.29 Å. The colour of these opaque minerals in hand specimen is black with a metallic luster; they have a greenish grey streak, a Mohs hardness of 7, and a calculated density of 5.22 g/cm³. The optical character is isotropic (Anthony *et al.*, 1997).

De Waal (1978) interpreted these minerals to be intermediate members in a replacement reaction. Later, cochromite and nichromite became altered to trevorite. The trevorite forms a rim around grains of cochromite and nichromite. Furthermore, De Waal (1978) reported that these minerals typically occur within larger interstitial masses of silicates.

The present known occurrences of these minerals are limited to the Bon Accord in nature. The IMA approved them in 1978 (Barthelmy, 2010).

Table 1.10 General chemical composition of cochromite and nichromite in wt% (Barthelmy, 2010).

	cochromite	nichromite
Mg	1.17	-
Al	5.19	3.67
Cr	35.00	30.65
Fe	8.06	12.66
Co	14.17	10.69
Ni	5.64	13.31
O	30.77	29.02

Trevorite $NiFe^{3+}_2O_4$ and Ferroan Trevorite $(Ni,Fe^{2+})Fe^{3+}_2O_4$

According to the Nickel-Strunz classification, trevorite belongs to the oxides with a metal:oxygen ratio 3:4, with only medium-sized cations, and according to the Dana classification, trevorite is the Ni-analogue of the spinel group $(Co,Cu,Fe^{2+},Ge,Mg,Mn,Ni,Ti,Zn)(Al,Cr,Fe^{2+},Fe^{3+},Mg,Mn,Ti,V)_2O_4$ (Barthelmy, 2010). Table 1.11 gives the general chemical composition of trevorite. Its crystal system is cubic, the cell parameter is a = 8.839 Å.

Table 1.11 General chemical composition of trevorite in wt% (Barthelmy, 2010).

Mg	0.42
Al	0.12
Fe	55.16
Ni	16.71
O	27.6

In the thinnest fragments, the, mineral's colour in hand specimen is black with a greenish hue with a metallic luster; it has a black streak, a Mohs hardness of 5, and a calculated density of 5.1 g/cm³. The optical character is isotropic (Anthony *et al.*, 1997).

According to De Waal (1969) and De Waal (1972), trevorite forms a series with magnetite. Identification by optical microscopy alone is almost impossible, as the reflectivity in reflected light differs only insignificantly. The reflectivity of trevorite is 24 %, ferroan trevorite has a reflectivity of 21 % like magnetite. Trevorite has six to eight Ni ions per 32 O, ferroan trevorite four to six, nickeloan magnetite two to four and magnetite up to two. Trevorite, ferroan trevorite and nickeloan magnetite are strongly magnetic and show the same properties in reflected light as magnetite, but the rosy tint is less pronounced. Trevorite is weakly anisotropic. This mineral occurs in clusters of minute grains, commonly showing octahedral habit, embedded in willemseite. The trevorite may have replaced cochromite and nichromite (De Waal, 1978).

Trevorite (and ferroan trevorite) is also known from the Morokweng impact crater in South Africa, from a nickel-sulphide deposit at Mount Clifford in Australia, from a MORB from the southern East Pacific Rise, as well as from fuel crud deposits in pressurized water reactors, together with bunsenite and bonaccordite, as described by Henshaw *et al.* (2006) and Sawicki (2008). The IMA approved it as a grandfathered phase (Barthelmy, 2010).

1.2.3 Carbonates

Gaspéite $NiCO_3$

According to the Nickel-Strunz classification, gaspéite belongs to the alkali-earth (and other divalent metal) carbonates, and according to the Dana classification, it is the Ni-analogue of the calcite group $(Ca,Cd,Co,Fe,Mg,Mn,Ni,Zn)CO_3$ (Barthelmy, 2010). Table 1.12 gives the general chemical composition of

gaspéite. Its crystal system is hexagonal, the cell parameters are a = 4.608 Å and c = 14.805 Å. This translucent mineral's colour in hand specimen is light green with a vitreous to dull luster; it has a yellow-green streak, a Mohs hardness of 4.5 to 5, and a calculated density of 3.7 g/cm³. The optical character is uniaxial negative. Gaspéite has been observed to occur as aggregates of rhombic crystals, in nodular concretions, and commonly compact and massive.

Table 1.12 General chemical composition of gaspéite in wt% (Barthelmy, 2010).

Mg	6.75
Fe	5.17
Ni	32.58
C	11.11
O	44.4

Examined under the microscope in transmitted light, with uncrossed polarizers, gaspéite appears pale green to bright grass-green to olive green with weak pleochroism (Anthony *et al.*, 2003).

It was first discovered at Mount Albert, Gaspé Peninsula, in Canada. Besides this location and Bon Accord, gaspéite is only known from Kambalda in Western Australia and Bosnia and Herzegovina. The IMA accepted it to be a new mineral species in 1966 (Barthelmy, 2010).

Reevesite $Ni_6Fe^{3+}_2(CO_3)(OH)_{16} * 4(H_2O)$

According to the Nickel-Strunz classification, reevesite belongs to the carbonates with additional anions, with H_2O, with medium-sized cations, and according to the Dana classification it is the Ni-analogue of the sjogrenite-hydrotalcite group $(Mg,Ni)_6(Al,Cr,Fe^{3+},Mn)_2(CO_3)(OH)_{16} * 4(H_2O)$ (Barthelmy, 2010). Table 1.13 gives the general chemical composition of reevesite. Its crystal system is hexagonal, the cell parameters are a = 6.15 Å and c = 45.54 Å. This semitransparent mineral's colour in hand specimen is green-yellow to light yellow with a pearly luster; it has a white streak, a Mohs hardness of 2, and a calculated density of 2.8 g/cm³. The optical character is uniaxial negative.

Table 1.13 General chemical composition of reevesite in wt% (Barthelmy, 2010).

Fe	12.87
Ni	40.57
H	2.79
C	1.38
O	42.39

Examined under the microscope in transmitted light, with uncrossed polarizers, reevesite appears golden yellow without pleochroism (Anthony *et al.*, 2003). De Waal and Viljoen (1971) reported this mineral to form hexagonal platelets, occurring often in close proximity to violarite.

Reevesite has been reported first from the Wolf Creek meteorite occurrence in Western Australia, as well as from Clear Creek in California and on chromitite in Unst in Scotland. The IMA accepted it as a new mineral species in 1967 (Barthelmy, 2010).

1.2.4 Borates

Bonaccordite $Ni_2Fe^{3+}BO_5$

According to the Nickel-Strunz classification, bonaccordite belongs to the monoborates with additional anions, and according to the Dana classification, it is the isostructural Ni-analogue of the ludwigite group $(Fe^{2+},Mg,Ni)_2(Fe^{3+},Mn,Mg,Al,Sb,Ti)BO_5$ (Barthelmy, 2010). Table 1.14 gives the general chemical composition of bonaccordite. Its crystal system is orthorhombic, the cell parameters are a = 9.213 Å, b = 12.229 Å and c = 3.001 Å. This opaque mineral's colour in hand specimen is reddish brown

Table 1.14 General chemical composition of bonaccordite in wt% (Barthelmy, 2010).

Fe	21.15
Ni	44.46
B	4.09
O	30.30

with a vitreous luster; it has a brown streak, a Mohs hardness of 7, and a calculated density of 5.17 g/cm^3. The optical character is biaxial (Anthony *et al.*, 2003).

Examined under the microscope in transmitted light, with uncrossed polarizers, De Waal *et al.* (1974) described it reddish brown, without pleochroism; in reflected light, it is grey with a brownish tinge, also without reflection pleochroism. They observed it to be vein-forming but also developed as rosette-like radiating groups enclosed in the minerals liebenbergite and trevorite. Its anisotropism is medium to strong.

The present known occurrences of this mineral are limited to the Bon Accord in nature as well as fuel crud deposits in pressurized water reactors, together with bunsenite and trevorite, as described by Henshaw *et al.* (2006) and Sawicki (2008). The IMA approved it in 1974 (Barthelmy, 2010).

1.2.5 Unknown minerals

Besides these uncommon minerals, Tredoux *et al.* reported in 2006 at the Goldschmidt Conference the presence of a Ni-As-Sb phase, considered to be a new mineral species. This alloy has been observed in liebenbergite with a size generally smaller than 30 μm. Its composition was reported to vary between 15 % to 74 % Ni, 10 % to 80 % Sb and As less than 1 % to 20 %. Iron and S are sometimes present in minor amounts, less than 1 %. Arsenic and Sb seem to enter the same lattice position because of their inverse relationship. The suggested mineral formula is $Ni_7(As,Sb)_3$ and does not match with any known mineral. An origin by replacement of an Fe or S mineral has been excluded by Tredoux *et al.* (2006).

1.3 Rock classifications of the Bon Accord

The rocks from the Bon Accord deposit were classified by De Waal (1977) and Tredoux *et al.* (1989). De Waal (1977) described the material in a very detailed way, and his observations led to three groups and five subgroups, rock type I to V. The three main groups are the core zone, which means the centre of the deposit, the reaction zone, where alteration took place, and the metasomatic zone which contains the last of the subgroups, ending in the country rocks. The NiO concentration in the core zone of the deposit is about 36 % with depletion down to 10 % NiO in the last subgroup. Shearing increases in intensity from type I to type V.

Rock type I has been described as a massive trevorite-népouite rock with tightly packed trevorite-rich nodules that are embedded in the népouite. It is not sheared. This group's mineral assemblage has been reported to be trevorite, bunsenite, népouite, nimite, liebenbergite, gaspéite and bonaccordite as the major constituents; millerite, violarite, heazlewoodite and breithauptite are present in minor amounts. Chemical studies by De Waal (1979) reveal that bunsenite to occur in two generations, Fe-rich and Fe-poor. The Fe-rich generation has been interpreted to have formed concomitantly with liebenbergite, trevorite and bonaccordite whereas the second generation, the Fe-poor bunsenite, was formed during the serpentinization process. The first generation of bunsenite occurs in close association with trevorite, whereas the second generation occurs embedded in népouite. Prior to the serpentinization, he suggested that the primary assemblage was trevorite, liebenbergite, bonaccordite and, in part, bunsenite. Népouite, gaspéite, nimite and the bulk of bunsenite are considered to have formed during serpentinization. The trevorite, bunsenite and silicate occur in nodules and are arranged in a grid structure. Bonaccordite has been observed to form veins of acicular crystals throughout the whole

primary assemblage. In places, the bonaccordite veins are enclosed in liebenbergite and trevorite. The minute crystals of millerite occur with a patchy distribution enclosed in trevorite. Breithauptite, heazlewoodite and violarite are observed to be invariably associated with the hydrous phases but never to be enclosed in trevorite or liebenbergite. De Waal (1977) assumed this rock type to have existed only close to the present surface because it has never been encountered in the main mining pit. Between rock type I and rock type II there is a sharp contact with a sudden transition of népouite, liebenbergite and bunsenite to willemseite. De Waal (1977) reported the composition of trevorite to remain unchanged.

Rock type II is described to be a massive to sheared, fine-textured trevorite-willemseite rock. It is the least sheared rock type. The trevorite nodules appear pulled apart but still building coherent units. Traces of bunsenite are observed to remain enclosed in trevorite. Here, the mineral assemblage is reported to be trevorite, willemseite, nimite, gaspéite, millerite, violarite, heazlewoodite and remnants of bunsenite. The peculiar orbicular structures are interpreted by De Waal (1977) to result from the segregation of the trevorite in the trevorite-silicate nodules. The centres of these structures are reported to coincide roughly with the centres of the original trevorite-silicate nodules.

Rock type III is described to be a schistose ferroan trevorite – magnesian willemseite – nimite rock (De Waal, 1977). This type is sheared so that the original nodular units are pulled apart to form dispersed segregations of ferroan trevorite crystals. Prominent parallel veins of nimite and the alignment of willemseite flakes impart a schistosity. The bulk assemblage here is ferroan trevorite, magnesian willemseite, nimite and gaspéite; millerite and heazlewoodite but also goethite, violarite and reevesite form minor amounts.

Rock type IV is described by De Waal (1977) as mixed magnesian willemseite – chlorite – nickeloan magnetite schist. This schistose rock has mixed interlayered slabs consisting of a fine-textured schist, interpreted by De Waal (1977) to be related in origin to rock type III, and a coarse-textured schist, containing large crystals of nickeloan magnetite, resembling rock type V in structure. The contact between the fine-textured and the coarse-textured schist is sharp. The latter is regarded by De Waal (1977) as a recrystallization product of the fine-textured type. The bulk assemblage is magnesian willemseite, chlorite and nickeloan magnetite; pecoraite, reevesite and quartz are present in minor amounts in weathered material.

Rock type V is described to be nickeloan talc – nickeloan clinochlore – nickeloan magnetite schist, having the highest level of schistosity of all of the five rock types. According to De Waal (1977), the sheet silicates contain large crystals of nickeloan magnetite. Their size is up to 5 mm in diameter, whereas the trevorite and the ferroan trevorite are observed to be about 1 mm in diameter. The main assemblage is formed by nickeloan clinochlore, nickeloan talc and nickeloan magnetite. The minor assemblage is formed by pecoraite, reevesite and quartz in weathered material, as is the case in type IV. De Waal (1977) reported this type to follow the contact schist intermittently from the main mining pit to some 20 m to the east and lensing out in the country rock. De Waal (1977) interpreted this type to be a nickel-metasomatized variety of the contact schist.

In contrast to this detailed subdivision by De Waal (1977), Tredoux *et al.* (1989) subdivided their samples into visibly undeformed (type A) and visibly deformed (type B), whereupon these groups differ significantly in

their geochemistry. The Bon Accord A samples, representing the undeformed core of the deposit, are enriched in Sb, Ni and Fe, whereas the Bon Accord B samples, representing the deformed rim of the deposit, are enriched in As and LREE (Tredoux *et al.*, 1989). Both schemes of classification are presented in table 1.15.

Table 1.15 Classification of the Bon Accord after De Waal (1986) and Tredoux et al. (1989).

Tredoux et al. (1989)	undeformed core	deformed rim				
De Waal (1986)						
Structure	core zone: massive with modular structure	reaction zone: massive-to-sheared with pull-apart textures			metasomatic zone: schist	
Rock type	I	II	III	IV	V	country rock

The author prefers to use the classification of Tredoux *et al.* (1989). It appears to be more useful to allocate the samples in the deposit, because for some samples, one knows only from which part of the deposit they were taken, but without further details. An allocation of the samples after De Waal (1986) is not possible with the information available.

1.4 Formation of the Bon Accord

Bon Accord is a very unusual deposit. There is no occurrence of Ni mineralisation known to date having about 36 % NiO with the presence of S and Cu only in trace amounts. Also, its size with 3 m x 6 m x 0.35 m, is very restricted. The mineral paragenesis is uncommon as well. Several minerals have been described from this locality for the first time: trevorite, nimite, willemseite, reevesite, liebenbergite, bonaccordite, cochromite and nichromite. Népouite, gaspéite and bunsenite were known before De Waal's investigation (1977). These unique features led to very controversial discussions about the formation of the Bon Accord. This chapter is focused on the two main-hypotheses about the formation of this deposit and why other possibilities should be excluded.

1.4.1 The palaeometeorite hypothesis

De Waal (1977) is of the opinion that Bon Accord is the remnant of a Ni-Fe meteorite that experienced oxidation and further reaction with a peridotitic komatiite-type magma or rock. He regarded this mode of origin as capable of producing such a deposit. The necessary mass of a meteorite needed to be the precursor would have been 0.6 m^2 and does not seem to be unlikely (op. cit.); also the fall of a meteorite fits in the time of the late heavy bombardment, a period of meteorite impacts on the Earth, moon etc., as part of the late phase of formation of the solar system from 4.5 Ga to 3.5 Ga (De Waal, 1977; Press and Siever, 1995).

Bon Accord's special features and the dissimilarity with awaruite and josephinite led De Waal (1977) to assume that no terrestrial origin could have been responsible for the formation of such a deposit, especially because he assumed the deposit to be rootless, and that there is no sign of related material in the surrounding ultramafic host-rock (De Waal, 1979). Bon Accord as the result of an oxidized and reworked lump of awaruite is invalidated because of the high Ni to Fe ratio of awaruite, 1.8 to 3, relative to 1 for the deposit (De Waal, 1977; Chamberlain *et al.*, 1965; Tredoux *et al.*, 1989). In addition, the biggest known lump of awaruite has a

weight of 45 kg, which does not tally with the size and apparent rootless nature of the deposit (Dick, 1974; De Waal, 1977) at least as De Waal (1977) interpreted it. In his opinion, neither magmatic segregation nor simple residual enrichment seem to be possible mechanisms for such a high Ni content. A Ni-lateritic oxide deposit in a low-oxygen atmosphere is also regarded as unlikely. Furthermore the fact that Bon Accord shows chemical similarity with Ni-rich meteorites is seen to support the hypothesis of an altered Ni-Fe meteorite. De Waal (1979) proposed that his hypothesis is supported by the presence of Fe-poor Chromian spinel. The idea of Anhaeusser (1964) that aqueous solutions, derived from the Nelspruit granite, leached nickel from the ultramafic rocks and were finally precipitating their load in the shear zone on the interface of the quartzite and the talc-serpentine schist was ruled out by De Waal (1977), because the deformation event, which created these shear zones, predated the emplacement of the Nelspruit granite intrusion. A hydrothermal origin was eliminated by De Waal (1977) also because of the absence of a vuggy nature, the mineral zonation and the small size of the crystals; large ones are more typical of hydrothermal deposits. In addition to this, the Nelspruit granite [3.1 Ga (Oosthuyzen, 1970)] as well as the Stentor tonalite [3.1 Ga (Dziggel *et al.*, 2002)] postdate the 3.5 Ga old Bon Accord (De Waal, 1986; Tredoux *et al.*, 1989). Was Bon Accord an original sulphide deposit later involved in processes of desulphidation? De Waal (1977) also excluded this hypothesis because he saw no reason to favour the occurrence of such a process in a specific geological environment like this. One thing De Waal (1977) could not explain is the presence of bonaccordite in the primary assemblage, because boron is almost absent in meteorites, but enriched in the ultramafic rocks of the Barberton greenstone belt (Rankama and Sahama, 1968; De Waal, 1977; Byerly and Palmer, 1991) and known to concentrate in the fluid phase of magmas producing these rocks (De Waal, 1977). De Waal's (1977) only explanation for this is the possible supply of B by the initial reaction of the meteorite xenolith with the enveloping magma. Bird *et al.* (1974) suggested that Bon Accord could be an oxidized and partly altered body of core-derived Ni-Fe. De Waal (1977) ruled out this hypothesis, because of the unknown physical appearance and composition of such material.

1.4.2 The Earth's core hypothesis

Tredoux *et al.* (1989) took up the idea of Bird *et al.* (1974), that Bon Accord could represent a piece of the core-mantle boundary. Their model suggests that a metal-enriched mass formed in the lower mantle during inefficient separation of Fe-Ni alloy from the protomantle, which was destined for the core. This mass could have fractionated and become oxidized during its ascent through the mantle in a thermal plume, derived from the D" layer in the lowermost mantle. Some of its residue could finally have been incorporated as pods into the lithospheric mantle during the formation of the Achaean oceanic crust.

The hypothesis of De Waal (1977) was ruled out by the clearly different overall chemical character of Bon Accord from C-1 chondrites and Fe-rich meteorites (Tredoux *et al.*, 1989). It is reported to differ with the notable enrichment of Bon Accord in Ni, Au, As, Sb and LREE, relative to Fe-rich meteorites, and a slight depletion in Co and the very strong depletion in Fe. Moreover, the PGE trends do not match with those of meteorites; various interelement ratios are much higher in Bon Accord than those of any meteorites. On the contrary, the PGE trends of the Bon Accord A samples "are similar to those of Ni-Cu ore deposits associated with Archaean komatiites […] although absolute concentrations of these ore deposits are an order of magnitude lower than those of BA" (Tredoux *et al.*, 1989, page 805-806). Furthermore, the fact that the differences between the PGE patterns seem to be much greater for Os and Ir than for the other PGE was interpreted by Tredoux *et al.* (1989)

as indicative of a high-temperature process being involved, which would fit with the idea of the lower mantle as origin for the formation of Bon Accord. In summary, Tredoux *et al.* (1989) found neither geological nor geochemical data to support an extraterrestrial origin for the Bon Accord deposit. The formation of Bon Accord due to secondary alteration of a massive Ni-sulphide orebody was disposed of Tredoux *et al.* (1989) by the dissimilarity of the deposit's composition to Archaean sulphide deposits. Also a major desulphidation process would have been necessary to remove the S, but is not indicated by the mineralogical evidence. Could the Bon Accord deposit be chromitite pods that are associated with the lowermost peridotites of ophiolites? However, as a mode of origin for Bon Accord appears to Tredoux *et al.* (1989) to be unlikely because of the very distinctive PGE patterns of such pods, which do not match the patterns of Bon Accord. The formation of Bon Accord due to serpentinization during mid-ocean-ridge-type metamorphism is ruled out because the petrography of the Bon Accord rocks indicates the formation of népouite from liebenbergite after the liebenbergite-bunsenite assemblage (Tredoux *et al.*, 1989). The barrenness of PGE in awaruite is one more reason named by Tredoux *et al.* (1989). Also the formation of Bon Accord due to dynamothermal metamorphism during the emplacement of the granites is not accepted as a possibility by Tredoux *et al.* (1989). It was argued that Bon Accord, with its age of 3.5 Ga, predates the Stentor pluton [3.1 Ga (Dziggel *et al.*, 2002)], but the deposit could have been altered by later metasomatic fluids (Tredoux *et al.*, 1989). Also the possibility that Bon Accord has been originally a sulphide deposit is invalidated since there is no evidence for a desulphidation (Tredoux *et al.*, 1989). A hydrothermal – volcanic-exhalative origin is regarded as unlikely by Tredoux *et al.* (1989), as well. The general geochemistry of the deposit seems not to compare well with those of common volcanic-exhalative – hydrothermal ores (Tredoux *et al.*, 1989). These ores are generally enriched in chalcophile elements and depleted in siderophile elements, which is the opposite of the trend observed for Bon Accord. Again there is the lack of evidence for desulphidation *(op. cit.)*.

Though the palaeometeorite hypothesis and the Earth's core hypothesis are still very controversial, De Waal (1977) and Tredoux *et al.* (1989) each created a list of characteristics, that any model should attempt to explain.

List 1 – by De Waal (1977, page 94-95):

"Uniquity
Change in chemistry from rock I through rock IV to a peridotitic komatiite-type composition
Projected chemistry of the parent rock if the deposit represents a xenolith
High temperature mineral assemblage of rock I
Presence of bonaccordite and the fact that the mineral is, in places, enclosed in trevorite and liebenbergite
Internal structure of rock I
Sharp contact between the fine-textured and coarse-textured rock IV types
Size and apparent rootles (?) nature of the body
Increase in shearing and disruption of original trevorite-rich nodules from rock I to rock IV
The marked difference in the structure and texture of rock I to rock IV relative to the surrounding rocks
Absence of typical hydrothermal wall rock alteration
Absence of granitic material in the deposit"

List 2 – by Tredoux *et al.* (1989, page 806-807):

"The exceptionally high Ni contents of the ore and its unusual mineralogy
The position of the body within an extensive sheet of coarse-grained, chemically depleted ophiolitic ultramafics
Similar compositions of the chromite-spinels of BA and those of other local peridotites
The unusual trace element geochemistry, including the very low S and Cu contents
The fact that the Pb isotopes do not occur with meteoritic values and that they indicate an ancient U enrichment event
The strong similarity between the Pb-Pb and Sm-Nd isotopic data of BA and those of mafic-ultramafic rocks at other localities in the greenstone belt
The agreement of the available Os initial ratio with the Luck-Allegre mantle evolution line
The consistent bimodal grouping of the chemistry and isotopic ratios, which appears to reflect the control of two distinct mineral assemblages
The PGE geochemistry which is not only extraordinary in absolute concentrations of these elements but also in the two trends displayed between the groups
The association of BA with hornblende-tourmaline schist along its upper margin
The occurrence of a Pt-rich hematite-magnetite-chromite body, and low-grade Ni-sulphides in talc rocks, along strike from BA, as well as the complementary PGE patterns between BA and the HM body"

1.5 Objectives

The Bon Accord, with an age of 3.5 Ga is a very special Ni-oxide deposit in the Barberton region, South Africa, hosted by metaperidotites. Besides its small size of 6 m x 3 m x 0.35 m it is also special in terms of the composition of its rare minerals (bonaccordite, trevorite etc.) as well as the depletion in S and Cu. The deposit graded about 36 % NiO, but it was completely mined out several decades ago. The formation of the Bon Accord is still very controversial, with the two main hypotheses invoking a palaeometeorite and the Earth's core as a mode of origin. As no material is left in the pit and available sample material is very rare, it is difficult to study one of the most unusual deposits in the world.

Though several new minerals from the Bon Accord have been described, there is still need for a detailed documentation of the minerals there occurring, their texture and fabric as well as their mutual relations. Furthermore detailed mineral compositions are needed to better document the assemblages developed there. With these new data, the information gap about the extent of alteration, hydrothermal fluids and degree of metamorphosm can be filled and the influence on the mineralogy can be examined. Such information is necessary to draw conclusions about the primary mineral assemblage, prior to any change. This could help to focus the discussion about the existing hypotheses proposed to explain the origin and formation of this special deposit.

This investigation of the microscopic phases in the Bon Accord Ni-oxide body contains the following key questions:

Which minerals occur, and are further new minerals possibly present?
Which textural and fabric features can be observed?

What is the compositional variation of the minerals?

What are the relations amongst the minerals?

To what extent is the Bon Accord affected by external influences?

What was the primary mineral assemblage?

What could the parent rock of the Bon Accord have been?

Answers to these questions will contribute to a better understanding of the processes that led to this occurrences and possible analogues elsewhere.

2. Methodology

2.1 The samples

The Bon Accord deposit has been mined out since several decades; no material is left in situ. For this study, a total of 19 samples from old collections were gathered; the study was based on two polished in epoxy-resin-embedded sections, five polished and uncovered thin sections, and eleven small pieces of rock. Those pieces of rock are weathered, in part billets, in part simple pieces. The additional cut-rock samples were also prepared to acquire polished and uncovered thin sections at the Department of Geology, University of the Free, South Africa, and at the Department of Geoscience, Martin-Luther-University, Germany.

As no documentation now exists about the affiliation of most of the samples, it was not known if all of the samples belong solely to the Bon Accord Ni-oxide body or if there were also samples from the surrounding rocks amongst the collection. Eight samples (BA 83-1, BA 84-1, BA 84-2, BA 87-4, NCH7, NCJ5, NCJ8 and NCK6) were known to be definitely Bon Accord material right from the start, and one sample (BAE-2) to be definitely taken from the hematite-magnetite body. By use of the optical microscope and EPMA it was possible to identify and assign the samples. So in summary the samples BA 83-1, BA 84-1, BA 84-2, BA 87-1, BA 87-3, BA 87-4, BAD, BAU, NCH7, NCJ5, NCJ8 and NCK6 can be assigned to the Bon Accord Ni-oxide body, the samples cB S 1088 3a, cB S 1088 3b, cB S 1088 13a and BAE-2 can be assigned to the hematite-magnetite body, the samples BA-A S1 and BA-B S2 can be assigned to the chert and sample BAR9 can be assigned to the tourmaline-hornblende schist. All the samples are shown in figure 2.1a-f.

For intended TEM-analyses on some unknown ore-minerals in sample BA 87-4, three parts were cut out for further preparation (red marks in figure 2.1c). However, the material is so brittle that the final preparation for this method failed since the mineral of interest just broke.

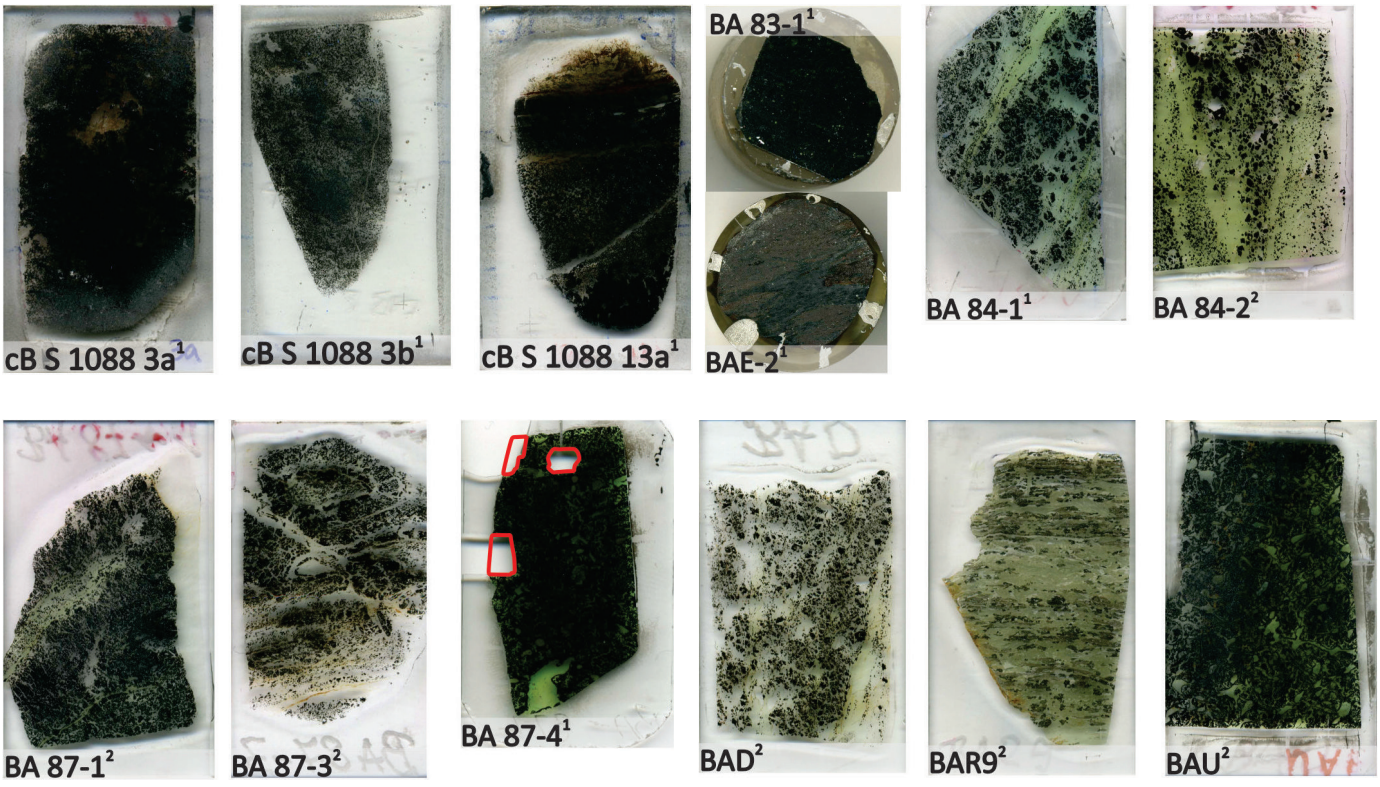

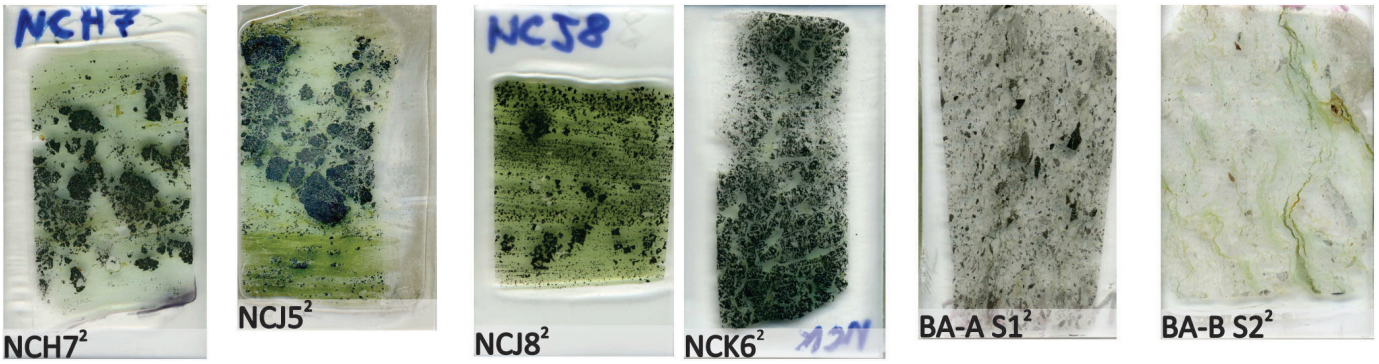

Figure 2.1 The samples. Starting from the top on the left: cB S 1088 3a, cB S 1088 3b, cB S 1088 13a, BA 83-1, BAE-2, BA 84-1, BA 84-2, BA 87-1, BA 87-3, BA 87-4, BAD, BAR9, BAU, NCH7, NCJ5, NCJ8, NCK6, BA-A S1 and BA-B S2. From sample BA 87-4 specific areas were cut out for analyses (red marks). [1]Received as thin section respectively in epoxy-resin embedded section; [2] Received as rock samples. Full-sized images of each sample are shown in Appendix 9A.

The use of a magnet pen revealed that the samples BA 84-2, BAD, BA 83-1, BA 84-1, BAU, BA 87-1, BA 87-3, BAE-2, BA 87-4 and cB S 1088 13a are magnetic, whereas BAR9, BA-B S2, BA-A S1, cB S 1088 3a and cB S 1088 3b are not.

2.2 Methods used for investigation

2.2.1 Optical microscopy in transmitted and reflected light

For optical microscopy, in epoxy-resin-embedded and polished and uncovered thin sections were used. Three different microscopes were used: an Olympus microscope with camera attachment, at the University of the Free State, a Nikon Optiphot 2 microscope with Pentax istDS camera attachment, at the University of Leipzig, Germany, and an Olympus BH2 microscope with camera attachment at McGill University in Montreal, Canada (figure 2.2). Photos were taken with a Canon DS126191 camera.

Figure 2.2 An Olympus BH2 microscope with tube for camera attachment (Linkenheld, 2010).

With the use of optical microscopy, it is possible to determine the minerals in the samples by their properties. For the identification of ore minerals, reflected light was used; the other minerals were determined with transmitted light. Every mineral has its own properties, for instance colour, pleochroism and cleavage. With knowledge of these properties, it is possible to identify the minerals. This and the textural and structural features in the sample provide information about the character of the material, from which it is possible to draw conclusions about the sample's mode of formation. Nevertheless, it is important to see that thin sections and epoxy-resin-embedded samples represent only a small portion of a formation. Point counting gives information about the modal proportions and was accomplished with a James Swift point counter.

2.2.2 Scanning Electron Microscope (SEM)

To become familiar with the rare minerals of the Bon Accord deposit, the SEM of the Centre for Microscopy at the University of the Free State) was used. The Shimadzu SSX550 instrument (figure 2.3) is equipped with an energy-dispersive X-ray analysis detector. Polished and uncovered thin sections as well as epoxy-resin-embedded sections of samples cB S 1088 3a, cB S 1088 3b, cB S 1088 13a, BA 84-1 and BA 87-4 have been analysed. The samples were coated with carbon and were fixed in the sample holder with carbon tape to prevent electrical charging, which affects the quality of measurements and mapping. The aim of these analyses was to identify the rare minerals. As no calibration was made on the SEM, only semiquantitative concentrations were obtained with cumulated results to 100 %. Quantitative results of the measurements are disregarded in this thesis. Elemental mapping was done as well; the maps are recorded in this thesis.

Figure 2.3 The SEM at the Centre of Microscopy at the University of the Free State, South Africa. This instrument is of the type Shimadzu SSX550 (UFS, 2011).

A SEM leads to a non-destructive analysis of solid surfaces. Its mode of operation is the creation of an electron beam in an electron source. The hot cathode, containing a tungsten filament, becomes heated and emits electrons. These electrons become accelerated in an electrical field of 30 kV. The electron beam created is used for the screening process in a high vacuum. With the support of magnetic coils the electron beam gets focused at one specific point at the surface of the sample. When the electron beam impinges on the sample, different interactions are possible. Their detection gives information about the composition of the sample.

2.2.3 Electron Probe Micro Analyser (EPMA)

To gain chemical data about the minerals in the samples, a JEOL 8900 EPMA (figure 2.4) from was used at McGill University in Canada. The polished and uncovered thin sections and epoxy-resin-embedded sections had to be coated with carbon and mounted in the sample holder.

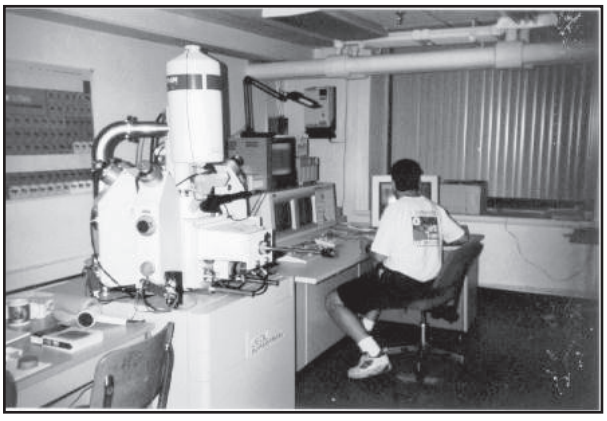

Figure 2.4 The JEOL 8900 EPMA at the McGill University, Canada (McGill, 2011).

The EPMA provides a non-destructive analysis of solid surfaces. Being fundamentally the same as the SEM, an electron beam is created and gets focused at a specific point of interest on the sample. X-rays are emitted. They are characteristic of every element, so it is possible to determine the proportion of emitted elements at the point of interest (figure 2.5). In this way, elements starting from the atomic number four (Be) are detectable. There is for every element a detection limit, dependent on the element's weight. The detection limits of the conducted analyses of the present study can be found in the appendix. This instrument has five wavelength-dispersive spectrometers (WDS), including one with a small Rowland

circle for trace elements, and four crystal spectrometers. The full integration of WDS and electron-dispersive spectrometers (EDS) allows simultaneous work on both of them. Secondary and back-scattered electron images are possible in a magnification range from 40 to 300.000 times and 70 nm resolution. Images can be acquired digitally by further processing with specific software. It is also possible to use high-resolution digital X-ray mapping with both WDS and EDS. For quantitative analyses, calibration of the EPMA for the minerals which are intended to be measured, has to been done to gain proper results. The results are dependent on the matrix of the elements. To be sure to analyse for every element present, EDS was done before each measurement. If there were other elements than it were calibrated for, those minerals were measured in another session with the correct calibration. Altogether, three measurement programs were prepared: one for oxides and silicates one for sulphides, sulphosalts, alloys and elements, and one for the silicates in sample BAR9 which contains minerals with boron, so different standards had to be used. All oxide and silicate minerals, including those of BAR9, are measured as oxides (for example SiO_2). The standards used for the single minerals are given in table 2.1. The measurement program for oxides and silicates contained in the first few measurement sessions ZnO, Na_2O and K_2O. Upon realising that those concentrations were predominantly zero, it was decided to leave them out for the further sessions since each measurement is more time-intensive, with the detection of 13 element oxides instead of ten. The measurements of

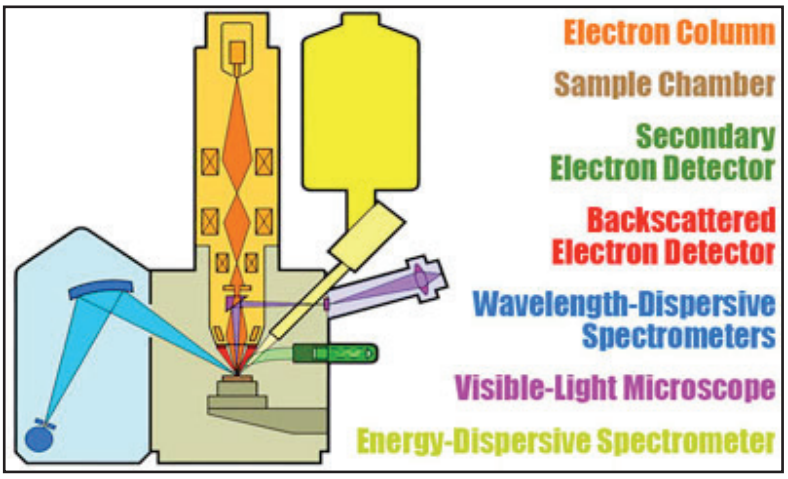

Figure 2.5 Schematic overview about the functionality of an EPMA (SERC, 2011).

Table 2.1 List of the standards used for the calibration of the EPMA. For different minerals different standards had to be used to obtain the best possible totals.

Measurement program	Element	Valence	Standards used		
Oxides and silicates	Si	4	olivine	Diopside	willemite
	Mg	2	chromite	olivine	Cal-STD
	Fe	2	Fe2O3_FeO	chromite	olivine
	Ca	2	Diopside		
	Ni	2	NiO		
	Al	3	chromite	Orthoclase	
	Cr	3	chromite		
	Ti	4	tio2		
	Zn	2	willemite		
	Co	2	Co	CanMetCoNiAs	
	Mn	2	spessartine		
	Na	1	Albite		
	K	1	Orthoclase		
Sulphides, sulphosalts, alloys, elements	As	5	CanMetCoNiAs	As	
	Fe	2	CanmetPyri	AstimexPend	
	S	6	CanmetCuS	CanmetPyri	NiS
	Ni	2	CanMetCoNiAs	Ni	NiS
	Co	2	CanMetCoNiAs	Co	
	Sb	5	CanmetStibnite	Sb	
	Zn	2	CanMetZnS		
	Te	4	CdTe		
	Cu	2	CanmetCuS	CanmetCPY	CPY
BAR9	Na	1	Tourmaline		
	F	-1	CaF2		
	K	1	CamecaOrth		
	Cl	1	vana2		
	Fe	2	Tourmaline		
	Mg	2	Diopside		
	Si	4	olivine		
	Ti	4	tio2		
	Ca	2	Diopside		
	Mn	2	spessartine		
	Al	3	Tourmaline		

the sulphides, sulphosalts, alloys and elements were problematic because of to their small size, being mostly less than 10 µm. Indeed, the electron beam was adjusted, but nevertheless elements from the surrounding minerals were picked up and distorted the analytical results. That is why for some analyses, one can trust the concentration of the major elements but not the concentration of the trace elements. These results have to be regarded with suspicion and are presented in Chapter four. The presence of divalent plus trivalent Fe within one mineral as well as poor preparation of some thin sections and epoxy-resin-embedded samples are one reason for low totals. Results with inacceptably low totals are disregarded.

2.2.4 Proton-Induced X-ray Emission Spectrometry on Micro Scale (µPIXE)

For special points of interest on a selected sample, the µPIXE at iThemba labs in Cape Town, South Africa, was used. The µPIXE is a nuclear-physics method for chemical, non-destructive analyses of different types of specimen, for example organic or geological samples. This method is very time-consuming, with several hours per measurement. For that reason, only one sample was selected for analyses, BA 87-4, which is definitely known to be Bon Accord A and being therefore least altered. The polished and uncovered thin section had to be coated with carbon and mounted on the sample holder. To prevent charging, carbon glue was applied on the glass. Depending on the elements of interest, a specific filter, where the beam transmits, had to be selected. If the interest is on heavy elements, as for instance Sn or Sb, it is difficult to observe the peaks owing to strong overlaps by lighter elements, for instance Si. For this reason, it is necessary to use a suitable filter for the elements of interest and to cut the detection of lighter elements so that only element peaks starting from a specific atomic number are detected.

The basic principle of the µPIXE is the creation of a charged proton beam in a proton accelerator (figure 2.6). The beam is defined by the object aperture and is sent to an evacuated chamber, which hosts the sample (figure 2.7 and 2.8). As in the case of the SEM and EPMA, the electrons in the innermost shells of the atoms become excited, and X-rays are emitted and recorded with a Si(Li) detector. The pulses from the detector are amplified and become registered in a pulse-height analyser. The quadrupole lenses give a demagnified image of the object aperture at the surface of the specimen. The detected spectrum contains peaks of all the elements in the area of interest, so peaks can easily overlap. For processing these data, specific software is necessary. To gain the chemical data on a specific point of interest, it is necessary to select this region and to fit the peaks.

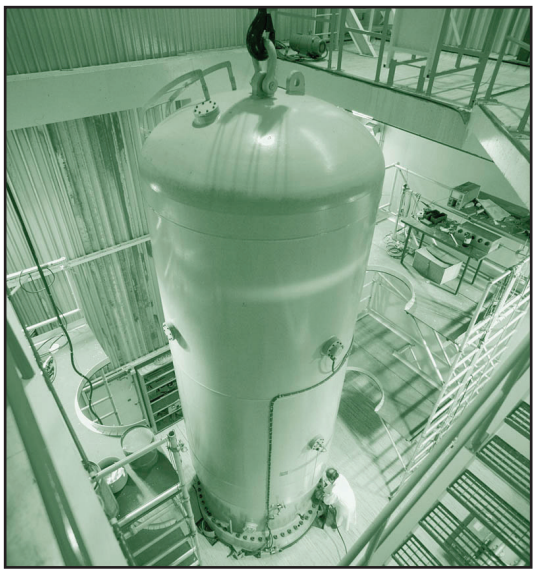

Figure 2.6 Van der Graaf accelerator as the one used for the beam generation. (EU, 2012).

The aim of this method is to obtain quantitative elemental maps of selected regions on the sample. Each pixel of the map represents its own quantitative analysis. GeoPIXE software (based on the IDL platform) was used for data processing, for example to determine the trace element composition of selected minerals, and the composition of selected regions or traverses. This method is dependent on the matrix of

the material, so subsequent data processing was necessary. The advantage of the µPIXE in comparison to an EPMA is the much lower detection limit for each element. But this is dependent on the scanning duration; the longer the measurement, the better the results (Winefordner, 1995).

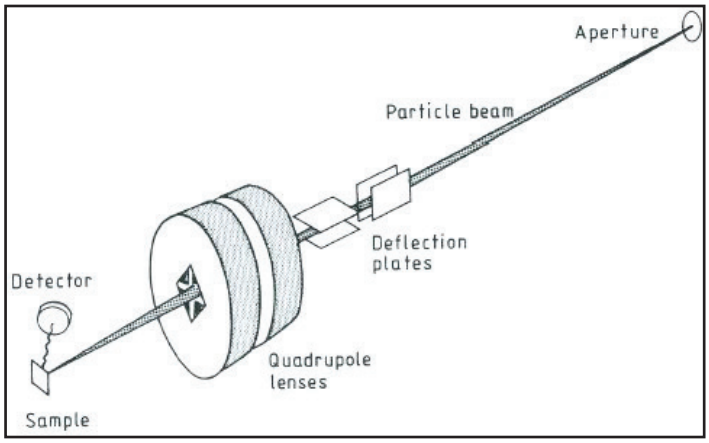

Figure 2.7 (left) The last part of the beam pipe with connection to the e Figure 2.9 A PANalytical WD-XRF Axios spectrometer as the one used in the Department of Geology at the University of the Free State, South Africa. (ETH, 2011). vacuated sample chamber of the µPIXE at iThemba labs in Cape Town, South Africa.
Figure 2.8 (right) A schematic sketch of the functional principle of the µPIXE. (Winefordner, 1995).

2.2.5 X-Ray Fluorescence (XRF)

As described, EPMA and µPIXE are the suitable methods to obtain in situ, mineral-chemical data, but to gain geochemical whole-rock data the XRF is a good analytical tool, but a destructive method. X-ray fluorescence means the emission of characteristic fluorescent X-rays from a material excited by bombardment with high-energy X-rays. Before the measurement, it is necessary to remove the weathered crust of the rock samples to provide fresh material. After this the rock needs to be crushed and milled to produce a fine and homogenized powder to avoid texture effects. This powder must be weighed and dried at about 100°C for about 24 hours and weighed again to determine the loss of adsorbed water. Then the dried powder has to be heated once more for four to five hours at 1000°C and weighed again. Now it is possible to calculate the loss on ignition (including the loss of organic matter). After this, the material needs to be mixed with 8 g analyte material and 3 g Hoechst wax in a mortar until homogenization is reached. Pellets have to be pressed from this mixture. These become inserted into the XRF (figure 2.9). The mode of operation of this machine is the ionization of the sample's atoms by exposition to short-wavelength X-rays, so that the sample material emits fluorescent radiation. These signals get processed as peaks and build a spectrum. With this method it is possible

Figure 2.9 A PANalytical WD-XRF Axios spectrometer as the one used in the Department of Geology at the University of the Free State, South Africa. (ETH, 2011).

to determine all elements from Be to U.

Since sample material of the Bon Accord is very rare and only available in limited quantities, the whole-rock composition data of Madala (2009) were used, because XRF is a destructive method. Four samples of the Bon Accord (BA 83-1, BA 87-1, BA 87-3, BA 84-1), one sample of the tourmaline-hornblende schist (BAR9) as well as one sample of the chert (BA-A S1) were examined within the present study. These match the material analysed by Madala (2009) material. The samples have been analysed for the ten major constituents SiO_2, TiO_2, Al_2O_3, Fe_2O_3, Cr_2O_3, MnO, CoO, MgO, CaO, K_2O. As the major constituent minerals at Bon Accord contain significant amounts of NiO on percent level, NiO was also included in the major element routine. In addition, the same set of samples has also been analysed for the 28 trace elements Sc, V, Cu, Zn, Ga, Ge, As, Br, Rb, Sr, Y, Zr, Nb, Mo, Cd, Sn, Sb, I, Ba, Yb, Hf, Ta, W, Hg, Tl, Pb, Bi and Th.

3. Petrography

3.1 Mineralogical description

This chapter deals with the microscopic description of the minerals bonaccordite, bunsenite, cochromite (including cobaltian chromite), liebenbergite, népouite, nimite, trevorite (including ferroan trevorite and nickeloan magnetite), willemseite, chromite, feruvite, hematite, ilmenite, magnesio-hornblende, magnetite, quartz and wüstite which could be determined under the optical microscope, sorted after Nickel-Strunz classification. The correct identification of the minerals is supported with EPMA measurements.

The minerals anilite, antimony, bornite, breithauptite, brookite, chalcocite, chalcopyrite, copper, digenite, gersdorffite, heazlewoodite, marcasite, millerite, nickel, nickeline, nisbite, orcelite, unknown #2, unknown #3, unknown #4, unknown #5, unknown #6, unknown #7 and wairauite were too small to be doubtless determined under the optical microscope but they were detected with the EPMA, so they are not described in this chapter. Unknown #1b and unknown #1c are indicated to be a new mineral species but it could not be proven in the present study. So here, unknown #1b and unknown #1c are for simplification attributed to trevorite. The silicate in the samples cB S 1088 3a, cB S 1088 3b could not be doubtless determined by use of both the optical microscope and the EPMA, and is therefore named unidentified silicate 1 for the samples cB S 1088 3a and cB S 1088 3b.

The silicate in sample BAE-2 could not be identified by use of the EPMA. Since this sample is an in epoxy-resin embedded sample, the optical microscope could not be used for identification, so this mineral is not described and named unidentified silicate 2.

The mineral actinolite could not be identified by use of the optical microscope but it is detected with the EPMA. Limonite, a mixture of goethite and lepidocrocite, occurs only as pigment and is therefore also not described.

The appearance of the minerals under the optical microscope in transmitted light (single and crossed polarizers) respectively reflected light is described. Bunsenite, liebenbergite, bonaccordite and hematite are described in reflected light as well to understand their relationship with in reflected light very similar ore minerals and to distinguish them from each other.

The mean reflectivity R of the minerals is estimated on the given values from Cameron (1966) and always compared with the reflectivity of trevorite which is about the same as magnetite.

The hardness of the minerals is described always in comparison with trevorite as reference point since trevorite / ferroan trevorite / nickeloan magnetite are present in most of the samples.

3.1.1 Silicates

Liebenbergite Ni_2SiO_4

Liebenbergite (figure 3.1) is an anisotropic mineral with grainy shape. The cleavability is indistinct and the relief is positive, moderately high (n = 1.6-1.7). Its colour in transmitted light is always yellow without pleochroism. The interference colour is a second order pink and green, with incomplete extinction. In reflected light the colour is dark grey, with an estimated reflectivity of R ~10 %. Liebenbergite appears to be slightly harder than trevorite, showing less intense polishing scratches. This mineral is observed to occur as inequigranular

single grains.

Népouite $Ni_3Si_2O_5(OH)_4$

Népouite (figure 3.2) is an anisotropic mineral with lath-shape but mostly flaky shape. The cleavability is clear and the relief is positive, moderately (n = 1.6-1.7), to no relief (n = 1.55-1.6). Its colour in transmitted light is differing significantly from sample to sample. The népouite appears colourless without pleochroism, showing interference colours of first order pink, yellow, blue and green; slightly pinkish greenish with weak pleochroism, showing interference colours of second order pink and green; but also colourless with weak pleochroism to slightly greenish, showing interference colours of first order brownish, dark grey and greyish white. This mineral is observed to occur as inequigranular single grains but also interwoven with each other and with willemseite.

Nimite $Ni_5Al(Si_3Al)O_{10}(OH)_8$

Nimite (figure 3.3) is an anisotropic mineral with mostly foliaceous but also flaky shape. The cleavability is distinct and the relief is positive, moderately to clearly high (n = 1.6-1.8). Its colour in transmitted light is varying clearly in the different samples. The nimite appears light yellow with weak pleochroism to yellowish green and greenish yellow, showing interference colours of first order brown, yellow, orange, light blue and light green; yellowish green with clear pleochroism to mint green and green, showing interference colours of first order grey and white, deformed crystals show first order yellow, pink, blue and green; slightly greenish without pleochroism, showing interference colours of first order grey, white, yellow and orange; colourless with very weak pleochroism to slightly greenish, showing interference colours of first order grey; yellowish green with clear pleochroism to green, showing interference colours of second order pink and green; yellowish green with weak pleochroism to applegreen, showing interference colours of first order orange, pink, blue and green. This mineral is observed to occur as inequigranular single flakes but also interwoven with willemseite.

Quartz SiO_2

Quartz (figure 3.4) is an anisotropic mineral with xenomorphic to grainy shape. The cleavability is indistinct and the relief is negative (n <1.55). In transmitted light it is colourless without pleochroism. The interference colour is of first order grey to white to yellowish, with undulatory extinction. This mineral is observed to occur mostly cryptocrystalline but also as inequigranular single grains.

Willemseite $Ni_3Si_4O_{10}(OH)_2$

Willemseite (figure 3.5) is an anisotropic mineral with mostly folicaceous, but also flaky and grainy shape. The cleavability is distinct and the relief negative (n <1.55). In transmitted light it is mostly colourless, often with very weak pleochroism to slightly pinkish and greenish, but it occurs also yellowish greenish without pleochroism. The interference colours differ significantly from sample to sample, showing first to fourth order but also abnormal interference colours. Those grains with slightly pinkish and greenish colours show always these colours as interference colours in different orders. Willemseite is observed to occur as inequigranular single flakes, but also as snarly tangle.

Unidentified silicate 1

This mineral (figure 3.6) is an anisotropic mineral with foliaceous and flaky shape. The cleavability is distinct and the relief is positive, moderately (n = 1.6-1.7). In transmitted light it is colourless without showing pleochroism. The interference colour is of first order grey, white and yellow, in places blue, with undulatory extinction. This mineral is inequigranular.

Magnesio-hornblende $Ca_2[(Mg,Fe)_4Al](Si_7Al)O_{22}(OH)_2$

Magnesio-hornblende (figure 3.7) is an anisotropic mineral with long-prismatic, actinomorphic shape. The cleavability is distinct and the relief is positive, clearly high (n = 1.7-1.8). In transmitted light it is pale brownish-yellow with very clear pleochroism to green. The interference colour is of first order orange, pink, purple and light blue. The magnesio-hornblende is inequigranular.

Feruvite $(Ca,Na)(Fe,Mg,Ti)_3(Al,Mg,Fe)_6(BO_3)_3Si_6O_{18}(OH)$

Feruvite (figure 3.8) is an anisotropic mineral with long-prismatic shape. The cleavability is indistinct and the relief is positive, extremely high (n > 1.8). In transmitted light it is light brown-reddish, in places also bluish-brown with strong pleochroism to dark brown. The interference colour is abnormal bluish green and greenish brown. The feruvite is inequigranular.

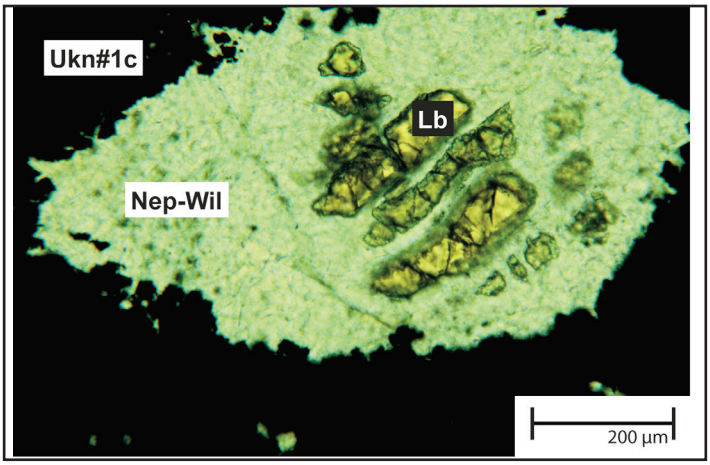

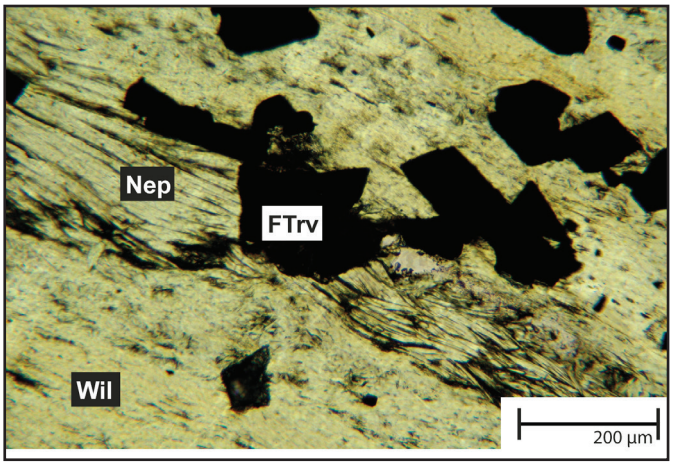

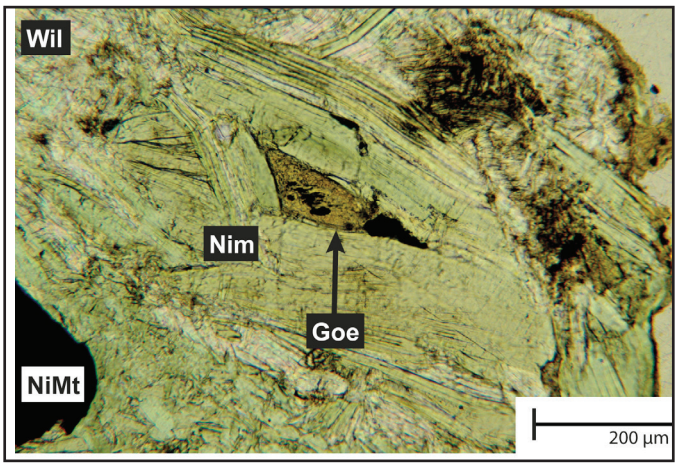

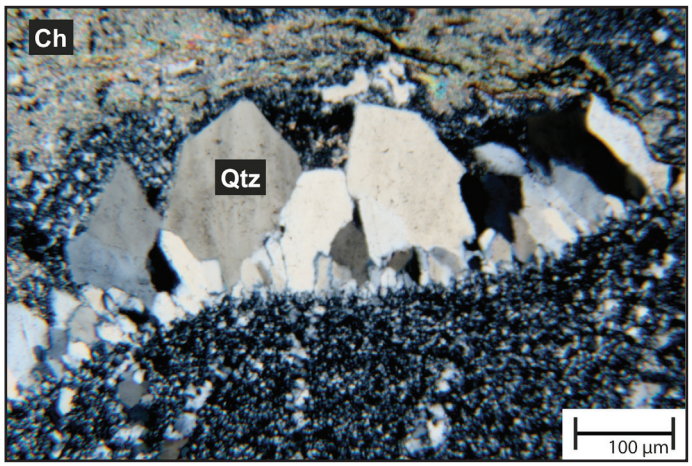

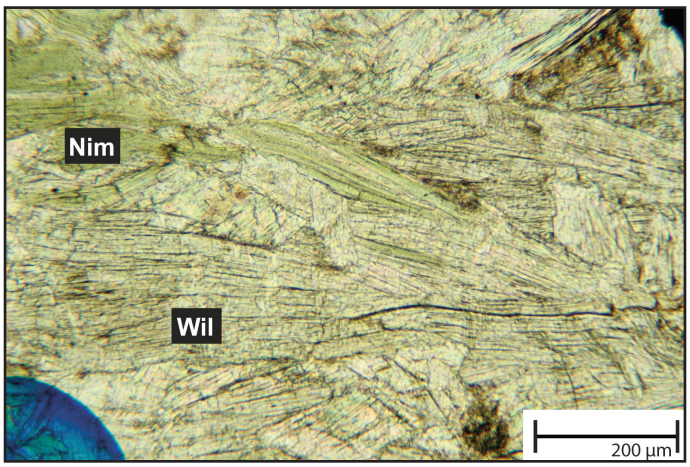

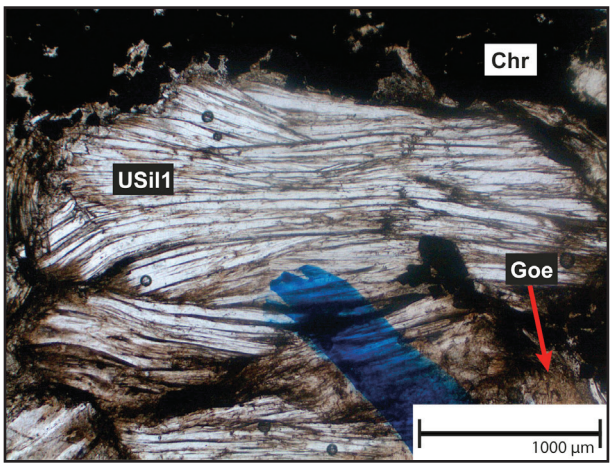

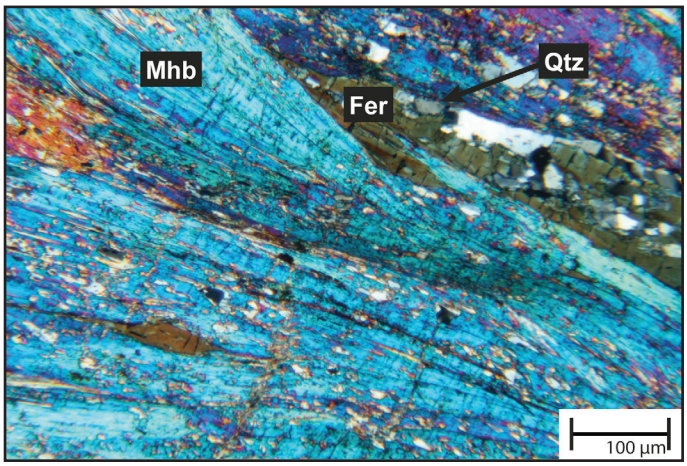

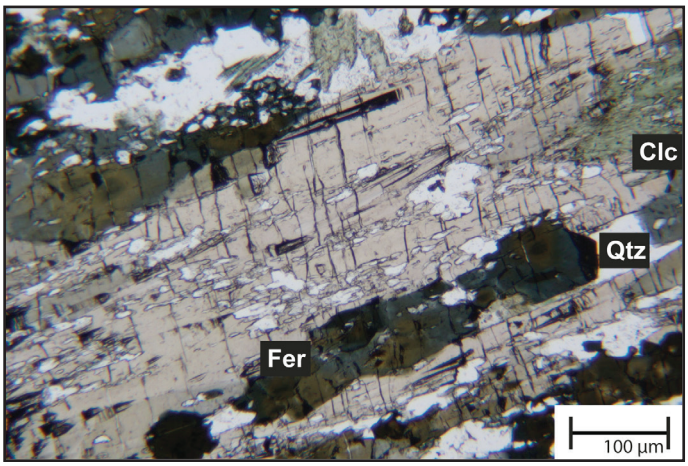

Figure 3.1 (previous page, top-left) Liebenbergite in a népouite-willemseite assemblage, together with unknown #1c – sample BA 87-4. Optical microscope, transmitted light, plane polarizer.
Figure 3.2 (previous pages, top-right) Népouite, together with willemseite and ferroan trevorite – sample NCJ8. Optical microscope, transmitted light, plane polarizer.
Figure 3.3 (previous page, bottom-left) Nimite, together with willemseite and nickeloan magnetite, altered with goethite – sample BA 84-2. Optical microscope, transmitted light, plane polarizer.
Figure 3.4 (previous page, bottom-right) Palisadequartz and cryptocrystalline quartz – sample BA-B S2. Optical microscope, transmitted light, crossed polarizer.
Figure 3.5 (top-left) Willemseite, together with nimite – sample BA 84-2. The blue colour is a mark from a pen. Optical microscope, transmitted light, plane polarizer.
Figure 3.6 (top-right) Unidentified silicate 1 together with chromite, altered with goethite – sample cB S 1088 3a. The blue colour is a mark from a pen. Optical microscope, transmitted light, plane polarizer.
Figure 3.7 (bottom-left) Magnesio-hornblende together with feruvite and quartz – sample BAR9. Optical microscope, transmitted light, crossed polarizer.
Figure 3.8 (bottom-right) Feruvite together with clinochlore and quartz – sample BAR9. Optical microscope, transmitted light, single polarizer.

3.1.2 Oxides and hydroxides

Bunsenite NiO

Bunsenite (figure 3.9) is an isotropic mineral with mostly xenomorphic and rarely grainy shape. The cleavability is indistinct and the relief is positive, clearly high (n = 1.7-1.8). Its colour in transmitted light varies from an intense dark green and yellowish green to greenish brown without pleochroism. The interference colour is abnormal dark bluish green. In reflected light the colour is dark grey with slight purple tint, with an estimated reflectivity of R ~10-15 %. Bunsenite appears to be way softer than the trevorite, showing much deeper polishing scratches. This mineral is observed to occur always as inequigranular crystal accumulations.

In one sample, bunsenite is enveloped by trevorite.

Cochromite $CoCr_2O_4$ and Cobaltian Chromite $(Fe,Co)Cr_2O_4$

Cochromite (figure 3.10) and cobaltian chromite were not distinguishable from each other with the optical microscope; they could only be distinguished from each other with the EPMA. Both minerals are isotropic with mostly hypidiomorphic shape. In some cases the rim appears diffuse. The cleavability is indistinct, the relief is positive, extremely high (n >1.8). Their colour in transmitted light is fuliginous without pleochroism. In reflected light the colour is grey with bluish tint, with an estimated reflectivity of R ~10-15 %. Cochromite and cobaltian chromite appear to have the same hardness as trevorite – the polishing scratches show the same intensity. These minerals are only observed as inequigranular single grains, enveloped by trevorite respectively enveloping the trevorite.

Trevorite $NiFe_2O_4$

Trevorite (figure 3.11) is an isotropic mineral with mostly xenomorphic and grainy shape, seldom hyp- to idiomorphic (four- and six-sided), lath-shaped trevorite is observed as well, also tiny roundish to lath-shaped trevorites in liebenbergites. The cleavability is not observable, the relief is positive, extremely high (n >1.8), but a little lower than the relief of cochromite and cobaltian chromite. Its colour in transmitted light is greyish black, a little lighter than cochromite and cobaltian chromite, without pleochroism. In reflected light the colour is white to cream white, with an estimated reflectivity of R ~20-25 %. Trevorite shows several slight but also deeper polishing scratches (figure 3.11). This mineral is observed to occur mostly as crystal accumulations but also as single crystals, being inequigranular, independent from the shape. It was impossible to distinguish trevorite, ferroan trevorite and nickeloan magnetite from each other so they are not described separately.

Chromite $FeCr_2O_4$

Chromite (figure 3.12) is an isotropic mineral with mostly hypidiomorphic but also xenomorphic shape. The cleavability is not observable, the relief is positive, extremely high (n >1.8). Its colour in transmitted light is ironblack with brown translucent rims without pleochroism. In reflected light the colour is dark grey with bluish tint, the rims are light grey. The inner part of the chromite shows an estimated reflectivity of R ~10 %, the rim is about R ~20 %. Chromite is harder than trevorite, the polishing scratches are much less intense than those of the trevorite. This mineral is observed as crystal accumulations but also as single grains, being inequigranular.

Hematite Fe_2O_3

Hematite (figure 3.13) is an anisotropic mineral. The cleavability is not observable, the relief is positive, moderately high (n = 1.6-1.7). Its colour in transmitted light is blood red without pleochroism. The interference colour is abnormal dark blood red. In reflected light the colour is grey, with an estimated reflectivity of R ~25 %. The hardness is not observable due to the small grain size. The mineral is observed as drops around wüstite, also as a vein, and as pigment – no crystal shapes and no grains are present. Hematite is also present as martite in wüstite.

Ilmenite $FeTiO_3$

Ilmenite (figure 3.14) is an anisotropic mineral with mostly xenomorphic shape. The cleavability is not observable, the relief is positive, moderately high (n = 1.6-1.7). Its colour in reflected light is brownish rosy with clear bireflectance, showing at the lightest position an estimated reflectivity of R ~20 %. Ilmenite is softer than trevorite, the polishing scratches are a little more intense than those of the trevorite. This mineral is observed as inequigranular grains in the trevorite but also as single grains in the willemseite.

Magnetite $Fe^{2+}Fe^{3+}{}_2O_4$

Magnetite (figure 3.15) is an isotropic mineral with grainy shape. The cleavability is not observed, the relief is positive, extremely high (n >1.8). Its colour in transmitted light is ironblack, without pleochroism. In reflected light the colour is whitish grey, with an estimated reflectivity of R ~20 %. No scratches could be observed. This mineral is observed to occur as inequigranular single grains and grain accumulations.

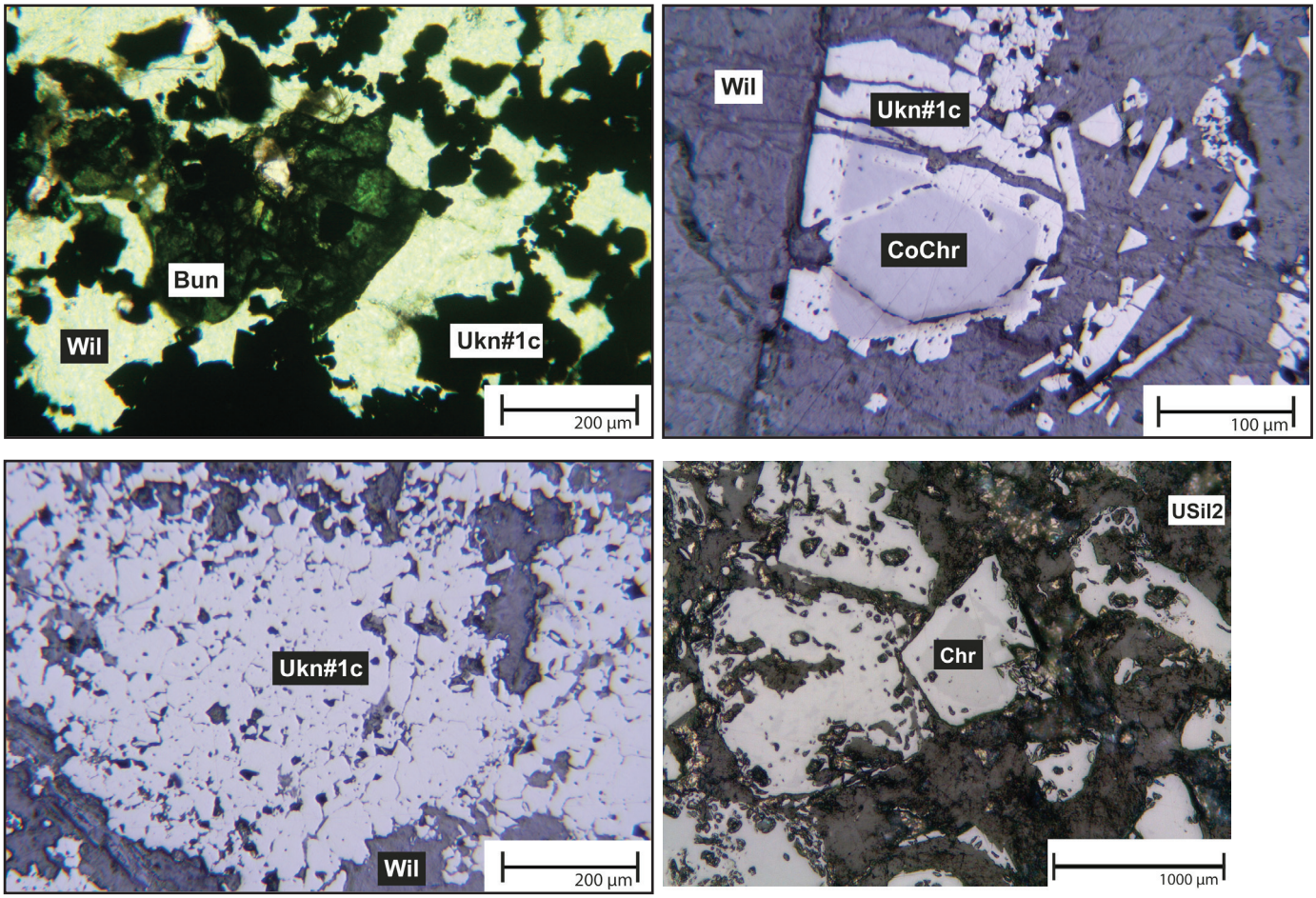

Figure 3.9 (top-left) Bunsenite in willemseite, together with unknown #1c – sample BA 87-4. Optical microscope, transmitted light, plane polarizer.
Figure 3.10 (top-right) Cochromite surrounded by unknown #1c in willemseite – sample BA 87-4. Optical microscope, reflected light, plane polarizer.
Figure 3.11 (bottom-left) Unknown #1c (no optical difference to trevorite) in willemseite – sample BA 87-4. Optical microscope, reflected light, plane polarizer.
Figure 3.12 (bottom-right) Chromite in unidentified silicate 2 – sample cB S 1088 3b. Optical microscope, reflected light, plane polarizer.

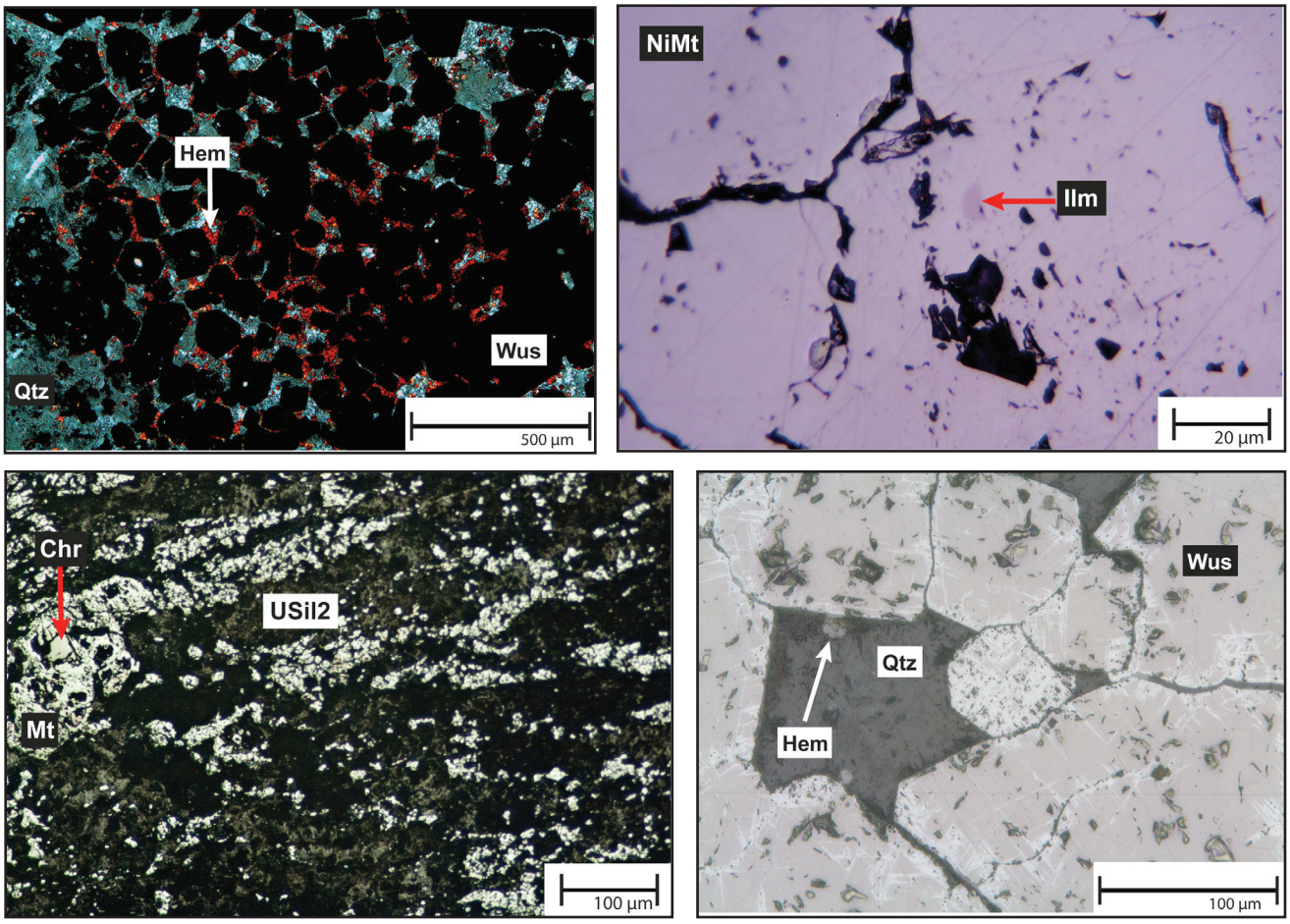

Figure 3.13 (top-left) Hematite around wüstite in quartz – sample cB S 1088 13a. Optical microscope, transmitted light, crossed polarizers.
Figure 3.14 (top-right) Ilmenite in nickeloan magnetite – sample BA 84-2. Optical microscope, reflected light, plane polarizer.
Figure 3.15 (bottom-left) Magnetite with chromite, in unidentified silicate 2 – sample BAE-2. Optical microscope, reflected light, plane polarizer.
Figure 3.16 (bottom-right) Wüstite with martitization (white) in quartz, hematite drops on the rim of wüstite – sample cB S 1088 13a. Optical microscope, reflected light, plane polarizer.

Wüstite FeO

Wüstite (figure 3.16) is an isotropic mineral with mostly idio- to hypidiomorphic shape (mostly six-sided, seldom four-sided), in some places the grains are grainy. The cleavability is distinct, the relief is positive, extremely high (n >1.8). Its colour in transmitted light is ironblack with brown translucent rims, without pleochroism. In reflected light the colour is grey with brownish tint, with an estimated reflectivity of R ~15 %. Wüstite shows several light but also deeper polishing scratches. This mineral is observed to occur as clear recognizable inequigranular single crystals, more or less martitized and surrounded by hematite drops (figure 3.16).

3.1.3 Borates

Bonaccordite Ni_2FeBO_5

Bonaccordite (figure 3.17) is an anisotropic mineral with acicular to prismatic shape. The cleavability is not observable and the relief is positive, moderately high (n = 1.6-1.7). Its colour in transmitted light is russet without

pleochroism. The interference colour is abnormal russet, the extinction could not be observed due to the small grain size. In reflected light the colour is grey, with an estimated reflectivity of R~15 %. Bonaccordite appears to be as hard as trevorite, the polishing scratches show the same intensity (figure 3.17). This mineral is observed to occur mostly as bunches of needles, but also as single needles and veinlets, being inequigranular.

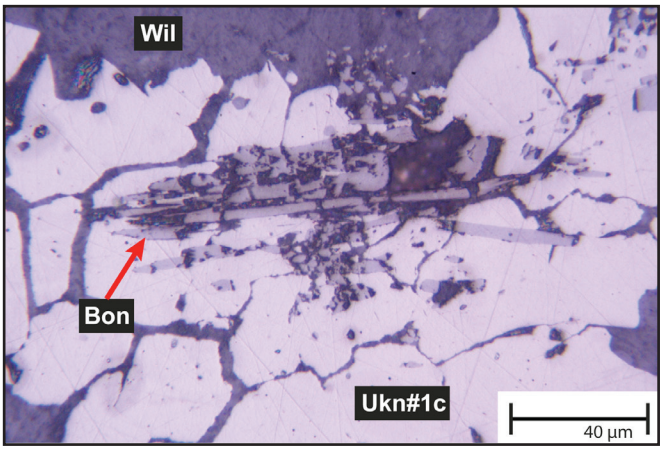

Figure 3.17 Bonaccordite in unknown #1c, together with willemseite – sample BA 87-4. Optical microscope, reflected light, plane polarizer.

3.2 Assignment of the samples

As mentioned in chapter 2 only the eight samples BA 83-1, BA 84-1, BA 84-2, BA 87-4, NCH7, NCJ5, NCJ8 and NCK6 were known right from the start to be definitely Bon Accord material; the sample BAE-2 is doubtless known to be definitely of the hematite-magnetite body. After detailed optical microscopy and the confirmation of the mineral identifications by use of the EPMA, the other samples can be palpably attributed. Since the samples BA 87-1, BA 87-3, BAD and BAU consist of the typical Bon Accord minerals bunsenite, cochromite / cobaltian chromite, liebenbergite, népouite, nimite, trevorite and willemseite it is doubtless sure that they belong to the Bon Accord body. The samples cB S 1088 3a, cB S 1088 3b and cB S 1088 13a resemble each other in their structure and consist mainly of chromite and magnetite resp. wüstite (plus hematite). Even though they do not resemble sample BAE-2 in their structure, it still suggests itself that these samples belong to the hematite-magnetite body as well due to their mineral composition. Sample BAR9 consists mainly of tourmaline and hornblende, due to that it can be attributed to the tourmaline-hornblende schist which occurs in the vicinity of Bon Accord. The samples BA-A S1 and BA-B S2 consist mainly of quartz so it can be assumed that these samples belong to the chert in the vicinity of Bon Accord.

3.3 Modal mineralogy

The modal proportions of all samples were determined by point counting, the results per sample are presented summarized in table 3.5 to 3.8. Detailed diagrams are provided in appendix B. For simplification the ore minerals (millerite, breithauptite, chalcocite etc.) are, where necessary, summarized after Nickel-Strunz classification accordingly as sulphides & sulphosalts and elements. For characterization of the modal mineralogy the terms major constituent for all minerals >5 %, minor constituent for all minerals between 1 % and 5 %, and accessory constituent for all minerals <1 % are used, supported with different shades of green, in which the dark green highlights the dominating minerals. The real amount of willemseite, liebenbergite and népouite in sample BA 83-1 could not be determined since this sample is embedded in epoxy-resin and these minerals are not clear identifiable in reflected light. Because of that the total amount of these three minerals is summarized and no detailed information is provided.Since it was not possible to distinguish the sulphides, arsenides, antimonides and elements from each other by use of the optical microscope, only their total percentage is given.

Table 3.1 Summary of the modal mineralogy of the Bon Accord samples. *) cochromite and nichromite are abbreviated with cochromite.

	Bon Accord A			contact	Bon Accord B							
	BA 87-4	BA 83-1	BAU	BA 87-1	BA 87-3	NCK6	BA 84-1	NCJ8	NCJ5	NCH7	BA 84-2	BAD
bonaccordite	1%	?										
bunsenite	3%	<1%	<1%									
liebenbergite	7%											
népouite	3%	47%	5%	35%	5%					3%		
willemseite	37%		45%	<1%	35%	50%	45%	45%	45%	47%	20%	30%
nimite	3%			17%	5%	3%	5%	25%	10%	10%	45%	25%
cochromite*	1%	<1%	<1%	<1%							<1%	
cobaltian chromite								<1%				
trevorite	40%	50%	45%	45%	50%			15%				
ferroan trevorite						45%	45%		35%	30%		
nickeloan magnetite											25%	30%
limonite			3%		5%			5%	5%	3%	1%	8%
ilmenite								<1%			1%	
sulphides, sulphosalts, elements	5%	3%	2%	3%	<1%	2%	5%	10%	5%	6%	8%	7%

Table 3.2 Summary of the modal mineralogy of the hematite-magnetite body samples.

	cB S 1088 13a	BAE-2	cB S 1088 3a	cB S 1088 3b
unidentified silicate 1			30%	50%
unidentified silicate 2		60%		
quartz	15%			
chromite		40%	70%	50%
magnetite				
hematite	5%			
wüstite	80%			
wairauite	<1%			
unknown #7	<1%			

Table 3.3 (left side) Summary of the modal mineralogy of the tourmaline-hornblende schist sample.
Table 3.4 (right side) Summary of the modal mineralogy of the chert samples.

	BAR9
magnesio-hornblende	57%
actinolite	<1%
feruvite	25%
quartz	17%
limonite	1%

	BA-A S1	BA-B S2
chromite		5%
wüstite		5%
hematite		10%
limonite		
brookite	5%	
quartz	85%	80%
sulphides & sulphosalts, elements	10%	<1%

In sample BAE-2 chromite and magnetite are also summarized to one value because it was not always possible to distinguish them from each other. The hematite and limonite in the chert sample BA-B S2 is summarized as well, a clear differentiation was not always possible.

3.3.1 The Bon Accord samples

Most of the Bon Accord samples are in general dominated by the major constituents trevorite / ferroan trevorite / nickeloan magnetite and willemseite with more or less the same percentage (table 3.1). The samples BA 87-1, NCJ8, BA 84-2 and BAD behave different. BA 87-1 is dominated by trevorite and népouite plus a distinct lesser amount of nimite. NCJ8 is clearly dominated by willemseite; nimite and ferroan trevorite belong also to the dominating majority but with definite decreased percentage. Liebenbergite, only present in Bon Accord A, nimite in the samples NCJ5 and NCH7, plus limonite in BAD are no dominating part but still present as major constituents. Bonaccordite and bunsenite are only observed in Bon Accord A being mostly accessory constituents; bonaccordite, bunsenite and népouite are also present as minor constituents in sample BA 87-4. Except from its dominating role in the contact, népouite is also a minor constituent in Bon Accord A and B. Willemseite is a dominating major constituent with the exception of the contact, there it occurs only as an accessory constituent. Apart from its dominating presence in the contact and Bon Accord B, nimite forms also a minor constituent in the latter and is also observed in sample BA 87-4 of Bon Accord A, being there a minor constituent as well. Cochromite / nichromite occurs as minor constituent in sample BA 87-4, else only as an accessory constituent. Ilmenite is only observed in Bon Accord B, being a minor and accessory constituent. Limonite occurs in Bon Accord A and B, except from sample BAD it is present as minor constituent. The sum

of the sulphides & sulphosalts and elements varies from being an accessory constituent in sample BA 87-3 to being also a major constituent in the samples NCH7, BA 84-2 and BAD. In the other samples they are minor constituents.

3.3.2 The hematite-magnetite body samples

The samples of the hematite-magnetite body differ in the distribution of their modal proportions (table 3.2). Sample cB S 1088 3a and cB S 1088 13a are dominated by chromite respectively wüstite. Unidentified silicate 1 respectively quartz are also major constituents but with clearly lesser percentage. Sample cB S 1088 3b is dominated by chromite and unidentified silicate 1, having the same values. BAE-2 is the only sample which is not dominated by the ore but by unidentified silicate 2, but magnetite plus chromite are also major constituents. Minor and accessory constituents are only present in sample cB S 1088 13a, being hematite, wairauite and unknown #7.

3.3.3 The tourmaline-hornblende schist sample

The sample of the tourmaline-hornblende schist shows a clear dominance of magnesio-hornblende, but feruvite and quartz are also major constituents (table 3.3). Limonite is present as a minor constituent, the actinolite occurs as accessory constituent (not observed but identified by use of the EPMA).

3.3.4 The chert samples

Both chert samples are extremely dominated by quartz, but hematite plus limonite in BA-B S2 and the sulphides and elements in BA-A S1 are also major constituents (table 3.4). Chromite, wüstite and brookite are present as minor constituents, the sulphides and elements in sample BA-B S2 are only accessory.

3.4 Texture and structure

In this chapter the fabric of the samples is described, sorted after the different sample groups Bon Accord, hematite-magnetite body, tourmaline-hornblende schist and chert. The samples are pictured in appendix A, each on one page.

3.4.1 The Bon Accord samples

Since the samples vary clearly in their texture and structure they are described in groups I-IV, group I being the most massive samples and group IV the least.

Group I: BA 87-4, BA 83-1 and BAU

The structure is isotropic and massy. Trevorite forms a grid structure, the silicates are arranged in nodules and orbicules (figure 3.18) with different size and shape, visible to the naked eye (appendix 9A). In sample BAU the grid structure is more loose, the nodules and orbicules are often interconnected and bigger than in sample BA 87-4 and BA 83-1. The orbicular structures contain mesh-textured relic liebenbergite, relic népouite and willemseite (figure 3.18). The relic liebenbergite grains in the orbicules extinct all at the same

time. Bonaccordite forms veins in the willemseite and is intergrown with trevorite (figure 3.17). Bunsenite in sample BAU occurs enveloped in trevorite, showing typical replacement texture by the trevorite (figure 3.19). Bunsenite in the samples BA 83-1 and BA 87-4 occurs in the willemseite, replacing the xenomorphic trevorite (figure 3.9); the cochromite / nichromite show resorption structure, becoming replaced by the trevorite (figure 3.10). Liebenbergite is strongly serpentinized and mesh-textured (figure 3.18). Most of the liebenbergite grains contain tiny inclusions of trevorite (figure 3.20). Népouite is strongly altered to willemseite, only relics of népouite surround the remnants of liebenbergite (figure 3.18). Nimite occurs in the willemseite as small flakes. Hypidiomorphic trevorite replaces cochromite, and the xenomorphic trevorite becomes replaced by bunsenite. The lath-shaped trevorite occurs around the liebenbergite (figure 3.20). The xenomorphic, hypidiomorphic and lath-shaped types of trevorite appear solved (figure 3.10, 3.14 and 3.20), sample BA 87-4 contains the least solved trevorite, in sample BA 83-1 it appears more solved and sample BAU contains the most solved trevorite in the samples of this group. Furthermore the trevorite in sample BAU encloses orcelite and unknown #4 (see chapter 4 for detailed mineral chemical analyses), all of them with embayment structure, typical for replacement by the surrounding mineral. Nisbite occurs in direct contact to trevorite, replacing it and filling the interstices of an unidentified mineral, replacing this as well, showing always typical embayment structure (figure 3.21). In sample BA 87-4 heazlewoodite (figure 3.22) and unknown #2 occur in the népouite-willemseite assemblage, becoming replaced by the latter. Nisbite is present in the népouite-willemseite assemblage as well, but in direct contact to the trevorite, showing solvation structure. The xenomorphic trevorites of sample BA 83-1 contain millerite, replacing it. Unknown #2 and unknown #3 occur in the népouite-willemseite assemblage, with slight to stronger embayment structure, typical for becoming replaced. Willemseite is the alteration product of liebenbergite and népouite, and forms the major part of the silicate mass.

Group II: BA 87-1 and NCK6

The structure is isotropic and massy but to a lesser extent than group I. In both samples the trevorite shows a more loose grid structure than the previous ones, being the loosest in sample NCK6. Orbicular structures are not observed, but the nodules are clear to see with the naked eye (appendix A). In sample BA 87-1 the népouite, the alteration product of liebenbergite, and nimite form together the groundmass. Furthermore, nimite forms wavelike veins of different size (figure 3.23), following one direction (appendix A), single-grained trevorite in and around these veins follows the waves. In general, the main part of the trevorite is xenomorphic, the minor part is four- and six-sided, some lath-shaped trevorite is present as well. The xenomorphic trevorite forms aggregates, the other trevorites occur as single grains. All of the trevorite is strongly solved (figure 3.24). The hypidiomorphic trevorite replaces cochromite, showing resorption structure (figure 3.24). The xenomorphic trevorite in sample BA 87-1 encloses breithauptite, heazlewoodite (figure 3.25) and orcelite, all of them showing embayment structure, typical for replacement by the trevorite. The xenomorphic trevorites of sample NCK6 enclose millerite with typical embayment structure. Marcasite occurs in the népouite-willemseite assemblage, showing embayment structure as well. In contrast to this the groundmass of sample NCK6 is formed by willemseite, the alteration product of népouite, with a little nimite; népouite is not present. Here, the nimite occurs as bigger flakes in the willemseite. Most of the trevorite is present as aggregates, some single grains are observed as well. All of the trevorite is strongly solved (figure 3.26). Millerite occurs enclosed in the trevorite aggregates with embayment structure, marcasite occurs in the willemseite, showing embayment structure as

well.

Group III: BA 84-1, BA 87-3 and BAD

The structure is isotropic and, in contrast to group I and II, loose. The trevorite occurs as aggregates and single grains, the grid structure is not present. Orbicules are absent; the nodules can be observed just roughly (appendix A). Nimite forms wavelike veins in sample BA 84-1 and BAD but occurs in all samples also as flakes with kink band deformation (figure 3.27). The nimite and willemseite together form the groundmass, containing flakes of népouite. Trevorite is strongly solved and forms xenomorphic aggregates (figure 3.28), four-sided single grains and lath-shaped trevorite is also present. The trevorite which occurs in the nimite veins follows the wavelike direction (figure 3.29). In sample BA 84-1 breithauptite, orcelite, millerite (figure 3.30) and unknown #5 are enclosed in the xenomorphic trevorite, showing embayment structure. Breithauptite, nickeline, orcelite, millerite and unknown #5 are enclosed in the xenomorphic trevorites of sample BAD. BA 87-3 contains sulphides and / or sulphosalts as well, but they could not be analysed due to their too small grain size.

Group IV: BA 84-2, NCJ8, NCJ5 and NCH7

These samples differ significantly in their texture and structure from the other groups. Sample BA 84-2 and NCJ8 are layered whilst NCJ5 is just partly layered; in sample NCH7 just a little part appears layered; all of these samples show glomerophyric texture. The grain size of trevorite differs considerably – xenomorphic megacrysts occur in a groundmass of nimite and willemseite, together with much smaller hypidiomorphic to grainy and lath-shaped trevorite. The smaller grains follow the layered structure; it is not distinguishable if the megacrysts follow the layering as well or not (appendix A). Except from sample BA 84-2 the nimite forms wavelike veins, the deformation is best observable in sample NCJ5 (figure 3.31). In sample BA 84-2 the nimite is present as flakes with isotropic structure (figure 3.3). The groundmass consists of nimite and willemseite which are interwoven with each other (figure 3.5). Flakes of népouite also occur in the groundmass. Cochromite and cobaltian chromite show resorption structure, becoming replaced by trevorite in sample BA 84-2 and NCJ8. All trevorite is extremely solved in comparison with the groups I, II and III (figure 3.32). Only the trevorite megacrysts in the samples NCJ8, NCJ5 and NCH7 contain mineral inclusions. These are for sample NCJ8 heazlewoodite, millerite, chalcocite (figure 3.33) and digenite; in sample NCJ5 it is breithauptite, millerite, unknown #5 and unknown #6; in sample NCH7 it is nickeline, millerite, unknown #5 and bornite. The xenomorphic trevorites in sample BA 84-2 contain inclusions of millerite. Nearly all of these inclusions show embayment structure, some of them still with hypidiomorphic shape (figure 3.33). Anilite and pure copper (figure 3.34) occur in the groundmass of sample BA 84-2 as well. Ilmenite occurs in the trevorite megacrysts and in the groundmass of the samples BA 84-2 and NCJ8 (figure 3.34).

Summary of the minerals found in the Bon Accord body

After detailed microscopy and chemical mineral identification it is possible to allocate the Bon Accord samples to the classification of Tredoux *et al.* (1989). The samples BA 87-4, BA 83-1 and BAU are the solely samples without any deformation, so they can be allocated to Bon Accord A, supported with the presence of

trevorite which occurs roughly in the centre of the deposit (De Waal, 1977). The samples NCK6, BA 84-1, BA 87-3, NCJ8, NCJ5, NCH7, BA 84-2 and BAD show clear deformation and belong definitely to Bon Accord B, supported with the presence of ferroan trevorite, occurring in the inner part of the rim (De Waal, 1977), and furthermore supported with the presence of nickeloan magnetite, occurring in the outer part of the rim (De

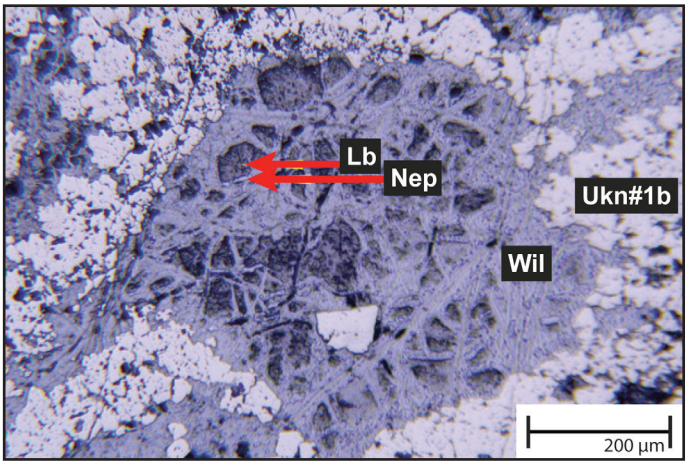

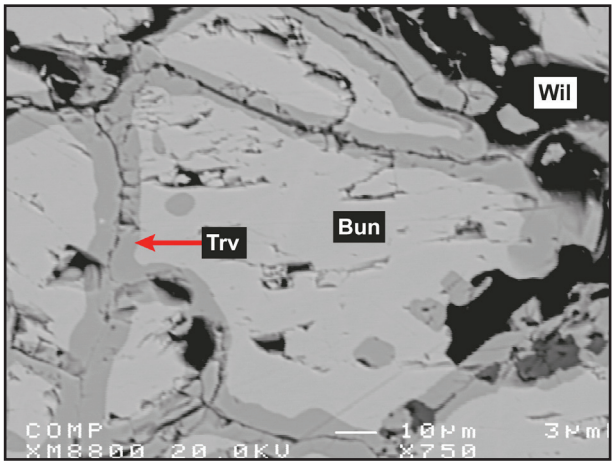

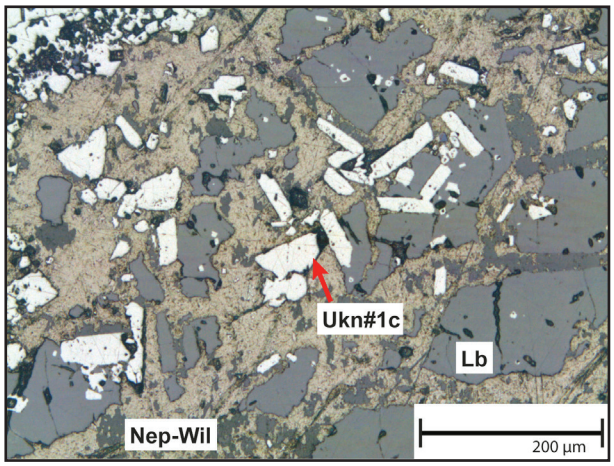

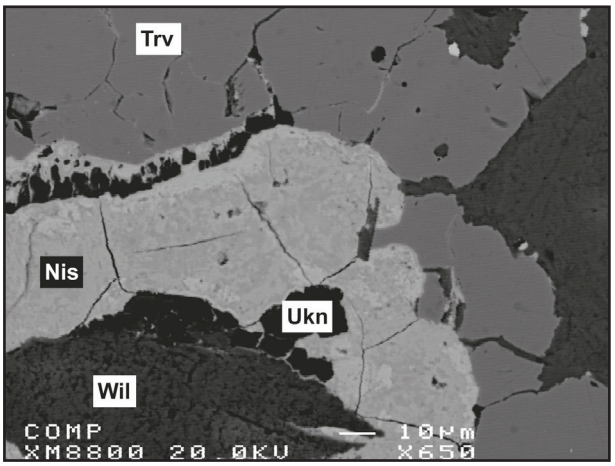

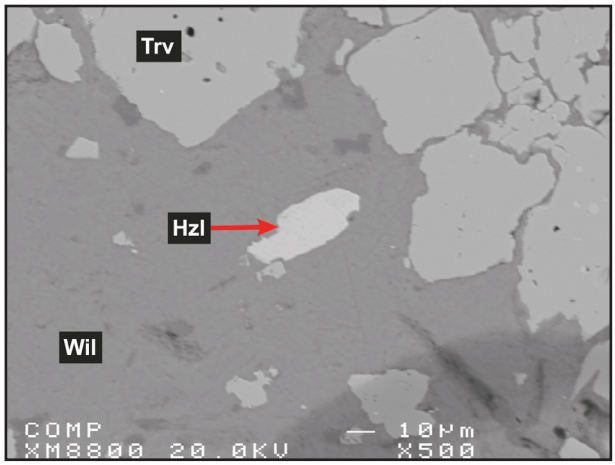

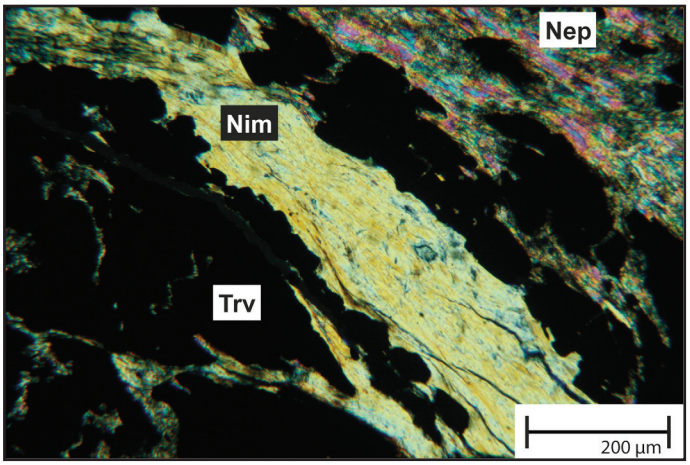

Figure 3.18 (top-left) Orbicular structure in sample BA 83-1. Relic liebenbergite with relic népouite on the margin, in willemseite, surrounded by xenomorphic unknown #1b – sample BA 83-1. Optical microscope, reflected light, single polarizer.
Figure 3.19 (top-right) Bunsenite enveloped by trevorite in willemseite – sample BAU. EPMA, backscatter image.
Figure 3.20 (middle-left) Relic liebenbergite containing small grains of unknown #1c, surrounded by lath-shaped unknown #1c, with relic népouite in willemseite; xenomorphic unknown #1c is around – sample BA 87-4. Optical microscope, reflected light, single polarizer.
Figure 3.21 (middle-right) Nisbite, surrounded by an unidentified mineral and willemseite, replacing trevorite – sample BA 83-1. EPMA, backscatter image.

Figure 3.22 (previous page, bottom-left) Heazlewoodite with embayment structure in willemseite, surrounded by trevorite with unidentified inclusions – sample BA 87-4. EPMA, backscatter image.
Figure 3.23 (previos page, bottom-right) Nimite vein surrounded by trevorite together with népouite– sample BA 87-1. Optical microscope, transmitted light, crossed polarizer.

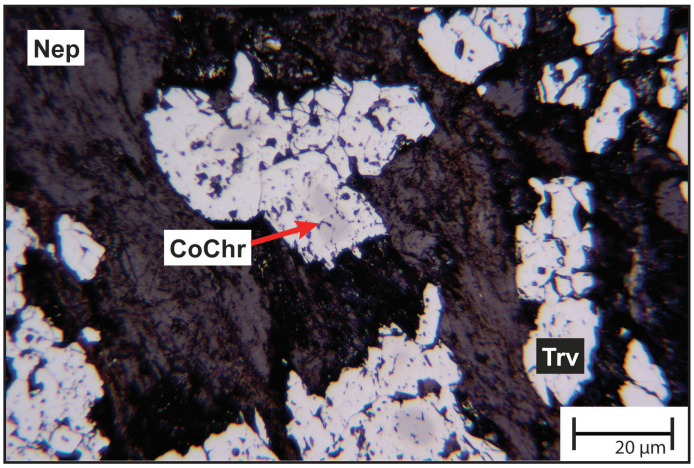

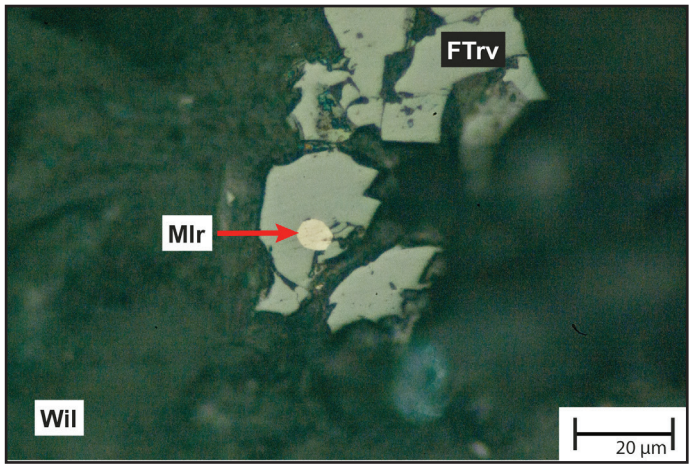

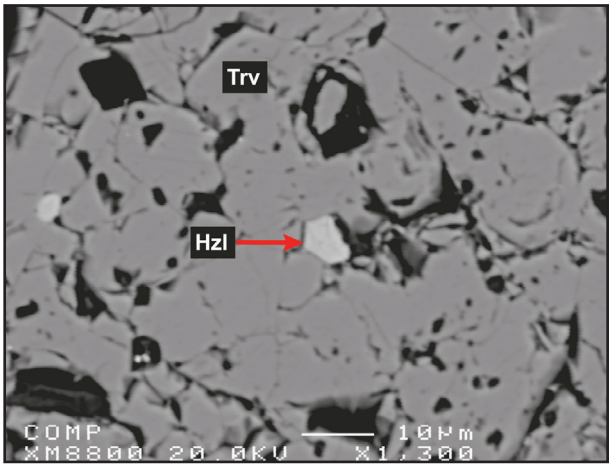

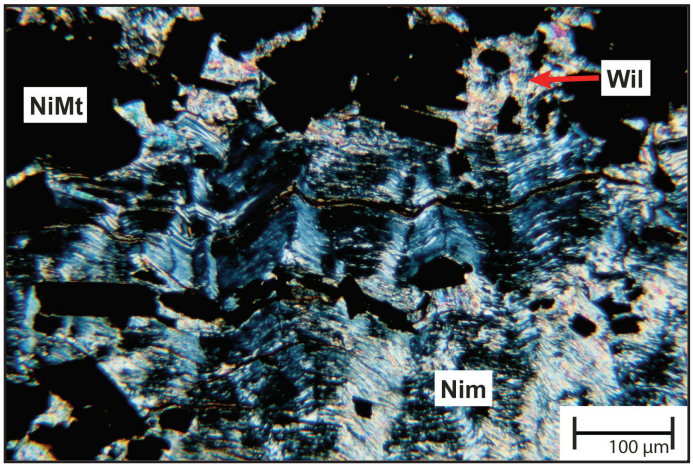

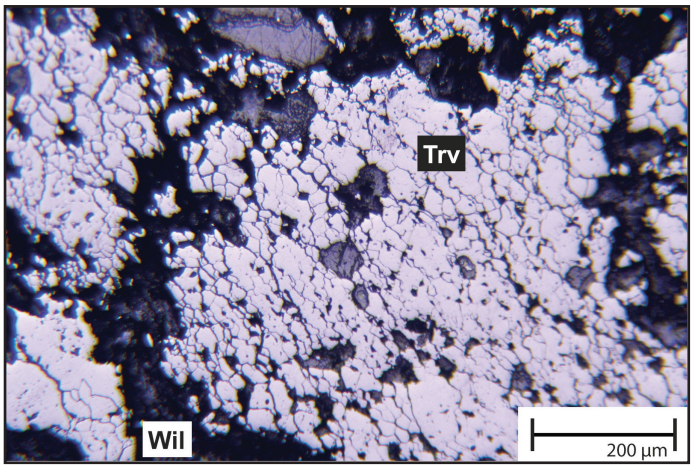

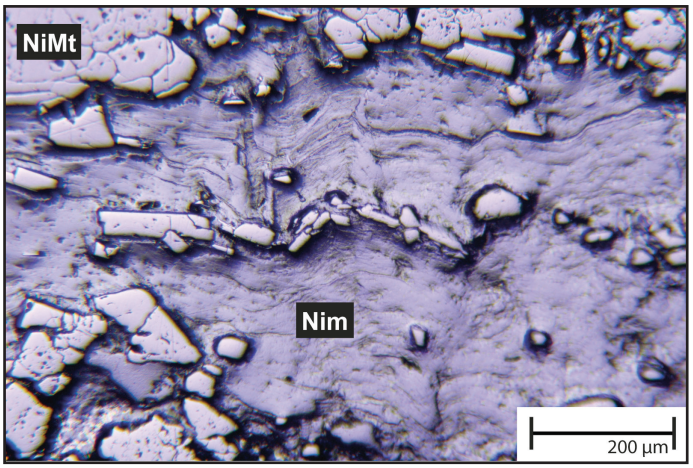

Figure 3.24 (top-left) Strongly solved xenomorph trevorite replacing cochromite in népouite– sample BA 87-1. Optical microscope, reflected light, single polarizer.
Figure 3.25 (top-right) Heazlewoodite in trevorite– sample NCK6. EPMA, backscatter image.
Figure 3.26 (middle-left) Strongly solved xenomorphic ferroan trevorite replacing millerite, in willemseite – sample BA 87-1. Optical microscope, reflected light, single polarizer.
Figure 3.27 (middle-right) Kink banded nimite surrounded by nickeloan magnetite and willemseite – sample BAD. Optical microscope, transmitted light, crossed polarizer.
Figure 3.28 Aggregates of xenomorphic trevorite in willemseite – sample BA 87-3. Optical microscope, reflected light, single polarizer.
Figure 3.29 Lath-shaped and grainy nickeloan magnetite following the kink band deformation of nimite – sample BAD. Optical microscope, reflected light, single polarizer.

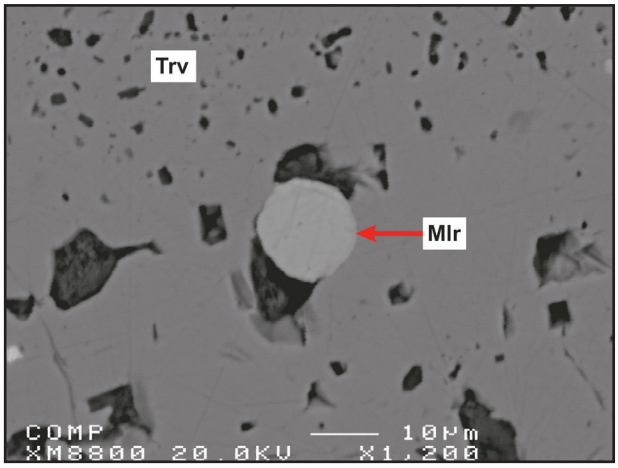

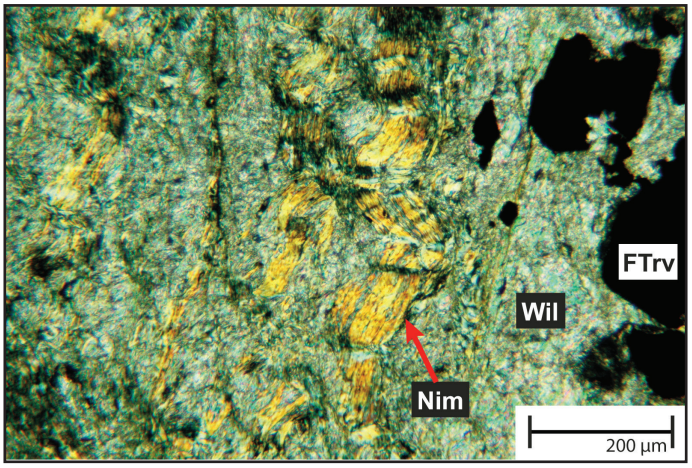

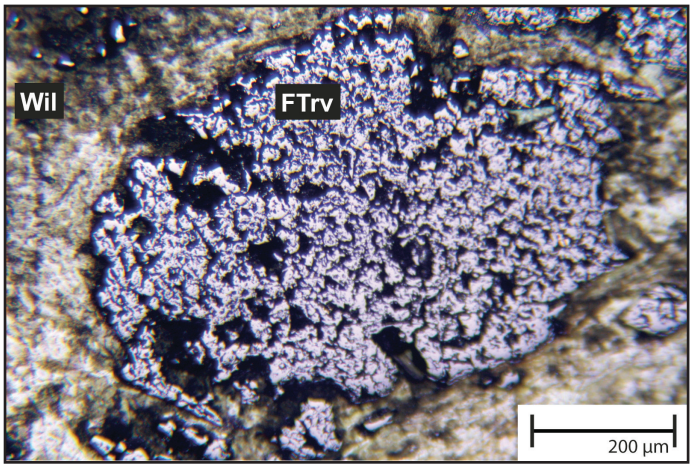

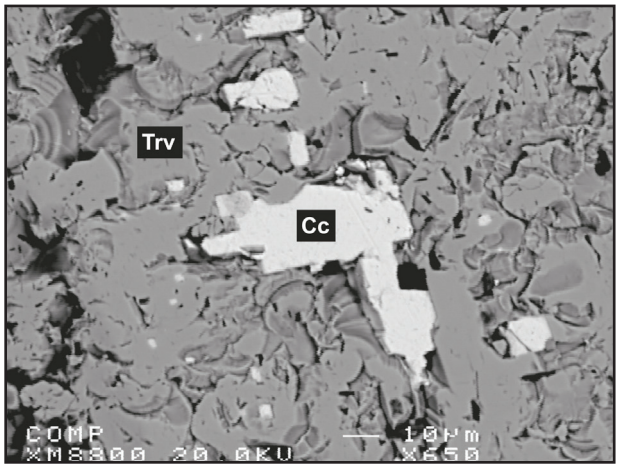

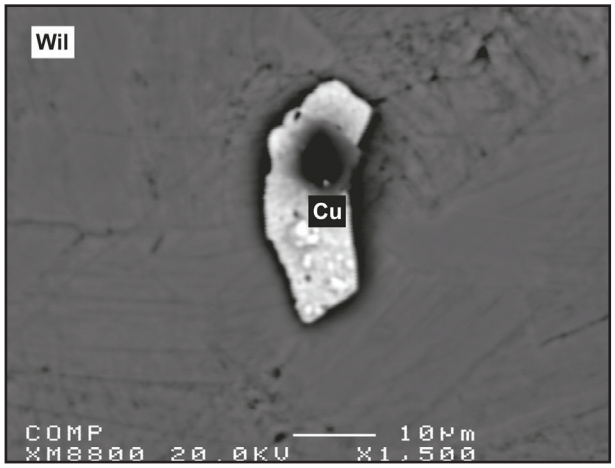

Figure 3.30 (top-left) Millerite in strongly solved trevorite – sample BA 84-1. EPMA, backscatter image.
Figure 3.31 (top-right) Wavelike nimite vein together with willemseite and ferroan trevorite – sample NCJ5. Optical microscope, transmitted light, crossed polarizer.
Figure 3.32 (middle-left) Extremely solved ferroan trevorite megacrysts in willemseite – sample NCH7. Optical microscope, reflected light, single polarizer.
Figure 3.33 (middle-right) Chalcocite in extremely solved trevorite – sample NCJ8. EPMA, backscatter image.
Figure 3.34 (bottom) Pure copper with black spot from EPMA measurement in willemseite – sample BA 84-2. EPMA, backscatter image.

Waal, 1977). Sample BA 87-1 takes an intermediate position, showing deformation but also the structures as in the Bon Accord A samples. Due to that, the author extends the classification of Tredoux *et al.* (1989) by addition of a contact between Bon Accord A and Bon Accord B.

Table 3.5 presents the detailed sample assignment and the presence of the occurring minerals in the samples. The bonaccordite in sample BA 83-1 (in epoxy-resin embedded sample) is occupied with an interrogation mark because this mineral is not always visible in reflected light. For sample BA 87-3 the sulphides, sulphosalts and elements are occupied with interrogation marks because the occurring ore grains, which were observed in reflected light, were too small for identification and too small as well to be detected with the EPMA. Bonaccordite, bunsenite, liebenbergite, antimony, nisbite, unknown #2, unknown #3 and unknown #4 are only

Table 3.5 Presence of the minerals in the Bon Accord samples. The samples are classified after Tredoux et al. (1989) plus a contact zone. *) cochromite and nichromite are abbreviated with cochromite. ?) It is doubtful if this mineral occurs in this sample. Green colour: mineral observed and identified with the EPMA. Orange colour: mineral only observed.

		Bon Accord A			contact	Bon Accord B							
		BA 87-4	BA 83-1	BAU	BA 87-1	BA 87-3	NCK6	BA 84-1	NCJ8	NCJ5	NCH7	BA 84-2	BAD
Ni_2FeBO_5	bonaccordite		?										
NiO	bunsenite												
Ni_2SiO_4	liebenbergite												
$Ni_3Si_2O_5(OH)_4$	népouite												
$Ni_3Si_4O_{10}(OH)_2$	willemseite												
$Ni_5Al(Si_3Al)O_{10}(OH)_8$	nimite												
$CoCr_2O_4$ / $NiCr_2O_4$	cochromite*												
$(Fe,Co,Ni)Cr_2O_4$	cobaltian chromite												
$NiFe_2O_4$	trevorite												
$(Ni,Fe)Fe_2O_4$	ferroan trevorite												
$(Fe,Ni)Fe_2O_4$	nickeloan magnetite												
$FeO(OH)•nH_2O$	limonite												
$FeTiO_3$	ilmenite												
NiS	millerite					?							
Ni_3S_2	heazlewoodite					?							
Sb	antimony					?							
$NiSb$	breithauptite					?							
$NiSb_2$	nisbite					?							
$NiAs$	nickeline					?							
Ni_5As_2	orcelite					?							
$Ni_3(As,Sb)$	unknown #2					?							
Ni_3Sb	unknown #3					?							
Ni_3Sb_2	unknown #4					?							
$(Ni,Fe)_3As_2$	unknown #5					?							
Ni_7AsS_5	unknown #6					?							
FeS_2	marcasite					?							
Cu_5FeS_4	bornite					?							
Cu_2S	chalcocite					?							
Cu_7S_4	anilite					?							
Cu_9S_5	digenite					?							
Cu	copper					?							

present in Bon Accord A. Trevorite, ferroan trevorite, nickeloan magnetite, ilmenite, nickeline, unknown #6, marcasite, bornite, chalcocite, anilite, digenite and pure copper are only present in Bon Accord B. Minerals of the contact are always present in Bon Accord A and / or Bon Accord B. Népouite, willemseite, nimite, co-/ nichromite (including cobaltian chromite), heazlewoodite, breithauptite, orcelite and unknown #5 can be observed in Bon Accord A, the contact and Bon Accord B.

3.4.2 The hematite-magnetite body samples

The samples of the hematite-magnetite body are isotropic and massy; sample cB S 1088 13a and BAE-2 are in parts layered (appendix A). The chromite in sample cB S 1088 3a and cB S 1088 3b occur as strongly solved single grains (figure 3.35) whereas the martitized wüstite in sample cB S 1088 13a occurs as aggregates and single grains with idiomorphic to grainy shape (figure 3.16), with hematite drops around the grains (figure 3.13). Wairauite and unknown #7 is observed in the wüstite (figure 3.36). The strongly solved chromite and magnetite in sample BAE-2 is present as layered aggregates but also as panidiomorphic single grains (figure 3.37). The unidentified silicate in sample cB S 1088 3a and cB S 1088 3b shows kink band deformation (figure 3.38) as well as curved and buckled crystals, forming the groundmass in these samples. The groundmass in sample cB S 1088 13a consists of quartz, and in sample BAE-2 of unidentified silicate.

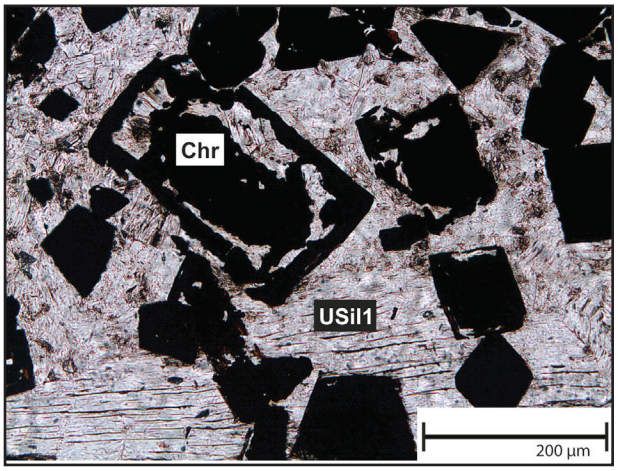

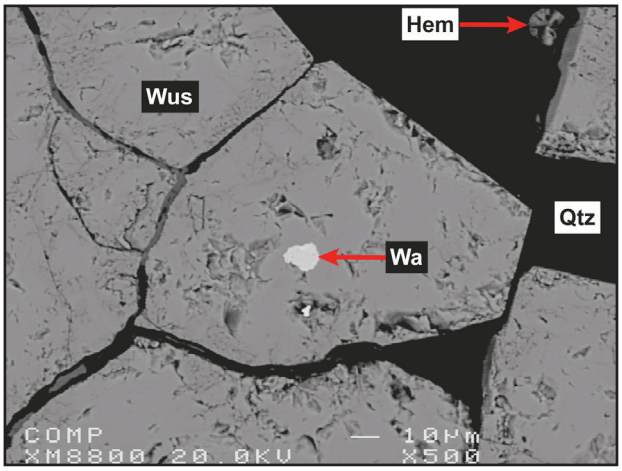

Figure 3.35 (left) Strongly solved chromite grains with unidentified silicate 1 as groundmass – sample cB S 1088 3b. Optical microscope, transmitted light, single polarizer.
Figure 3.36 (right) Wairauite in wüstite with quartz as groundmass and hematite drops – sample cB S 1088 13a. EPMA, backscatter image.

Table 3.6 shows the presence of the minerals in the hematite-magnetite body samples. Unidentified silicate 2 occurs in the samples 3a and 3b, whereas unidentified silicate 1 is present in sample BAE-2, and quartz in sample cB S 1088 13a. Chromite is the major ore in the samples cB S 1088 3a and cB S 1088 3b; in sample BAE-2 it occurs together with magnetite, whereas wüstite is the major ore in sample cB S 1088 13a. Hematite and wairauite are only present in sample cB S 1088 13a.

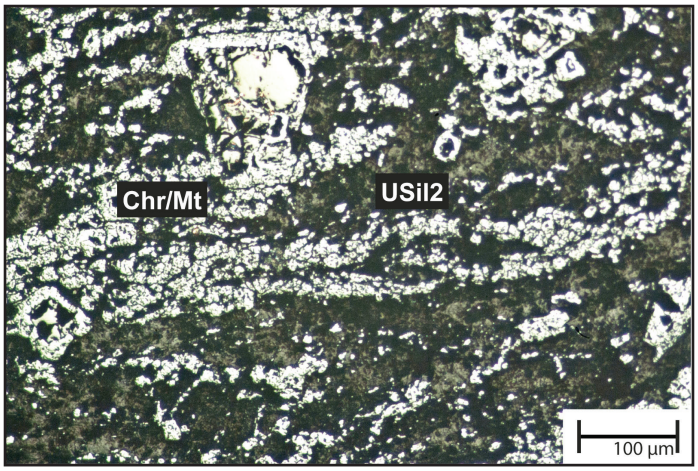

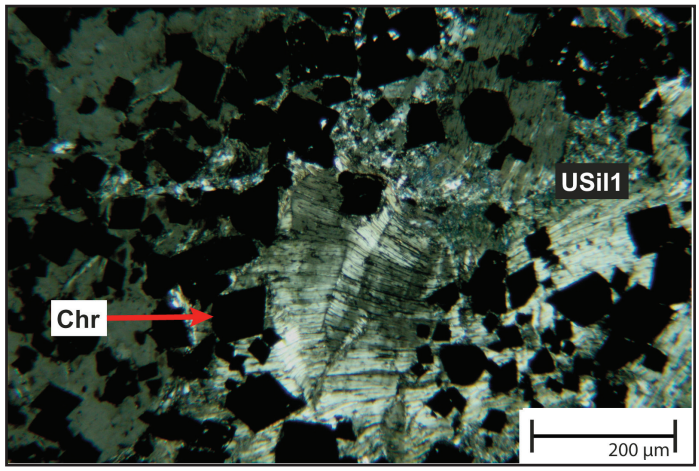

Figure 3.37 (left) Strongly solved chromite and magnetite grains with unidentified silicate 2 as groundmass – sample BAE-2. Optical microscope, reflected light, single polarizer.
Figure 3.38 (right) Unidentified silicate 1 with kink band deformation, together with chromite– sample cB S 1088 3b. Optical microscope, transmitted light, crossed polarizer.

Table 3.6 Presence of the minerals of the hematite-magnetite body.

		cB S 1088 13a	BAE 2	cB S 1088 3a	cB S 1088 3b
unidentified silicate 1					
unidentified silicate 2					
SiO_2	quartz				
$FeCr_2O_4$	chromite				
Fe_3O_4	magnetite				
Fe_2O_3	hematite				
FeO	wüstite				
CoFe	wairauite				
Co(Ni,Fe)	unknown #7				

3.4.3 The tourmaline-hornblende schist sample

Examined with the naked eye the structure of this sample appears anisotropic (appendix A), but contemplated with the optical microscope only the feruvite is anisotropic. The structure of the magnesio-hornblende is isotropic. Quartz occurs as grainy accumulations (figure 3.39) but also as inclusions in the poikiloblastic feruvite and poikiloblastic magnesio-hornblende (figure 3.40). Feruvite and magnesio-hornblende appear nematoblastic. Table 3.7 presents the minerals of the tourmaline-hornblende schist sample. Magnesio-hornblende, Fe-Mg-Mn-Li-amphibole, feruvite, quartz and limonite occur together.

Table 3.7 Presence of the minerals of the tourmaline-hornblende schist sample. Green colour: mineral observed and identified with the EPMA. Orange colour: mineral only observed.

		BAR9
$Ca_2[(Mg,Fe)_4Al](Si_7Al)O_{22}(OH)_2$	magnesio-hornblende	
$Ca_2(Mg,Fe)_5Si_8O_{22}(OH)_2$	actinolite	
$(Ca,Na)(Fe,Mg,Ti)_3(Al,Mg,Fe)_6(BO_3)_3Si_6O_{18}(OH)_4$	feruvite	
SiO_2	quartz	
$FeO(OH)•nH_2O$	limonite	

3.4.4 The chert samples

The samples BA-A S1 and BA-B S2 are both isotropic and consist mainly of chert. The chert is cryptocrystalline with sub-grain formation, containing recrystallized quartz (figure 3.41). Bigger single quartz grains and palisade quartz is present in both samples (figure 3.4). Sample BA-A S1 contains also brookite, gersdorffite, marcasite (figure 3.42) and pure nickel, all with embayment structure. In contrast to this, sample BA-B S2 consists in addition of wüstite, hematite and chromite. In this sample a grain of zoned wüstite with alternating layers occurs (figure 3.43). Hypidiomorphic Chalcopyrite is present as well, showing slight embayment structure (figure 3.44). Table 3.8 presents the minerals of the chert samples. Only quartz occurs in both samples. Brookite, gersdorffite, marcasite and nickel are present in sample BA-A S1; chromite, wüstite, hematite, limonite and chalcopyrite are present in sample BA-B S2.

Table 3.8 Presence of the minerals of the chert samples. Green colour: mineral observed and identified with the EPMA. Orange colour: mineral only observed.

		BA-A S1	BA-B S2
$FeCr_2O_4$	chromite		
FeO	wüstite		
Fe_2O_3	hematite		
$FeO(OH)•nH_2O$	limonite		
TiO_2	brookite		
SiO_2	quartz		
$NiAsS$	gersdorffite		
FeS_2	marcasite		
$CuFeS_2$	chalcopyrite		
Ni	nickel		

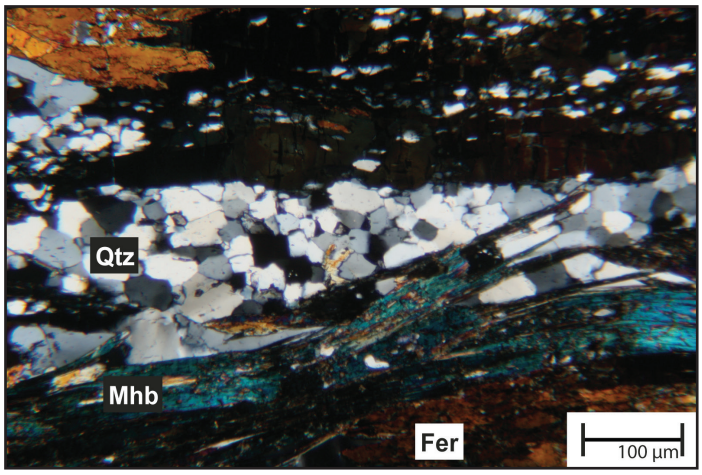

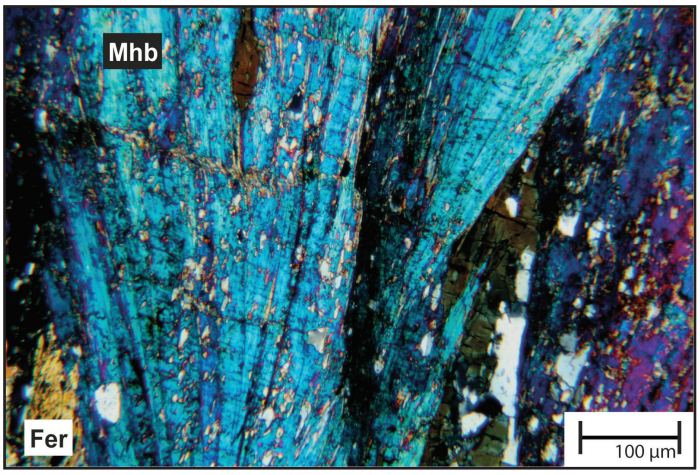

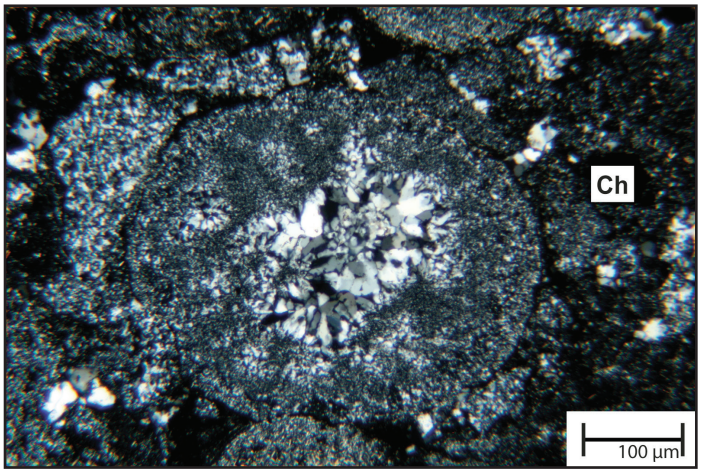

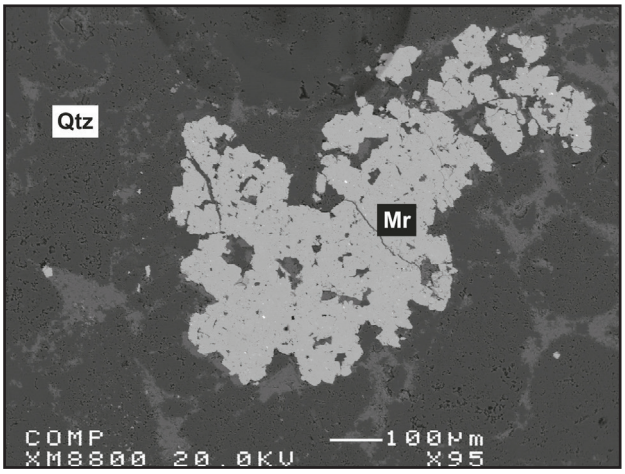

Figure 3.39 (top-left) Accumulation of grainy undulatory quartz, surrounded by feruvite and magnesio-hornblende – sample BAR9. Optical microscope, transmitted light, crossed polarizer.
Figure 3.40 (top-right) Poikiloblastic magnesio-hornblende and poikiloblastic feruvite– sample BAR9. Optical microscope, transmitted light, crossed polarizer.
Figure 3.41 (bottom-left) Sub-grained quartz – sample BA-A S1. Optical microscope, transmitted light, crossed polarizer.
Figure 3.42 (bottom-right) Marcasite in quartz – sample BA-A S1. EPMA, backscatter image.

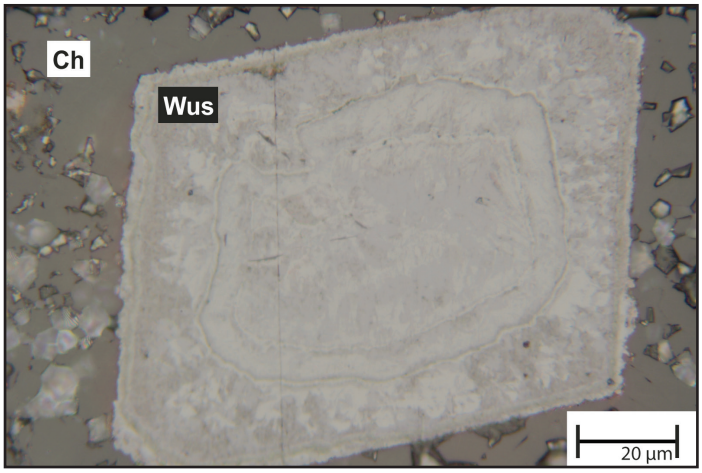

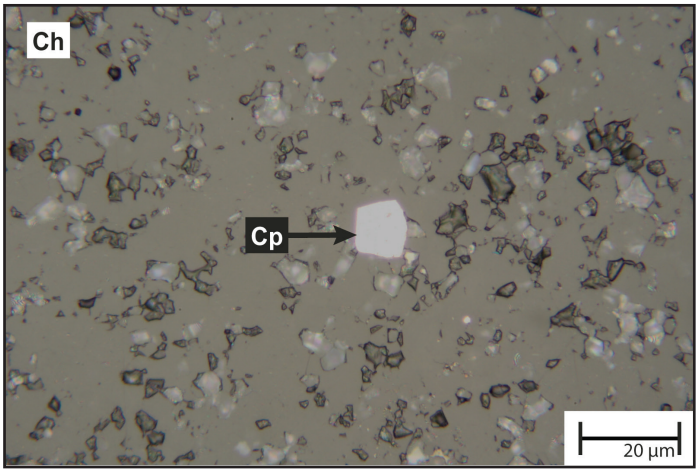

Figure 3.43 (left) Zoned wüstite with alternating layers in chert – sample BA-B S2. Optical microscope, reflected light, single polarizer.
Figure 3.44 (right) Chalcopyrite in chert – sample BA-B S2. Optical microscope, reflected light, single polarizer.

4. Mineral Chemistry and Geochemistry

This chapter presents the results of the mineral chemical analyses of the most abundant minerals from Bon Accord as well as one selected mineral from the hematite-magnetite body. The data are obtained by the use of the EPMA and µPIXE. Due to huge beam instabilities of the µPIXE during the measurement processes the obtained concentrations need to be neglected and are therefore not provided but the element maps are still useable. The µPIXE was set up to analyse elements with atomic number higher than those of Cr, so lighter element were not considered. In addition, the whole rock chemistry of four samples of the Bon Accord Ni-oxide body, one sample of the chert as well as one sample of the tourmaline-hornblende schist, based on the data of Madala (2009), is presented. Altogether 26 different minerals from Bon Accord, nine different minerals from the hematite-magnetite body, nine different minerals from the chert and four different minerals from the tourmaline-hornblende schist are investigated by use of the EPMA. Typical and important mineral compositions and important trends are emphasized in this chapter, the complete data set is provided in the appendix D to I. All concentrations for FeO refer always to the total concentration of Fe, except for minerals including only trivalent Fe. Furthermore it is important to notice that for several different minerals only a few of one species could be examined. These data are therefore not representative. A few analysed minerals are quite small, even though the beam size was adjusted to a small size, so the EPMA might have picked up elements from surrounding minerals. Very often, the different minerals contain outliers, so the average calculations for the wt% and the cation proportions are always done by the use of the median, which is more robust towards outliers than the mean.

4.1 Silicates

4.1.1 Liebenbergite $(Ni,Mg,Fe,Co)_2SiO_4$

In total ten liebenbergites, all clearly altered, are analysed on the two samples BA 87-4 and BA 83-1. The major elements NiO, MgO and SiO_2 vary significantly. NiO varies about 2.59 wt% with an average concentration of 55.79 wt%, being 54.43 wt% in the minimum and 57.02 wt% in the maximum concentration. The variance for MgO is 1.58 wt% with an average concentration of 7.04 wt%, being 6.38 wt% in the minimum and 7.11 wt% in the maximum concentration. SiO_2 shows relatively constant values with a variance of 0.97 wt%, being 30.65 wt% in the minimum and 31.62 wt% in the maximum concentration. The average concentration is 31.23 wt%. Regarding the general mineral formula of liebenbergite, FeO should not be present in significant amounts, but these liebenbergites contain an average concentration of 4.58 wt%. CoO is extremely enriched as well with an average of 1.99 wt%. MnO shows an average concentration of 0.20 wt% (table 4.1). ZnO, CaO, Al_2O_3, TiO_2 and Cr_2O_3 are not detected. This is an important feature since the occurrence of these impurities (including CoO)

Table 4.1 Summarized EPMA data of liebenbergite (n = 10) in wt%.

	FeO	NiO	CoO	ZnO	SiO_2	MgO	CaO	Al_2O_3	TiO_2	MnO	Cr_2O_3
average	4.58	55.79	1.99	0	31.23	7.04	0	0	0	0.20	0
minimum	4.05	54.43	1.78	0	30.65	6.38	0	0	0	0.18	0
maximum	5.52	57.02	2.13	0	31.62	7.96	0	0	0	0.23	0

is dependent on the genesis of the olivine (Krivolutskaya and Bryanchaninova, 2011).

Chemical zoning of NiO, MgO and FeO is excluded by EPMA-mapping – the elements are homogeneously distributed (figure 4.1).

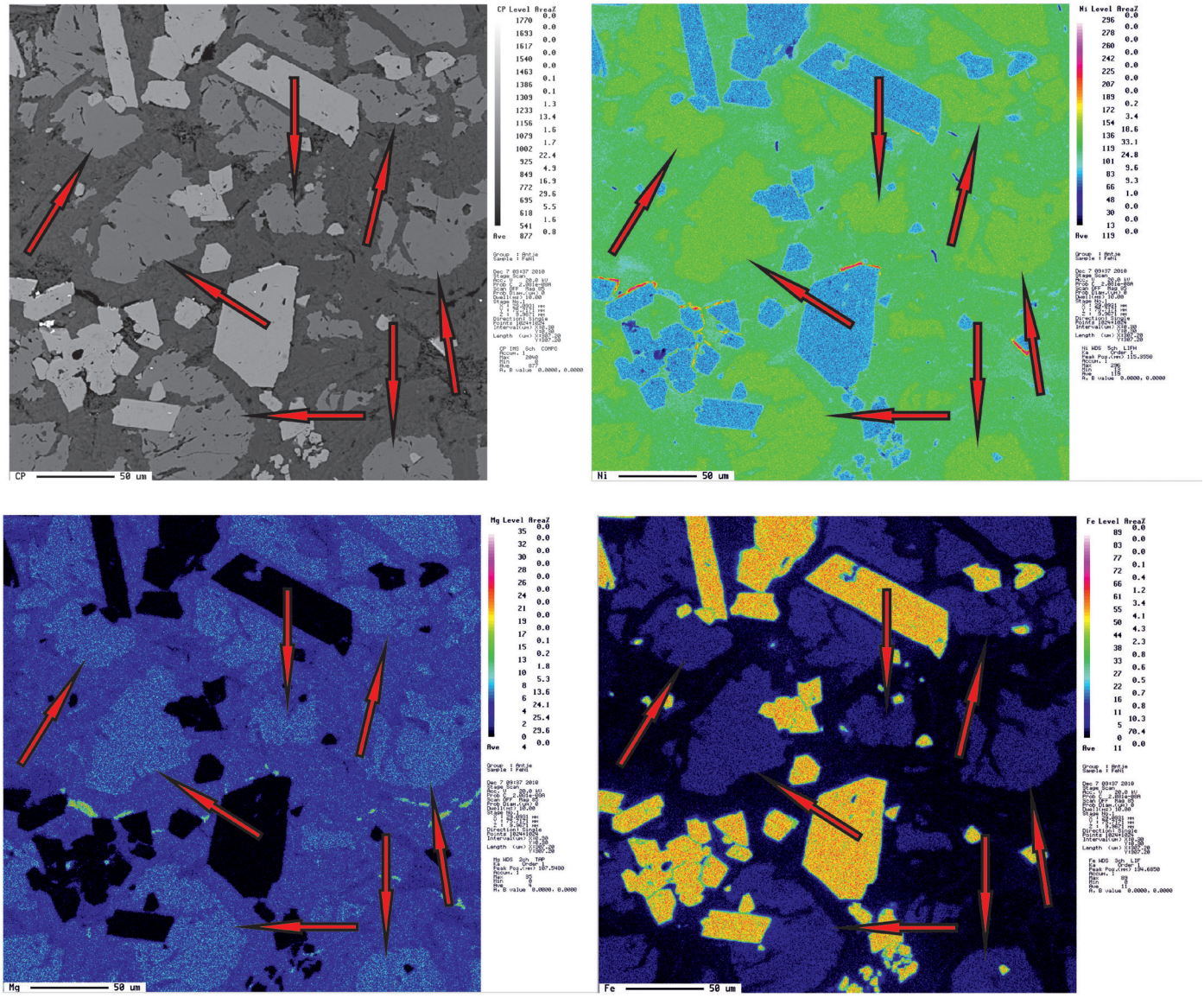

Figure 4.1 EPMA maps of a selected area in sample BA 83-1. Top left: Backscatter image of an area consisting of liebenbergite (grey; examples indicated by arrows), trevorite (light grey) and népouite-willemseite mixture (dark grey). Top right: Ni-map of the same area – the arrows indicate examples of liebenbergite. Bottom left: Mg-map of the same area – the arrows indicate examples of liebenbergite. Bottom right: Fe-map of the same area – the arrows indicate examples of liebenbergite.

Due to the significant variations of NiO, MgO and FeO, the data are plotted in a ternary liebenbergite-forsterite-fayalite diagram, including data from other authors (figure 4.2). The liebenbergites of the present study correlate well with the by De Waal and Calk (1973) examined liebenbergites from the Bon Accord. The other natural liebenbergites, which are reported by Andreoli *et al.* (1999) from the melt sheet of the Morokweng impact crater in South Africa, are a little richer in Ni and Fe than those of the present study. Matsui and Syono (1968) proved experimentally the forsterite-liebenbergite solid solution, and Annersten *et al.* (1982) the fayalite-liebenbergite solid solution. General olivine compositions of the forsterite-fayalite solid solution of different origin are shown with the data of Li *et al.* (2003), who reported olivine from a MORB, Arai (1994),

who reported olivine from lherzolite and harzburgite at the Japan island arc, Ishimaru and Arai (2008), who reported olivine from a peridotite xenolith from the Avacha volcano at the Kamchatca arc in Russia, as well as Nwe (1976), who reported olivine from the Skaergaard intrusion at East Greenland. The only Ni-enriched olivine is reported by Ishimaru and Arai (2008), but these data plot still close to forsterite.

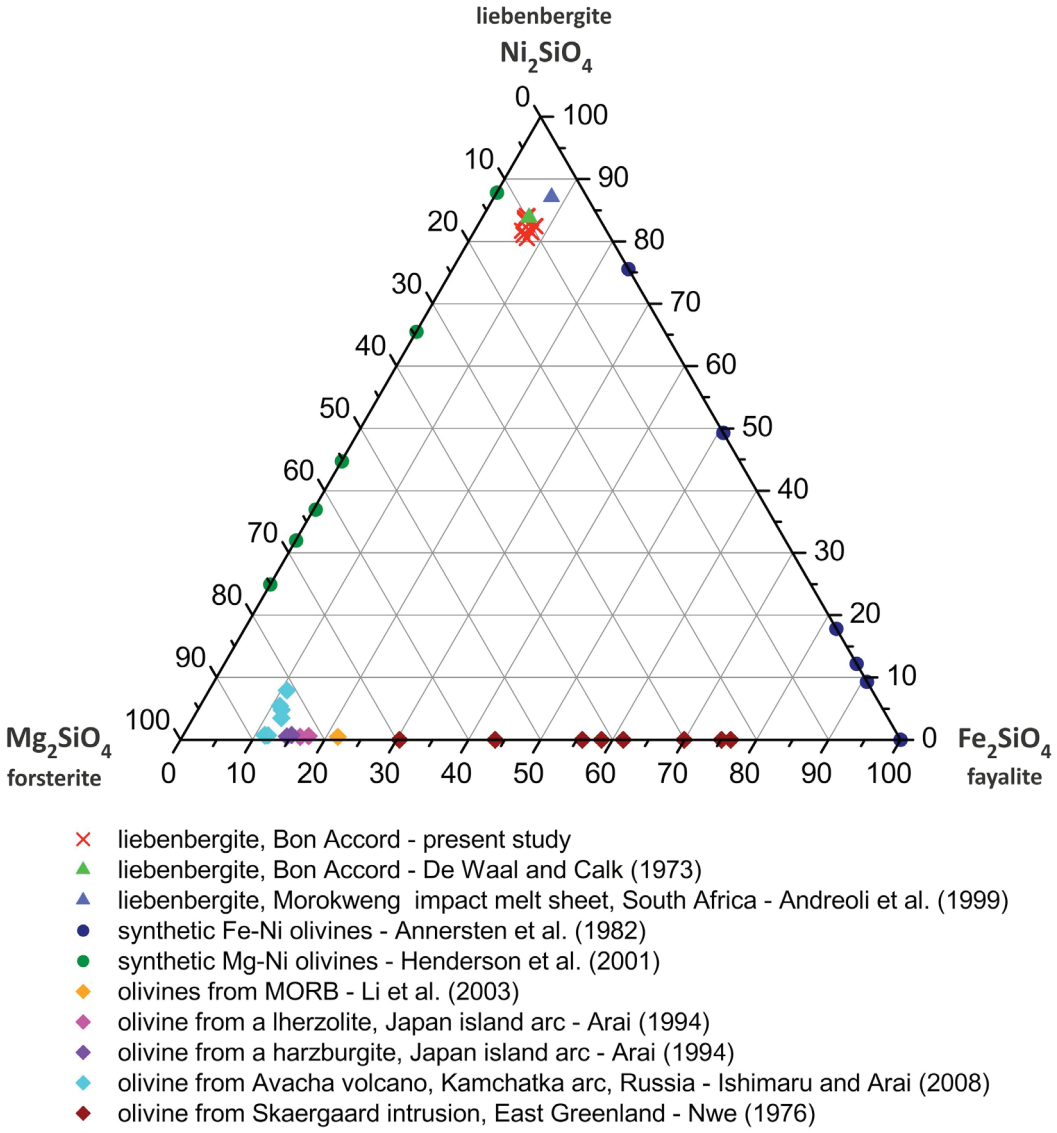

Figure 4.2 Liebenbergite composition in a ternary liebenbergite-forsterite-fayalite diagram, together with other selected liebenbergite, synthetic olivines of the fayalite-liebenbergite and forsterite-liebenbergite solid solution, and several natural olivines of the forsterite-fayalite solid solution. The concentrations were normalized to 100 wt%.

The substitution of Ni with Mg, Fe and Co is shown in figure 4.3, using the cation proportions. Mg shows the most obvious positive trend towards Ni, decreasing with the increase of Ni. The same applies with a less pronounced trend for Fe and Co towards Ni. Mn is present with so low traces, that no trend towards Ni or the other plotted elements can be noted.

With the substitution of Ni, Mg, Fe and Co, the average empirical formula is $Ni_{1.46}Mg_{0.33}Fe_{0.12}Co_{0.05}Si_{1.01}O_4$ and can be summarized to the mineral formula $(Ni,Mg,Fe,Co)_{1.96}SiO_4$ (table 4.2).

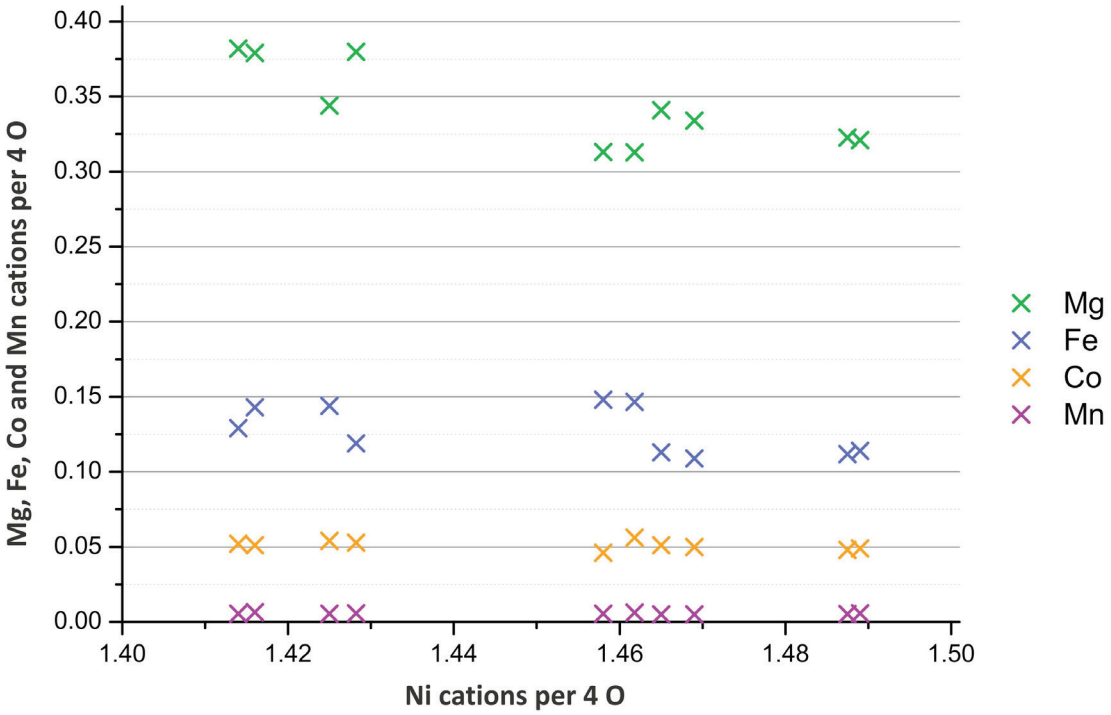

Figure 4.3 Ni cations vs. Mg, Fe, Co and Mn cations in the liebenbergites. The cation proportions are calculated per 4 O.

Table 4.2 Summary of the cation proportions for liebenbergite (n = 10), cations per 4 O.

	Fe	Ni	Co	Zn	Si	Mg	Ca	Al	Ti	Mn	Cr
average	0.1240	1.4599	0.0510	0	1.0111	0.3375	0	0	0	0.0054	0
minimum	0.1090	1.4140	0.0460	0	1.0020	0.3129	0	0	0	0.0050	0
maximum	0.1480	1.4890	0.0562	0	1.0160	0.3820	0	0	0	0.0064	0

µPIXE analyses on liebenbergite

Additionally three selected liebenbergite grains of a specific area of interest in sample BA 87-4 were analysed with the µPIXE. The selected liebenbergites of this area are marked with arrow number 5 to 7. From the µPIXE spectrum the elements Fe, Co, Ni, Cu, Ge, As, Sn, Pb, Zn, Ga, Mo, Cd, In and Sb are identified. But due to the high error and the very low concentration Zn, Ga, Mo, Cd, In and Sb could not be quantified. Figure 4.4 shows the most significant element maps of the whole area which are Fe, Ni, Co, Ge, As, Sb and Pb.

In agreement with EPMA-analyses, Fe is present only as a minor constituent and appears blotchy in the element map. Spots of Fe within the liebenbergites belong to the tiny enclosed trevorites. Ni, also not homogeneously distributed but definitely a major constituent, is displayed to be present with high concentrations. The Co-enrichment in contrast to the surrounding minerals is significant, whereas the trevorites, népouites and willemseites are clearly impoverished in CoO. The liebenbergites are depleted in Ge. Single spots with significantly higher concentrations of Ge are trevorites. Also As is only present in very low amounts, containing single tiny spots with higher concentration. Sb is even less and below detection limit, and Pb is also present in traces.

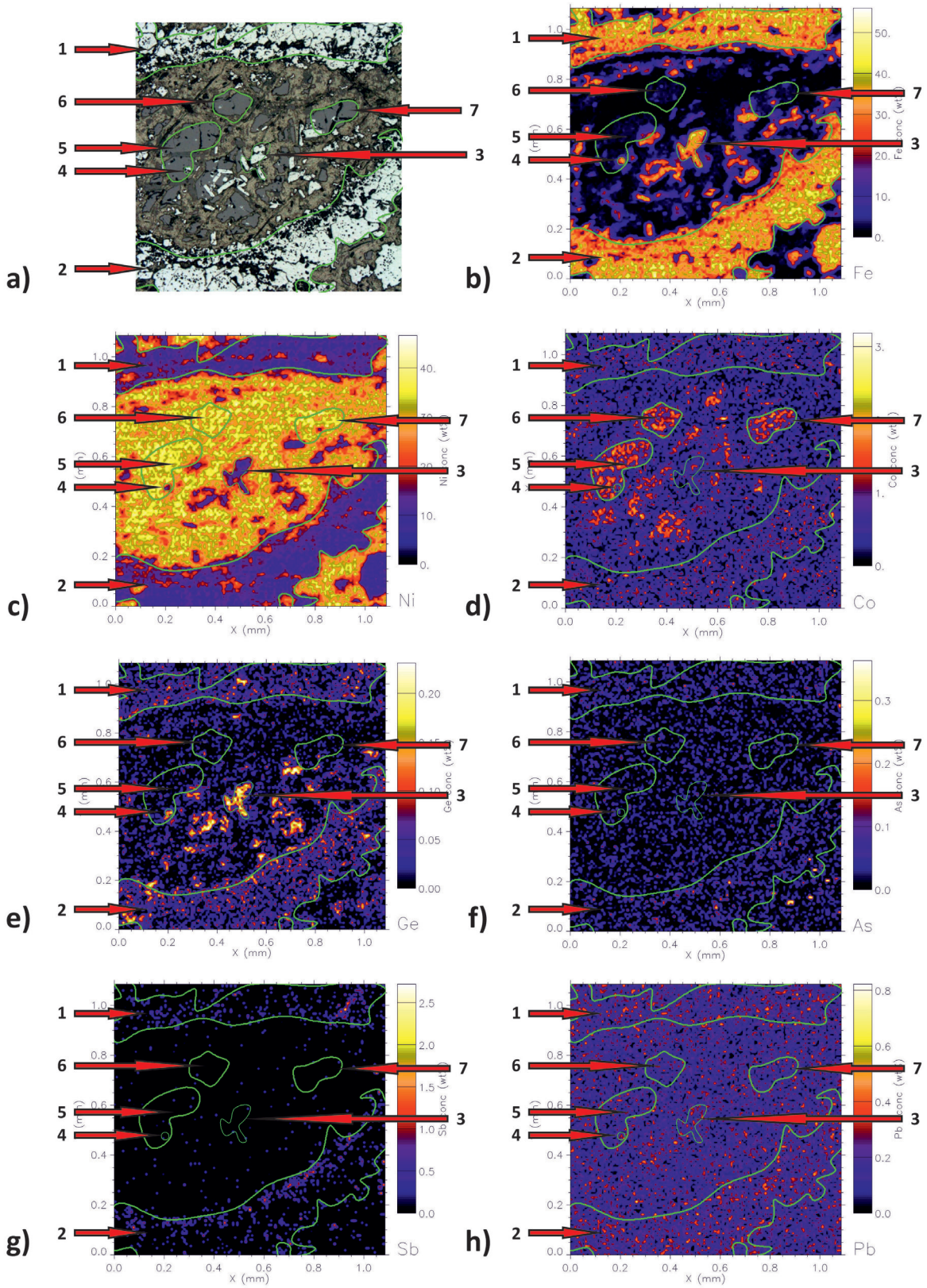

Figure 4.4 µPIXE element maps of a selected area of interest in sample BA 87-4. Arrow 1 and 2 mark xenomorphic trevorite, arrow 3 marks lath-shaped trevorite, arrow 4 marks trevorite within liebenbergite, 5, 6 and 7 mark liebenbergite. a) Overview about the selected area in reflected light (whitish: trevorite, dark grey: liebenbergite, brownish-grey: népouite-willemseite assemblage). b) Fe-map. c) Ni-map. d) Co-map. e) Ge-map. f) As-map. g) Sb-map. h) Pb-map. The concentrations are wt% and need to be examined carefully due to the strong beam instabilities during the measurement process.

4.1.2 Népouite $Ni_3Si_2O_5(OH)_4$

In total 27 népouites were analysed in the six samples BA 87-4, BA 83-1, BAU, BA 87-1, BA 87-3 and NCH7. For identification of the népouite, these data and those from liebenbergite and willemseite are plotted in an MgO-SiO_2-(FeO + NiO) ternary diagram (figure 4.5), together with the general compositions of these minerals. It is obvious that the general liebenbergite and willemseite compositions plot in very different areas and disagree significantly with those of the 27 analysed minerals. All the 27 analysed minerals can doubtless be attributed to népouite, since NiO and MgO substitute for each other, forming in general a solid solution to lizardite (Brindley and Wan, 1975).

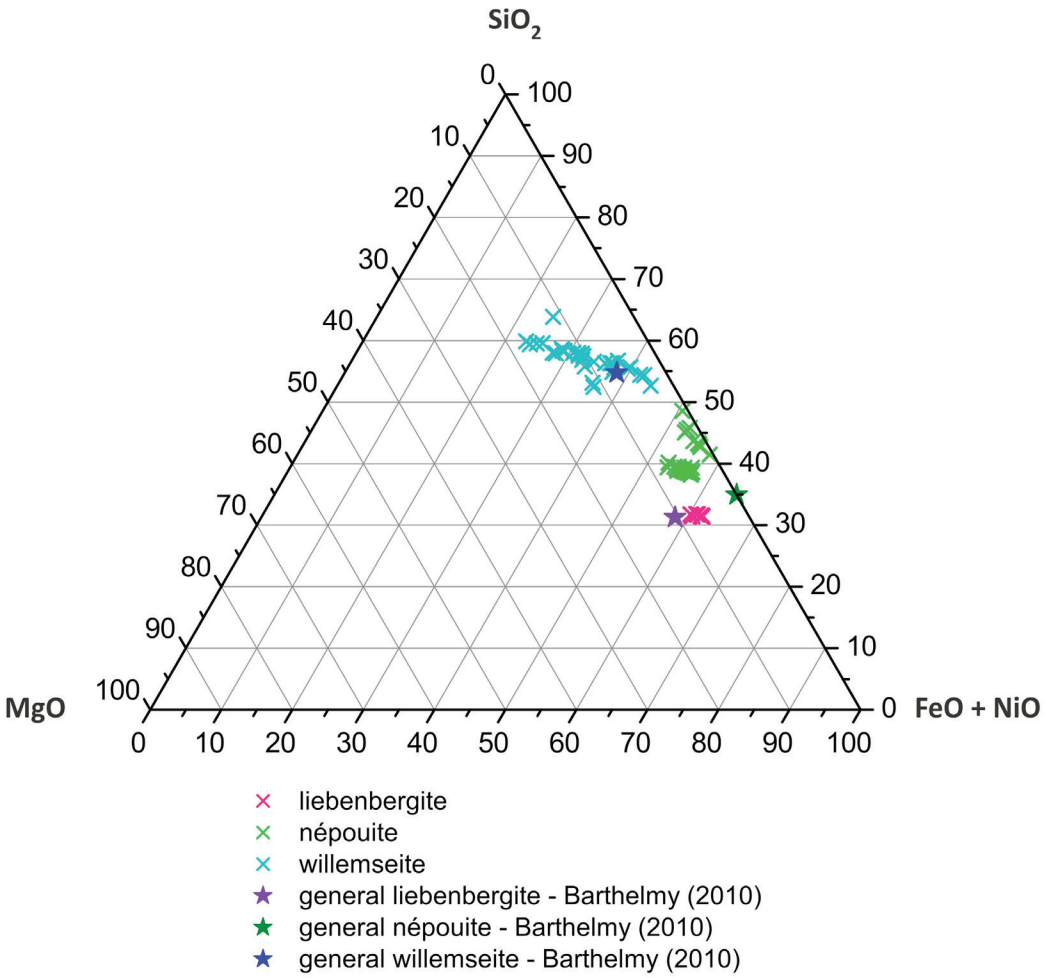

Figure 4.5 The data of népouite, general népouite (Barthelmy, 2010), liebenbergite, general liebenbergite (Barthelmy, 2010), willemseite and general willemseite (Barthelmy, 2010) compositions, plotted in a ternary MgO-SiO_2-(FeO + NiO) diagram. The concentrations were normalized to 100 wt%.

SiO_2 and NiO as well as MgO and FeO vary significantly (table 4.3). SiO2 varies significantly about 7.00 wt%, being 32.80 wt% in the minimum and 39.80 wt% in the maximum concentration, with an average concentration of 34.88 wt%. NiO shows an average concentration of 47.55 wt%, varying in the range of 9.40 wt%, with a minimum of 40.04 wt% and a maximum concentration of 50.42 wt%. MgO varies significantly about 6.38 wt% with an average concentration of 4.27 wt%, being 0.45 wt% in the minimum and 6.83 wt% in

the maximum concentration. FeO shows an average concentration of 0.91 wt%, being in the minimum 0.18 wt% and in the maximum concentration 2.59 wt%. CoO behaves similar with an average concentration of 0.36 wt%, varying from 0.21 wt% in the minimum and 0.58 wt% in the maximum concentration. CaO, Al_2O_3 and MnO are mostly not detected. So the maximum concentration of CaO is 0.37 wt%, for Al_2O_3 it is 0.30 wt% and for MnO it is 0.07 wt%. ZnO, TiO_2 and Cr_2O_3 are not detected (figure 4.6).

Table 4.3 Summarized EPMA data of népouite (n = 27) in wt%.

	FeO	NiO	CoO	ZnO	SiO_2	MgO	CaO	Al_2O_3	TiO_2	MnO	Cr_2O_3
average	0.91	47.55	0.36	0	34.88	4.27	0	0	0	0	0
minimum	0.18	40.04	0.21	0	32.80	0.45	0	0	0	0	0
maximum	2.59	50.42	0.58	0	39.80	6.83	0.37	0.30	0	0.07	0

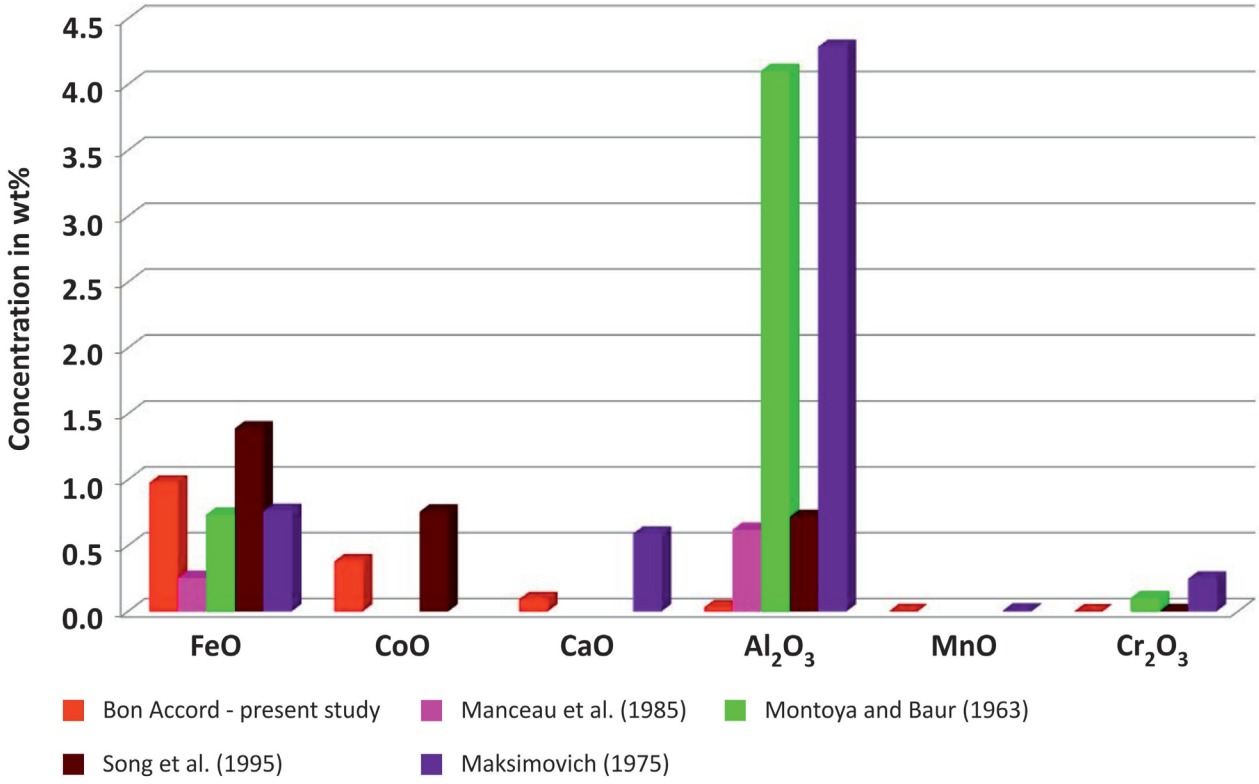

Figure 4.6 Overview about the averaged trace element distribution of the népouites from Bon Accord, in comparison with the népouites of Manceau et al. (1985), Montoya and Baur (1963), Song et al. (1995) and Maksimovich (1975). At blank positions, this oxide was not detected.

Nine of 27 népouites are clearly enriched in the (NiO + FeO) constituent, so that the results can be divided into two groups – group 1, rich in (NiO + FeO), and group 2, poor in (NiO + FeO). It is conspicuous that group 1 contains only samples of Bon Accord A and group 2 only samples of Bon Accord B and the contact (figure 6.7 and table 4.4). NiO, MgO and CaO are most eye-catching in their different average concentrations; group 1 is with an NiO average concentration of 48.80 wt% about 7.12 wt% richer than group 2. MgO of group 1 is with an average concentration of 4.93 wt% about 4.01 wt% richer than group 2. CaO of group 1 is mostly not detected, in contrast to group 2, which shows a CaO average concentration of 0.25 wt%. The results for SiO_2 scatter, even though the average concentrations of both groups are close, with 34.83 wt% for group 1 and

35.48 wt% for group 2. Whilst the SiO_2 concentrations of group 1 are relatively stable with 33.92 wt% as the minimum and 35.71 wt% as the maximum concentration, the SiO_2 content of group 2 varies stronger from 32.87 wt% in the minimum to 39.80 wt% in the maximum. The CoO concentrations are relatively equal in both groups with 0.37 wt% on average for group 1 and 0.34 wt% on average for group 2. Al_2O_3 is mostly not detected. MnO is in group 1 never detected, but sometimes in group 2.

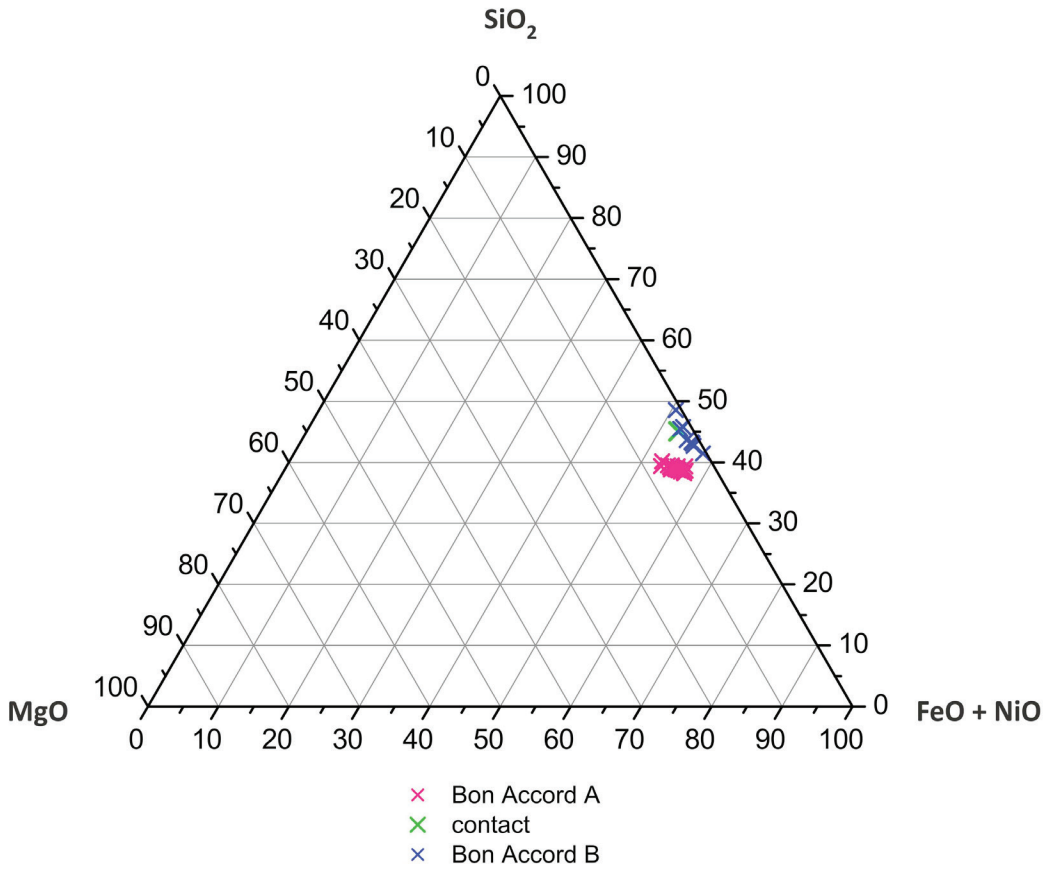

Figure 4.7 Népouite compositions in the ternary MgO-SiO_2-(FeO + NiO) diagram, subdivided into Bon Accord A, the contact and Bon Accord B. The concentrations were normalized to 100 wt%.

Table 4.4 Summarized EPMA data of népouite, subdivided into group 1 (n = 18) and group 2 (n = 9) in wt%.

	FeO	NiO	CoO	ZnO	SiO_2	MgO	CaO	Al_2O_3	TiO_2	MnO	Cr_2O_3
Group 1											
average	0.99	48.80	0.37	0	34.83	4.93	0	0	0	0	0
minimum	0.50	45.33	0.25	0	33.92	3.68	0	0	0	0	0
maximum	2.59	50.42	0.58	0	35.71	6.83	0.08	0.30	0	0	0
Group 2											
average	0.53	41.68	0.34	0	35.48	0.92	0.25	0	0	0	0
minimum	0.18	40.04	0.21	0	32.87	0.45	0.17	0	0	0	0
maximum	1.50	48.04	0.57	0	39.80	1.79	0.37	0.09	0	0.07	0

Even though the elements are fairly distributed they fit well with data of népouites from other locations (figure 4.8). Due to the lizardite-népouite solid solution, the data for those are included in this diagram for

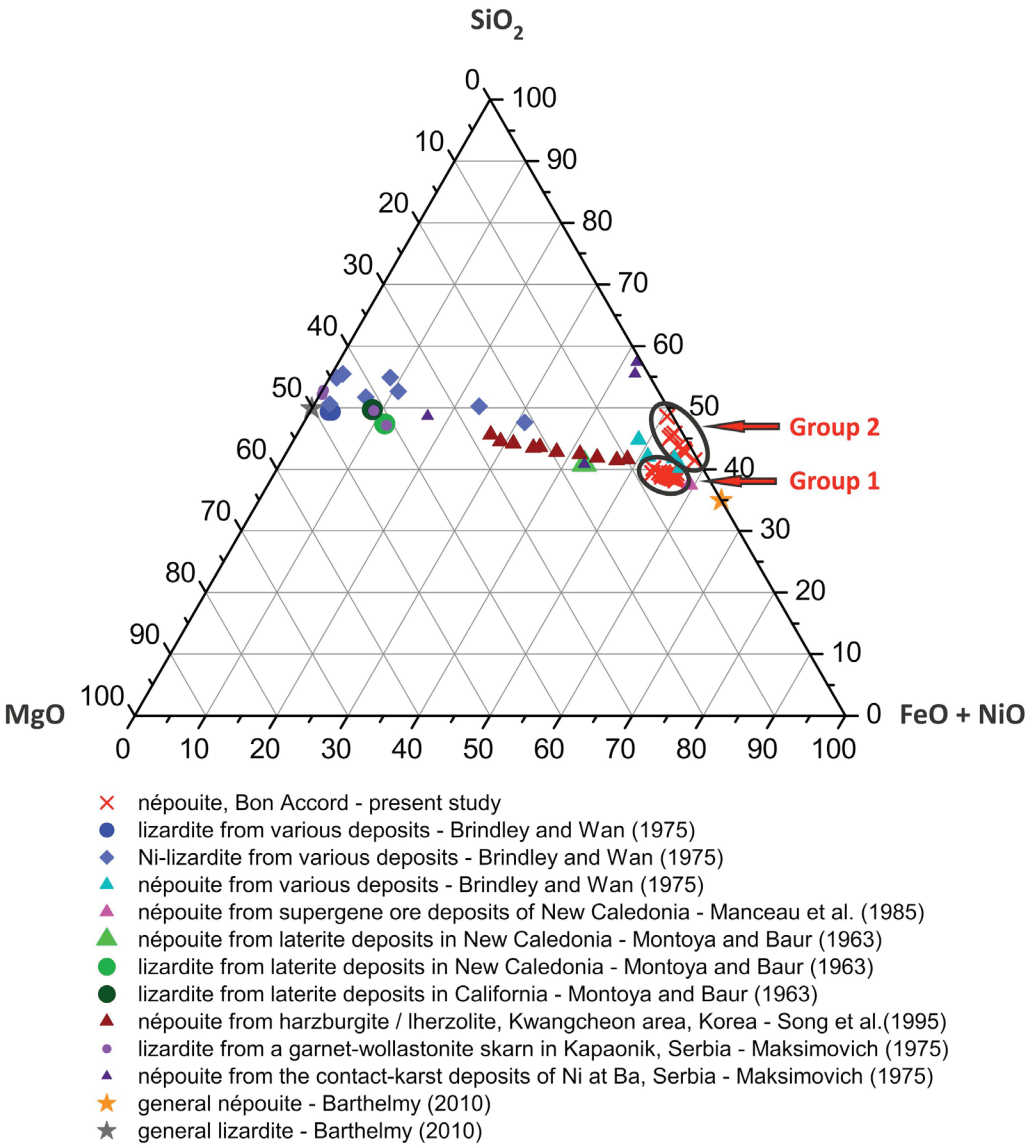

Figure 4.8 Népouite composition in a ternary MgO-SiO_2-(FeO + NiO) diagram, together with selected népouites from different types of deposits, and data for lizardite to illustrate the lizardite-népouite solid solution. The concentrations were normalized to 100 wt%.

comparative purpose. The népouites from Brindley and Wan (1975) take an intermediate position between group 1 and group 2, whereas the népouite from Manceau *et al.* (1985) equal in their composition with group 1. The lizardite and Ni-lizardite which are reported by Brindley and Wan (1975) follow the solid solution between népouite and lizardite. The népouite from Maksimovich (1975) contains even more SiO_2 than those from Bon Accord, but plot also at the SiO_2 level of group 1. The népouites from Song *et al.* (1995) show clearly the lizardite-népouite solid solution series, starting with the most MgO-impoverished ones at the same SiO_2 level as group 1, and ending with the most MgO-enriched ones at the same SiO_2 level as group 2. Manceau *et al.* (1985) analysed népouites from a supergene ore deposit in New Caledonia. Montoya and Baur (1963) investigated népouites from a laterite deposit in New Caledonia. Their népouites plot also with the approximate similar SiO_2 content as group 1, but are significantly richer in MgO. Song *et al.* (1995) examined népouites from harzburgites in Korea. Their népouites follow very well the solid solution from népouite to lizardite, taking an intermediate position between group 1 and group 2 in the SiO_2 concentration. Maksimovich (1975) analysed

népouites from a contact-karst deposit in Serbia, and lizardite from a garnet-wollastonite skarn from Kapaonik in Serbia. His analysed népouites scatter extremely in their SiO_2 concentration, being with it in two népouites significantly higher than those of Bon Accord. The népouites and lizardites indicate also well the solid solution between each other.

Also the cation proportions scatter significantly (table 4.5). Figure 4.9 shows that also here the grouping in the népouites is conspicuous. Also here, the gap in Si between group 1 and group 2 is observable. Si of group 2 scatters significantly, which is not the case for group 1. Also the scattering of Ni and Mg is in group 2 stronger than in group 1, in contrast to Mg and Fe which scatter a little stronger in group 2. The substitution of Ni and Mg is clear to see – the decrease in Ni is accompanied by the increase in Mg and opposite.

Table 4.5 Summary of the cation proportions for népouite (n = 27), cations per 2 Si.

	Fe	Ni	Co	Zn	Si	Mg	Ca	Al	Ti	Mn	Cr
average	0.0438	2.1951	0.0164	0	2.0000	0.3735	0.0013	0	0	0	0
minimum	0.0088	1.6607	0.0102	0	2.0000	0.0378	0	0	0	0	0
maximum	0.1219	2.3769	0.0267	0	2.0000	0.5707	0.0218	0.0199	0.0012	0.0034	0.0027

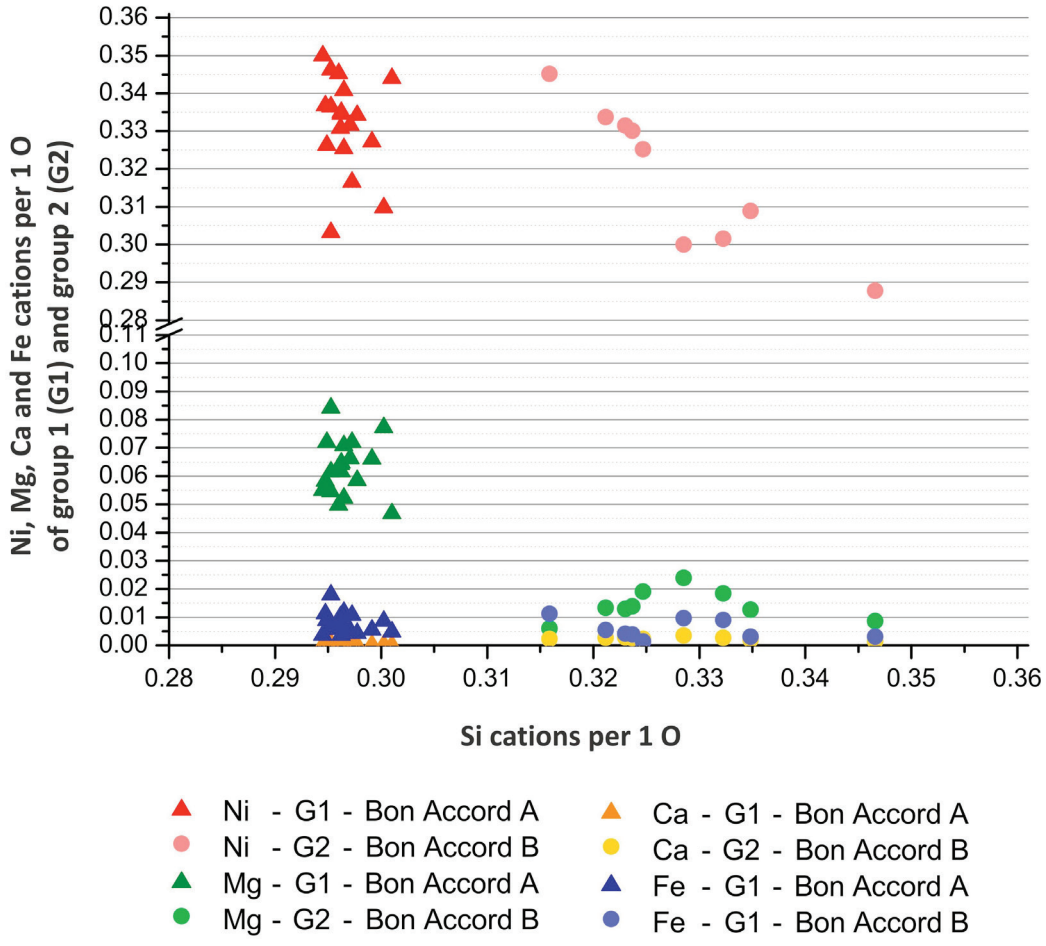

Figure 4.9 Overview about the differences of Ni, Mg, Ca and Fe versus Si for group 1 and group 2. Group 1 (G1) contains solely népouites from Bon Accord A, and group 2 (G2) contains solely népouites from Bon Accord B. All plotted concentrations are cation proportions per 1 O.

These distinctive differences are explainable with the different alteration stages from liebenbergite to népouite and from népouite to willemseite. Due to that, the cation proportions of these népouites need also to be grouped (table 4.6). So, the empirical formula is $Ni_{2.25}Mg_{0.43}Si_2O_5(OH)_4$ for group 1 and can be summarized to $(Ni,Mg)_{2.68}Si_2O_5(OH)_4$. These népouites can be attributed to the transition from liebenbergite to népouite, so the real content of O and (OH) is unknown and falsifies therewith all the other cations. But to facilitate a comparison, the cations are calculated on the basis of 2 Si, and O and (OH) are assumed to be $O_5(OH)_4$. Due to this, (Ni,Mg) is lower than in the general mineral formula which is $Ni_3Si_2O_5(OH)_4$.

The empirical formula for group 2 is $Ni_{2.01}Mg_{0.08}Si_2O_5(OH)_4$ and can be summarized to $(Ni,Mg)_{2.09}Si_2O_5(OH)_4$. These népouites can be attributed to the transition from népouite to willemseite, so also here the real content of O and (OH) is unknown, falsifying therewith all the other cations. But to facilitate a comparison, the cations are calculated on the basis of 2 Si, and O and (OH) are assumed to be $O_5(OH)_4$. Due to this, (Ni,Mg) is significantly lower than in the general mineral formula which is $Ni_3Si_2O_5(OH)_4$.

Table 4.6 Summary of the cation proportions for népouite subdivided into group 1 (n = 18) and group 2 (n = 9), cations per 2 Si.

	Fe	Ni	Co	Zn	Si	Mg	Ca	Al	Ti	Mn	Cr
Group 1											
average	0.0475	2.2517	0.0168	0	2.0000	0.4251	0.0008	0.0009	0	0.0004	0
minimum	0.0248	2.0542	0.0117	0	2.0000	0.3106	0	0	0	0	0
maximum	0.1219	2.3769	0.0267	0	2.0000	0.5707	0.0051	0.0199	0.0007	0.0014	0.0008
Group 2											
average	0.0257	2.0034	0.0155	0	2.0000	0.0835	0.0162	0	0	0.0011	0.0014
minimum	0.0088	1.6607	0.0102	0	2.0000	0.0378	0.0094	0	0	0	0.0005
maximum	0.0711	2.1854	0.0231	0	2.0000	0.1461	0.0218	0.0059	0.0012	0.0034	0.0027

4.1.3 Willemseite $(Ni,Mg)_3Si_4O_{10}(OH)_2$

In total 31 willemseites from the ten samples BA 83-1, BAU, BA 87-1, NCK6, BA 84-1, BA 87-3, NCJ5, NCH7, BA 84-2 and BAD were analysed. NiO is 28.32 wt% in average and varies about 24.90 wt%, being 15.32 wt% in the minimum and 40.22 wt% in the maximum concentration (table 4.7). MgO varies about 13.05 wt% from 3.05 wt% in the minimum to 16.12 wt% in the maximum concentration, being 10.09 wt% on average. SiO_2 varies significantly as well, being 41.11 wt% in the minimum and 56.62 wt% in the maximum concentration, showing an average concentration of 53.41 wt%. FeO varies strongly as well with a range of 4.93 wt%, being 1.92 wt% on average, with a minimum of 0.65 wt% and a maximum concentration of 5.58 wt%. CoO is enriched with an average concentration of 0.45 wt%. Traces of Al_2O_3 are detected in only eleven willemseites with a maximum concentration of 3.96 wt%. ZnO is detected in only one willemseite with a concentration of 0.05 wt%. CaO is detected in five willemseites with a maximum concentration of 0.20 wt%. TiO_2, MnO and Cr_2O_3 are not detected.

Together with willemseite and talc data from other authors, the willemseites are plotted in a ternary MgO-SiO_2-(FeO + NiO) diagram (figure 4.10). The broad scattering of the concentrations of MgO, SiO_2 and (FeO + NiO) is clear to see, some outliers as well. De Waal (1970b) analysed willemseite from the Bon Accord as

well. The published average concentration plots well with the MgO-poorer willemseites of the present study. Eggleton *et al.* (2011) analysed Ni-laterite in Australia, which has been a serpentinized harzburgite from an ophiolite in origin. Those plot more to the (FeO + NiO) side, matching well with the MgO-poorest willemseites of this study. Andreoli *et al.* (1999) observed also willemseite in the melt sheet of the Morokweng impact crater in South Africa. Their willemseite plots very well with the MgO-enriched willemseites of the present study. Nevertheless there are still some more MgO-enriched willemseites than that in the present study, indicating well the willemseite-talc solid solution (Galí *et al.*, 2009; Villanova-de-Benavent *et al.*, 2011).

Table 4.7 Summarized EPMA data of willemseite (n = 31) in wt%.

	FeO	NiO	CoO	ZnO	SiO_2	MgO	CaO	Al_2O_3	TiO_2	MnO	Cr_2O_3
average	1.92	28.32	0.45	0	53.41	10.09	0	0	0	0	0
minimum	0.65	15.32	0.22	0	41.11	3.05	0	0	0	0	0
maximum	5.58	40.22	0.72	0.05	56.62	16.12	0.20	3.96	0	0	0

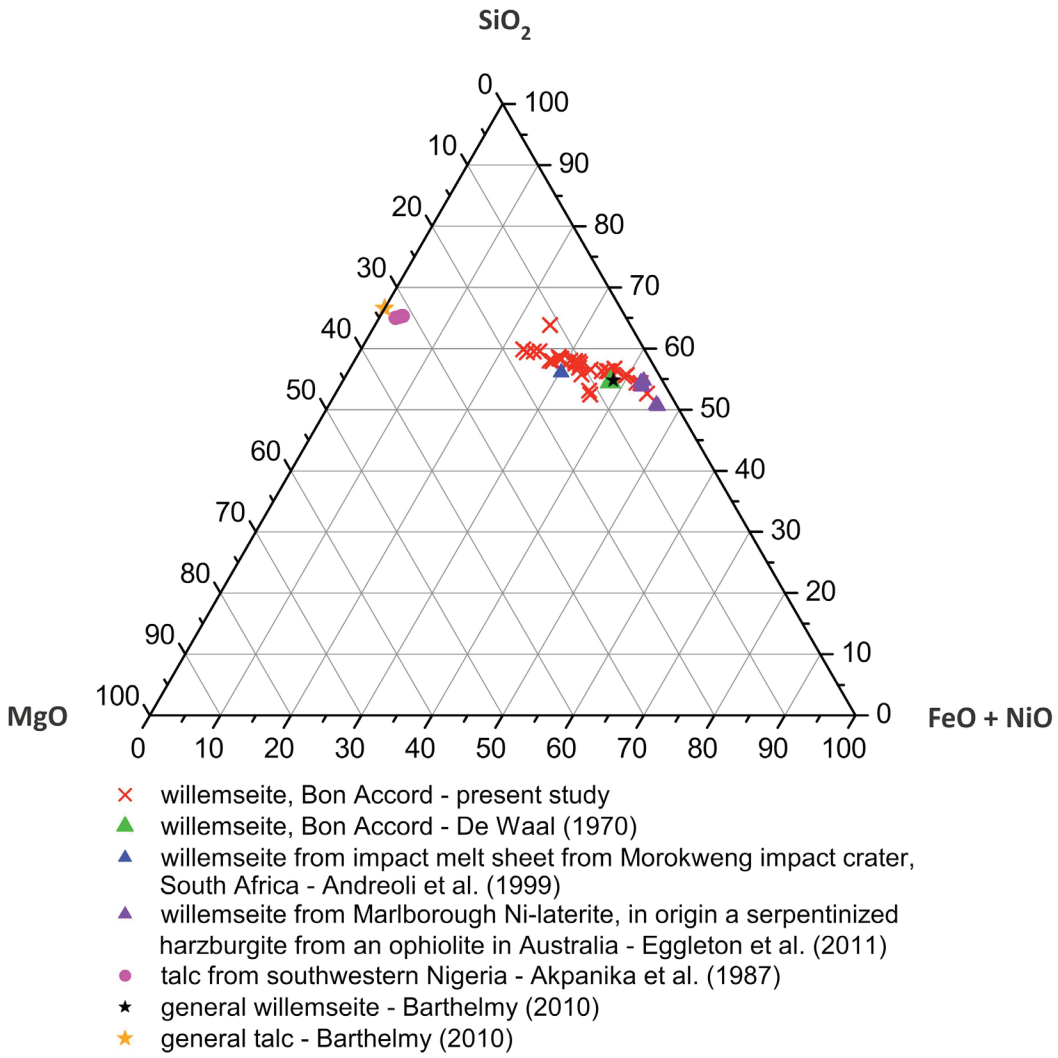

Figure 4.10 Willemseite composition in a ternary MgO-SiO_2-(FeO + NiO) diagram, together with selected willemseites from different types of deposits, and data for talc to illustrate the talc-willemseite solid solution. The concentrations were normalized to 100 wt%.

Except from De Waal (1970b), none of the other authors published the trace element oxide concentrations of their willemseites. The average CoO concentration of De Waal (1970b), 0.46 wt%, fits perfectly with the average concentration of this study, being 0.45 wt%.

His average concentration for CaO is 0.28 wt%. His Al_2O_3 average concentration is 0.38 wt%, which is only sporadically detected in the willemseites of the present study (figure 4.11).

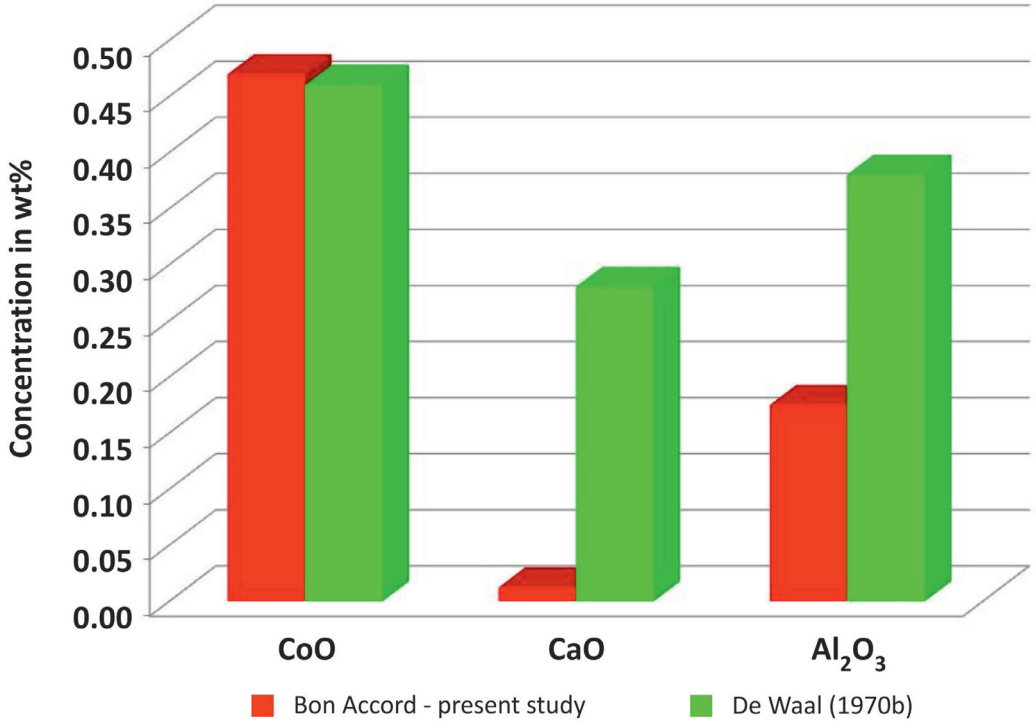

Figure 4.11 Overview about the averaged trace element oxide distribution of the willemseites from Bon Accord, in comparison with the willemseite from Bon Accord of De Waal (1970b).

On closer inspection of the single willemseite concentrations an explicit trend is observed (figure 4.12). The willemseites of Bon Accord A are clearly enriched in (FeO + NiO), whereas the willemseites of Bon Accord B are impoverished in (FeO+NiO), and very enriched in MgO. The willemseites from the contact take an intermediate position, they are impoverished in (FeO + NiO) and enriched in MgO.

Figure 4.13 illustrates the behaviour of Mg, Fe and Co cations towards Ni. Mg shows a significant negative trend towards Ni – the increase in Ni is accompanied with the decrease in Mg, indicating very well the solid solution between willemseite and talc. The Bon Accord A samples contain the Ni-richest and Mg-poorest samples, followed by the decrease in Ni and increase in Mg from Bon Accord A to Bon Accord B. Fe and Co show no trend or relation to another element.

The average cation proportions (table 4.8) give the empirical formula $Ni_{1.72}Mg_{1.11}Si_4O_{10}(OH)_2$ and can be summarized to $(Ni,Mg)_{2.83}Si_4O_{10}(OH)_2$. Since the willemseites are partly in the alteration transition from népouite to willemseite, the real content of O and (OH) is unknown and falsifies therewith all the other cations. But for simplification, the cations are calculated on the basis of 4 Si, and O and (OH) are assumed to be $O_{10}(OH)_2$. Due to this, (Ni,Mg) is lower than in the general mineral formula which is $(Ni,Mg)_3Si_4O_{10}(OH)_2$.

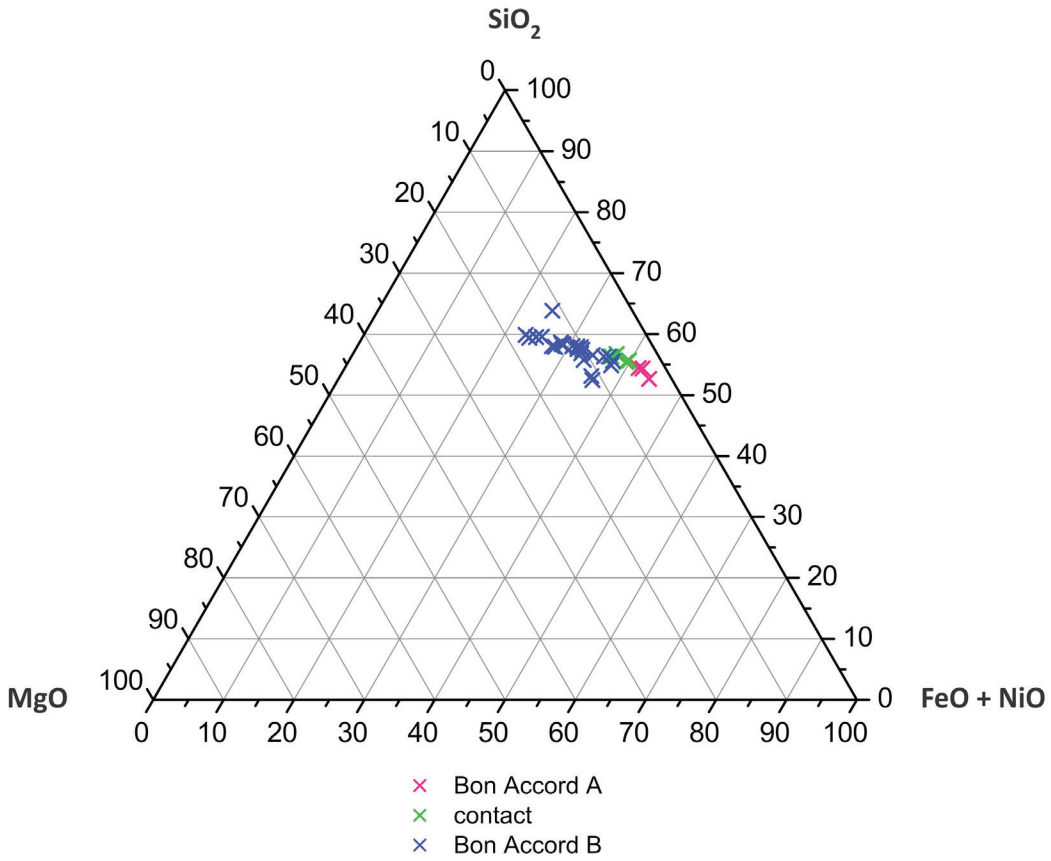

Figure 4.12 Willemseite compositions in the ternary MgO-SiO_2-(FeO + NiO) diagram, subdivided into Bon Accord A, the contact and Bon Accord B. The concentrations were normalized to 100 wt%.

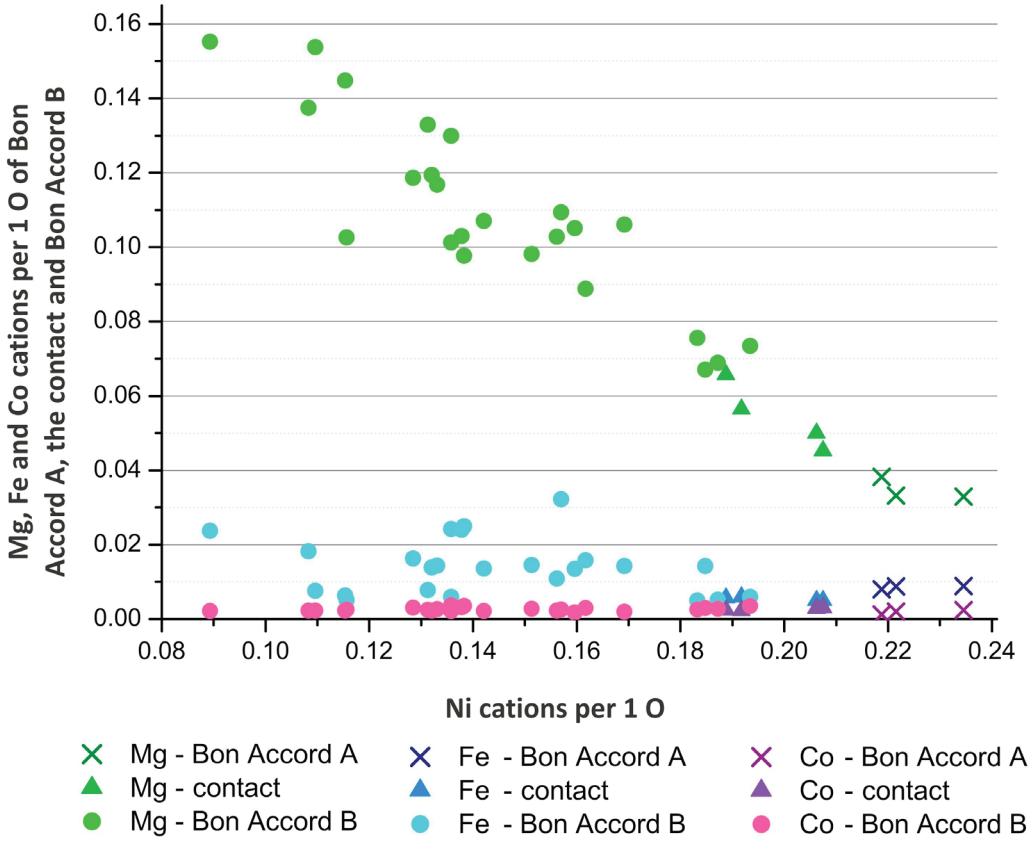

Figure 4.13 Overview about the behavior of the Mg, Fe and Co cation proportions towards Ni. A subdivision of the elements in Bon Accord A, the contact and Bon Accord B visualizes the development of the willemseite composition. All plotted concentrations are cation proportions per 1 O.

Table 4.8 Summary of the cation proportions for willemseite (n = 31), cations per 4 Si.

	Fe	Ni	Co	Zn	Si	Mg	Ca	Al	Ti	Mn	Cr
average	0.1199	1.7174	0.0272	0	4.0000	1.1043	0.0011	0.0035	0	0.0005	0
minimum	0.0529	0.9828	0.0134	0	4.0000	0.3622	0	0	0	0	0
maximum	0.3700	2.6033	0.0412	0.0027	4.0000	1.7096	0.0174	0.3936	0.0022	0.0016	0.0014

4.1.4 Nimite $(Ni,Mg,Fe)_5Al(Si_3Al)O_{10}(OH)_8$

In total 30 nimites from the ten samples BA 87-4, BA 87-1, NCK6, BA 84-1, BA 87-3, NCJ8, NCJ5, NCH7, BA 84-2 and BAD were analysed. NiO, MgO, FeO, Al_2O_3 and SiO_2 vary significantly (table 4.9). NiO shows the most significant variation with 31.11 wt%, being 15.83 wt% in the minimum and 46.94 wt% in the maximum concentration, showing an average of 25.07 wt%. The second largest range of variation is that of MgO with 14.48 wt%, being 3.59 wt% in the minimum and 18.07 wt% in the maximum concentration, showing an average concentration of 12.23 wt%. FeO varies about 9.04 wt%, being 1.50 wt% in the minimum and 10.54 wt% in the maximum concentration, showing an average of 5.79 wt%. The average concentration of Al_2O_3 is 14.98 wt%, showing a range of 12.92 wt% with 4.72 wt% in the minimum and 17.64 wt% in the maximum concentration. SiO_2 varies significantly as well, but least of all about 8.72 wt%, being 26.68 wt% in the minimum and 35.40 wt% in the maximum concentration, showing an average of 28.46 wt%. The trace elements behave relatively stable with CoO showing an average concentration of 0.57 wt%, CaO is only in four nimites detected, showing a maximum concentration of 0.05 wt%. MnO is on average 0.04 wt%. Cr_2O_3 is detected in only three nimites and shows a maximum concentration of 0.30 wt%. TiO_2 is detected in only one nimite with 0.09 wt%. ZnO is not detected.

Table 4.9 Summarized EPMA data of nimite (n = 30) in wt%.

	FeO	NiO	CoO	ZnO	SiO_2	MgO	CaO	Al_2O_3	TiO_2	MnO	Cr_2O_3
average	5.79	25.07	0.57	0	28.46	12.23	0	14.98	0	0.04	0
minimum	1.50	15.83	0.41	0	26.68	3.59	0	4.72	0	0	0
maximum	10.54	46.94	0.91	0	35.40	18.07	0.05	17.64	0.09	0.07	0.30

Together with the data of De Waal (1970a) and of Zhan and Guggenheim (1995), all nimites are plotted in a ternary Al_2O_3-SiO_2-(FeO + NiO + MgO) diagram (figure 4.14). The nimites of the present study show a clear segregation into two groups. Group 1 is with five nimites enriched in (FeO + NiO + MgO) and impoverished in Al_2O_3, whereas group 2 behaves inverse with 23 nimites. The two outliers can be attributed to group 2 and are richer in SiO_2 than the other ones. It is conspicuous that group 1 contains only samples of Bon Accord A and group 2 only samples of Bon Accord B and the contact. The average nimite of De Waal (1970a) from the Bon Accord plots perfectly with the nimites of group 2, whereas the average nimite of Zhan and Guggenheim (1995), donated from the Woodline Well Ni-sulphide deposit in a strongly serpentinized peridotite, in Australia, plots still within the range of group 2 but is the most Al_2O_3-impoverished data point. The average concentration of the nimite, which is described by De Waal (1970a), differs only slightly from that of the present study. His FeO

concentration is a little lower whilst NiO is higher. MgO in the nimites of the present study is higher, whereas Al_2O_3 is lower than in the nimites of De Waal (1970a). His average CoO-concentration is a little lower, the CaO-concentration is higher, MnO is about the same concentration, the same applies for Cr_2O_3 (figure 4.15). Concentrations for ZnO and TiO_2 are not published. Zhan and Guggenheim (1995) published only the trace element oxide concentration for TiO_2 which is enriched, whereas no TiO_2 is detected in the nimites from Bon Accord.

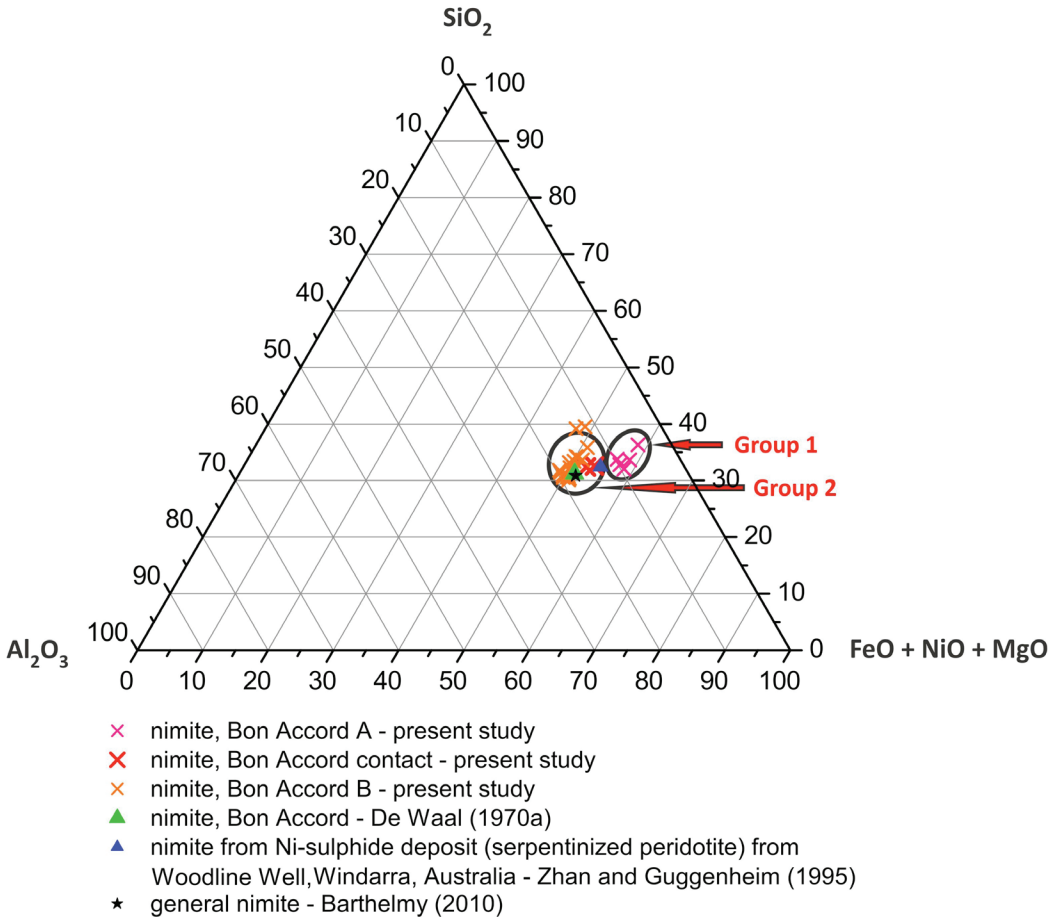

Figure 4.14 Nimite compositions in the ternary Al_2O_3-SiO_2-(FeO + NiO + MgO) diagram (subdivided into Bon Accord A, the contact and Bon Accord B) in the ternary Al_2O_3-SiO_2-(FeO + NiO + MgO) diagram, together with selected nimite data from other authors. The concentrations were normalized to 100 wt%.

Upon detailed consideration of group 1 and 2 it is conspicuous that group 1 contains only samples of Bon Accord A and group 2 only samples of Bon Accord B and the contact (figure 4.14). Table 4.10 shows the clear differences of the element concentrations which are also illustrated in figure 4.16. The average of FeO increases from Bon Accord A to the contact about 1.43 wt% and once more to Bon Accord B about 3.46 wt%. The same applies for MgO – the contact samples are about 5.13 wt% richer than Bon Accord A, and about 3.92 wt% poorer than Bon Accord B. The same applies as well for Al_2O_3. The contact is about 4.48 wt% richer than Bon Accord A, and with 2.73 wt% poorer than Bon Accord B. NiO behaves vice versa. Bon Accord A is the richest with 45.90 wt%, whilst a decrease of about 10.51 wt% has to be noted for the contact and a further decrease of about 11.42 wt% for Bon Accord B. The SiO_2 concentration decreases just slightly. Bon Accord A is about 0.85

wt% higher than in the contact, and about 0.94 wt% higher than in Bon Accord B. These differences are also observable in the cation proportions as illustrated in figure 4.17. Mg, Fe as well as Al show a distinct negative trend towards Ni – all of them decrease with increasing Ni, indicating clearly the substitution of Mg, Fe and Al with Ni. Co shows no significant trend to any other element. No correlation of the elements amongst each other can be observed. It is also here conspicuous that the Bon Accord A samples contain the Ni-richest and Mg-, Fe- and Al-poorest samples, followed by the decrease in Ni and increase in Mg, Fe and Al from Bon Accord A to Bon Accord B.

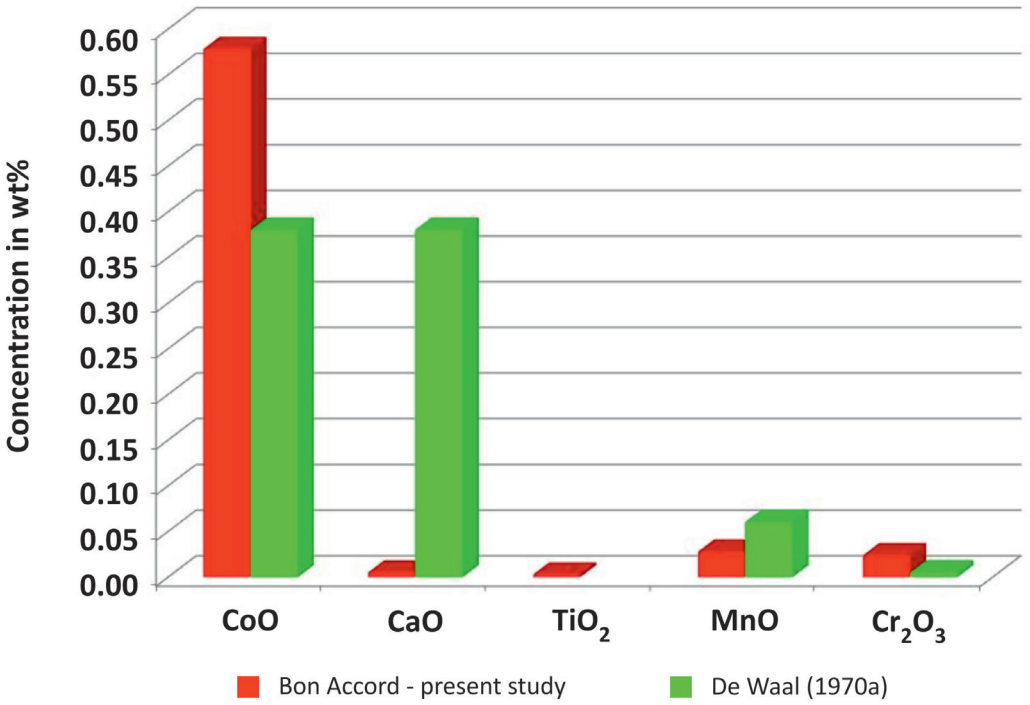

Figure 4.15 Overview about the averaged trace element oxide distribution of the nimites from Bon Accord, in comparison with the nimite from Bon Accord of De Waal (1970a).

Table 4.10 Summarized EPMA data of nimite, subdivided into Bon Accord A (n = 5), the contact (n = 2) and Bon Accord B (n = 23), in wt%.

	FeO	NiO	CoO	ZnO	SiO_2	MgO	CaO	Al_2O_3	TiO_2	MnO	Cr_2O_3
Bon Accord A											
average	1.80	45.90	0.53	0	29.84	3.69	0	8.38	0	0	0
minimum	1.50	45.20	0.50	0	28.38	3.59	0	4.72	0	0	0
maximum	2.95	46.94	0.56	0	32.93	4.26	0	8.73	0	0	0.21
contact											
average	3.23	35.39	0.55	0	28.99	8.82	0.02	12.86	0	0	0
n 1	3.41	35.00	0.54	0	29.14	8.86	0.04	13.54	0	0	0
n 2	3.04	35.77	0.55	0	28.84	8.77	0	12.17	0	0	0
Bon Accord B											
average	6.69	23.97	0.60	0	28.05	12.74	0	15.59	0	0.04	0
minimum	3.50	15.83	0.41	0	26.68	10.30	0	10.47	0	0	0
maximum	10.54	28.78	0.91	0	35.40	18.07	0.05	17.64	0.09	0.07	0.30

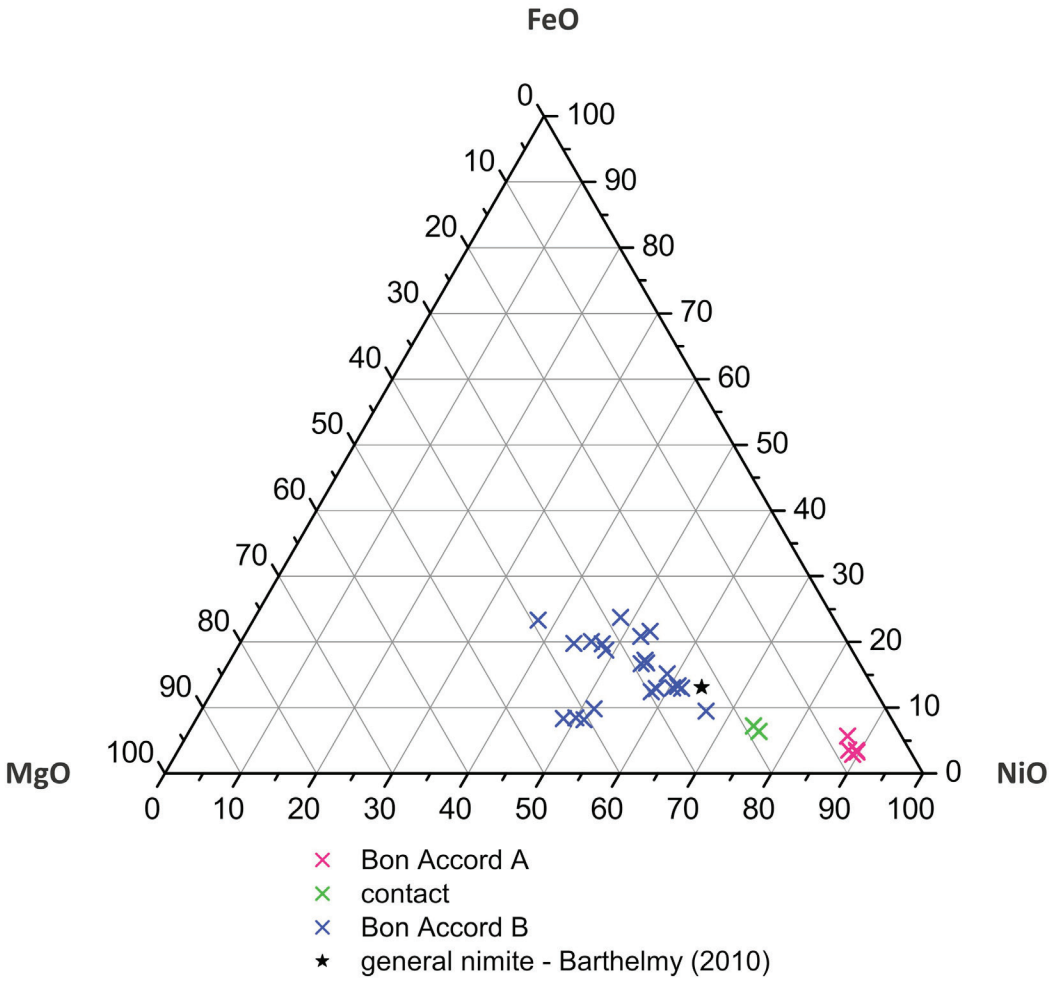

Figure 4.16 Nimite compositions in the ternary MgO-FeO-NiO diagram, subdivided into Bon Accord A, the contact and Bon Accord B. The nimites of Bon Accord A belong to the Al_2O_3-impoverished group 1 and those of the contact and Bon Accord B belong to the Al_2O_3-enriched group 2. The concentrations were normalized to 100 wt%.

The average cation proportions (table 4.11) give the empirical formula $Ni_{2.17}Mg_{1.95}Fe_{0.52}Al_{0.93}Si_3Al_{0.93}O_{10}(OH)_8$ and can be summarized to $(Ni,Mg,Fe)_{4.64}Al_{0.93}(Si_3Al_{0.93})O_{10}(OH)_8$. Since the nimites are alteration products in different steps of progress, the real content of O and (OH) is unknown and falsifies therewith all the other cations. But for simplification, the cations are calculated on the basis of 3 Si, and O and (OH) are assumed to be $O_{10}(OH)_8$. Due to this, (Ni,Mg,Fe) and Al are lower than in the general mineral formula which is $(Ni,Mg,Fe)_5Al(Si_3Al)O_{10}(OH)_8$.

The calculation of the empirical formula, divided into the groups Bon Accord A, the contact and Bon Accord B, shows a variation in the formula with significant deviation (table 4.12). For Bon Accord A the average empirical formula is $Ni_{3.77}Mg_{0.58}Fe_{0.14}Al_{0.51}Si_3Al_{0.51}O_{10}(OH)_8$ and can be summarized to $(Ni,Mg,Fe)_{4.48}Al_{0.51}(Si_3Al_{0.51})O_{10}(OH)_8$. For the contact it is $Ni_{2.95}Mg_{1.36}Fe_{0.28}Al_{0.78}Si_3Al_{0.78}O_{10}(OH)_8$ and can be summarized to $(Ni,Mg,Fe)_{4.58}Al_{0.78}(Si_3Al_{0.78})O_{10}(OH)_8$.
And for Bon Accord B it is $Ni_{2.03}Mg_{2.05}Fe_{0.60}Al_{0.99}Si_3Al_{0.99}O_{10}(OH)_8$ and can be summarized to $(Ni,Mg,Fe)_{4.68}Al_{0.99}(Si_3Al_{0.99})O_{10}(OH)_8$. The latter fits best with the general mineral formula.

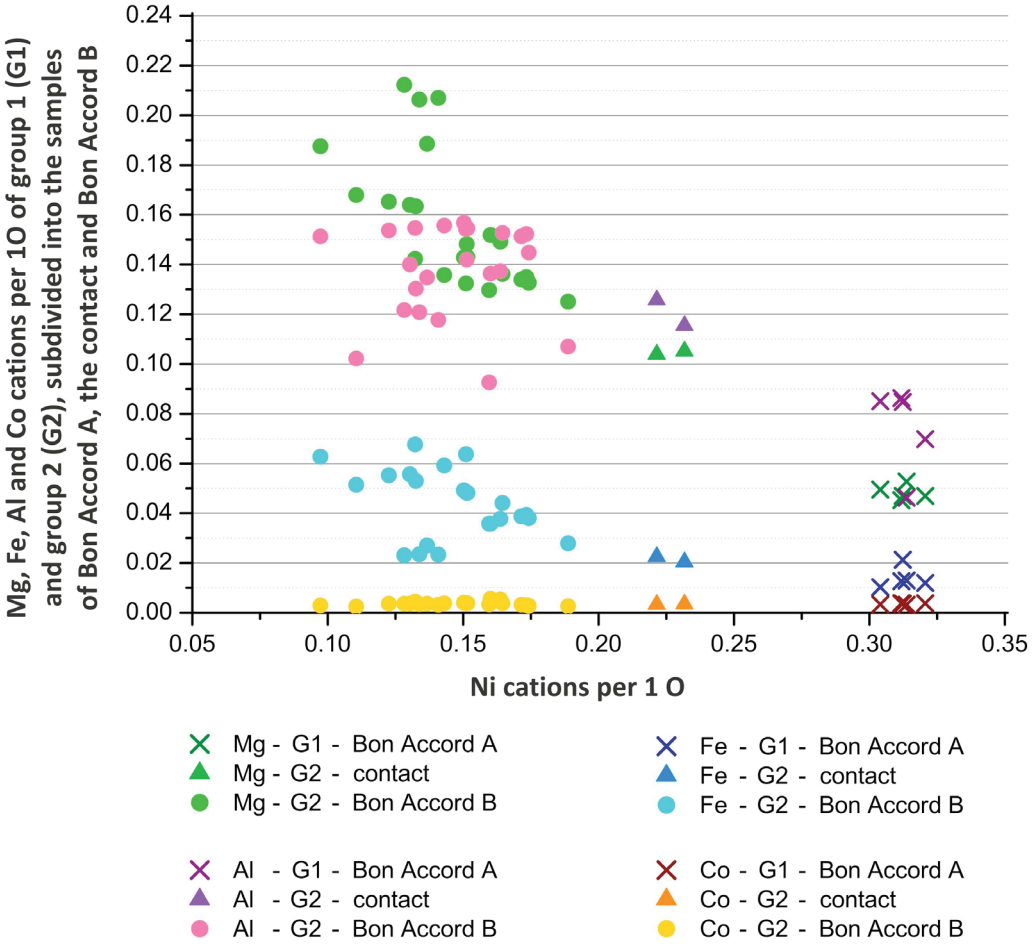

Figure 4.17 Overview about the behavior of the Mg, Fe, Al and Co cation proportions towards Ni. A subdivision of the elements in Bon Accord A, the contact and Bon Accord B visualizes the development of the nimite composition. All plotted concentrations are cation proportions per 1 O.

Table 4.11 Summary of the cation proportions for nimite (n = 31), cations per 3 Si.

	Fe	Ni	Co	Zn	Si	Mg	Ca	Al	Ti	Mn	Cr
average	0.5224	2.1688	0.0464	0	3.0000	1.9518	0.0015	1.8482	0.0011	0.0013	0.0033
minimum	0.1218	1.2937	0.0301	0	3.0000	0.5490	0	0.5068	0	0	0
maximum	0.9667	3.8431	0.0767	0.0010	3.0000	2.8315	0.0053	2.2525	0.0261	0.0067	0.0065

Table 4.12 Summary of the cation proportions for nimite, subdivided into Bon Accord A (n = 5), the contact (n = 2) and Bon Accord B (n = 23), cations per 3 Si.

	Fe	Ni	Co	Zn	Si	Mg	Ca	Al	Ti	Mn	Cr
Bon Accord A											
average	0.1425	3.7669	0.0444	0	3.0000	0.5781	0.0024	1.0099	0.0035	0	0
minimum	0.1218	3.4384	0.0362	0	3.0000	0.5490	0.0012	0.5068	0	0	0
maximum	0.2615	3.8431	0.0461	0	3.0000	0.5881	0.0027	1.0465	0.0173	0.0018	0.0031
contact											
average	0.2795	2.9445	0.0453	0	3.0000	1.3595	0.0037	1.5679	0.0054	0.0005	0.0023
n 1	0.2941	2.8954	0.0444	0	3.0000	1.3595	0.0039	1.6438	0.0059	0.0010	0.0020
n 2	0.2648	2.9935	0.0462	0	3.0000	1.3595	0.0036	1.4919	0.0048	0	0.0026
Bon Accord B											
average	0.6029	2.0268	0.0513	0	3.0000	2.0489	0.0011	1.9724	0.0004	0.0014	0.0039
minimum	0.3079	1.2937	0.0301	0	3.0000	1.4642	0	1.0459	0	0	0.0010
maximum	0.9667	2.4722	0.0767	0.0010	3.0000	2.8315	0.0053	2.2525	0.0261	0.0067	0.0065

4.2 Oxides

4.2.1 Bunsenite NiO

In total six bunsenites from the three samples BA 87-4, BA 83-1 and BAU were analysed. The average NiO content in bunsenite is 97.73 wt% and varies about 1.43 wt% with a minimum of 96.98 wt% and a maximum of 98.41 wt% (table 4.13). Bunsenite is enriched in FeO, being 0.80 wt% on average. CoO is also enriched with an average concentration of 1.28 wt%. MgO is enriched as well with an average concentration of 0.38 wt%. No other elements are detected. The bunsenite compositions that are reported by De Waal (1977) at the Bon Accord, as well as by Andreoli *et al.* (1999) from the melt sheet of the Morokweng impact crater in South Africa, fit well with the data of the present study.

Table 4.13 Summarized EPMA data of bunsenite (n = 6) in wt%.

	FeO	NiO	CoO	ZnO	SiO_2	MgO	CaO	Al_2O_3	TiO_2	MnO	Cr_2O_3
average	0.80	97.73	1.28	0	0	0.38	0	0	0	0	0
minimum	0.21	96.98	1.20	0	0	0.33	0	0	0	0	0
maximum	1.71	98.41	1.40	0	0	0.45	0	0	0	0	0

The variance of the elements is best observable in figure 4.18, which contains the cation proportions. Fe shows the most significant trend – its decrease is accompanied with the increase in Ni, showing substitution. Co shows a slight positive trend towards Ni, increasing with the increase in Ni. No trend is observable for MgO towards any element, but also not for Fe towards Co.

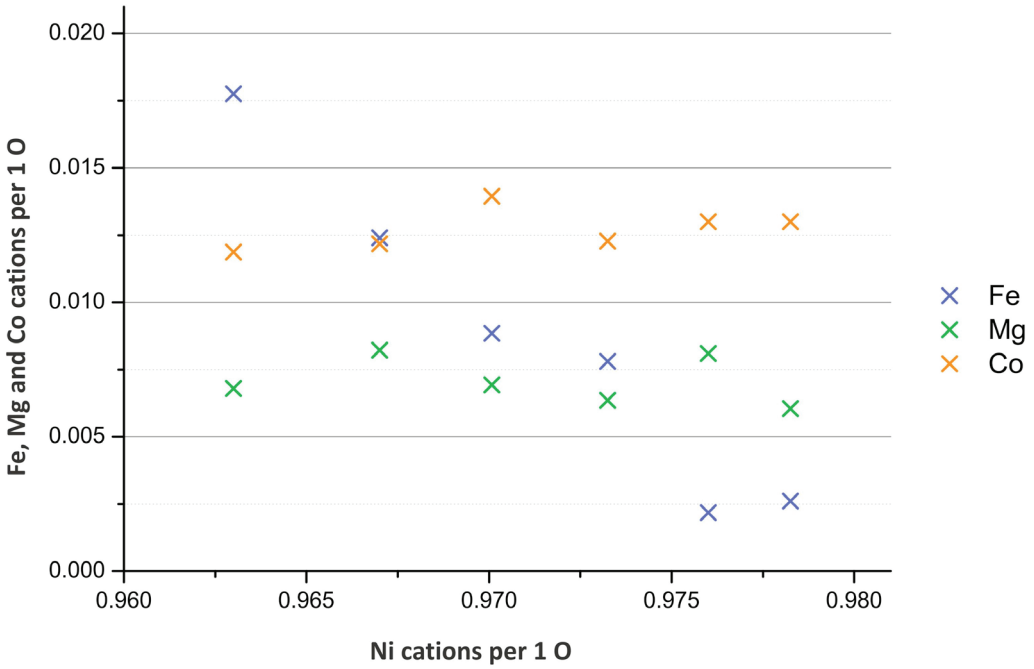

Figure 4.18: Overview about the behavior of the cations Fe, Mg and Co towards Ni in the bunsenite. All plotted concentrations are cation proportions per 1O.

The average cation proportions (table 4.14) give the empirical formula $Ni_{0.97}O$, which fits very well with the general mineral formula NiO. The slight discrepancy of 0.03 in the electrical charge of the cations is balanced

with the sum of the trace elements.

Table 4.14 Summary of the cation proportions for bunsenite (n = 6), cations per 1 O.

	Fe	Ni	Co	Zn	Si	Mg	Ca	Al	Ti	Mn	Cr
average	0.0084	0.9717	0.0127	0	0	0.0069	0	0	0	0.0002	0
minimum	0.0022	0.9630	0.0119	0	0	0.0061	0	0	0	0.0001	0
maximum	0.0178	0.9783	0.0140	0	0	0.0082	0.0002	0	0.0001	0.0003	0.0002

4.2.2 Cochromite $(Co,Ni,Fe)(Cr,Al)_2O_4$ and Cobaltian Chromite $(Fe,Co,Mg,Ni)_{0.98}(Cr,Al)_{1.94}O_4$

In total seven mineral grains from the three samples BA 87-4, BA 83-1 and NCJ8 were analysed. The major elements vary significantly. CoO is 13.88 wt% on average and varies about 10.42 wt% from 6.48 wt% in the minimum to 16.90 wt% in the maximum concentration. NiO varies much less with 6.05 wt% from 0.76 wt% in the minimum to 6.81 wt% in the maximum concentration, being 5.70 wt% on average. The FeO concentration varies significantly between a minimum of 10.49 wt% and a maximum of 23.93 wt% about 13.44 wt%, being 11.85 wt% on average (table 4.15). Cr_2O_3 and Al_2O_3 vary significantly as well, but to a little lower extent. The average concentration of Cr_2O_3 is 49.38 wt% with a variance of 9.06 wt%, being 45.50 wt% in the minimum and 54.56 wt% in the maximum concentration. Al_2O_3 is 13.57 wt% on average, ranging about 5.54 wt% from the minimum of 9.63 wt% to the maximum of 15.17 wt%. The minerals are all enriched in the trace elements MgO, ZnO, TiO_2 and MnO. MgO shows an average concentration of 1.83 wt%, for ZnO it is 0.88 wt%, TiO_2 is 1.05 wt% on average and MnO 0.67 wt%. SiO_2 and CaO are not detected.

Table 4.15 Summarized EPMA data of cochromite (n = 7) in wt%.

	FeO	NiO	CoO	ZnO	SiO_2	MgO	CaO	Al_2O_3	TiO_2	MnO	Cr_2O_3
average	11.85	5.70	13.88	0.88	0	1.83	0	13.57	1.05	0.67	49.38
minimum	11.61	0.76	6.48	0.65	0	0.98	0	9.63	0.47	0.57	45.50
maximum	23.60	6.81	16.90	1.58	0	3.24	0	15.17	1.44	1.31	54.56

Figure 4.19 illustrates the distribution of the major elements, together with data from other authors for cochromite, cobaltian chromite, nichromite and chromite. Because of the known substitution of CoO, NiO, MgO and FeO in cochromite, they represent one axis; the different types of chromite are subdivided in this ternary diagram. Because of the clear enrichment in MgO, which can occupy the same position (the end member is magnesiochromite), its concentration is also added to those three elements. Two data points of the minerals of the present study are a little more enriched in Cr_2O_3 and impoverished in Al_2O_3 and CoO + NiO + FeO + MgO, but they still plot well with the cochromites of De Waal (1978) and Tredoux *et al.* (1989). In contrast to the chromites from chondrites, pallasites, eucrites and iron meteorites of Sack and Ghiorso (1991), only the chromites of the Critical Zone of the Bushveld Complex in South Africa from Cameron (1977) plot close to the minerals of the present study.

Figure 4.20 shows the variation of CoO, NiO and FeO, which allows a subdivision into two groups. Group 1 contains only samples of Bon Accord A and group 2 contains those from Bon Accord B. Group 1 plots near the general cochromite composition, whereas group 2 is very enriched in FeO and depleted in CoO and NiO. In

group 1 only one cochromite fits very well with the general cochromite whereas the other cochromites of this group show a clear trend in FeO enrichment and CoO and NiO impoverishment.

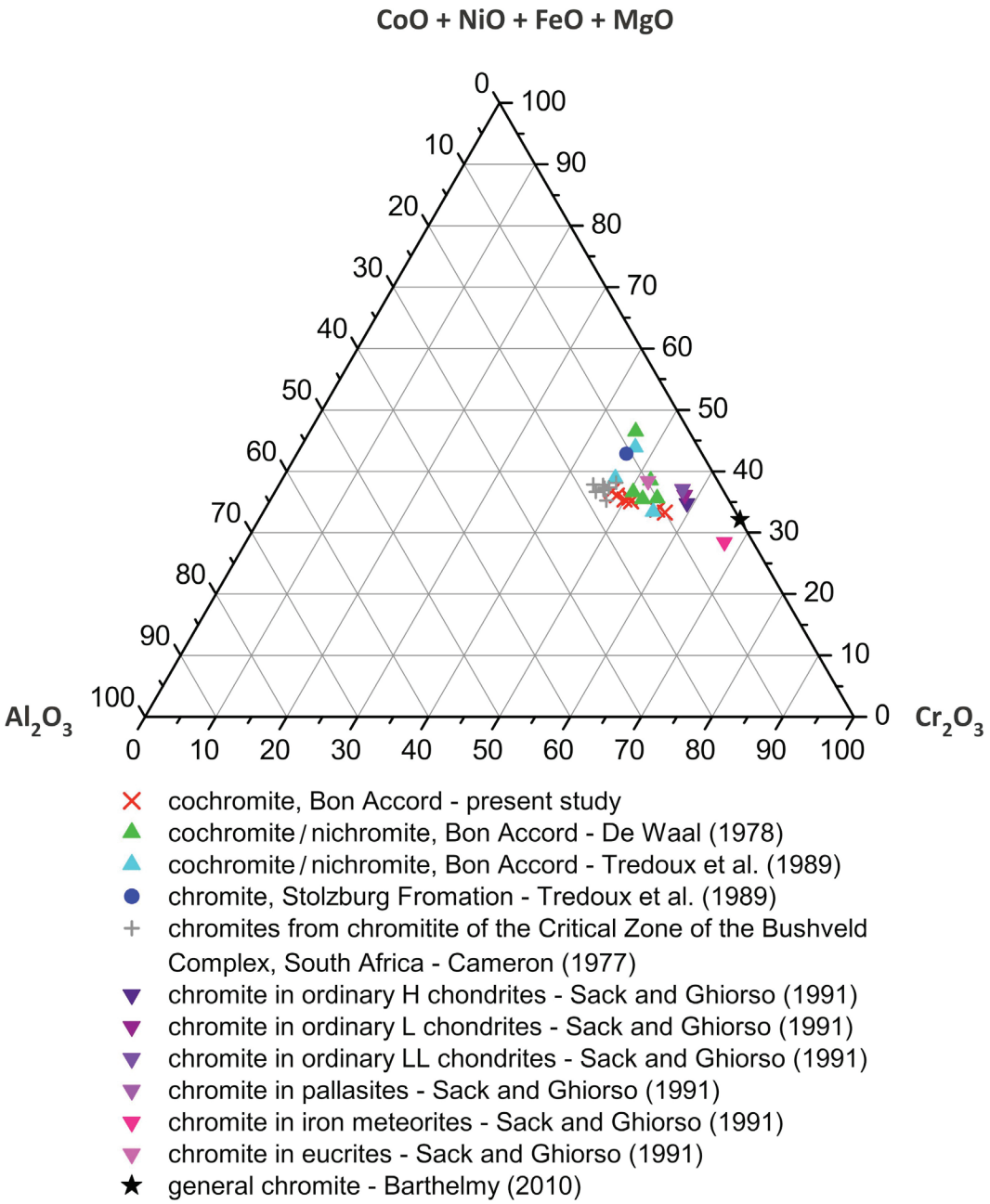

Figure 4.19 Cochromite compositions in the ternary (CoO + NiO + FeO + MgO)-Al_2O_3-Cr_2O_3 diagram, together with selected cochromite, nichromite and chromite data from other authors. The concentrations were normalized to 100 wt%.

Regarding the separated average concentrations of group 1 and group 2, the average element compositions differ significantly (table 4.16). CoO of group 1 is with an average concentration of 13.94 wt% significantly higher than that of group 2 which is 6.59 wt%. NiO of group 1 is with an average of 5.72 wt% also much higher than that of group 2 with 0.82 wt%. FeO of group 1 is with an average concentration of 11.76 wt% impoverished in comparison to group 2 which shows an FeO average concentration of 23.76 wt%. MgO differs a little, being 2.06 wt% on average for group 1, and 1.11 wt% on average for group 2. Cr_2O_3 differs as well, being 48.27 wt% on average for group 1, and 53.93 wt% on average for group 2. Also Al_2O_3 varies between both groups, being

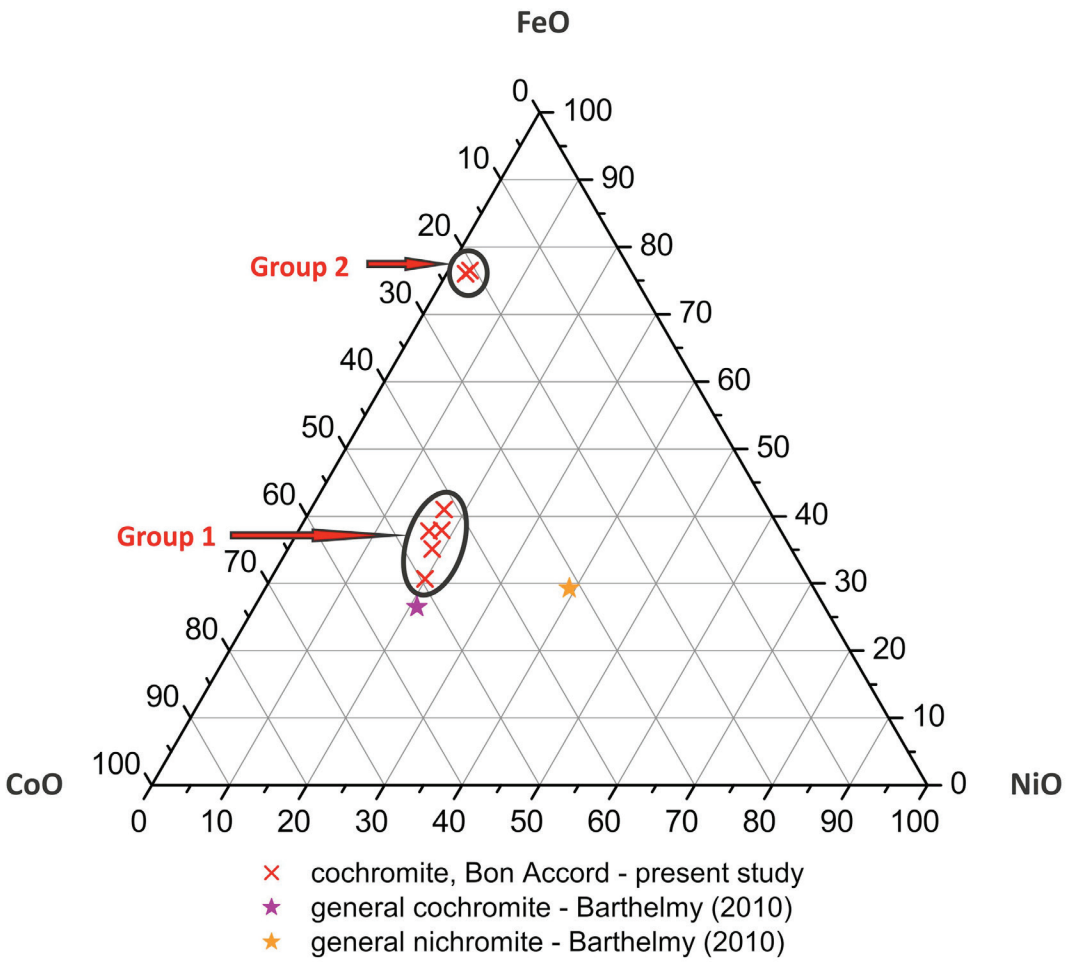

Figure 4.20 Distribution of the substituting element oxides CoO, NiO and FeO in the cochromites of the present study, together with ideal compositions for cochromite and nichromite. The concentrations were normalized to 100 wt%.

Table 4.16 Summarized EPMA data of cochromite subdivided into group 1 (n = 5) and group 2 (n = 2) in wt%.

	FeO	NiO	CoO	ZnO	SiO_2	MgO	CaO	Al_2O_3	TiO_2	MnO	Cr_2O_3
Group 1											
average	11.76	5.72	13.94	0.80	0	2.06	0	14.15	1.15	0.61	48.27
minimum	10.49	5.19	13.54	0.65	0	1.10	0	13.42	0.91	0.57	45.50
maximum	13.61	6.81	16.90	1.06	0	3.24	0	15.17	1.44	0.71	49.84
Group 2											
average	23.76	0.82	6.59	1.53	0	1.11	0	10.04	0.48	1.27	53.93
n 1	23.93	0.88	6.48	1.58	0	1.23	0	10.44	0.50	1.31	53.31
n 2	23.60	0.76	6.69	1.49	0	0.98	0	9.63	0.47	1.23	54.56

14.15 wt% on average for group 1, and 10.04 wt% on average for group 2. ZnO, TiO_2 and MnO vary as well, but not that distinctive (figure 4.21). For comparison the data for cochromite and cobaltian chromite from Bon Accord of De Waal (1978), and the data for cochromite and chromite from Bon Accord of Tredoux *et al.* (1989) are opposed. The minerals of group 1 take with ZnO an intermediate position between the cobaltian chromite of De Waal (1978) and the cochromite of Tredoux *et al.* (1989) whilst the minerals of group 2 show the highest ZnO concentration. With MgO group 1 fits very well with the cochromite of De Waal (1978) and group 2 with the cobaltian chromite of De Waal (1978). The cochromite of Tredoux *et al.* (1989) is the lowest

in MgO and a little poorer than group 2. MgO of the chromite from Tredoux et al (1989) is a little lower than group 1 but still fitting roughly. The TiO_2 concentration of group 1 is in relative accordance to the cochromite and cobaltian chromite of De Waal (1978). Group 2 shows a clearly lower concentration than that, coinciding with the chromite of Tredoux *et al.* (1989). The cochromite of Tredoux et al. (1989) is the highest and not in agreement with any other plotted cochromite. MnO of group 1 fits very well with the cochromite of De Waal (1978). His cobaltian chromite and the cochromite of Tredoux *et al.* (1989) are indeed a little higher but still in agreement with that. The MnO concentration of group 2 exceeds that of the others except for the chromite of Tredoux *et al.* (1989), which is numbers higher. For the minerals of group 1 and 2 no SiO_2 and CaO is detected, whereas the cochromites, cobaltian chromites and chromites contain a little of both.

Figure 4.21 Overview about the averaged minor and trace element distribution of the cochromites from Bon Accord, subdivided into group 1 and group 2, in comparison with the cochromite and cobaltian chromite from Bon Accord of De Waal (1978) and the cochromite and chromite from Bon Accord of Tredoux et al. (1989). Blank positions indicate that these elements were not detected. All plotted concentrations are wt%.

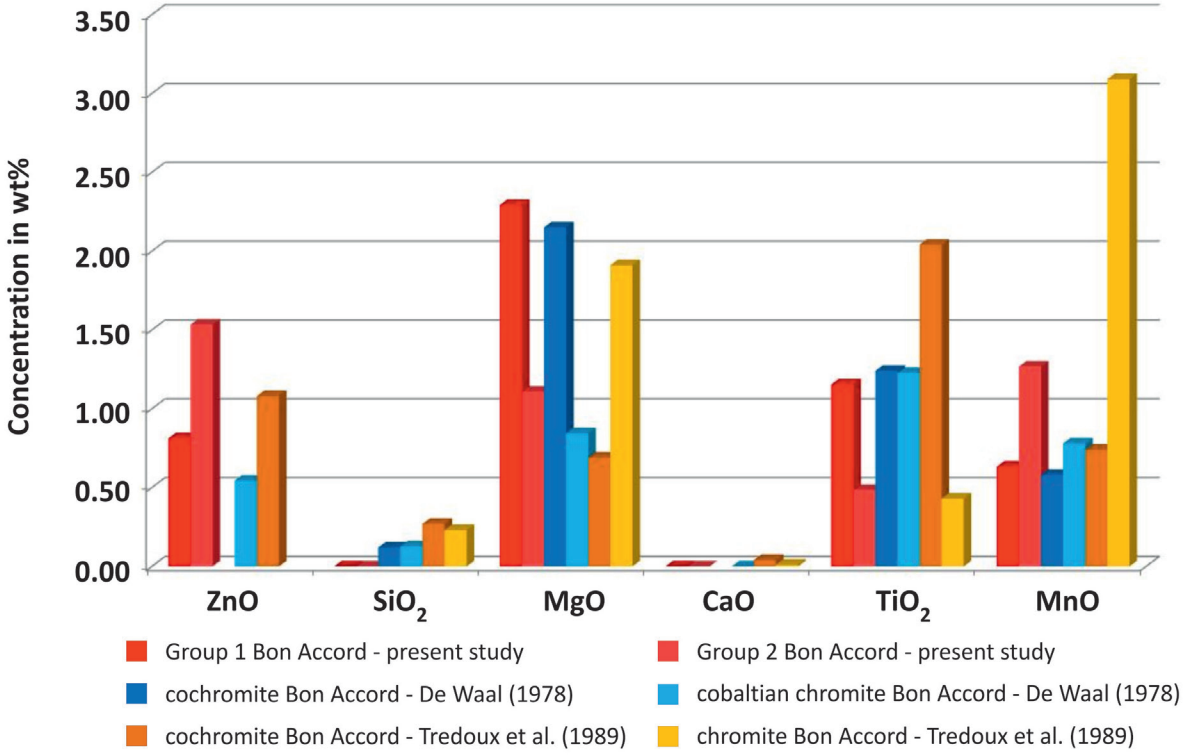

Figure 4.22 illustrates the behaviour of the cations of the elements towards Cr, subdivided into group 1 and group 2. The gap between both groups is clear to see. Al shows a negative trend towards Cr – the increase in Cr is accompanied with the decrease in Al, indicating well the substitution of each other. The same applies for Co towards Fe, Ni towards Fe, Mg towards Ni, and Mg towards Co, whereas Co and Ni show a positive correlation with each other as well as Mg and Fe. This indicates well the substitution of Co and Fe, Ni and Fe, Mg and Ni as well as Mg and Co. Ti and Mn show no clear trend.

The average cation proportions of all analysed mineral grains (table 4.17) give the empirical formula $Co_{0.38}Fe_{0.34}Ni_{0.16}Mg_{0.09}Cr_{1.36}Al_{0.55}O_4$ and can be summarized to $(Co,Fe,Ni,Mg)_{0.97}(Cr,Al)_{1.91}O_4$.

Regarding the grouping of cochromite the respective average cation proportions differ as well (table 4.18). So the empirical formula for group 1 is $Co_{0.39}Fe_{0.34}Ni_{0.16}Mg_{0.11}Cr_{1.33}Al_{0.58}O_4$ and can be summarized to $(Co,Fe,Ni,Mg)_{0.99}(Cr,Al)_{1.90}O_4$. The empirical formula for group 2 is $Fe_{0.71}Co_{0.19}Mg_{0.06}Ni_{0.02}Cr_{1.52}Al_{0.42}O_4$ and can be summarized to $(Fe,Co,Mg,Ni)_{0.98}(Cr,Al)_{1.94}O_4$. Therewith it becomes clear that group 2 cannot be regarded anymore as a cochromite but as cobaltian chromite.

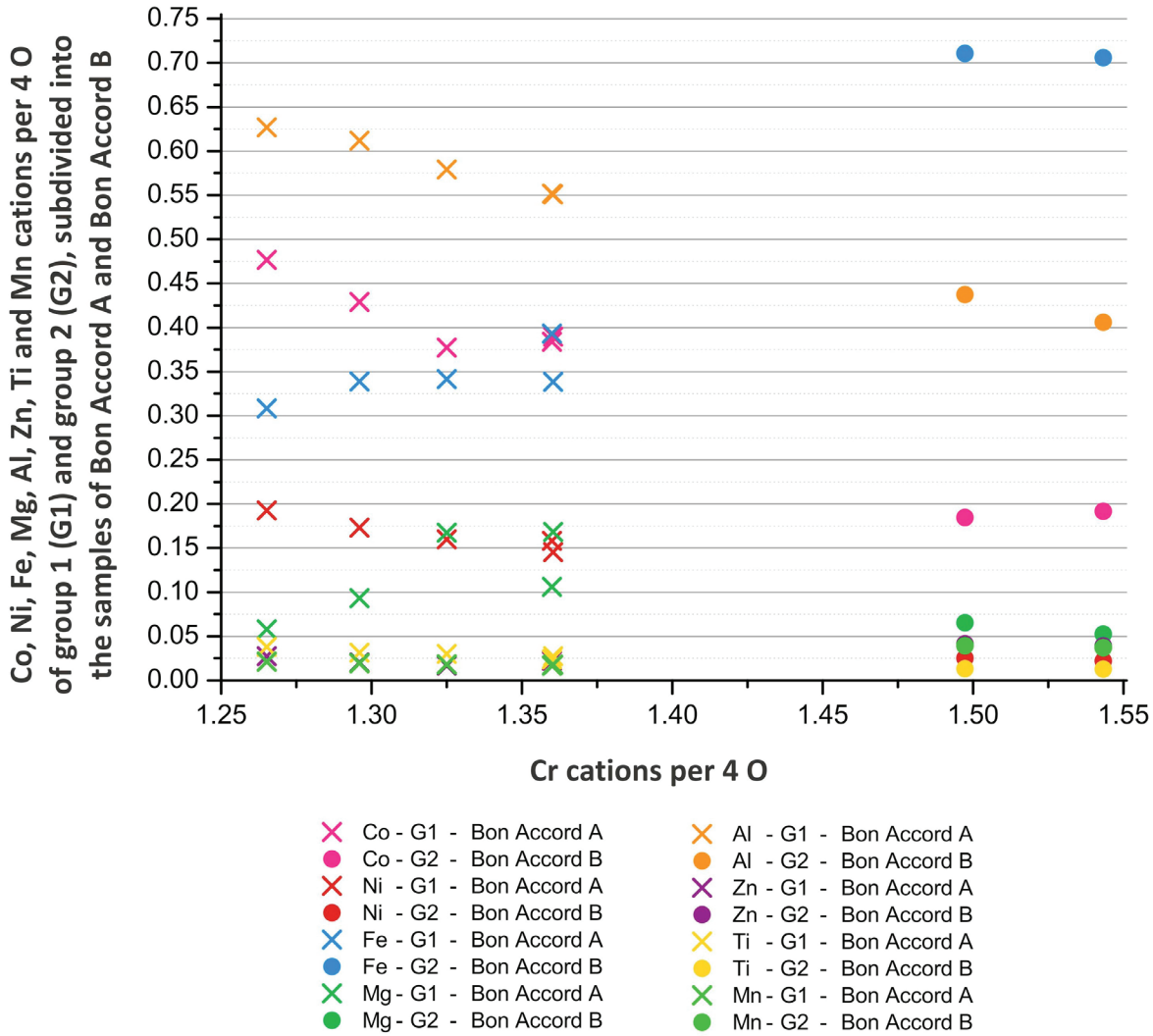

Figure 4.22 Overview about the behavior of the cations Co, Ni, Fe, Mg, Al, Zn, Ti and Mn towards Cr, subdivided into group 1 (G1) of Bon Accord A and group 2 (G2) of Bon Accord B. All plotted concentrations are the cation proportions per 4 O.

Table 4.17 Summary of the cation proportions for cochromite (n = 7), cations per 4 O.

	Fe	Ni	Co	Zn	Si	Mg	Ca	Al	Ti	Mn	Cr
average	0.3414	0.1580	0.3840	0.0223	0.0011	0.0930	0.0002	0.5520	0.0275	0.0193	1.3600
minimum	0.3085	0.0219	0.1846	0.0166	0	0.0524	0	0.4061	0.0126	0.0167	1.2652
maximum	0.7109	0.1925	0.4767	0.0414	0.0024	0.1681	0.0005	0.6268	0.0380	0.0393	1.5432

Table 4.18 Summary of the cation proportions for cochromite subdivided in groups (n = 7), cations per 4 O.

	Fe	Ni	Co	Zn	Si	Mg	Ca	Al	Ti	Mn	Cr
Group 1											
average	0.3390	0.1598	0.3895	0.0203	0.0008	0.1060	0.0003	0.5790	0.0301	0.0180	1.3250
minimum	0.3085	0.1454	0.3771	0.0166	0	0.0577	0	0.5511	0.0237	0.0167	1.2652
maximum	0.3930	0.1925	0.4767	0.0274	0.0017	0.1681	0.0005	0.6268	0.0380	0.0213	1.3603
Group 2											
average	0.7084	0.0235	0.1883	0.0404	0.0018	0.0588	0.0001	0.4217	0.0130	0.0383	1.5202
n 1	0.7109	0.0250	0.1846	0.0414	0.0024	0.0652	0	0.4373	0.0134	0.0393	1.4972
n 2	0.7059	0.0219	0.1919	0.0393	0.0011	0.0524	0.0002	0.4061	0.0126	0.0372	1.5432

µPIXE-analyses on cochromite

Additionally to the EPMA-analyses, one cochromite of the sample BA 87-4 is mapped with the µPIXE. The detected elements are Cr, Fe, Co, Ni, Zn, Ga, Ge, Mo, Ru and Sb. Since it could not be detected for Al due to special adjustments, a cochromite of sample BA 83-1 is mapped with the EPMA, including the elements Al, Cr, Co, Fe and Ni. Figure 4.23 shows the most significant element maps of Fe, Ni, Co, Cr, Zn, Ge and Mo. This cochromite, marked with arrow 2, contains only a little Fe, except from some tiny spots of higher concentration. The outer rim of this cochromite shows without interruption approximately the same concentration. Ni shows a gradation outwards from the interior where the concentration is impoverished in comparison with all surrounding minerals. Co behaves opposed, having higher concentrations in the interior of the cochromite as in its rim. Cr appears to be distributed inhomogeneously with varying concentrations. In comparison to all surrounding minerals, this cochromite is enriched in Zn. Ge is present in low concentrations, the same applies for Mo.

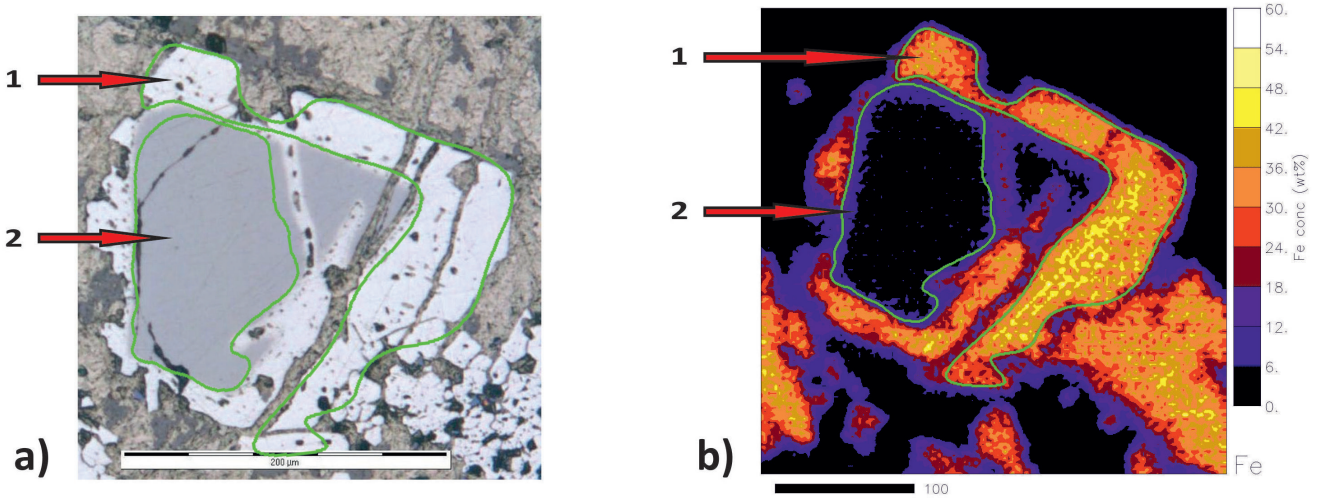

Figure 4.23 µPIXE elementmaps of a selected are of interest in sample BA 87-4. Arrow 1 marks trevorite that replaces cochromite, marked by arrow 2. a) Overview about the selected area in reflected light (whitish: trevorite, dark grey: cochromite, brownish-grey: népouite-willemseite assemblage). b) Fe-map. c (following page)) Ni-map. d (following page)) Co-map. e (following page)) Cr-map. f (following page)) Zn-map. g (following page)) Ge-map. h (following page)) Mo-map. The concentrations are wt% and need to be examined carefully due to the strong beam instabilities during the measurement process.

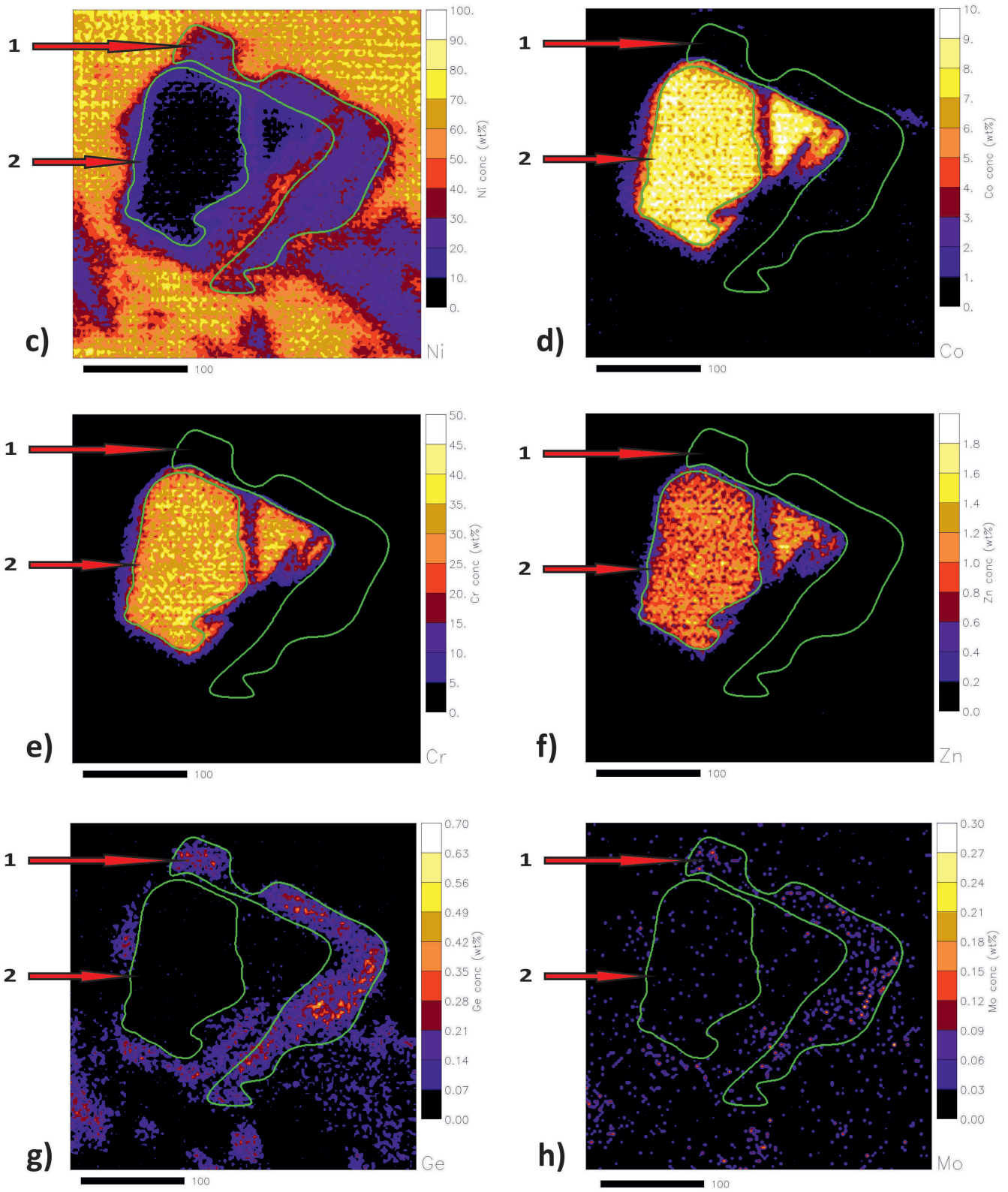

4.2.3 Minerals of the isomorphous magnetite-trevorite series

In total 86 minerals of this series from the twelve samples BA 83-1, BA 87-1, BA 87-4, BAU, BA 84-1, BA 87-3, NCH7, NCJ5, NCJ8, NCK6, BA 84-2 and BAD were analysed. Due to the very difficult determination between trevorite, ferroan trevorite and nickeloan magnetite the cation proportions per 32 O are calculated.

Figure 4.24 illustrates the distribution of the Fe cations vs. Ni cations of all analysed grains, since Ni and Fe are known to substitute for each other. The by De Waal (1969) defined ranges in the Ni ions per 32 O for trevorite, ferroan trevorite, nickeloan magnetite and magnetite are symbolized by dashed lines. All grains of sample BA 87-1 plot well within the trevorite field. Five of seven grains of BA 87-3 plot well in the trevorite field as well, but more to the boundary line to ferroan trevorite. One of five grains of sample NCJ8 plots exactly on the boundary line trevorite – ferroan trevorite, being a little poorer in Fe and Ni as all the other grains of BA 87-3. Two of seven grains of sample BA 87-3 plot very well together with all grains of the samples NCK6, BA 84-1, NCJ5 and NCH7 in the ferroan trevorite field. The grains of NCJ8 and one grain of BA 87-3 are richest in Ni in this field. The decrease in Ni and the accompanied increase in Fe has the further sample succession NCK6, BA 84-1, NCJ5 with NCH7. Two of seven grains of NCJ8 plot very well together within the trend, whereas the remaining two grains of this sample are a little poorer in Fe but not richer in Ni. All grains of BA 84-2 and BAD plot well in the nickeloan magnetite field, but four of eight grains of BA 84-2 plot near the boundary line to ferroan trevorite.

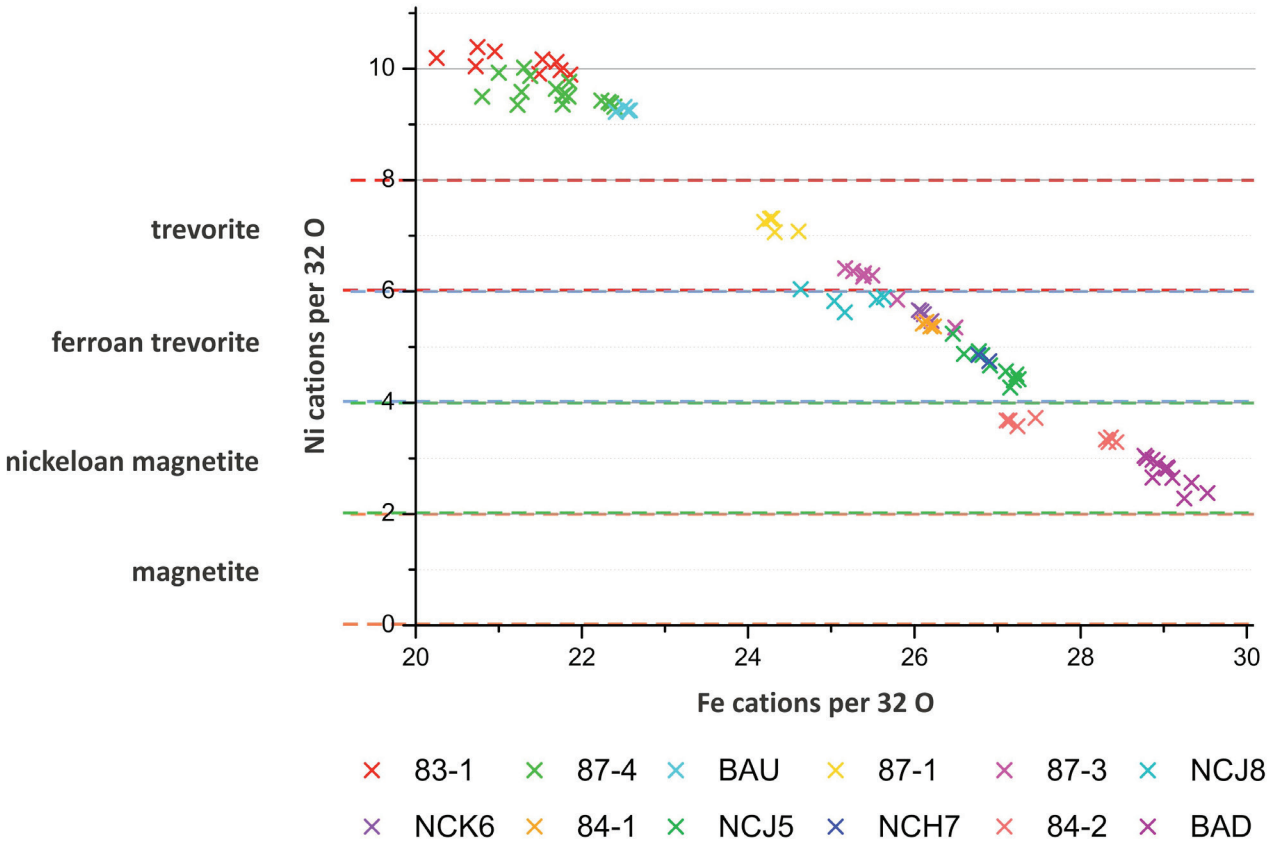

Figure 4.24 Overview about the distribution of trevorite, ferroan trevorite and nickeloan magnetite in a Ni vs. Fe cation based binary plot. The cations are calculated on the basis of 32 O. The red dashed line indicates the range of Ni ions per 32 O for trevorite, the blue dashed line for ferroan trevorite, the green dashed line for nickeloan magnetite and the orange dashed line for magnetite (according to the definition of De Waal (1969)).

All grains of BA 83-1, BA 87-4 and BAU plot above the trevorite field, between nine and eleven Ni, being the highest in Ni and poorest in Fe. Given that eight Ni-ions per 32 O are the maximum of divalent Ni in a unit cell of the isomorphous magnetite-trevorite series (De Waal, 1969), then all analysed trevorite grains of the Bon

Accord A samples exceed this. The only explanation is the presence of trivalent Ni which enters the position of the trivalent Fe. It is assumable that the linear relation between the number of Ni-ions per 32 O in a unit cell continues with $Ni^{2+}(Fe^{3+},Ni^{3+})_2O_4$ for 8-10 Ni-ions, $Ni^{2+}(Ni^{3+},Fe^{3+})_2O_4$ for 10-12 Ni-ions and $Ni^{2+}Ni^{3+}{}_2O_4$ for the maximum of 12-14 Ni-ions per 32 O. Figure 4.25 shows clearly that all trevorites of sample BAU as well as all of sample BA 87-4, with one exception, plot perfectly in the range of 8-10 Ni-ions. All trevorites of sample BA 83-1 plus one of sample BA 87-4 plot within the range of 10-12 Ni-ions per 32 O. Though the concentration of divalent and trivalent Ni together in one mineral cannot be proven by use of the EPMA it is nevertheless suggested to name the latter unknown #1b with the mineral formula $Ni^{2+}(Ni^{3+},Fe^{3+})_2O_4$ and those trevorites which contain between 8-10 Ni-ions per 32 O, unknown #1c with the mineral formula $Ni^{2+}(Fe^{3+},Ni^{3+})_2O_4$. Consequently the existence of unknown #1a $Ni^{2+}Ni^{3+}{}_2O_4$ can be expected in nature as well. Indeed, it is not reported to date to occur in nature, but from experiments (Barbier *et al.*, 2000). Due to the uncertainty about this particular issue and to avoid confusion, unknown #1b and unknown #1c are in the following named trevorite as well.

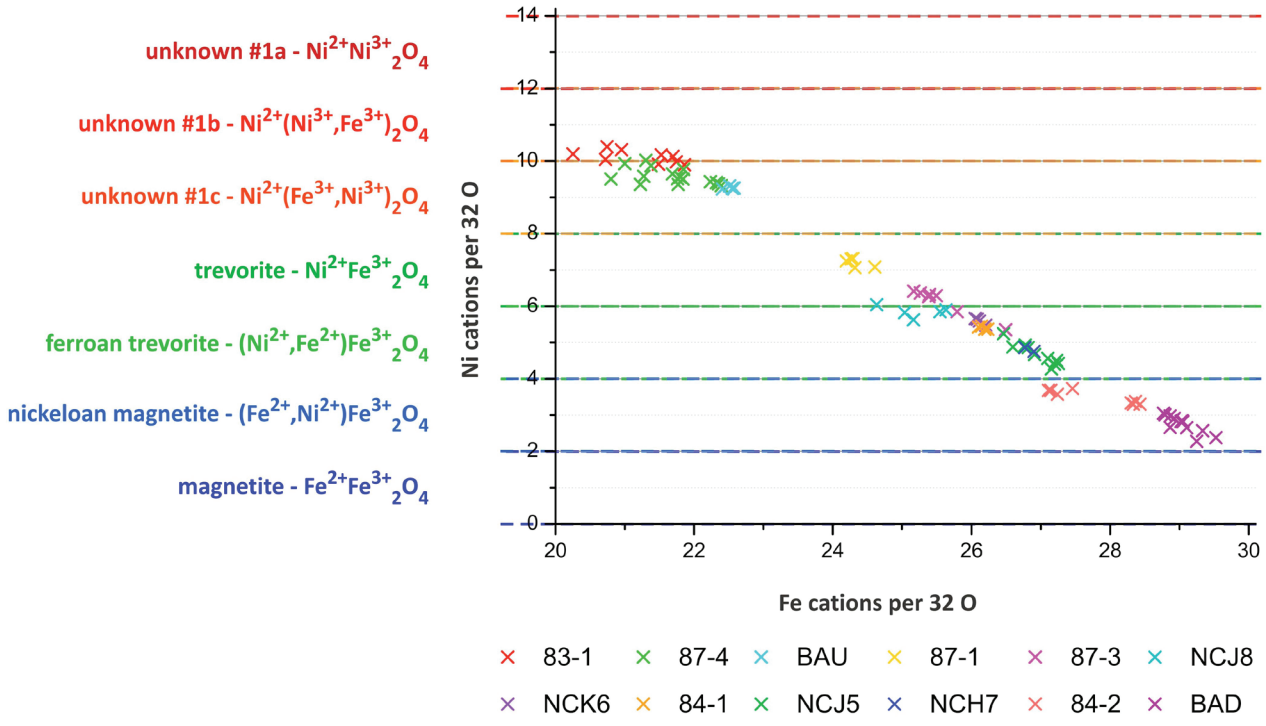

Figure 4.25 Overview about the distribution of nickeloan magnetite, ferroan trevorite, trevorite and unknown #1a-c in a Ni vs. Fe cation based binary plot. The dashed lines indicate the ranges of Ni ions per 32 O for magnetite, nickeloan magnetite, ferroan trevorite and trevorite (according to the definition of De Waal (1969)) - plus the expected next steps for unknown #1a-c. The cations are calculated on the basis of 32 O.

Figure 4.26 illustrates the variation in the FeO and NiO concentrations of trevorite, ferroan trevorite and nickeloan magnetite. For exemplification of differences the trevorite is subdivided into trevorite of Bon Accord A, the contact and Bon Accord B. To avoid the loss of track, the detailed subdivision of the respective minerals in the samples is presented only in appendix J. Trevorite, ferroan trevorite and nickeloan magnetite plot due to their significant differences in their FeO and NiO concentration clearly different from each other. Additionally, distinct groups can be distinguished since the respective minerals show significant differences in their FeO and NiO concentrations as well.

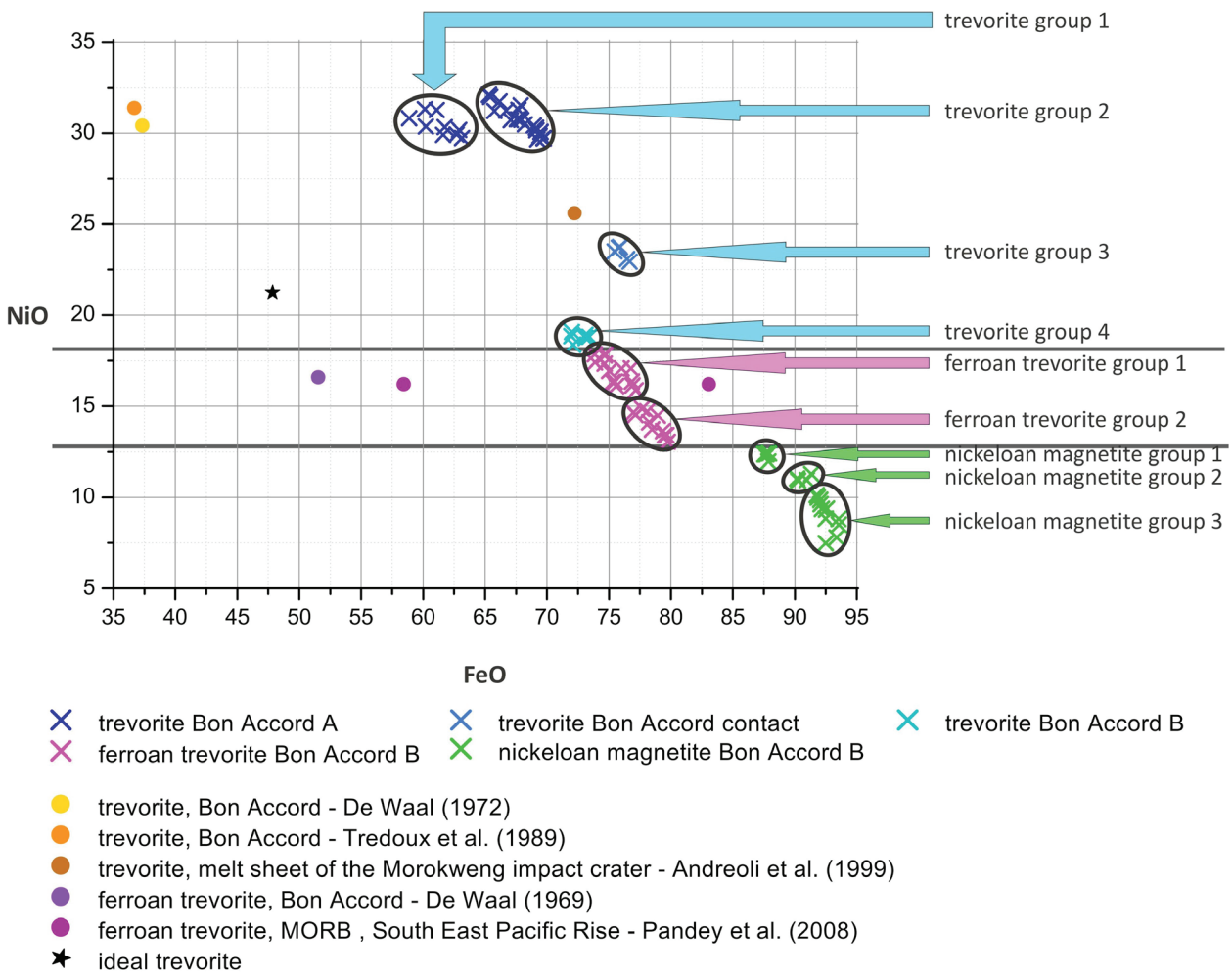

Figure 4.26 Overview about the distribution of trevorite per sample, subdivided into trevorite of Bon Accord A, the contact and Bon Accord B, ferroan trevorite and nickeloan magnetite in a binary FeO-NiO diagram. The dark grey lines indicate the boundary line from trevorite to ferroan trevorite resp. from ferroan trevorite to nickeloan magnetite. Data for trevorite resp. ferroan trevorite from De Waal (1969), De Waal (1972) and Tredoux et al. (1989) from Bon Accord, and from Andreoli et al. (1999) from the melt sheet of the Morokweng impact crater in South Africa and from Pandey et al. (2008) from a MORB at the Southern East Pacific Rise are plotted for comparison to the data of the present study. All plotted concentrations are wt%.

The differences in the FeO concentration (figure 4.26) are explainable with the presence of divalent and trivalent Fe in the ferroan trevorite, nickeloan magnetite and in traces also in trevorite. According to Barthelmy (2010), the ideal trevorite contains stoichiometric an amount of 0.3 divalent Fe and 1.99 trivalent Fe. By dividing Fe^{3+} by Fe^{2+} one gets the proportion of 0.15. Regarding this as a constant factor it is possible to calculate the rough proportion of Fe^{3+} to Fe^{2+} from the EPMA analyses. Even though this calculation is not equal to the real amount of Fe^{3+} and Fe^{2+} it still gives an impression if the differences in the FeO concentrations can be reduced to the different amounts of divalent and trivalent Fe per grain or not. Figure 4.27 shows the proportions of $Fe^{2+}/(Fe^{2+} + Ni)$ to $Fe^{3+}/(Fe^{3+} + Ni)$ for all trevorites, ferroan trevorites and nickeloan magnetites of the present study. Since in this schematic overview all analysed grains plot very well in one line it is obvious that the different FeO concentrations are due to the different valences of Fe.

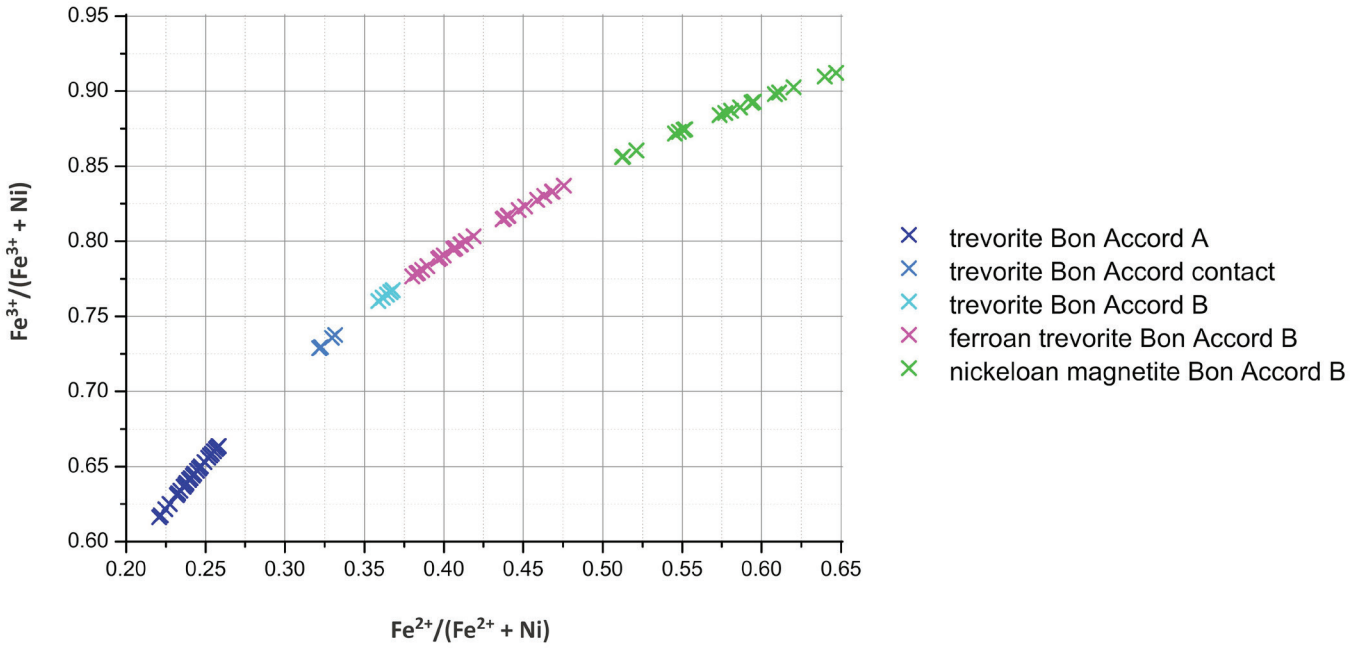

Figure 4.27 Schematic overview about the proportion of divalent Fe to Ni and trivalent Fe to Ni of all trevorites, ferroan trevorites and nickeloan magnetites of the present study.

In matters of cation proportions it has to be pointed out that the EPMA measurement program was set at divalent Fe, which is most common in the oxide and silicate minerals, but trevorite, ferroan trevorite and nickeloan magnetite contain divalent as well as trivalent Fe. This different valences cause insofar incorrect Fe cations, which should be lower for trivalent Fe than they are, which falsifies the mineral formula.

Trevorite $NiFe_2O_4$

All in all, the elements of trevorite vary significantly (table 4.19). The NiO concentration ranges from the minimum of 18.39 wt% to a maximum of 32.12 wt%, being 30.16 wt% on average. FeO varies from the minimum of 58.88 wt% to 76.66 wt%, being 68.06 wt% on average. The trevorite is enriched in CoO which shows an average concentration of 0.43 wt%. Al_2O_3 is present in 34 trevorites and shows an average concentration of 0.23 wt%. SiO_2 is present in 18 trevorites, being 1.38 wt% in the maximum concentration. Twelve trevorites contain TiO_2 with a maximum of 0.38 wt%. Cr_2O_3 is present in seven trevorites, showing a maximum of 1.63 wt%. Three trevorites contain MgO, showing a maximum of 0.09 wt%. ZnO, CaO and MnO are not detected.

Table 4.19 Summarized EPMA data of trevorite (n = 40) in wt%.

	FeO	NiO	CoO	ZnO	SiO_2	MgO	CaO	Al_2O_3	TiO_2	MnO	Cr_2O_3
average	68.06	30.16	0.43	0	0	0	0	0.23	0	0	0
minimum	58.88	18.39	0.33	0	0	0	0	0	0	0	0
maximum	76.66	32.12	0.61	0	1.38	0.09	0	1.22	0.38	0	1.63

Trevorite forms four distinct groups, with group 1 and 2 consisting of trevorites from only Bon Accord A, group 3 consisting of trevorites only from the contact and group 4 consisting of the remaining trevorites from Bon Accord B (figure 4.26). Group 1 contains only the trevorites of sample BA 83-1, group 2 unexceptional

those of BA 87-4 and BAU, group 3 contains only the trevorites of sample BA 87-1 and group 4 the trevorites of sample BA 87-3 and NCJ8. Group 1 and 2 are highest in NiO and poorest in FeO, but group 2 is richer in FeO though the same range of NiO is covered. Furthermore it should be noticed that within group 2 the trevorites of sample BAU are the poorest in NiO in comparison to the trevorites of sample BA 87-4 within the same group and to group 1. There is a big gap between these two groups and group 3 which is clearly richer in FeO and poorer in NiO. Another big gap exists between group 3 and group 4. The latter is poorer in NiO, but also poorer in FeO instead of being richer in that.

Group 1 of trevorite shows with the NiO concentration a range of 1.60 wt% from the minimum of 29.73 wt% to the maximum of 31.33 wt%, being 30.33 wt% on average (table 4.20). The variance of FeO is bigger with 4.26 wt%, being 58.88 wt% in the minimum and 63.14 wt% in the maximum concentration, showing an average of 61.62 wt%. Since Ni and Fe substitute for each other the number of decrease in NiO and the number of increase in FeO should be the same, which is not the case; a gap of 2.66 wt% between the ranges remains. However, the clear trend in NiO decrease with FeO increase is visible.

For group 2 of trevorite the difference between the NiO minimum of 29.66 wt% and the maximum of 32.12 wt% is 2.46 wt%, being 30.73 wt% on average. The difference between the FeO minimum of 65.32 wt% and the maximum of 69.72 wt% is 4.40 wt%, showing an average concentration of 67.90 wt%. The resulting gap of 1.94 wt% between the NiO and FeO ranges is smaller than that of group 1.

Group 3 of trevorite shows clearly smaller differences. NiO covers a range of 0.81 wt% with a minimum of 22.94 wt% and a maximum concentration of 23.75 wt%, being 23.51 wt% on average. The variance of FeO is with 1.22 wt% bigger. Its minimum concentration is 75.44 wt% and the maximum concentration is 76.66 wt%, being 75.89 wt% on average. Here the gap between the ranges of NiO and FeO is with 0.41 wt% clearly lower than that of group 2.

Table 4.20 Summarized EPMA data of trevorite, subdivided into group 1 (n = 9), group 2 (n = 20), group 3 (n = 5) and group 4 (n = 6), in wt%.

	FeO	NiO	CoO	ZnO	SiO_2	MgO	CaO	Al_2O_3	TiO_2	MnO	Cr_2O_3
Group 1											
average	61.62	30.33	0.43	0	0.16	0	0	0.25	0.08	0	0
minimum	58.88	29.73	0.33	0	0	0	0	0	0	0	0
maximum	63.14	31.33	0.46	0	0.57	0	0	1.02	0.32	0	0.71
Group 2											
average	67.90	30.73	0.41	0	0.26	0	0	0.24	0	0	0
minimum	65.32	29.66	0.36	0	0	0	0	0	0	0	0
maximum	69.72	32.12	0.49	0	1.38	0.08	0	1.22	0.38	0	0.70
Group 3											
average	75.89	23.51	0.43	0	0	0	0	0.34	0	0	0
minimum	75.44	22.94	0.38	0	0	0	0	0.23	0	0	0
maximum	76.66	23.75	0.46	0	0	0	0	0.52	0.21	0	0
Group 4											
average	72.60	18.84	0.52	0	0	0	0	0.12	0	0	0
minimum	71.95	18.39	0.34	0	0	0	0	0	0	0	0
maximum	73.40	19.09	0.61	0	0	0.09	0	0.22	0.28	0	1.63

For group 4 of trevorite the difference between the NiO minimum of 18.39 wt% and maximum of 19.09 wt% is 0.70 wt%, being 18.84 wt% on average. The variance of FeO is 1.45 wt% with a minimum of 71.95 wt% and a maximum concentration of 73.40 wt%, being 72.60 wt% on average. The resulting gap of 0.75 wt% is a little bigger than that of group 3, but smaller than that of group 2.

An element mapping for the lath-shaped trevorite in the sample BA 83-1 is done for Fe, Ni and Cr (figure 4.28). It is clear to see that only the distribution of Cr in the trevorites shows inhomogeneities, whereas Fe and Ni are homogeneously distributed.

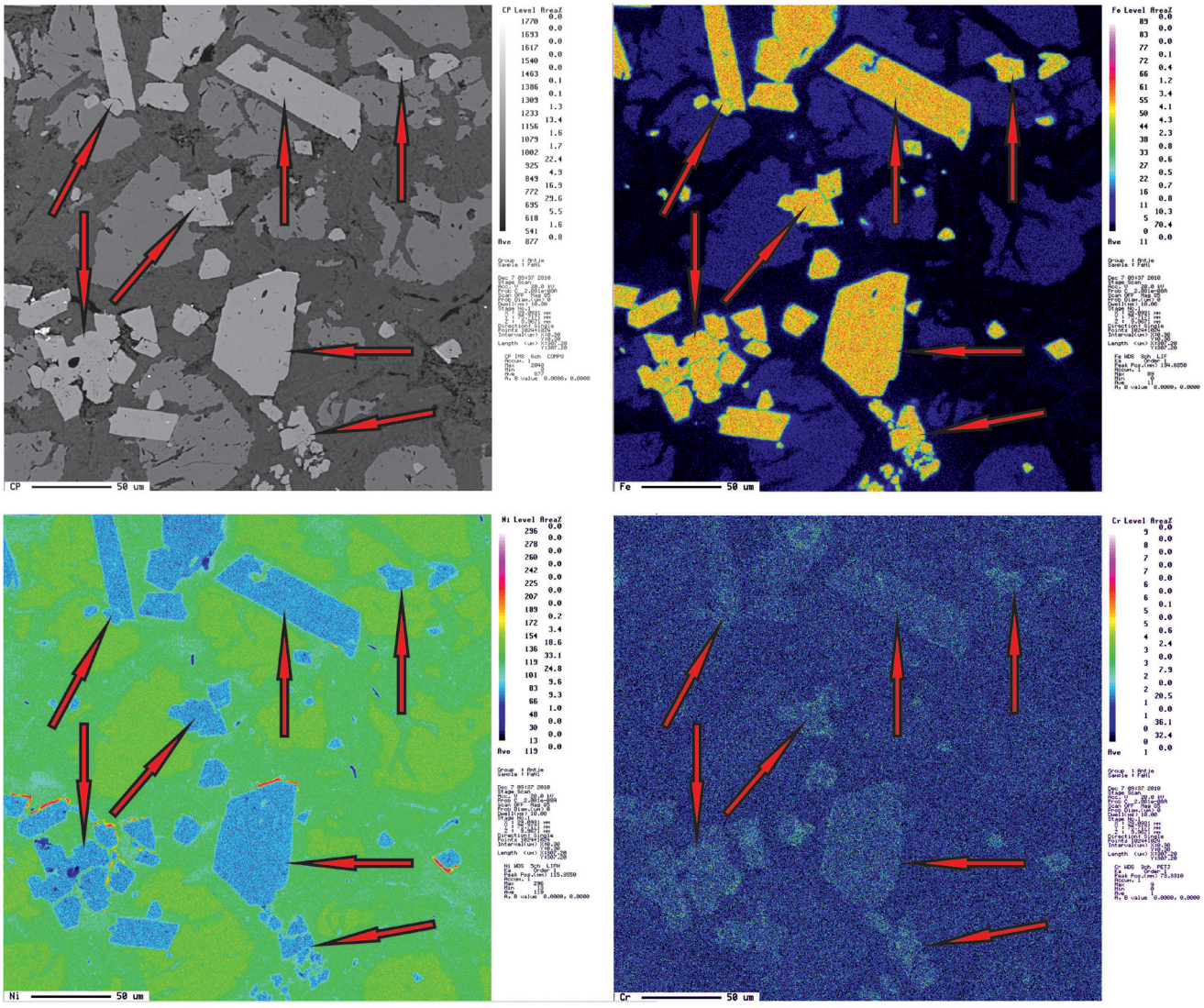

Figure 4.28 EPMA maps of a selected area in sample BA 83-1. Top left: Backscatter image of an area consisting of trevorite (light grey - examples indicated by arrows), liebenbergite (grey) and népouite-willemseite mixture (dark grey). Top right: Fe-map of the same area – the arrows indicate examples of trevorite. Bottom left: Ni-map of the same area – the arrows indicate examples of trevorite. Bottom right: Cr-map of the same area – the arrows indicate examples of trevorite; a slight zoning of Cr within the trevorites is present.

The average empirical formula for all trevorites is $Ni_{1.18}Fe^{2+}_{2.73}O_4$ (table 4.21). Considering the subdivisions, the empirical formula for the trevorites of group 1 is $Ni_{1.26}Fe^{2+}_{2.69}O_4$, of group 2 $Ni_{1.18}Fe^{2+}_{2.73}O_4$, of group 3 $Ni_{0.91}Fe^{2+}_{3.04}O_4$, and of group 4 $Ni_{0.79}Fe^{2+}_{3.17}O_4$ (table 4.22).

Table 4.21 Summary of the cation proportions for trevorite (n = 40), cations per 4 O.

	Fe	Ni	Co	Zn	Si	Mg	Ca	Al	Ti	Mn	Cr
average	2.7317	1.1775	0.0164	0	0.0027	0.0012	0	0.0135	0.0013	0.0004	0.0005
minimum	2.5317	0.7551	0.0134	0	0	0	0	0.0003	0	0	0
maximum	3.1865	1.2988	0.0257	0.0017	0.0654	0.0066	0.0008	0.0677	0.0132	0.0015	0.0660

Table 4.22 Summary of the cation proportions for trevorite, subdivided into group 1 (n = 9),group 2 (n = 20), group 3 (n = 5) and group 4 (n = 6), cations per 4 O.

	Fe	Ni	Co	Zn	Si	Mg	Ca	Al	Ti	Mn	Cr
Group 1											
average	2.6858	1.2661	0.0178	0	0.0081	0	0	0.0152	0.0032	0.0001	0.0003
minimum	2.5317	1.2988	0.0134	0	0	0	0	0.0003	0	0	0
maximum	2.7324	1.2374	0.0190	0	0.0294	0.0025	0.0008	0.0618	0.0123	0.0005	0.0289
Group 2											
average	2.7275	1.1835	0.0159	0	0.0123	0.0011	0	0.0135	0.0012	0.0002	0.0009
minimum	2.6000	1.1540	0.0136	0	0	0	0	0.0009	0	0	0
maximum	2.8220	1.2530	0.0189	0	0.0654	0.0059	0.0005	0.0677	0.0137	0.0008	0.0263
Group 3											
average	3.0360	0.9060	0.0164	0	0.0009	0	0	0.0193	0.0021	0.0005	0
minimum	3.0240	0.8830	0.0146	0	0	0	0	0.0132	0.0003	0	0
maximum	3.0760	0.9140	0.0177	0.0004	0.0021	0.0029	0.0007	0.0295	0.0075	0.0007	0.0009
Group 4											
average	3.1656	0.7884	0.0216	0	0.0008	0.0035	0.0005	0.0074	0.0006	0.0009	0
minimum	3.0789	0.7551	0.0201	0	0	0.0026	0	0.0036	0.0003	0.0002	0
maximum	3.1865	0.8023	0.0257	0.0017	0.0017	0.0066	0.0008	0.0138	0.0107	0.0015	0.0660

Ferroan Trevorite (Ni,Fe)Fe_2O_4 and Nickeloan Magnetite (Fe,Ni)Fe_2O_4

The elements of ferroan trevorite vary as well, but clearly lesser than those of trevorite (table 4.23). NiO ranges from 13.05 wt% in the minimum to 17.87 wt% in the maximum concentration, being 16.13 wt% on average. FeO varies from the minimum of 73.85 wt% to the maximum of 79.75 wt%, being 76.88 wt% on average. Ferroan trevorite is enriched in CoO as well, showing an average concentration of 0.40 wt%. Al_2O_3 is present in 21 ferroan trevorites and shows an average concentration of 0.11 wt%. 21 ferroan trevorites contain TiO_2, being 0.14 wt% on average. SiO_2 is present in six ferroan trevorites, showing a maximum of 0.32 wt%. Cr_2O_3 shows a maximum concentration of 0.74 wt% and is present in five ferroan trevorites. Two ferroan trevorites contain MgO, being 0.21 wt% in the maximum concentration. CaO is detected in only one ferroan trevorite, and shows a concentration of 0.08 wt%. The same case applies for MnO, which shows a concentration of 0.07 wt%. ZnO is not detected. In comparison to trevorite, the average concentration of CoO and MgO is about the same. ZnO is always zero, the same applies for CaO and MnO, disregarding the outliers. SiO_2, Al_2O_3 and Cr_2O_3 are a little lesser whereas TiO_2 is a little higher.

Ferroan trevorite forms two clear groups, but lesser distinctive that those of trevorite. Group 1 contains all ferroan trevorites of the samples BA 87-3, NCJ8, NCK6 and BA 84-1 plus one ferroan trevorite of sample NCJ5 (figure 4.26). Group 2 contains the remaining ferroan trevorites of sample NCJ5 and all of sample NCH7. Group 1 is clearly richer in NiO and poorer in FeO than group 2, and adjoins group 4 of trevorite, marking

therewith the boundary line of the transition trevorite to ferroan trevorite. The gap between group 4 of trevorite and group 1 of ferroan trevorite is extremely small and mostly denoted by the difference trevorite – ferroan trevorite. The gap between group 1 and group 2 is very small as well, but group 2 appears shifted with slightly lower FeO whilst NiO decreases.

A clear order of the samples in the increase of FeO und accompanied decrease of NiO in both groups can be noted. Within group 1 the ferroan trevorites of NCJ8 are highest in NiO and poorest in FeO whilst one ferroan trevorite of sample BA 87-3 is just a little lower in NiO than those, but also a little lower in FeO. The increase in FeO and decrease in NiO continues with sample NCK6 which constitute the middle part of group 1, followed by all ferroan trevorites of sample BA 84-1, the remaining one of BA 87-3 and the only ferroan trevorite of sample NCJ5. Group 2 consists of the remaining ferroan trevorites of sample NCJ5, which form the bulk mass in this group. The two ferroan trevorites of sample NCH7 plot in the upper array of group 2.

Table 4.23 Summarized EPMA data of ferroan trevorite (n = 26) in wt%.

	FeO	NiO	CoO	ZnO	SiO_2	MgO	CaO	Al_2O_3	TiO_2	MnO	Cr_2O_3
average	76.88	16.13	0.40	0	0	0	0	0.11	0.14	0	0
minimum	73.85	13.05	0.26	0	0	0	0	0	0	0	0
maximum	79.75	17.87	0.52	0	0.32	0.21	0.08	0.18	1.18	0.07	0.74

In group 1 of the ferroan trevorite the variance for NiO between the minimum of 15.89 wt% and the maximum concentration is 1.98 wt%, being 16.95 wt% on average (table 4.24). FeO shows a range of 3.04 wt% with a minimum of 73.85 wt% and a maximum of 76.89 wt%, being 75.37 wt% on average. The gap between both ranges is 1.06 wt%.

Group 2 ranges in NiO about 1.81 wt%, with a minimum of 13.05 wt% and a maximum concentration of 14.86 wt%, being 14.13 wt% on average. FeO varies about 2.78 wt% from the minimum concentration of 76.97 wt% to the maximum of 79.75 wt%, being 78.46 wt% on average. The resulting gap between both groups is 0.97 wt%.

Table 4.24 Summarized EPMA data of ferroan trevorite, subdivided into group 1 (n = 15) and group 2 (n = 11) in wt%.

	FeO	NiO	CoO	ZnO	SiO_2	MgO	CaO	Al_2O_3	TiO_2	MnO	Cr_2O_3
Group 1											
average	75.37	16.95	0.40	0	0	0	0	0.12	0.18	0	0
minimum	73.85	15.89	0.26	0	0	0	0	0	0	0	0
maximum	76.89	17.87	0.52	0	0.32	0.21	0.08	0.18	1.18	0.07	0.53
Group 2											
average	78.46	14.13	0.39	0	0	0	0	0.10	0.13	0	0
minimum	76.97	13.05	0.34	0	0	0	0	0	0	0	0
maximum	79.75	14.86	0.41	0	0.21	0	0	0.16	0.18	0	0.74

The average empirical formula for all ferroan trevorites it is $Ni_{0.67}Fe^{2+}_{3.29}O_4$ (table 4.25). Considering the subdivisions, the empirical formula for the ferroan trevorites of group 1 the empirical formula is $Ni_{0.70}Fe^{2+}_{3.26}O_4$, and of group 2 it is $Ni_{0.58}Fe^{2+}_{3.36}O_4$ (table 4.26).

Table 4.25 Summary of the cation proportions for ferroan trevorite (n = 26), cations per 4 O.

	Fe	Ni	Co	Zn	Si	Mg	Ca	Al	Ti	Mn	Cr
average	3.2936	0.6701	0.0162	0	0.0012	0.0022	0	0.0066	0.0053	0.0006	0.0001
minimum	3.2244	0.5341	0.0106	0	0.0002	0	0	0.0014	0	0	0
maximum	3.4066	0.7312	0.0213	0.0008	0.0163	0.0157	0.0046	0.0113	0.0449	0.0028	0.0214

Table 4.26 Summary of the cation proportions for ferroan trevorite, subdivided into group 1 (n = 15) and group 2 (n = 11), cations per 4 O.

	Fe	Ni	Co	Zn	Si	Mg	Ca	Al	Ti	Mn	Cr
Group 1											
average	3.2628	0.6988	0.0165	0	0.0009	0.0022	0.0003	0.0070	0.0069	0.0004	0.0002
minimum	3.1296	0.6552	0.0106	0	0.0002	0.0006	0	0.0030	0	0	0
maximum	3.3114	0.7372	0.0213	0	0.0163	0.0157	0.0046	0.0113	0.0449	0.0028	0.0214
Group 2											
average	3.3639	0.5841	0.0161	0	0.0018	0.0021	0	0.0062	0.0051	0.0006	0.0001
minimum	3.3464	0.5341	0.0140	0	0.0009	0	0	0.0014	0.0019	0.0001	0
maximum	3.4066	0.6156	0.0171	0.0008	0.0110	0.0036	0.0016	0.0098	0.0069	0.0015	0.0299

Nickeloan Magnetite (Fe,Ni)Fe_2O_4

The elemental composition of nickeloan magnetite varies, but to a lesser extent than those of ferroan trevorite and trevorite (table 4.27). FeO varies from 87.55 wt% in the minimum to 93.54 wt% in the maximum, being of 91.95 wt% on average. NiO ranges from a minimum of 7.49 wt% to a maximum concentration of 12.42 wt%, being 9.93 wt% on average. The nickeloan magnetite is enriched in CoO and shows an average concentration of 0.18 wt%. TiO_2, present in 16 nickeloan magnetites, is 0.10 wt% on average. Five nickeloan magnetites contain SiO_2, showing a maximum concentration of 1.09 wt%. MgO is present in four nickeloan magnetites, and shows a maximum concentration of 0.32 wt%. Cr_2O_3, present in five nickeloan magnetites, shows a maximum concentration of 0.81 wt%. Three nickeloan magnetites contain Al_2O_3 with a maximum concentration of 0.26 wt%. ZnO, CaO and MnO are not detected.

Table 4.27 Summarized EPMA data of nickeloan magnetite (n = 20) in wt%.

	FeO	NiO	CoO	ZnO	SiO_2	MgO	CaO	Al_2O_3	TiO_2	MnO	Cr_2O_3
average	91.95	9.93	0.18	0	0	0	0	0	0.10	0	0
minimum	87.55	7.49	0.11	0	0	0	0	0	0	0	0
maximum	93.54	12.42	0.42	0	1.09	0.32	0	0.26	0.28	0	0.81

In comparison to ferroan trevorite and trevorite, the average concentration of CoO is clearly lower in the nickeloan magnetite; Al_2O_3 is less often detected as in ferroan trevorite and trevorite. The maximum concentration of SiO_2 is similar with that of trevorite. MgO is richest in the nickeloan magnetite. TiO_2 takes an intermediate position between ferroan trevorite and trevorite, whereas Cr2O3 is about the same as in ferroan trevorite. ZnO is never detected, and CaO and MnO are only in the ferroan trevorite present.

Nickeloan magnetite forms three distinct groups with group 1 and 2 consisting only of nickeloan magnetites from sample BA 84-2, and group 3 of only nickeloan magnetites from sample BAU (figure 4.26). Group 1 is the

richest in NiO and poorest in FeO concentration, followed by group 2. The nickeloan magnetites of group 3 are lesser in the NiO concentration than group 2 and a little richer in FeO. Between group 1 of nickeloan magnetite and group 2 of ferroan trevorite there is a big gap. Group 1 is just a little lower in NiO than group 2 of ferroan trevorite but much richer in FeO. Nevertheless the boundary line from ferroan trevorite to nickeloan magnetite can be observed. Group 3 is characterized by a very clear decrease in the NiO concentration while the increase in FeO is only a little.

In group 1 of the nickeloan magnetite NiO covers a range of 0.44 wt%, being 11.98 wt% in the minimum and 12.42 wt% in the maximum concentration, showing an average of 12.36 wt% (table 4.28). FeO varies about 0.35 wt% with a minimum of 87.55 wt% and a maximum concentration of 87.90 wt%, being 87.78 wt% on average. In this case, the range of NiO is bigger than that of FeO.

NiO of group 2 varies about 0.37 wt% with a minimum concentration of 10.92 wt% and a maximum of 11.29 wt%, being 11.00 wt% on average. FeO varies about 1.13 wt% with a minimum of 90.19 wt% and a maximum of 91.32 wt%, being 90.61 wt% on average. Here, the range of NiO is again bigger than that of FeO. The resulting gap between NiO and FeO is with 0.76 wt% bigger than that of group 1, as well as that of both groups of ferroan trevorite plus group 3 and 4 of trevorite.

The differences in group 3 are bigger. NiO ranges about 2.63 wt% from 7.49 wt% in the minimum to 10.12 wt% in the maximum concentration, being 9.35 wt% on average. FeO varies about 1.77 wt%, being 91.77 wt% in the minimum and 93.54 wt%in the maximum, showing an average concentration of 92.50 wt%. As observed in group 1 and 2, the range of NiO is again bigger than that of FeO. The resulting gap is with 0.83 wt% the biggest within the three groups of nickeloan magnetite but still smaller than that of group 3 and 4 of trevorite as well as both groups of ferroan trevorite.

Table 4.28 Summarized EPMA data of nickeloan magnetite, subdivided into group 1 (n = 4), group 2 (n = 4) and group 3 (n = 12) in wt%.

	FeO	NiO	CoO	ZnO	SiO_2	MgO	CaO	Al_2O_3	TiO_2	MnO	Cr_2O_3
Group 1											
average	87.78	12.36	0.37	0	1.06	0.27	0	0.05	0.12	0	0
minimum	87.55	11.98	0.29	0	1.05	0.13	0	0	0.12	0	0
maximum	87.90	12.42	0.42	0	1.09	0.32	0	0.26	0.15	0	0
Group 2											
average	90.61	11.00	0.25	0	0	0	0	0	0.17	0	0.08
minimum	90.19	10.92	0.23	0	0	0	0	0	0.10	0	0
maximum	91.32	11.29	0.28	0	0	0	0	0.09	0.28	0	0.23
Group 3											
average	92.50	9.35	0.14	0	0	0	0	0	0.08	0	0
minimum	91.77	7.49	0.11	0	0	0	0	0	0	0	0
maximum	93.54	10.12	0.19	0	0.07	0	0	0	0.10	0	0.81

The average empirical formula for all nickeloan magnetites it is $Ni_{0.37}Fe^{2+}_{3.60}O_4$ (table 4.29). Considering the subdivisions, the empirical formula for the nickeloan magnetites of group 1 is $Ni_{0.46}Fe^{2+}_{3.40}O_4$, of group 2 it is $Ni_{0.42}Fe^{2+}_{3.54}O_4$ and of group 3 it is $Ni_{0.35}Fe^{2+}_{3.63}O_4$ (table 4.30).

Table 4.29 Summary of the cation proportions for nickeloan magnetite (n = 20), cations per 4 O.

	Fe	Ni	Co	Zn	Si	Mg	Ca	Al	Ti	Mn	Cr
average	3.6035	0.3740	0.0067	0	0.0015	0.0012	0.0004	0.0024	0.0033	0	0.0005
minimum	3.3890	0.2850	0.0041	0	0	0	0	0	0.0013	0	0
maximum	3.6910	0.4660	0.0157	0.0010	0.0507	0.0218	0.0018	0.0144	0.0099	0.0010	0.0298

Table 4.30 Summary of the cation proportions for nickeloan magnetite, subdivided into group 1 (n = 4), group 2 (n = 4) and group 3 (n = 12), cations per 4 O.

	Fe	Ni	Co	Zn	Si	Mg	Ca	Al	Ti	Mn	Cr
Group 1											
average	3.3990	0.4600	0.0139	0	0.0491	0.0187	0.0002	0.0052	0.0044	0.0006	0.0005
minimum	3.3890	0.4470	0.0107	0	0.0220	0.0088	0	0.0036	0.0040	0	0
maximum	3.4320	0.4660	0.0157	0.0010	0.0507	0.0218	0.0005	0.0144	0.0053	0.0010	0.0005
Group 2											
average	3.5440	0.4145	0.0096	0.0003	0.0016	0.0006	0.0006	0.0031	0.0060	0	0.0050
minimum	3.5380	0.4120	0.0085	0	0.0007	0	0	0.0022	0.0036	0	0.0007
maximum	3.5540	0.4220	0.0105	0.0006	0.0020	0.0014	0.0018	0.0051	0.0099	0.0004	0.0085
Group 3											
average	3.6290	0.3525	0.0053	0	0.0011	0.0004	0.0005	0.0017	0.0028	0	0.0003
minimum	3.5960	0.2850	0.0041	0	0	0	0	0	0.0013	0	0
maximum	3.6910	0.3810	0.0080	0.0006	0.0034	0.0032	0.0009	0.0043	0.0036	0.0005	0.0298

Comparison of trevorite, ferroan trevorite and nickeloan magnetite with data from other authors

For comparison the data of De Waal (1972) and Tredoux *et al.* (1989) for trevorite from Bon Accord, Andreoli *et al.* (1999) for trevorite from the melt sheet of the Morokweng impact crater in South Africa, the data of De Waal (1969) for ferroan trevorite from Bon Accord, and Pandey *et al.* (2008) for ferroan trevorite from a MORB at the South East Pacific Rise are plotted with the data of the present study in figure 4.26. The trevorites of De Waal (1972) and Tredoux *et al.* (1989) plot at about the same NiO concentration as the trevorites of group 1 and 2 but are significantly poorer in FeO. The trevorite of Andreoli *et al.* (1999) plots close to the trevorites of group 3 but is a little richer in NiO, but of the same FeO concentration as the trevorites of group 4. The ferroan trevorite of De Waal (1969) shows the approximate same NiO concentration as the ferroan trevorites of group 1 but is much poorer in FeO, showing a lower FeO concentration as the trevorites of group 1, which are the poorest in FeO in the present study. The ferroan trevorites of Pandey *et al.* (2008) coincide well with the NiO concentration of the ferroan trevorites of De Waal (1969) and the ferroan trevorites of group 1, whereas they differ significantly in their FeO concentration from each other. One ferroan trevorite is rich and one is poor in FeO. The FeO-poor ferroan trevorite is a little richer in FeO than that of De Waal (1969), but contains about the same FeO concentration as the FeO-poorest trevorite of group 1. The FeO-rich ferroan trevorite contains even more FeO than the ferroan trevorites of group 1 and 2 but less than the nickeloan magnetites. None of all examined trevorites of the present study as well as the trevorites from De Waal (1972), Tredoux *et al.* (1989) and Andreoli *et al.* (1999) plots well with the general trevorite composition. On closer examination of the trace elements clear trends are scarcely observable (figure 4.29 and table 4.20, 4.24 and 4.28). The most significant trace element is CoO. Within the groups for trevorite there is an increase in the average concentration. Group

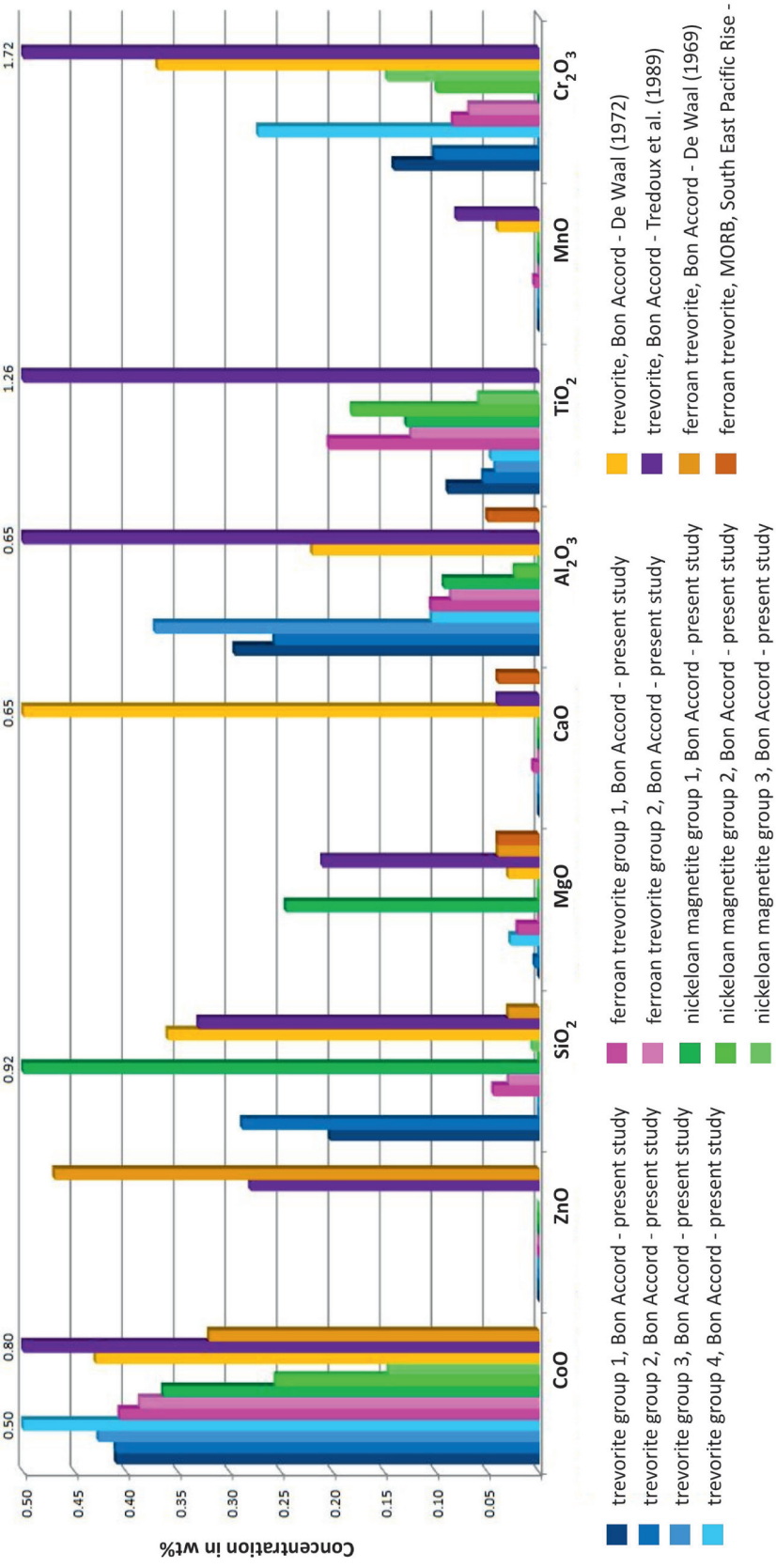

Figure 4.29 Overview about the trace element oxides of trevorite group 1 to 4, ferroan trevorite group 1 and 2, and nickeloan magnetite group 1 to 3. Data for trevorite resp. ferroan trevorite from De Waal (1969), De Waal (1972) and Tredoux et al. (1989) from Bon Accord, and from Pandey et al. (2008) from a MORB at the South East Pacific Rise are plotted for comparison to the data of the present study. All concentrations are wt%.

1, 2 and 3 show about the same concentration level, whilst there is a slight increase in group 4 to 0.43 wt%, being the richest in CoO. The ferroan trevorites show a decrease to the level of trevorites group 1, 2 and 3. The decrease in CoO continues also in the three groups of nickeloan magnetite with group 3 being the poorest one. For Al_2O_3 there is a rough trend in decrease from trevorite to nickeloan magnetite. Highest concentrations are present in the trevorites, and group 3 of the nickeloan magnetite is the poorest. In contrast to CoO and Al_2O_3, TiO_2 increases from trevorite to nickeloan magnetite. SiO_2, MgO and Cr_2O_3 vary so differently in their concentrations from trevorite to nickeloan magnetite, so that no trend is observable. MgO is just seldom present. CaO is never detected except for group 1 of the ferroan trevorites, but there the concentration of 0.01 wt% is close to the detection limit. The same applies for MnO with the only detected concentration of less than 0.01 wt% in the same group. ZnO is never detected.

The trace elements of the trevorites from De Waal (1972) show about the same CoO concentration as the trevorites of group 3, SiO_2 is clearly higher than the trevorites of group 2, and MgO shows about the same concentration as the trevorites of group 4 (figure 4.29). Al_2O_3 is also clearly higher than in the trevorites of group 4, but also clearly lower than group 1, group 2 and group 3. Clearly higher than all trevorite groups are the concentrations for MnO and Cr_2O_3 but especially for CaO. The trevorites of Tredoux *et al.* (1989) are significantly higher in all the analysed trace element oxides than all trevorite groups. The ferroan trevorites of De Waal (1969) are clearly richer in ZnO and MgO than both groups of ferroan trevorite. CoO is clearly lesser than in both ferroan trevorite groups but the SiO_2 concentration is about the same as ferroan trevorite group 2. The trevorites from Pandey *et al.* (2008) are richer in MgO and CaO, but clearly poorer in Al_2O_3 than the trevorites of the present study.

µPIXE-analyses on trevorites of different phenotype

In addition to the EPMA-analyses, trevorites of four different phenotype within sample BA 87-4 are analysed: type 1 – xenomorphic trevorite (figure 4.4, marked by arrow 1 and 2), type 2 – lath-shaped trevorite (figure 4.4, marked by arrow 3), type 3 – trevorite within liebenbergite (figure 4.4, marked by arrow 4) and type 4 – trevorite that replaces cochromite (figure 4.23, marked by arrow 1).

Fe, Co, Ni and Ge are detected above detection limit in all four trevorite types (table 4.31). Cr is detected only in type 4, also Pd, but below detection limit. Cu and Pb are detected only in type 1, 2 and 3, also Cd but below detection limit. Zn, Mo and In are detected in all four types but only in type 4 above detection limit. Ga and Sb are detected in all four types but only in type 1 and 4 above detection limit. As is detected in all four types, but only in type 1 and 2 above detection limit. Sn is detected in all four types but only in type 3 below detection limit.

Table 4.31 Comparison about the detected elements (obtained by use of the µPIXE) within the four different trevorite phenotypes. Present and above detection limit = a.d., present but below detection limit = b.d., not detected = n.d.

	Cr	Fe	Co	Ni	Cu	Zn	Ga	Ge	As	Mo	Pd	Cd	In	Sn	Sb	Pb
type 1	n.d.	a.d.	a.d.	a.d.	a.d.	b.d.	a.d.	a.d.	a.d.	b.d.	n.d.	b.d.	b.d.	a.d.	a.d.	a.d.
type 2	n.d.	a.d.	a.d.	a.d.	a.d.	b.d.	b.d.	a.d.	a.d.	b.d.	n.d.	b.d.	b.d.	a.d.	b.d.	a.d.
type 3	n.d.	a.d.	a.d.	a.d.	a.d.	b.d.	b.d.	a.d.	b.d.	b.d.	n.d.	b.d.	b.d.	b.d.	b.d.	a.d.
type 4	a.d	a.d.	a.d.	a.d.	n.d.	a.d.	a.d.	a.d.	b.d.	a.d.	b.d.	n.d.	a.d.	a.d.	a.d.	n.d.

Only the most significant element maps are chosen and therefore not throughout for the same elements.

Figure 4.4, which includes type 1 to 3, contains the maps for Fe, Ni, Co, Cr, Zn, Ge and Mo. Figure 4.23, which includes trevorite type 4, contains the maps for Fe, Ni, Co, Cr, Zn, Ge and Mo. Figure 4.4 and 4.23 show the approximate same range for the Fe-concentration in all four trevorite types. Also Ni is present within the same range. Spots of brighter colours mark holes within the trevorite and reveal silicate minerals. Co covers as well a similar range in all four types. In contrast to all surrounding minerals, all trevorite types are significantly enriched in Ge. But though it is present above detection limit in all types, considerable differences are still observable. The xenomorphic trevorite type 1 is significantly poorer in Ge than type 2, 3 and 4, including always separate tiny spots of higher intensity. Slight differences are also visible for As. Type 1 is a little richer than type 2. A clear gradation is observable for Sb. Type 1 is much richer than type 2 and 3. Type 1 is slightly richer in Pb than type 2 and 3. Though Cr is in type 4 present above detection limit - the same applies for Zn. Type 4 is richer in Mo than the surrounding minerals.

4.3 Unknown minerals

In total 28 analyses of the samples BA 83-1, BA 87-4, BAU, BA 84-1, BAD, NCH7, NCJ5 and cB S 1088 13a could not be allocated to any IMA-accepted mineral. 23 of these analyses can be accounted to the system Ni-As-Sb, three to the system Ni-As-S and two analyses to the system Co-Fe-Ni.

Plotted in the system Ni-As-Sb four distinct groups define. The unknown minerals, which are represented by groups, are named unknown #2, unknown #3, unknown #4 and unknown #5 (figure 4.30). These groups plot completely different from each other. Unknown #2 is the only group with Ni, As and Sb as the major constituents. No mineral matches with respectively is close to unknown #2. Unknown #3 is the only group with Ni and Sb as the major constituents and only traces of As, matching perfectly with Ni_3Sb which is reported first by Nixon *et al.* (1990) to occur in nature but also as an artificial product from Laufek *et al.* (2010). Though this mineral is reported to occur in nature it is still not accepted as a new valid species and therefore in the following still named unknown #3. In contrast to the latter mineral, unknown #4 contains Ni and Sb as the major constituents, but here As is present as a minor constituent. No mineral matches with respectively is close to unknown #4. Unknown #5 is the only group with Ni and As as the major constituents and only a minor amount of Sb, plotting close to general oregonite (with Ni and Fe added for this system), but also close to general maucherite, matching with none of them. Since unknown #5 consists of the major elements Ni, Fe and As it is also plotted in the ternary system Ni-Fe-As (figure 4.31). Also within this system no other mineral matches with unknown #5. Maucherite is here as well the closest mineral.

Plotted in the system Ni-As-S one distinct group defines and is named unknown #6 (figure 4.32). Ni, As and S are all together major constituents. Gersdorffite is the only IMA-accepted and known mineral with the same major constituents but is much poorer in Ni, much richer in As and a little poorer in S than unknown #6, so no mineral matches with respectively is close to unknown #6.

Plotted in the system Co-Fe-Ni two distinct groups define and are named unknown #7 and unknown #8 (figure 4.33). In group unknown #7 Co and Ni are the major constituents and Fe forms a minor constituent, whereas in group unknown #8 Co and Fe are the major constituents and Ni is the minor constituent. Wairauite

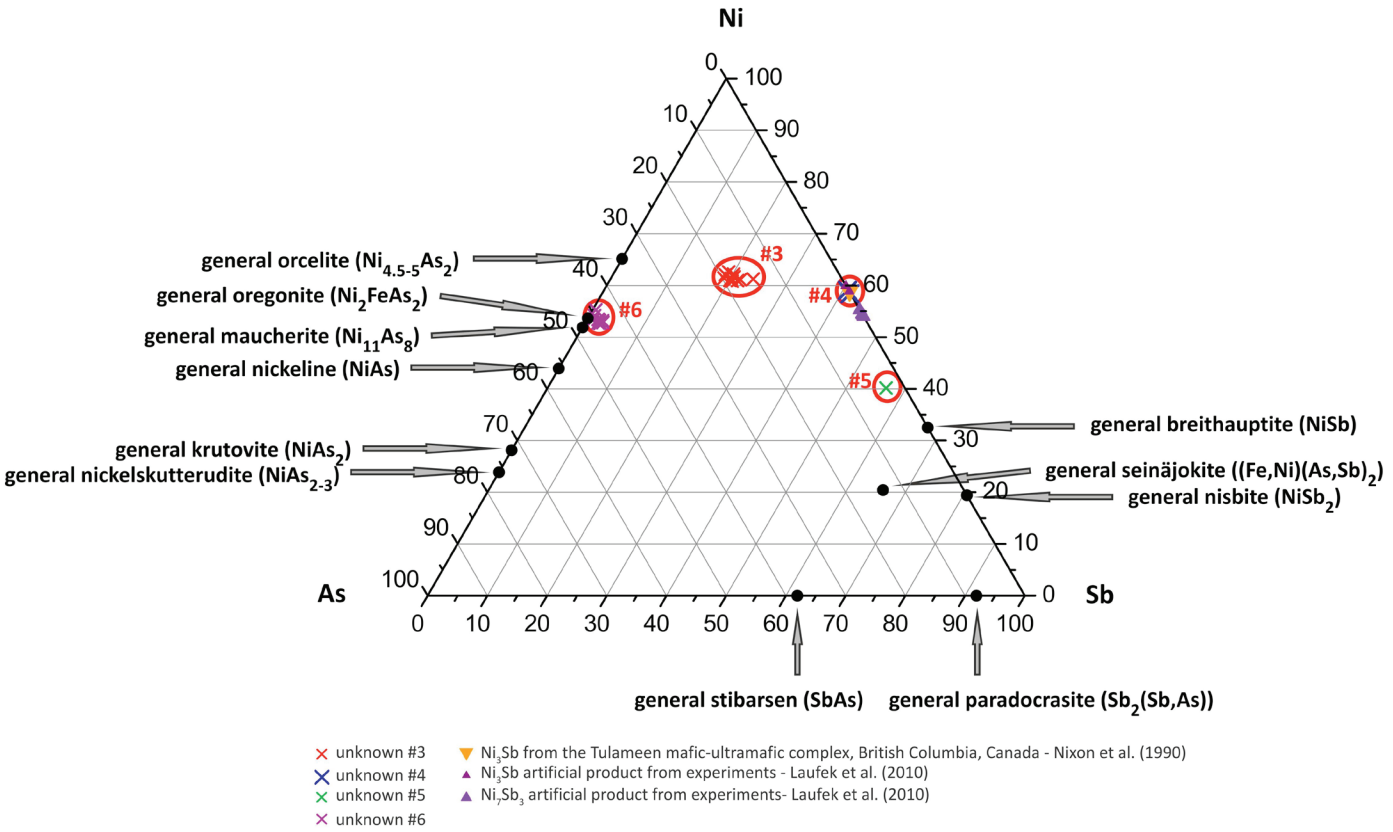

Figure 4.30 Distribution of the 23 unassignable analyses in the ternary system Ni-As-Sb, together with all known minerals of this system. The formation of the four distinct groups unknown #2, unknown #3, unknown #4 and unknown #5 can be observed. For unknown #5 and seinäjokite the Ni and Fe concentrations are added since they substitute for each other. All plotted concentrations are normalized to 100wt%.

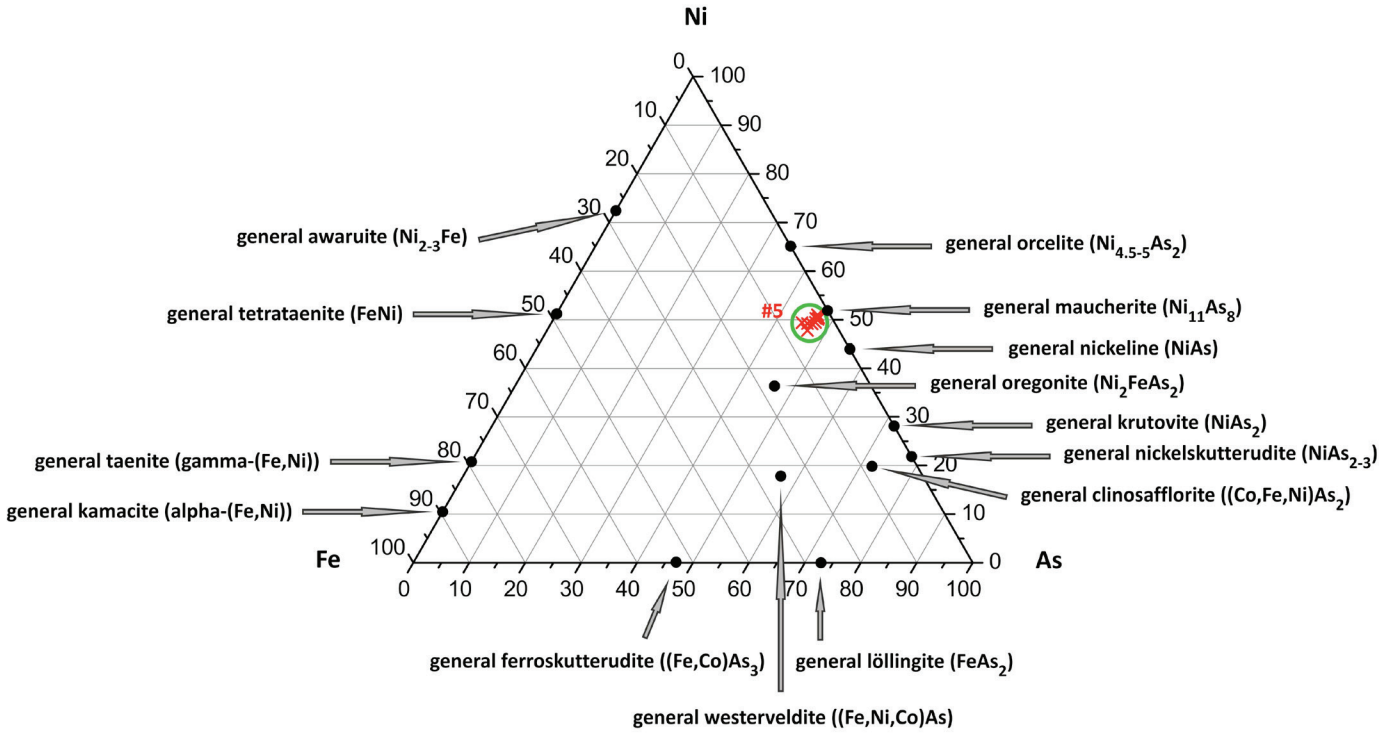

Figure 4.31 Distribution of the nine analysed mineral grains of the group of unknown #5 in the ternary system Ni-Fe-As, together with all known minerals of this system. For clinosafflorite and ferroskutterudite Co and Ni are added since they substitute for each other. All plotted concentrations are normalized to 100wt%.

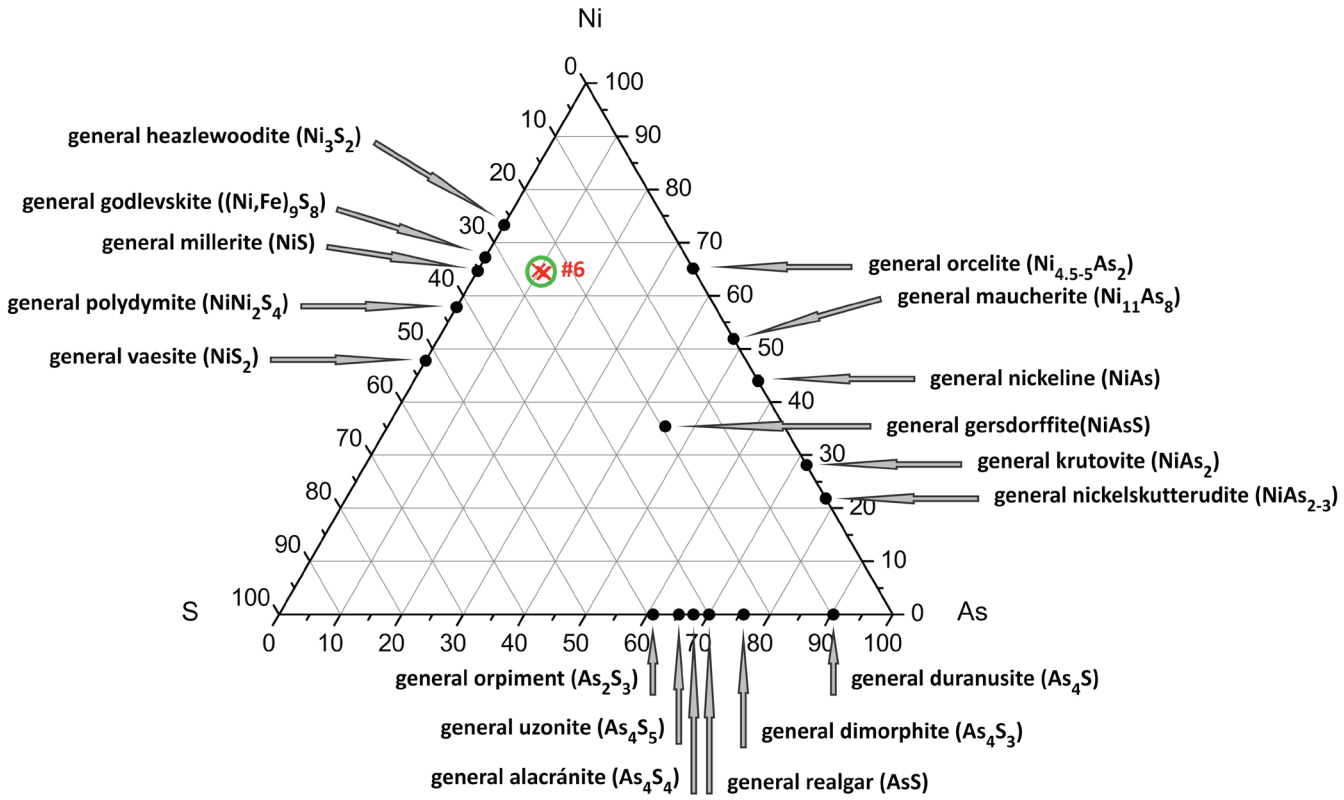

Figure 4.32 Distribution of the three analysed mineral grains of unknown #6 in the ternary system Ni-As-S, together with all IMA-accepted minerals of this system. For godlevskite Ni and Fe are added since they substitute for each other. All plotted concentrations are normalized to 100wt%.

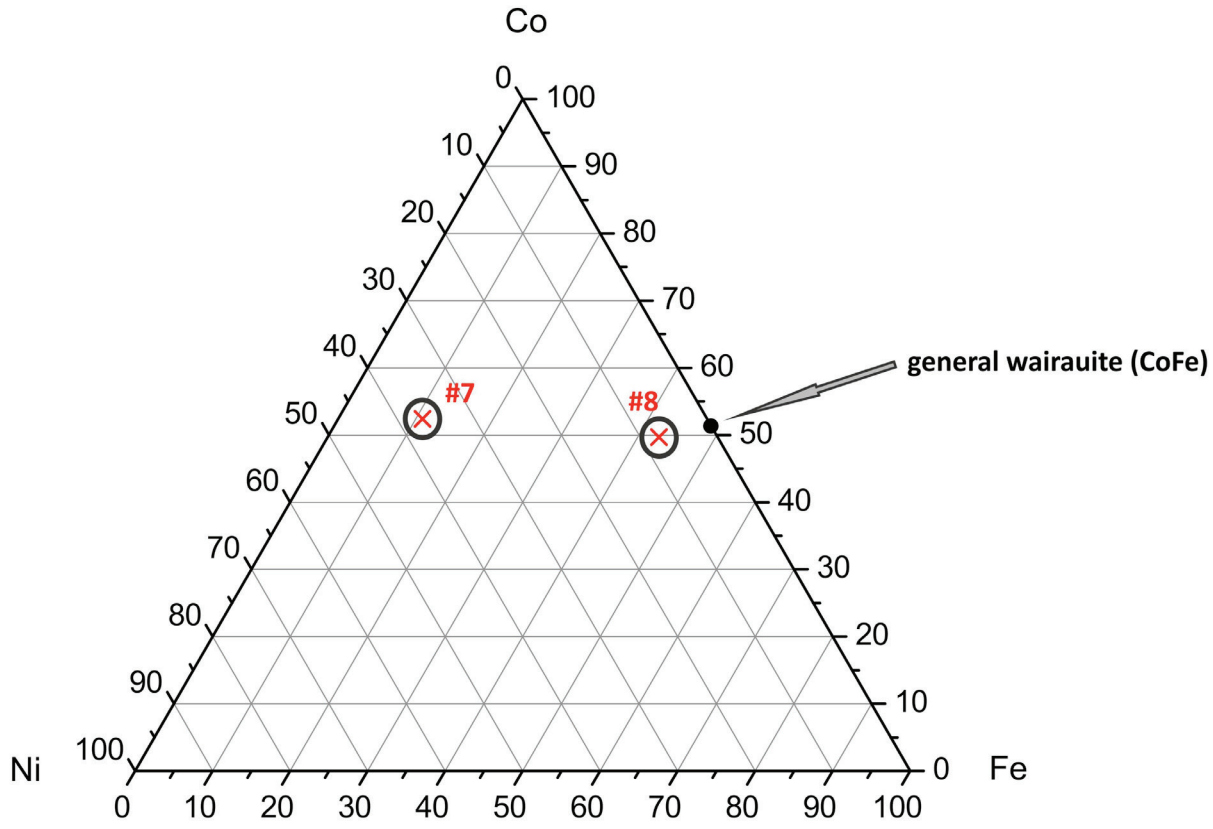

Figure 4.33 Distribution of the two analysed mineral grains unknown #7 and unknown #8 in the ternary system Co-Fe-Ni, together with all IMA-accepted minerals of this system. All plotted concentrations are normalized to 100wt%.

is the only known and IMA-accepted mineral in this system, but though it is relatively equal in the Co-content to unknown #7 and #8, it does not contain Ni. So neither unknown #7 nor unknown #8 matches with any known mineral, but the latter is relatively close to wairauite.

4.3.1 Unknown #2 $Ni_3(As,Sb)$

Detailed examination of the cation proportions suggests the mineral formula $Ni_3(As,Sb)$ (table 4.32). No mineral with such a mineral formula is reported to date, neither from experiments nor to occur in nature. To gain a full overview about the cation proportions the complete dataset is provided here. In total eleven mineral grains of unknown #2 with the mineral formula $Ni_3(As,Sb)$ are analysed. The average empirical formula is $Ni_{2.94}As_{0.60}Sb_{0.41}$ (table 4.32). Based on one (As + Sb) cation, the As cations vary from 0.5030 to 0.6274, and the Sb cations vary from 0.3726 to 0.4970.

Table 4.32 Cation proportions for unknown #2, $Ni_3(As,Sb)$, (n = 11), cations per 1 (As + Sb).

	Fe	Ni	As	Sb	S	Co	Zn	Te	Cu
average	0.0139	**2.9369**	**0.5952**	**0.4048**	0.0012	0.0012	0	0	0
minimum	0.0053	**2.8869**	**0.5030**	**0.3726**	0.0005	0	0	0	0
maximum	0.0673	**3.0334**	**0.6274**	**0.4970**	0.0028	0.0047	0	0	0
n 1	0.0131	**2.8869**	**0.5030**	**0.4970**	0.0011	0.0008	0	0	0
n 2	0.0246	**3.0237**	**0.6088**	**0.3912**	0.0020	0.0012	0	0	0
n 3	0.0120	**2.9810**	**0.5882**	**0.4118**	0.0005	0.0010	0	0	0
n 4	0.0139	**2.9657**	**0.5991**	**0.4009**	0.0028	0.0041	0	0	0
n 5	0.0323	**3.0334**	**0.6235**	**0.3765**	0.0013	0.0034	0	0	0
n 6	0.0053	**3.0497**	**0.6274**	**0.3726**	0.0020	0.0006	0	0	0
n 7	0.0077	**2.9140**	**0.5717**	**0.4283**	0.0011	0.0041	0	0	0
n 8	0.0362	**2.9310**	**0.5856**	**0.4144**	0.0007	0.0047	0	0	0
n 9	0.0109	**2.9049**	**0.5598**	**0.4402**	0.0009	0	0	0	0
n 10	0.0194	**2.9369**	**0.5952**	**0.4048**	0.0012	0.0025	0	0	0
n 11	0.0673	**2.9161**	**0.6043**	**0.3957**	0.0017	0	0	0	0

As shown in figure 4.34, As and Sb behave inverse to each other – the increase of As is coupled with a decrease in Sb and opposite. Fe is present as a trace constituent and shows no clear trend towards Ni. As shows furthermore a positive trend towards Ni – the increase of As is coupled with an increase in Ni and opposite. Sb shows a clear negative trend towards Ni – the increase of Ni is coupled with a decrease in Sb and opposite. Especially the latter two trends indicate that unknown #2 is a mixed crystal with the two end members Ni_3As and Ni_3Sb. The controversial mineral dienerite with the formula Ni_3As got pre-accepted by the IMA in 1921, but discredited in 2006 (Barthelmy, 2010), being nowadays known as the synonym for nickelskutterudite, having the mineral formula $NiAs_{2-3}$. To date there is no IMA-accepted mineral with the formula Ni_3Sb, but, besides unknown #4 in the present study, it is reported as a new species by Nixon *et al.* (1990) to occur in nature and by Laufek et al. (2010) from experiments. A certain scope of these values needs to be considered due to the small size of the mineral grains, being 10 µm to 20 µm for the grains in sample BA 83-1, and 10 µm to 40 µm in sample BA 87-4. Though the electron beam of the EPMA (< 1 µm) fits with the size of these grains, it is nevertheless possible that elements from the surrounding minerals might be picked up. The results are also influenced by impurities within some grains.

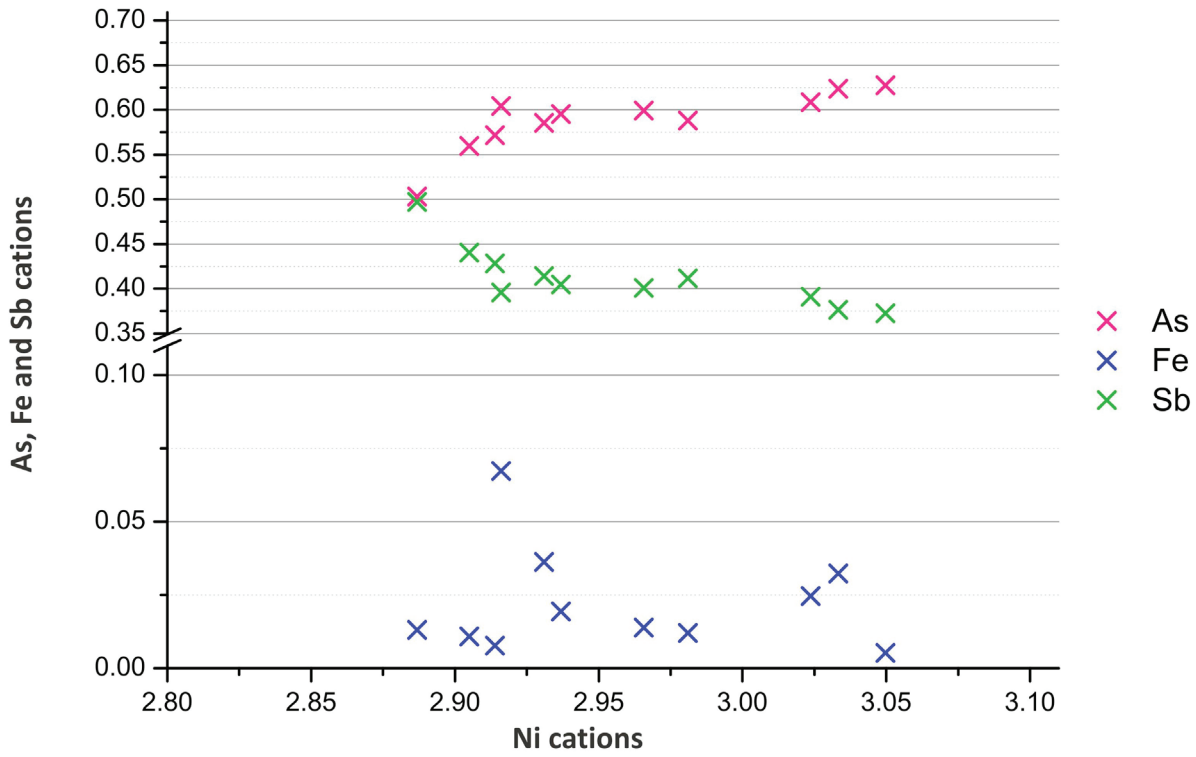

Figure 4.34 Binary scheme of the relations of As, Fe and Sb towards Ni of unknown #2. The plotted values are cation proportions, calculated per 1 (As + Sb).

The average major element concentrations for unknown #2, $Ni_3(As,Sb)$, are Ni 58.78 wt%, As 17.70 wt% and Sb 19.69 wt% (table 4.33). As, which substitutes with Sb, varies clearly about 4.13 wt% from the minimum concentration of 14.62 wt% to the maximum of 18.75 wt%. Sb varies also clearly about 5.40 wt% from 18.10 wt% in the minimum to 23.50 wt% in the maximum concentration. Ni varies lesser but still clearly about 3.90 wt% from the minimum concentration of 57.85 wt% to the maximum of 61.75 wt%. The trace element Fe varies clearly about 1.18 wt% from 0.10 wt% to 1.28 wt%, being 0.26 wt% on average. S is present in only one mineral grain with 0.03 wt%. Co, Zn, Te and Cu are not detected (figure 4.35).

Table 4.33 EPMA data of unknown #2, $Ni_3(As,Sb)$, (n = 11) in wt%.

	Fe	Ni	As	Sb	S	Co	Zn	Te	Cu
average	0.26	58.78	17.70	19.69	0	0	0	0	0
minimum	0.10	57.85	14.62	18.10	0	0	0	0	0
maximum	1.28	61.75	18.75	23.50	0.03	0	0	0	0
n 1	0.26	59.89	14.62	23.50	0	0	0	0	0
n 2	0.48	61.63	18.17	18.98	0	0	0	0	0
n 3	0.24	61.75	17.63	20.07	0	0	0	0	0
n 4	0.26	58.32	17.70	19.25	0.03	0	0	0	0
n 5	0.61	59.64	18.61	18.26	0	0	0	0	0
n 6	0.10	58.55	18.75	18.10	0	0	0	0	0
n 7	0.15	58.81	17.04	20.74	0	0	0	0	0
n 8	0.69	58.75	17.20	19.78	0	0	0	0	0
n 9	0.21	58.78	16.50	21.08	0	0	0	0	0
n 10	0.36	57.85	17.81	19.69	0	0	0	0	0
n 11	1.28	58.39	18.48	19.66	0	0	0	0	0

In addition to the EPMA-analyses, one mineral grain of unknown #2 in sample BA 87-4 is analysed with the µPIXE. The only detected elements are Ni, As, Sb, Fe and Co. Their distribution within unknown #2 is shown in the respective element maps (figure 4.36). In comparison to all surrounding minerals, unknown #2 is highest in Ni. The distribution of Ni is not homogeneous. It is clear to see, that the part on the right side of this mineral

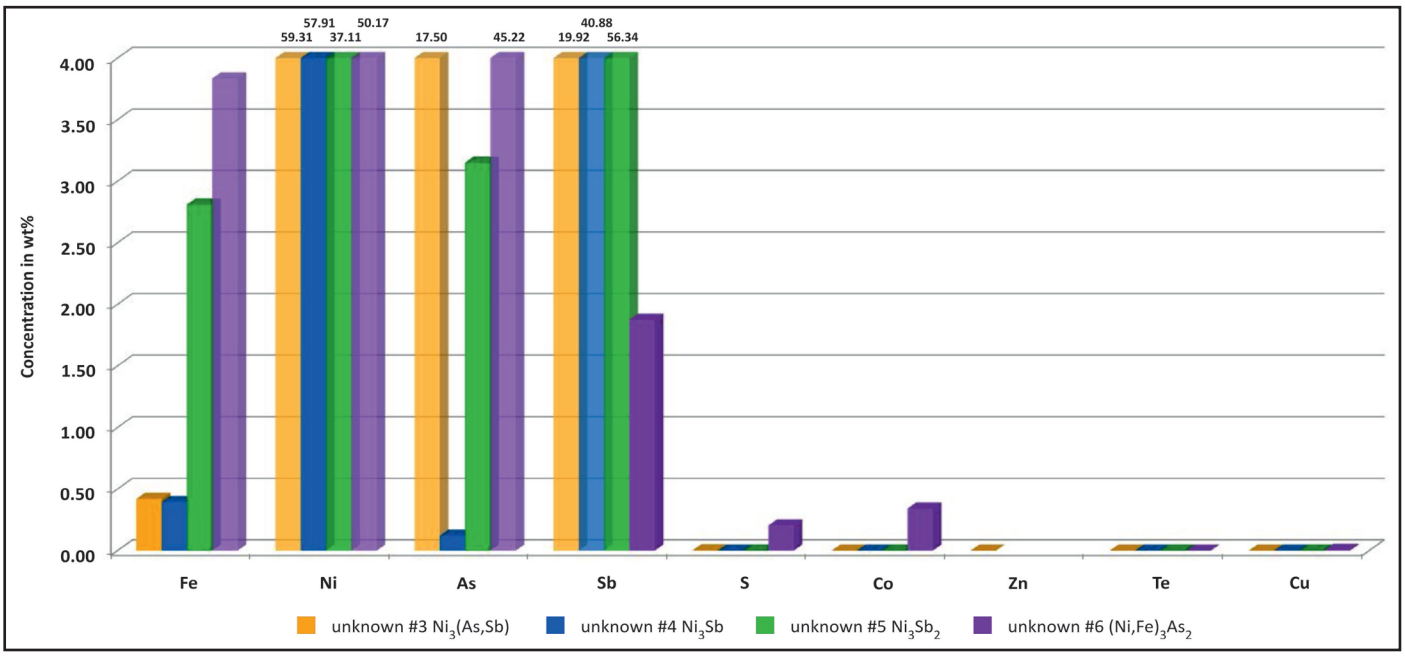

Figure 4.35 Element distribution in the minerals unknown #2, unknown #3, unknown #4 and unknown #5. The major elements per mineral are marked transparent. Blank positions mark not detected elements. All plotted concentrations are wt%.

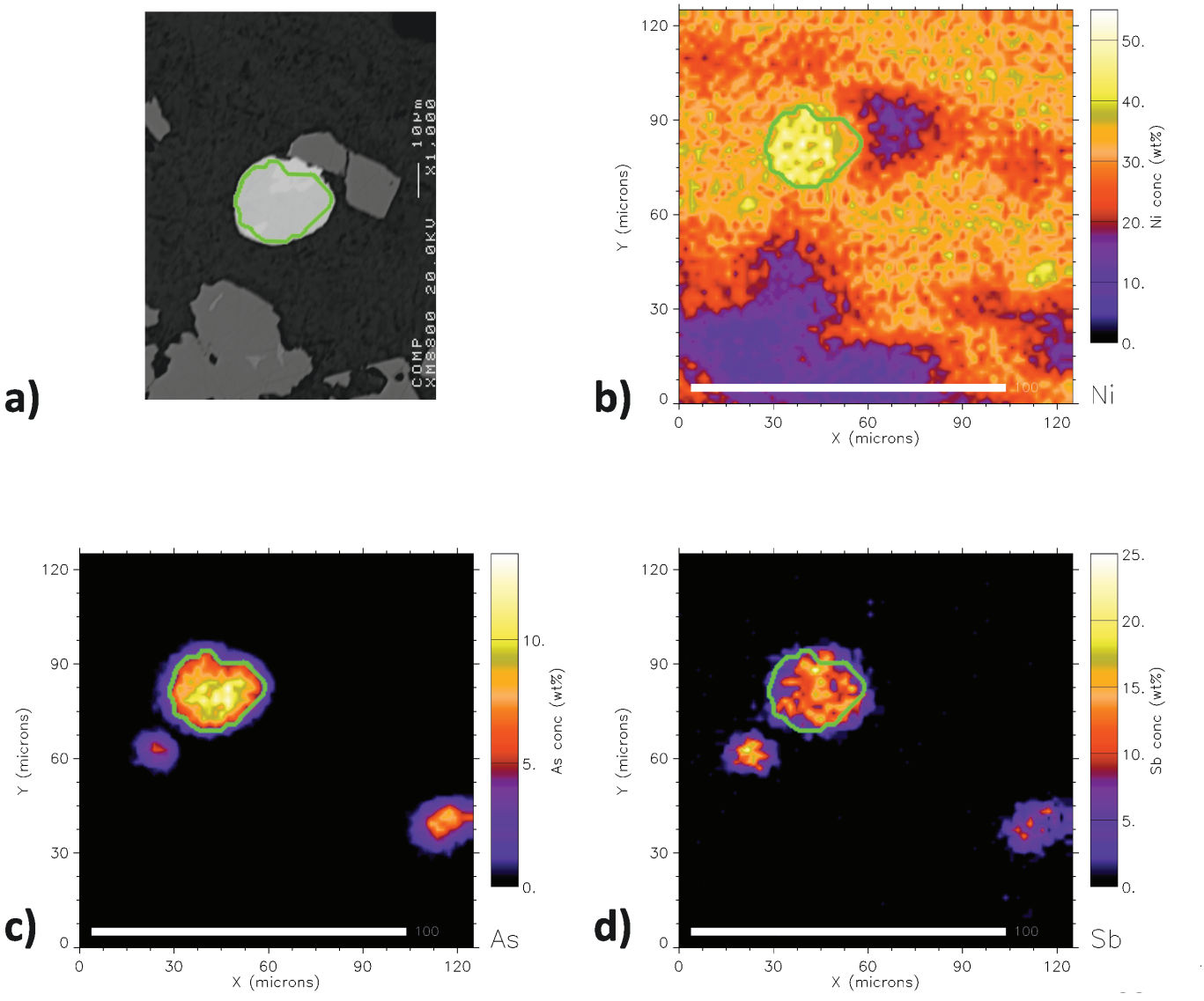

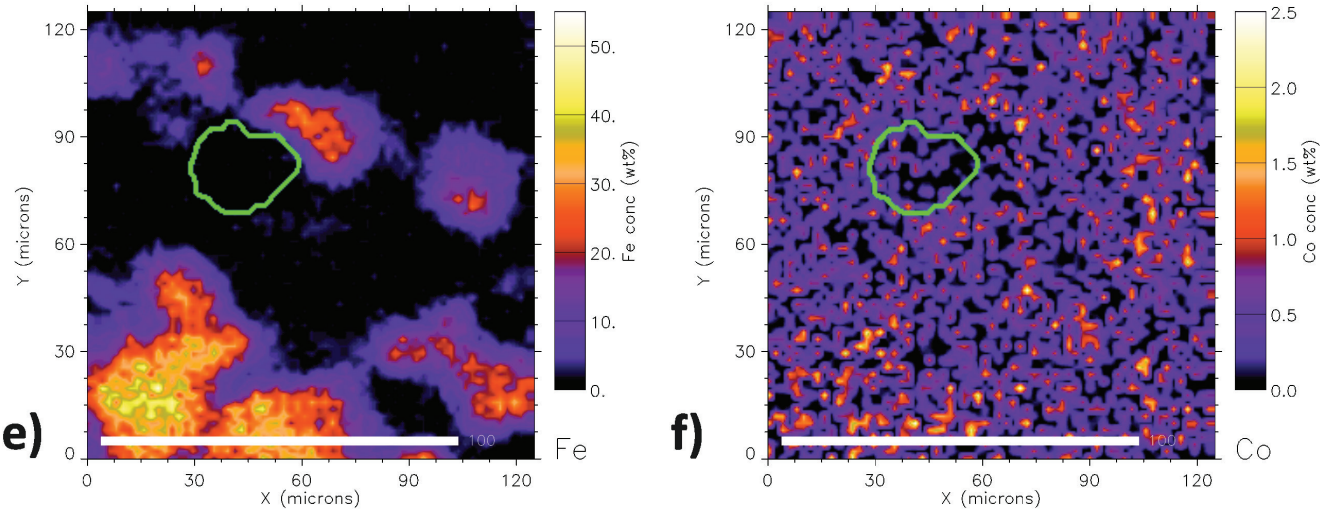

Figure 4.36 (continuation presvious page) µPIXE element maps of a selected area of interest in sample 87-4. The green shape marks unknown #2, which is analysed in detail. a) Overview about the selected area in reflected light (whitish: unknown #2, light grey: trevorite, dark grey: népouite-willemseite assemblage). b) Ni-map. c) As-map. d) Sb-map. e) Fe-map. f) Co-map. The concentrations are wt% and need to be examined carefully due to the strong beam instabilities during the measurement process.

is graded down. As is more intensive and clearer graded than Ni. The grain itself is rimmed by a corona. Two more insular As-accumulations of higher intensity are present in this area, but an exact attribution to a certain mineral is not possible. The rest of the area shows low concentrations. Sb is present in the whole grain but also graded from the centre with higher concentration to the rim with lower concentration. Like As, Sb shows a corona outside the grain. Sb is with higher intensity also present within the two insular As-accumulations, the rest of the whole area shows low concentrations. Fe is detected, but shows low concentrations. Co is present but with very low concentrations. Single tiny spots with higher concentration occur. All surrounding minerals show clearly higher Co-concentrations.

4.3.2 Unknown #3 Ni_3Sb

Detailed examination of the cation proportions suggests the mineral formula Ni_3Sb (table 4.34). Unknown #3 is reported by Laufek *et al.* (2010) from experiments, but also by Nixon *et al.* (1990) to occur in the Tulameen mafic-ultramafic complex in British Columbia, Canada, together with Ni_2Sb and Ni_7As_3. – For the latter no chemical composition is reported and Ni_2Sb contains a lot of Cu, therefore these two minerals are not plotted in figure 4.30. – Though it is already reported to occur in nature, it is still not accepted by the IMA as a valid new species. Therefore it is in the present study nevertheless regarded as an unknown mineral. To gain an overview about the cation proportions the full dataset is provided here.

Table 4.34 Summary of the cation proportions for unknown #3, Ni_3Sb, (n = 2), cations per 1 Sb.

	Fe	Ni	As	Sb	S	Co	Zn	Te	Cu
average	0.0211	**2.9383**	0.0048	**1.0000**	0.0006	0.0016	n.d.	0	0
n 1	0.0224	**2.8937**	0.0035	**1.0000**	0.0004	0.0012	n.d.	0	0
n 2	0.0198	**2.9829**	0.0061	**1.0000**	0.0008	0.0021	n.d.	0	0

In total two mineral grains of unknown #3 with the mineral formula Ni_3Sb are analysed. The average empirical formula is $Ni_{2.94}Sb_1$ (table 4.34). Based on one Sb cation, the Ni cations vary from 2.8937 to 2.9829. Also here a certain scope of these values needs to be considered due to the small size of the mineral grains, being 10 µm to 30 µm in sample BA 83-1.

The average major element concentrations for unknown #3, Ni_3Sb, are Ni 57.91 wt% and Sb 40.88 wt% (table 4.35). Ni varies clearly about 2.31 wt%, being 56.75 wt% in the minimum and 59.06 wt% in the maximum concentration. Sb varies insignificantly about 0.40 wt%, being 40.68 wt% in the minimum and 41.08 wt% in the maximum concentration. Fe and As are the only detected trace elements, varying insignificantly. Fe shows a minimum of 0.37 wt% and a maximum concentration of 0.42 wt%, being 0.40 wt% on average. As is lower with a minimum concentration of 0.09 wt% and a maximum of 0.16 wt%, being 0.12 wt% on average. S, Co, Te and Cu are not detected (figure 4.35).

Table 4.35 Summarized EPMA data of unknown #3, Ni_3Sb, (n = 2) in wt%.

	Fe	Ni	As	Sb	S	Co	Zn	Te	Cu
average	0.40	**57.91**	0.12	**40.88**	0	0	n.d.	0	0
n 1	0.42	**56.75**	0.09	**40.68**	0	0	n.d.	0	0
n 2	0.37	**59.06**	0.16	**41.08**	0	0	n.d.	0	0

4.3.3 Unknown #4 Ni_3Sb_2

Detailed examination of the cation proportions suggests the mineral formula Ni_3Sb_2 (table 4.36). No mineral with such mineral formula is reported to date, neither from experiments nor to occur in nature. To gain an overview about the cation proportions the full dataset is provided here.

Table 4.36 Summary of the cation proportions for unknown #4, Ni_3Sb_2, (n = 1), cations per 2 Sb.

	Fe	Ni	As	Sb	S	Co	Zn	Te	Cu
n 1	0.2172	**2.7329**	0.1818	**2.0000**	0	0	n.d.	0	0

Only one mineral grain of unknown #4 with the mineral formula Ni_3Sb_2 is analysed. Based on three Ni cations, the average empirical formula is $Ni_{2.73}Sb_2$ (table 4.36). Due to the very small grain size of about 7 µm in sample BAU and impurities within the grain a certain scope for these values needs to be considered.

For unknown #4, Ni_3Sb_2, only one analysis is available, so no statements can be made about the variation of the elements. The major element concentration of Ni is 37.11 wt% and for Sb it is 56.34 wt% (table 4.37). Also Fe was detected with 2.81 wt% and As with 3.15 wt%. S, Co, Te and Cu are not detected (figure 4.35).

Table 4.37 Summarized EPMA data of unknown #4, Ni_3Sb_2, (n = 1) in wt%.

	Fe	Ni	As	Sb	S	Co	Zn	Te	Cu
n 1	2.81	**37.11**	3.15	**56.34**	0	0	n.d.	0	0

4.3.4 Unknown #5 $(Ni,Fe)_3As_2$

Detailed examination of the cation proportions suggests the mineral formula $(Ni,Fe)_3As_2$ (table 4.38). No mineral with such mineral formula is reported to date, neither from experiments nor to occur in nature. To gain an overview about the cation proportions the full dataset is provided here

Table 4.38 Summary of the cation proportions for unknown #5, $(Ni,Fe)_3As_2$, (n = 9), cations per 2 As.

	Fe	Ni	As	Sb	S	Co	Zn	Te	Cu
average	0.2058	2.8504	2.0000	0.0593	0.0290	0.0168	n.d.	0	0
minimum	0.1358	2.7264	2.0000	0.0149	0.0029	0.0110	n.d.	0	0
maximum	0.3537	2.9183	2.0000	0.0808	0.0392	0.0309	n.d.	0.0008	0.0030
n 1	0.3537	2.8486	2.0000	0.0149	0.0410	0.0157	n.d.	0	0
n 2	0.3393	2.7264	2.0000	0.0518	0.0063	0.0110	n.d.	0	0
n 3	0.2434	2.7419	2.0000	0.0270	0.0078	0.0168	n.d.	0.0006	0
n 4	0.1562	2.8545	2.0000	0.0686	0.0290	0.0148	n.d.	0.0007	0
n 5	0.1358	2.9183	2.0000	0.0598	0.0292	0.0309	n.d.	0	0
n 6	0.1380	2.8536	2.0000	0.0593	0.0313	0.0284	n.d.	0	0
n 7	0.1793	2.9059	2.0000	0.0748	0.0392	0.0187	n.d.	0	0
n 8	0.2945	2.7918	2.0000	0.0237	0.0029	0.0162	n.d.	0.0008	0.0030
n 9	0.2058	2.8504	2.0000	0.0808	0.0052	0.0206	n.d.	0	0

In total nine mineral grains of unknown #5 with the mineral formula $(Ni,Fe)_3As_2$ are analysed. The average empirical formula is $Ni_{2.85}Fe_{0.21}As_2$ (table 4.38). The amount of Sb is too little as to include it in the formula, in contrast to Fe. Based on two As cations the Ni cations vary from 2.7264 to 2.9183, for Fe the cations vary from 0.1358 to 0.3537. As shown in figure 4.37, Fe shows a clear negative trend towards Ni – the Fe cations decrease with increasing Ni. A further negative correlation exists between the minor element Fe and the trace element

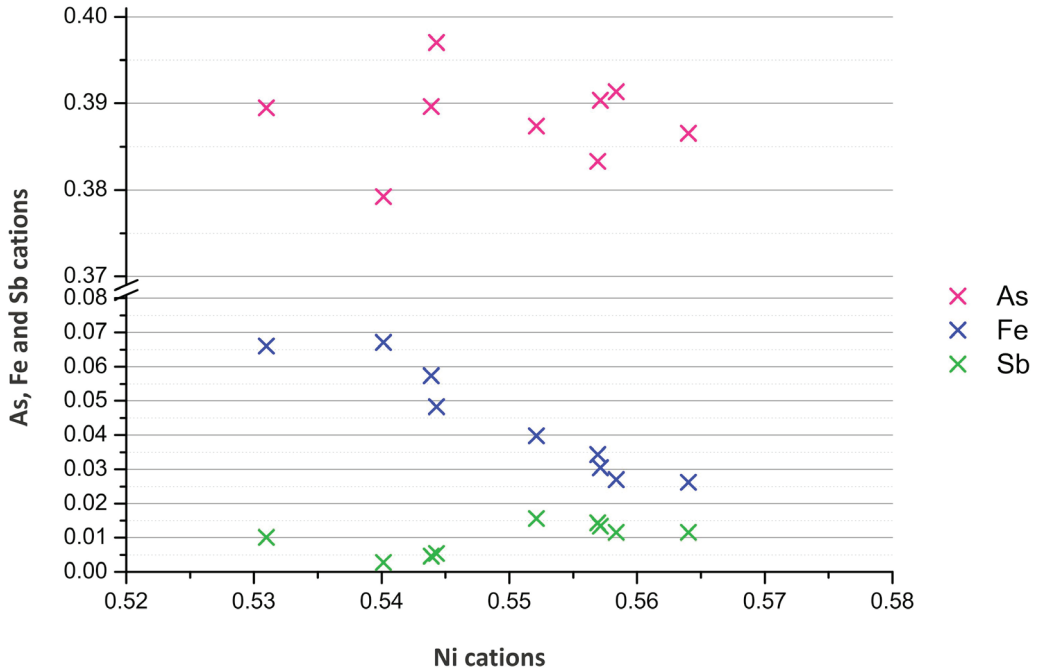

Figure 4.37: Binary scheme of the relations of As, Fe and Sb towards Ni of unknown #5. The plotted values are cations per 1 (Ni + As + Fe + Sb).

Sb, behaving absolutely converse to each other – increasing Fe cations are coupled to decreasing Sb cations and opposite. Here as well a certain scope for these values needs to be considered due to the partly pretty small grain size of about 5 µm in sample BA 84-1 and BAD, 10 µm in sample NCH7, and 5 µm to 20 µm in sample NCJ5.

The average major element concentrations for unknown #5, $(Ni,Fe)_3As_2$, are Ni 50.30 wt%, As 45.34 wt% and Fe 3.41 wt%. Ni, substituting about small amounts with Fe, varies a little about 2.45 wt% with a minimum concentration of 48.63 wt% and a maximum of 51.08 wt% (table 4.39). Fe varies with 3.59 wt% more than Ni, being 2.26 wt% in the minimum and 5.85 wt% in the maximum concentration. As varies with 2.77 wt% a little as well, showing a minimum concentration of 44.17 wt% and a maximum concentration of 46.94 wt%. The trace elements Sb, S and Co are present in all mineral grains whereas Cu is detected in only one grain and Te never. Sb varies clearly about 2.38 wt% with 0.54 wt% as the minimum and 2.92 wt% as the maximum concentration, being 2.17 wt% on average. S varies insignificantly with 0.36 wt%, being 0.03 wt% in the minimum and 0.39 wt% in the maximum concentration, showing an average concentration of 0.28 wt%. Co covers about the same range with 0.34 wt%. Its minimum concentration is 0.20 wt% and the maximum is 0.54 wt%, being 0.31 wt% on average. Cu is detected in only one mineral grain, showing a concentration of 0.06 wt% (figure 4.35).

Table 4.39 Summarized EPMA data of unknown #5, $(Ni,Fe)_3As_2$, (n = 9) in wt%.

	Fe	Ni	As	Sb	S	Co	Zn	Te	Cu
average	3.41	50.30	45.34	2.17	0.28	0.31	n.d.	0	0
minimum	2.26	48.63	44.17	0.54	0.03	0.20	n.d.	0	0
maximum	5.85	51.08	46.94	2.92	0.39	0.54	n.d.	0	0.06
n 1	5.85	49.54	44.38	0.54	0.39	0.28	n.d.	0	0
n 2	5.76	48.63	45.52	1.91	0.06	0.20	n.d.	0	0
n 3	4.26	50.43	46.94	1.03	0.08	0.31	n.d.	0	0
n 4	2.65	50.90	45.51	2.54	0.28	0.27	n.d.	0	0
n 5	2.26	51.08	44.67	2.17	0.28	0.54	n.d.	0	0
n 6	2.33	50.70	45.34	2.19	0.30	0.51	n.d.	0	0
n 7	2.95	50.30	44.17	2.69	0.37	0.32	n.d.	0	0
n 8	5.04	50.23	45.92	0.88	0.03	0.29	n.d.	0	0.06
n 9	3.41	49.70	44.50	2.92	0.05	0.36	n.d.	0	0

4.3.5 Unknown #6 Ni_7AsS_5

Detailed examination of the cation proportions results in the mineral formula Ni_7AsS_5. No mineral with such a formula is known or reported to date, neither to occur in nature, nor from experiments. To gain an overview about the cation proportions the full dataset is provided in table 4.40.

Three mineral grains of unknown #6 with the mineral formula Ni_7AsS_5 are analysed. The average empirical formula is $Ni_{7.07}As_{0.94}S_5$ (table 4.40). Based on five S cations, the Ni cations vary about 0.1192 from 6.9992 in the minimum to 7.1184 in the maximum, and As varies about 0.1281 from 0.8382 in the minimum to 0.9663 in the maximum.

Table 4.40 Summary of the cation proportions for unknown #6, Ni_7AsS_5, (n = 3), cations per 5 S.

	Fe	Ni	As	Sb	S	Co	Zn	Te	Cu
average	0.2513	**7.0694**	**0.9362**	0.0057	**5.0000**	0.1834	n.d.	0.0009	0
minimum	0.2489	**6.9992**	**0.8382**	0.0037	**5.0000**	0.1271	n.d.	0	0
maximum	0.4236	**7.1184**	**0.9663**	0.0081	**5.0000**	0.1835	n.d.	0.0040	0
n 1	0.2489	**6.9992**	**0.8382**	0.0057	**5.0000**	0.1835	n.d.	0.0040	0
n 2	0.2513	**7.1184**	**0.9663**	0.0037	**5.0000**	0.1834	n.d.	0.0009	0
n 3	0.4236	**7.0694**	**0.9362**	0.0081	**5.0000**	0.1271	n.d.	0	0

As shown in figure 4.38, there is no clear trend between As and Ni observable, in contrast to S and Ni. The slight increase in S is coupled to the increase in Ni. As and S show no clear correlation. Furthermore the substitution of the trace elements Fe and Co is observable – the decrease in Fe is coupled to the increase in Co.

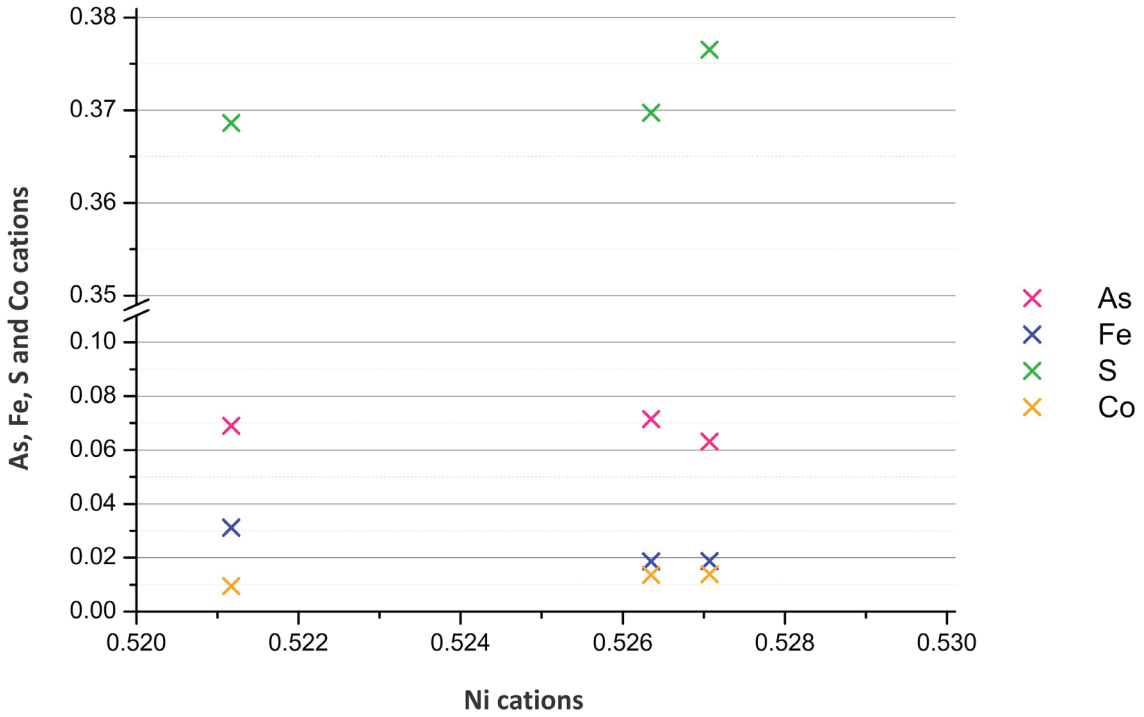

Figure 4.38 Binary scheme of the relations of As, S, Fe and Co towards Ni of unknown #6. The plotted values are cations per 1 (Ni + As + Fe + S + Co).

The average major element concentrations are Ni 62.42 wt%, As 10.48 wt% and S 23.96 wt% (table 4.41). Ni varies insignificantly about 1.44 wt% from 62.04 wt% in the minimum to 62.75 wt% in the maximum concentration. As varies with 1.22 wt% a little, being 9.59 wt% in the minimum and 10.81 wt% in the maximum concentration. S varies insignificantly about 0.54 wt% with 23.94 wt% in the minimum and 24.48 wt% in the maximum concentration. Fe, Sb, Co and Te are the detected trace elements (figure 4.39), whereas Cu is not detected. Unknown #6 is very enriched in Fe, which varies significantly about 1.44 wt% from 2.10 wt% in the minimum to 3.54 wt% in the maximum concentration, being 2.12 wt% on average. Co is very enriched as well with an average concentration of 1.61 wt%, varying significantly about 0.53 wt% from 1.12 wt% in the minimum to 1.65 wt% in the maximum concentration. Sb varies with 0.08 wt% insignificantly from 0.07 wt% in the minimum to 0.15 wt% in the maximum concentration, showing an average concentration of 0.11 wt%.

Te is present in only one mineral grain with a concentration of 0.08 wt%.

Table 4.41 Summarized EPMA data of unknown #6, Ni_7AsS_5, (n = 3) in wt%.

	Fe	Ni	As	Sb	S	Co	Zn	Te	Cu
average	2.12	62.42	10.48	0.11	23.96	1.61	n.d.	0	0
minimum	2.10	62.04	9.59	0.07	23.94	1.12	n.d.	0	0
maximum	3.54	62.75	10.81	0.15	24.48	1.65	n.d.	0.08	0
n 1	2.12	62.75	9.59	0.11	24.48	1.65	n.d.	0.08	0
n 2	2.10	62.42	10.81	0.07	23.94	1.61	n.d.	0	0
n 3	3.54	62.04	10.48	0.15	23.96	1.12	n.d.	0	0

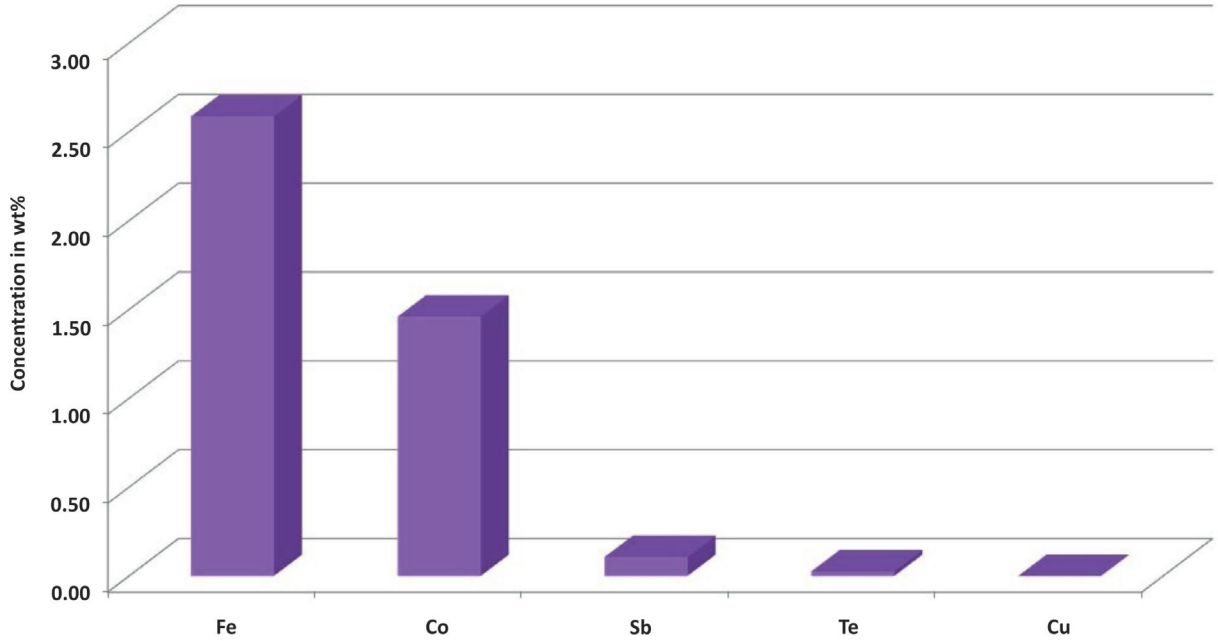

Figure 4.39 Trace element distribution of unknown #6. All plotted concentrations are wt%.

4.3.6 Unknown #7 Co(Ni,Fe)

Detailed examination of the cation proportions results in the mineral formula Co(Ni,Fe). No mineral with such a formula is known or reported to date, neither to occur in nature, nor from experiments. To gain an overview about the cation proportions the full dataset is provided here (table 4.42).

Table 4.42 Summary of the cation proportions for unknown #7, Co(Ni,Fe), (n = 1), cations per 1 Co.

	Fe	Ni	Co	Zn	Si	Mg	Ca	Al	Ti	Mn	Cr
n 1	0.2186	0.7030	1.0000	0	0.0001	0.0006	0.0002	0	0.0000	0.0016	0

Only one mineral grain of unknown #7 with the mineral formula Co(Ni,Fe) is analysed. Based on one Co cation, the average empirical formula is $CoNi_{0.70}Fe_{0.22}$ (table 4.42). This formula indicates that unknown #7 is a mixed crystal with the end members CoNi, which has never been reported to occur in nature nor from experiments, and CoFe, which is wairauite. Therewith unknown #7 can be regarded as ferroan CoNi which is a new mineral species.

For unknown #7 only one analysis is available, so no statements can be made about the variation of the elements. The major element concentration of Co is 52.28 wt%, for Ni it is 36.61 wt% and for Fe it is 10.83 wt% (table 4.43). Also Mn was detected with 0.08 wt%. Zn, Si, Mg, Ca, Al, Ti and Cr are not detected.

Table 4.43 Summarized EPMA data of unknown #7, Co(Ni,Fe), (n = 1) in wt%.

	Fe	Ni	Co	Zn	Si	Mg	Ca	Al	Ti	Mn	Cr
n 1	10.83	36.61	52.28	0	0	0	0	0	0	0.08	0

4.3.7 Unknown #8 Co(Fe,Ni)

Detailed examination of the cation proportions results in the mineral formula Co(Fe,Ni). No mineral with such a formula is known or reported to date, neither to occur in nature, nor from experiments. To gain an overview about the cation proportions the full dataset is provided here (table 4.44).

Table 4.44 Summary of the cation proportions for unknown #8, Co(Fe,Ni), (n = 1), cations per 1 Co.

	Fe	Ni	Co	Zn	Si	Mg	Ca	Al	Ti	Mn	Cr
n 1	0.9073	0.1530	1.0000	0	0	0	0	0	0.0002	0.0010	0

Only one mineral grain of unknown #8 with the mineral formula Co(Fe,Ni) is analysed. Based on one Co cation, the average empirical formula is $CoFe_{0.91}Ni_{0.15}$ (table 4.44). This formula indicates that unknown #8 is a mixed crystal with the end members CoFe, which is wairauite, and CoNi which has never been reported to occur in nature nor from experiments and is the end member of unknown #7. Therewith unknown #8 can be regarded as nickeloan wairauite and is not a new mineral species.

For unknown #8 only one analysis is available, so no statements can be made about the variation of the elements. The major element concentration of Co is 48.95 wt%, for Fe it is 42.09 wt% and for Ni it is 7.46 wt% (table 4.45). Also Mn was detected with 0.05 wt%. Zn, Si, Mg, Ca, Al, Ti and Cr are not detected.

Table 4.45 Summarized EPMA data of unknown #8, Co(Fe,Ni), (n = 1) in wt%.

	Fe	Ni	Co	Zn	Si	Mg	Ca	Al	Ti	Mn	Cr
n 1	42.09	7.46	48.95	0	0	0	0	0	0	0.05	0

The assumption of a solid solution series between wairauite and CoNi is supported with figure 4.40. Here, also one wairauite analysis of the same sample is plotted as well. The single mineral grains show clearly different steps of Ni-enrichment. For comparison, data from other authors are plotted as well. Chamberlain and Delabio (1965) reported wairauite from the Muskox intrusion in the Northwest Territories in Canada, and Challis and Long (1964) reported wairauite from the Red Hill serpentinites of the Wairau Valley in New Zealand. Xin et al. (1995) discovered ferroan wairauite (Fe_3Co_2) in the Ningqiang carbonaceous chondrite.

Plotting unknown #7, unknown #8 and wairauite towards Ni, Co does not show a significant trend, in contrast to Fe (figure 4.41). It is obvious that the Fe-concentration decreases about the value of the Ni-increase, indicating herewith the substitution of Fe and Ni.

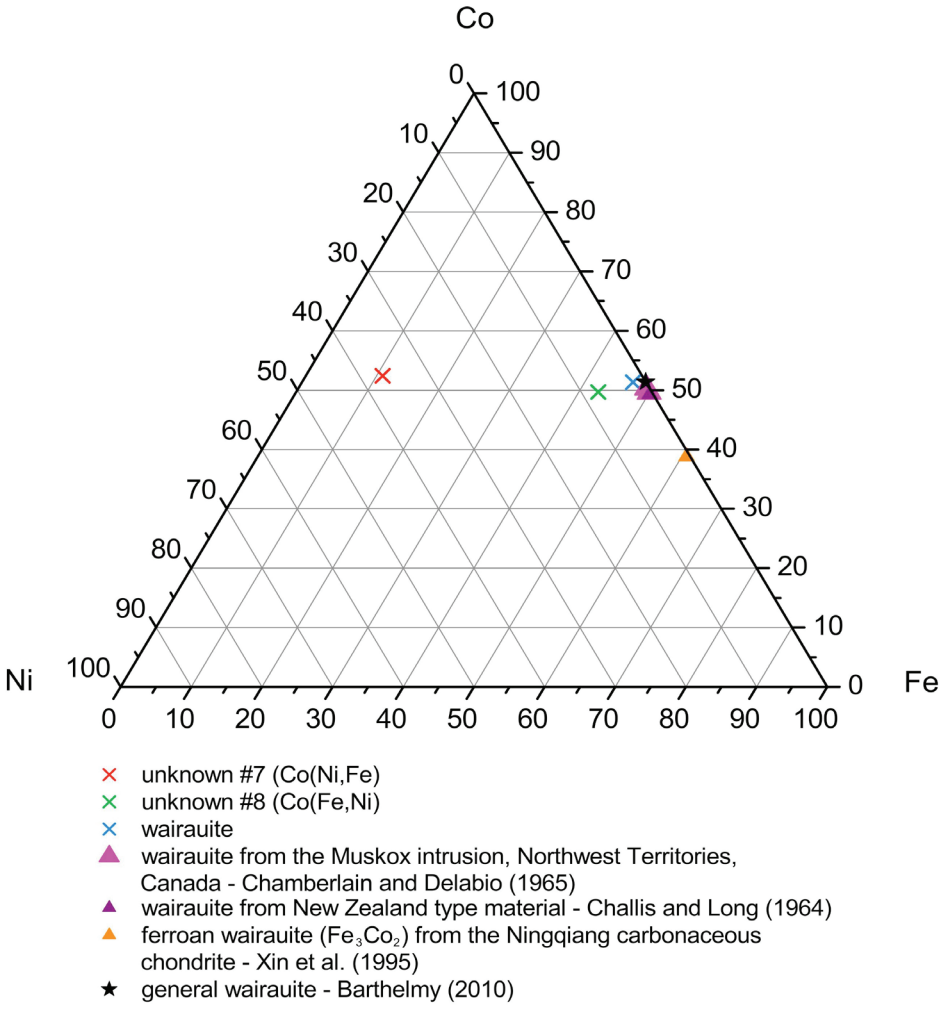

Figure 4.40 Compositional relation of unknown #7, unknown #8 and wairauite in the ternary Co-Fe-Ni diagram, together with wairauite data from Chamberlain et al. (1965) and Challis and Long (1964). For comparison, the data for ferroan wairauite (Fe3Co2) from Xin et al. (1995) are plotted. All concentrations are normalized to 100wt%.

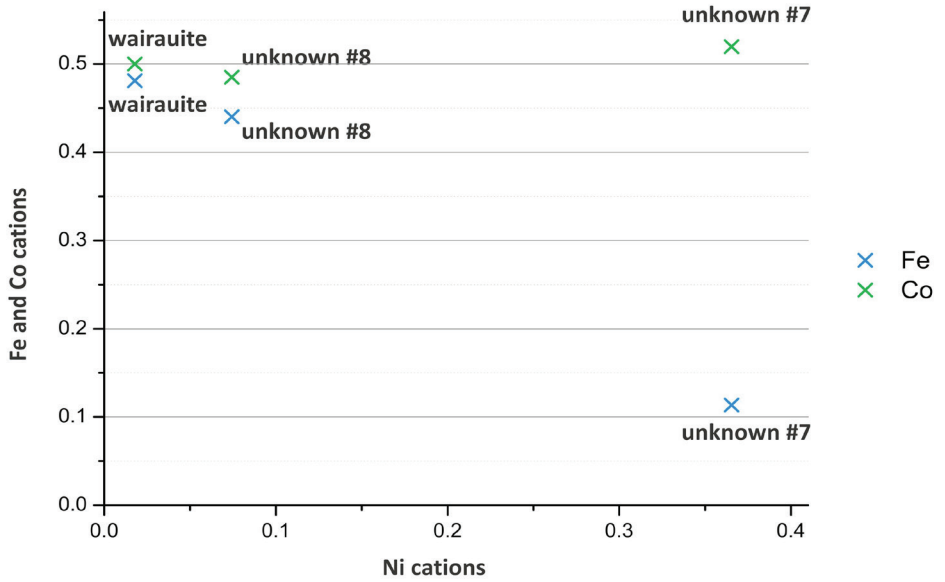

Figure 4.41 Dependence of Fe and Co towards Ni in the wairauite, unknown #7 and unknown #8 of the present study. All plotted concentrations are cations per 1 (Ni + Fe + Co).

4.4 Sulphides, sulphosalts and elements

In addition to the minerals unknown #2 to unknown #6, eleven further different sulphides / sulphosalts as well as two pure elements are analysed. These are two grains of nickeline in the samples BAD and NCH7; seven grains of orcelite in the samples BA 84-1, BA 87-1, BAD and BAU; six grains of breithauptite in the samples BA 84-1, BA 87-1, BAD and NCJ5; two grains of nisbite in sample BA 87-4; 35 grains of millerite in the samples BA 83-1, BA 84-1, BA 84-2, BAD, NCH7, NCJ5, NCJ8 and NCK6; ten grains of heazlewoodite in the samples NCJ8, NCJ5, BA 87-1, BAU and BA 87-4; one grain of anilite in sample BA 84-2; one grain of bornite in sample NCH7; six grains of chalcocite in sample NCJ8; one grain of digenite in sample NCJ8; one grain of marcasite in sample NCK6 are analysed as well as two grains of pure antimony in sample BAU and two grains of pure copper in sample BA 84-2. Their averaged concentrations are summarized in table 4.46; see appendix D for the full dataset. The major element concentrations of nickeline are 41.82 wt% Ni and 48.34 wt% As. Fe is enriched with 6.29 wt% as well as Sb with 3.49 wt%. Te and Cu are not detected. The major element concentration of orcelite is 63.45 wt% Ni and 33.13 wt% As. Fe is enriched with 5.37 wt% as well as Sb with 0.84 wt%. S, Co, Te and Cu are not detected. The major element concentration of breithauptite is 31.67 wt% Ni and 64.83 wt% Sb. Fe is enriched with 3.56 wt% and As with 0.77 wt%. S, Co, Te and Cu are not detected. The major element concentrations of nisbite are 14.54 wt% Ni and 77.44 wt% Sb. Fe is a little enriched with 0.61 wt%, As is also a little enriched with 0.32 wt%. Co, Zn, Te and Cu are not detected. The major element concentrations of millerite are 63.77 wt% Ni and 31.35 wt% S. Fe is enriched with 4.12 wt%, and Co with 1.14 wt%. As, Sb, Te and Cu are not detected. The major element concentrations of heazlewoodite are 71.05 wt% Ni and 26.40 wt% S. Fe is enriched with 3.85 wt%. As, Sb, Co and Cu are not detected. The major element concentrations of anilite are 73.58 wt% Cu and 20.87 wt% S. Fe is enriched with 4.39 wt% and Ni with 1.98 wt%. As, Sb and Te are not detected. The major element concentrations of bornite are 64.76 wt% Cu and 23.81 wt% S. Fe is very enriched with 7.02 wt% and Ni is enriched with 0.90 wt%. As, Sb and Te are not detected. The major element concentrations of chalcocite are 76.50 wt% Cu and 20.55 wt% S. Fe is enriched with 3.26 wt%. As, Sb and Te are not detected. The major element concentrations of digenite are 74.41 wt% Cu and 21.93 wt% S. Fe is enriched with 3.73 wt%, Ni is a little enriched with 0.51 wt%. As, Sb and Te are not detected. The major element concentrations of marcasite are 46.72 wt% Fe and 53.78 wt% S. As, Sb, Co, Te and Cu are not detected. The major element concentration of antimony is 97.48 wt% Sb. As is enriched with 2.30 wt%, Ni is a little enriched with 0.74 wt%. S, Co, Te and Cu are not detected. The major element concentration of copper is 89.89 wt% Cu. S is enriched with 3.15 wt%, Fe with 2.85 wt% and Ni with 1.84 wt%. Sb and Te are not detected. The elevated Fe- and Ni-concentrations might be picked up from the surrounding minerals (e.g. trevorite) since most of the mineral grains are very small. The low Cu-concentration in the pure copper are due to the very small size of both analysed grains and since they appear solved.

The cation proportions of the minerals are summarized in table 4.47; see appendix H for the full dataset. The empirical formula for nickeline is $Ni_{1.1}As_1$; for orcelite $Ni_{4.87}As_2$; for breithauptite $Ni_{1.01}Sb_1$; for nisbite $Ni_{0.81}Sb_2$; for millerite $Ni_{1.11}S_1$; for heazlewoodite $Ni_{2.92}S_2$; for anilite $Cu_{7.12}S_4$; for bornite $Cu_{5.5}S_4$; for chalcocite $Cu_{1.9}S_1$; for digenite $Cu_{8.56}S_5$ and for marcasite $Fe_{0.99}S_2$.

Table 4.46 Summarized averaged EPMA data of the sulphides, sulphosalts and elements (excluding the unknown minerals). N = 2 for nickeline, n = 7 for orcelite, n = 2 for antimony, n = 6 for breithauptite, n = 2 for nisbite, n = 35 for millerite, n = 10 for heazlewoodite, n = 1 for anilite, n = 1 for bornite, n = 6 for chalcocite, n = 1 for digenite, n = 2 for copper, n = 1 for marcasite. All concentrations are wt%. See appendix D for the whole dataset.

Formula	Mineral	Fe	Ni	As	Sb	S	Co	Zn	Te	Cu
NiAs	nickeline	6.29	**41.82**	**48.34**	3.49	0.14	0.23	n.d.	0	0
$Ni_{4.5-5}As_2$	orcelite	5.37	**63.45**	**33.13**	0.84	0	0	n.d.	0	0
Sb	antimony	0.15	0.74	2.30	**97.48**	0	0	n.d.	0	0
NiSb	breithauptite	3.56	**31.67**	0.77	**64.83**	0	0	n.d.	0	0
$NiSb_2$	nisbite	0.61	**14.54**	0.32	**77.44**	0.10	0	0	0	0
NiS	millerite	4.12	**63.77**	0	0	**31.35**	1.14	n.d.	0	0
Ni_3S_2	heazlewoodite	3.85	**71.05**	0	0	**26.40**	0	n.d.	0.07	0
Cu_7S_4	anilite	4.39	1.98	0	0	**20.87**	0.06	n.d.	0	**73.58**
Cu_5FeS_4	bornite	7.02	0.90	0	0	**23.81**	0.08	n.d.	0	**64.76**
Cu_2S	chalcocite	3.26	0.29	0	0	**20.55**	0.02	0.08	0	**76.50**
Cu_9S_5	digenite	3.73	0.51	0	0	**21.93**	0.06	0.08	0	**74.41**
Cu	copper	2.85	1.84	0.20	0	3.15	0.13	n.d.	0	**89.89**
FeS_2	marcasite	**46.72**	0.08	0	0	**53.78**	0	n.d.	0	0

Table 4.47 Summarized averaged cation proportions of the sulphides, sulphosalts and elements (excluding the unknown minerals). N = 2 for nickeline, n = 7 for orcelite, n = 6 for breithauptite, n = 2 for nisbite, n = 35 for millerite, n = 10 for heazlewoodite, n = 1 for anilite, n = 1 for bornite, n = 6 for chalcocite, n = 1 for digenite, n = 1 for marcasite. The cations for nickeline are per 1 As, for orcelite, per 2 As, for breithauptite per 1 Sb, for nisbite per 2 Sb, for millerite per 1 S, for heazlewoodite per 2 S, for anilite for 4 S, for bornite per 4 S, for chalcocite per 1 S, for digenite per 5 S and for marcasite per 2 S. See appendix H for the whole dataset.

Formula	Mineral	Fe	Ni	As	Sb	S	Co	Zn	Te	Cu
NiAs	nickeline	0.1743	**1.1039**	**1.0000**	0.0448	0.0067	0.0060	n.d.	0.0001	0
$Ni_{4.5-5}As_2$	orcelite	0.4539	**4.8659**	**2.0000**	0.0313	0.0023	0.0014	n.d.	0.0005	0
NiSb	breithauptite	0.1191	**1.0134**	0.0191	**1.0000**	0.0005	0.0007	n.d.	0	0
$NiSb_2$	nisbite	0.0353	**0.8135**	0.0116	**2.0000**	0.0053	0.0056	0	0	0
NiS	millerite	0.0757	**1.1055**	0.0008	0.0002	**1.0000**	0.0199	n.d.	0.0004	0
Ni_3S_2	heazlewoodite	0.1691	**2.9205**	0.0016	0	**2.0000**	0.0010	n.d.	0.0013	0
Cu_7S_4	anilite	0.4825	0.2075	0	0	**4.0000**	0.0058	n.d.	0	**7.1145**
Cu_5FeS_4	bornite	0.6765	0.0823	0	0	**4.0000**	0.0073	n.d.	0	**5.4890**
Cu_2S	chalcocite	0.0931	0.0077	0	0.0002	**1.0000**	0.0010	0	0	**1.8955**
Cu_9S_5	digenite	0.4888	0.0630	0	0.0018	**5.0000**	0.0072	0.0085	0.0005	**8.5621**
FeS_2	marcasite	**0.9973**	0.0017	0.0004	0.0001	**2.0000**	0.0006	n.d.	0	0

4.5 Additional minerals

In addition to the samples of the Bon Accord Ni-oxide body, also the samples of the hematite-magnetite body, chert and tourmaline-hornblende schist are analysed. For the hematite-magnetite body eight chromites are analysed (three chromites of sample cB S 1088 3a (in each case the centre and the rim of the grains), two chromites of sample cB S 1088 3b (in the same style), three chromites of sample BAE-2), ten grains of unidentified silicate 1 in the samples cB S 1088 3a and cB S 1088 3b, two grains of unidentified silicate 2 in sample BAE-2, two hematite drops in sample cB S 1088 13a, four magnetite grains in sample BAE-2, two quartz grains in sample cB S 1088 13a, six wüstite grains in sample cB S 1088 13a and two grains of wairauite in sample cB S 1088 13a. For the chert three brookite grains in sample BA-A S1, two chromite grains in sample BA-B S2, one wüstite grain in sample BA-B S2 (five analyses for each area of this zoned grain), nine quartz grains in the samples BA-A S1 and BA-B S2, six gersdorffite grains in sample BA-A S1, eight marcasite grains

in sample BA-A S1, one chalcopyrite grain in sample BA-B S2 as well as one pure nickel grain in sample BA-A S1 are analysed. In the sample of the tourmaline-hornblende schist (BAR9) three actinolite grains, two grains of magnesio-hornblende, four grains of feruvite and five quartz grains are analysed. Since the minerals of all these samples are not in the main focus of the present study, their mineral chemical data are shown in appendix E and I and are not included in this chapter.

4.6 Whole rock chemistry

In addition to the mineral chemical analyses, whole rock chemistry of the Bon Accord shall give a general impression about the unusual composition of the Bon Accord Ni-oxide body. Since sample material of this deposit is very rare and of limited availability, whole rock chemistry data of Madala (2009) are used, because XRF is a destructive method. Four samples of the Bon Accord (BA 83-1, BA 87-1, BA 87-3, BA 84-1), one sample of the tourmaline-hornblende schist (BAR9) as well as one sample of the chert (BA-A S1) are examined within the present study which match with the by Madala (2009) analysed material. The major and trace element data of Madala (2009) for the respective samples are summarized in table 4.48 and 4.49. Ni is always treated as a trace element in whole rock analyses, but in the Bon Accord Ni-oxide body Ni is present in major element concentrations. Since no adequate standard existed for this case, Madala (2009) recalculated Ni as a major element. These concentrations are remarkably high, ranging from 35.33 wt% NiO in sample BA 83-1 to 52.74 wt% NiO in sample BA 87-1 (table 4.48 and figure 4.42). Considering the lack of an adequate Ni-

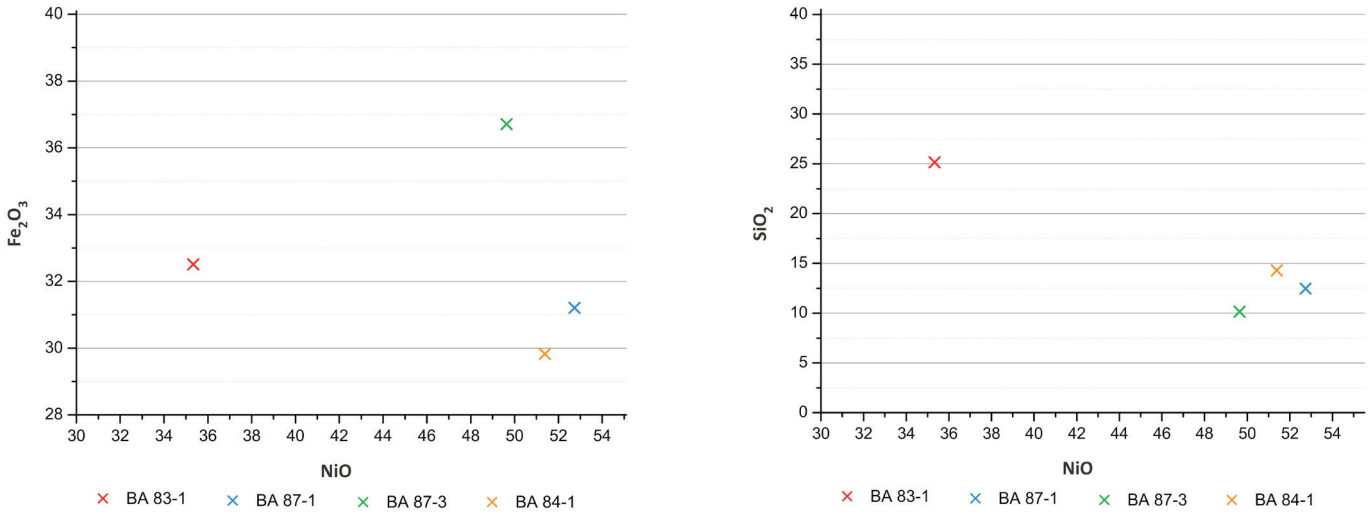

Figure 4.42 Binary plot of a) NiO vs. Fe_2O_3, and b) NiO vs. SiO_2 for the samples of the Bon Accord.

standard, an error of about 10 % can be assumed. Nevertheless the values are numbers higher than in any other reported rock type. The chert and tourmaline-hornblende schist, which occur also in the host rocks, are nearly devoid of Ni. Also Fe_2O_3 is high with a range of 29.83 wt% in the minimum and 36.71 wt% in the maximum concentration, being remarkably higher than Fe_2O_3 of the chert and tourmaline-hornblende schist. SiO_2 varies from 10.14 wt% in the minimum to 25.14 wt% in the maximum concentration, being significantly lower than in the chert and tourmaline-hornblende schist. MgO ranges from 2.05 wt% to 2.92 wt% in the Bon

Accord samples, which is only a little higher than in the chert and tourmaline-hornblende schist. Al_2O_3 is with a maximum of 2.03 wt% lower than the chert and the tourmaline-hornblende schist.

Table 4.48 Summarized major element data of the whole rock chemical analyses from Madala (2009). The total Fe-concentrations are expressed as Fe_2O_3. All concentrations are wt%.

Sample	NiO	TiO_2	Al_2O_3	Fe_2O_3	Cr_2O_3	MnO	CoO	SiO_2	MgO	CaO	K2O	LOI	Total
BA 83-1	**35.33**	0.25	**2.03**	**32.51**	0.23	0.19	0.46	**25.14**	**2.49**	0.09	0.28	0.98	99.98
BA 87-1	**52.74**	0.01	**0.43**	**31.21**	0.12	0.05	0.62	**12.47**	**2.08**	0.00	0.00	0.08	99.82
BA 87-3	**49.64**	0.11	**0.43**	**36.71**	0.18	0.01	0.55	**10.14**	**2.05**			0.08	99.90
BA 84-1	**51.38**	0.01	**0.61**	**29.83**	0.04	0.01	0.68	**14.28**	**2.92**			0.08	99.84
BA-A S1	**0.01**	0.63	**4.32**	**3.51**	0.04	0.03	0.00	**89.83**	**1.87**	0.04	0.47	0.07	100.82
BAR9	**0.04**	1.07	**11.78**	**1.11**	0.82	0.01	0.00	**82.01**	**0.58**	0.03	3.79	0.06	101.29

Considering the trace elements, the concentrations of Sb, Yb, Ta, Cu, Ge, As and V point out most significantly (table 4.49 and figure 4.43). Sample BA 83-1 is richest in Sb with a concentration of 13,179 ppm and poorest in sample BA 84-1 with a concentration of 134 ppm. Yb is richest in sample BA 84-1 with 2,124 ppm and lowest in sample BA 87-3 with 1,187 ppm. Neither Sb nor Yb are detected in the sample of the chert and tourmaline-hornblende schist.

Table 4.49 Summarized trace element data of the whole rock chemical analyses from Madala (2009). All concentrations are ppm.

Sample	Sc	V	Cu	Zn	Ga	Ge	As	Br	Rb	Sr
BA 83-1	44	**146**	**319**	75	48	**195**	**154**	0.2	20	28
BA 87-1		**57**	**415**	66	52	**275**	**99**	0.6	0.9	1
BA 87-3		**75**	**369**	56	65	**330**	**127**	1		
BA 84-1		**27**	**394**	70	50	**158**	**94**			0.4
BA-A S1	2	**61**	**24**		4		**17**		15	8
BAR9	48	**364**	**31**	140	11	**0.5**	**25**		126	4

Sample	Y	Zr	Nb	Mo	Cd	Sn	Sb	I	Ba	Yb
BA 83-1	1	11	2	3	5	24	**13179**	34	125	**1319**
BA 87-1	2	4	4	1		22	**1693**	16	23	**2062**
BA 87-3	1	4	4	3	15	44	**1897**	13	12	**1187**
BA 84-1	2	8	1		4	28	**134**	16	4	**2124**
BA-A S1	3	32	4		1	11		25	111	
BAR9	3	28	3		3	15		34	373	

Sample	Hf	Ta	W	Hg	Tl	Pb	Bi	Th
BA 83-1		**1034**		0.5	1	2	6	4
BA 87-1	9	**1372**		0.7		2	2	15
BA 87-3	3	**1205**		0.6		0.4	7	9
BA 84-1		**1280**		0.7		1	7	5
BA-A S1	1	**7**	25		0.2	5	4	8
BAR9	0.9	**6**	50		1	1	4	5

Ta is also present in significant amounts, ranging from 1,372 ppm in sample BA 87-1 to 1,034 ppm in sample BA 83-1, being present only in minor amounts in the chert sample and in the tourmaline-hornblende schist sample. Cu varies from 415 ppm in sample BA 87-1 to 319 ppm in sample BA 83-1. Ge varies from 330 ppm in sample BA 87-3 to 158 ppm in sample BA 84-1. As varies from 154 ppm in sample BA 83-1 to 94 ppm in sample BA 84-1. Cu, Ge and As are significantly higher in the samples of the Bon Accord than in the sample of the chert and of the tourmaline-hornblende schist. V behaves opposed, ranging from 146 ppm in sample BA 83-1 to 27 ppm in sample BA 84-1, whereas the chert sample contains 61 ppm V, and the sample of the tourmaline-hornblende schist contains 364ppm, which is numbers higher than in the Bon Accord.

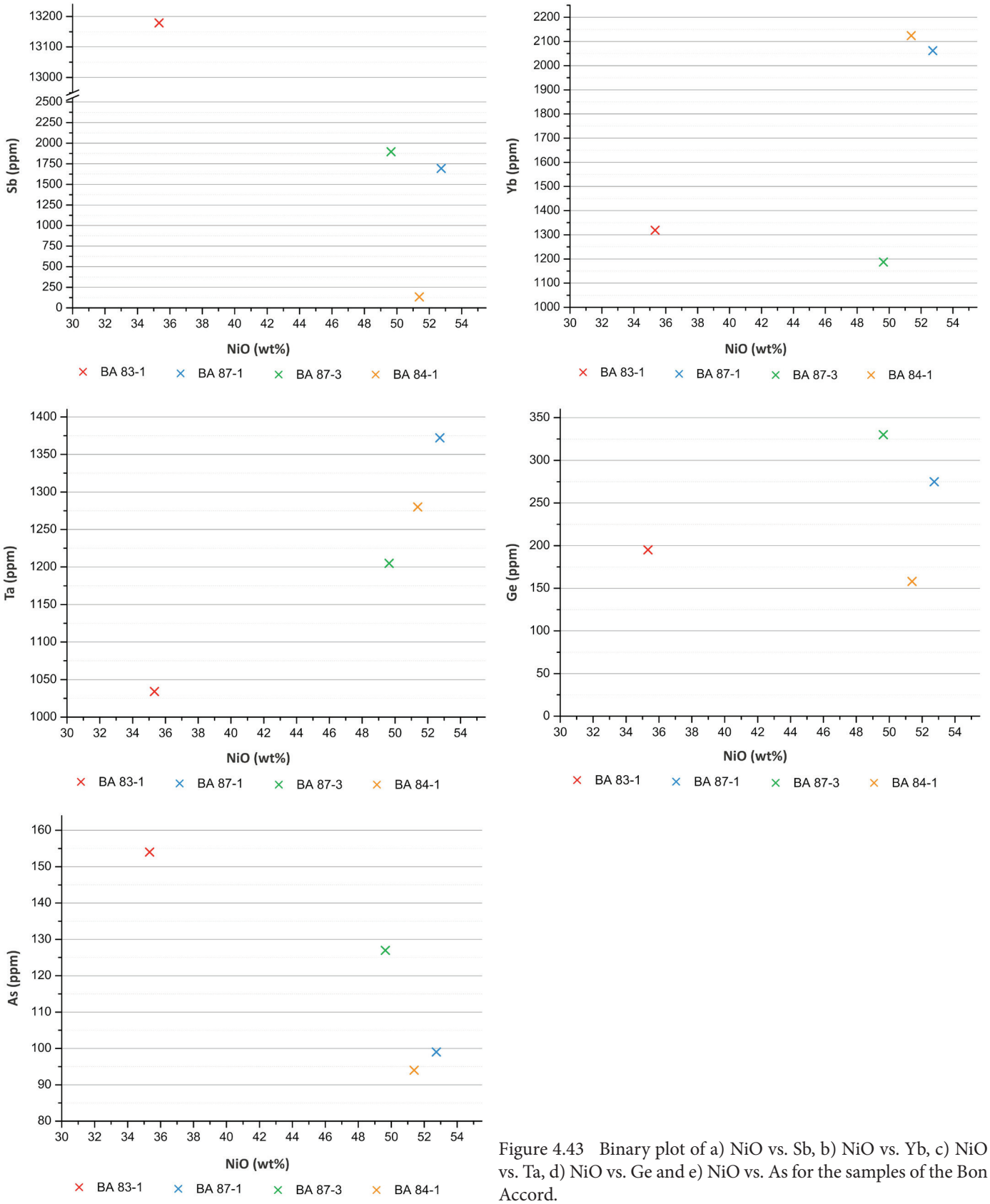

Figure 4.43 Binary plot of a) NiO vs. Sb, b) NiO vs. Yb, c) NiO vs. Ta, d) NiO vs. Ge and e) NiO vs. As for the samples of the Bon Accord.

5. Discussion

5.1 Introduction

Though the main objective of the present study is not the exact allocation of the Bon Accord samples in the deposit, it is nevertheless an important basis for most of the interpretations about this deposit. By use of detailed optical microscopy and mineral chemical analyses of all Bon Accord samples a final sample order from the core of the deposit to the outer rim is suggested. According to De Waal (1977), the undeformed core of the deposit consisted of about 36 wt% NiO and the deformed rim of about 10 wt% NiO. As explained in chapter 1, the succession of the by De Waal (1977) described five distinct rock types cannot fully be used for a sample attribution from the inner core to the outer rim. Nevertheless a relatively accurate sample order can be suggested. For this, the by De Waal (1977) described deformation degree for each rock type as well as the known succession of trevorite (in rock type I and II), ferroan trevorite (in rock type III) and nickeloan magnetite (in rock type IV and V) as well as willemseite as indicator minerals can be used as a basis. These minerals are present in significant amounts in each sample. The minerals of the magnetite-trevorite series show all together a range of about 31 wt% NiO to about 9 wt% NiO; the willemseite shows a range of 40 wt% NiO to about 15 wt% NiO. Following the decrease of Ni-ions per 32 O in the minerals of the magnetite-trevorite series, as well as the decrease of Ni-ions per 2 Si in the willemseite, consequently the sample order

BA 83-1, BA 87-4, BAU, BA 87-1, BA 87-3, NCJ8, NCK6, BA 84-1, NCH7, NCJ5, BA 84-2, BAD

from the assumed centre of the deposit (starting with BA 83-1) to the rim (ending with BAD) is suggested. This is also in agreement with the deformation observed by De Waal (1977) (table 5.1).

According to Madala (2009), the NiO whole rock concentration is with about 50 % highest in the samples of the deformed rim and the contact, whereas the sample of the undeformed core contains about 35 % NiO. The latter is in agreement with the whole rock data of the undeformed core by De Waal (1977), Crosse (1921) and Gray (1921), who run assay analyses to obtain quantitative whole rock chemistry data, whereas the concentration of about 50 % NiO in samples of the deformed rim is in contrast to De Waal (1977), who obtained a concentration of about 10 % NiO in the outer rim. From petrography and mineral chemistry of the present study, the Ni-depletion from the undeformed core to the deformed rim as it is observed De Waal (1977) can be supported, since the Ni-richest minerals (unknown #1b with at most about 30 % NiO, being the Ni-richest major constituent) are observed in the samples of the undeformed core, and the Ni-poorest minerals are observed in the samples of the deformed rim. In Bon Accord A unknown #1b, containing in average about 30 % NiO, is the most abundant major constituent, also minor amounts of bunsenite, being 100 % NiO, are present. In Bon Accord B the most abundant major constituent is ferroan trevorite (containing at most about 17 % NiO) as well as nickeloan magnetite in the outer part of the rim (containing at most about 12 % NiO). Only the presence of bunsenite, which is 100 % NiO, as a major constituent would explain the data of Madala (2009) with about 50 % NiO in the samples of the deformed rim. The samples of the present study are only small sections of the whole deposit and do not exclude the presence of big amounts of bunsenite in the deformed rim. All in all, the whole rock data of De Waal (1977), Crosse (1921), Gray (1921) and Madala (2009) need to be regarded carefully, since these data are obtained by the use of XRF without adequate Ni-standard (Madala, 2009) or by use of the inaccurate assay.

Table 5.1 Overview about the dependence of Ni-depletion in the minerals of the magnetite-trevorite series and willemseite towards the degree of deformation in the respective sample.

Sample	Mineral paragenesis	Number of Ni-ions per 32 O in the minerals of the magnetite-trevorite series	Number of Ni-ions per 4 Si in willemseite	Deformation
BA 83-1	Bunsenite, liebenbergite, népouite, willemseite, cochromite, trevorite, millerite, unknown #2, unknown #3	9.9-10.4	2.6	Undeformed
BA 87-4	Bonaccordite, bunsenite, liebenbergite, népouite, willemseite, nimite, cochromite, trevorite, heazlewoodite, nisbite, unknown #2	9.3-10.0	n.a.	Undeformed
BAU	Bunsenite, népouite, willemseite, cochromite/ cobaltian chromite, limonite, heazlewoodite, pure antimony, orcelite, unknown #4	9.2-9.3	2.4	Undeformed
BA 87-1	Népouite, willemseite, nimite, cochromite / cobaltian chromite, trevorite, heazlewoodite, breithauptite, orcelite, unknown #5	7.1-7.3	2.1-2.2	Wave-like veins
BA 87-3	Népouite, willemseite, nimite, trevorite, ferroan trevorite, limonite	5.4-6.4	1.2-2.1	Wave-like veins, kink-band deformation
NCJ8	Willemseite, nimite, cobaltian chromite, trevorite, ferroan trevorite, limonite, ilmenite, millerite, heazlewoodite, chalcocite, digenite	5.6-6.0	n.a.	Layered
NCK6	Willemseite, nimite, ferroan trevorite, millerite, marcasite	5.5-5.7	1.7-2.0	Wave-like veins
BA 84-1	Willemseite, nimite, ferroan trevorite, millerite, breithauptite, orcelite, unknown #5	5.4-5.5	1.6-2.0	Wave-like veins, kink-band deformation
NCH7	Népouite, willemseite, nimite, ferroan trevorite, limonite, millerite, nickeline, bornite	4.7-4.9	1.7-1.8	Little part is layered
NCJ5	Willemseite, nimite, ferroan trevorite, limonite, millerite, heazlewoodite, breithauptite, unknown #5, unknown #6	4.4-5.2	1.4-1.5	Partly layered
BA 84-2	Willemseite, nimite, cochromite / cobaltian chromite, nickeloan magnetite, limonite, ilmenite, millerite, anilite, pure copper	3.3-3.7	1.5	Layered
BAD	Willemseite, nimite, nickeloan magnetite, limonite, millerite, breithauptite, nickeline, orcelite, unknown #5	2.3-3.0	1.0-1.2	Wave-like veins, kink-band deformation

5.2 Discovery of seven new mineral species

As presented in Chapter 4, seven unknown minerals are analysed which could not be attributed to any IMA-accepted mineral (table 5.2). Unknown #1 to unknown #6 are only present in the samples of the Bon Accord Ni-oxide body – unknown #7 is the only new mineral which is present in sample cB S 1088 13a from the hematite-magnetite body.

Unknown #1 (figure 5.1) is subdivided into #1a, #1b and #1c with the mineral formula $Ni^{2+}(Fe^{3+},Ni^{3+})_2O_4$ for unknown #1c, $Ni^{2+}(Ni^{3+},Fe^{3+})_2O_4$ for unknown #1b, and $Ni^{2+}Ni^{3+}{}_2O_4$ for unknown #1a. Only unknown #1b and unknown #1c are observed, indicating the existence of the end member unknown #1a, which is reported by Barbier *et al.* (2000) from experiments, but not to occur in nature. Since the data are obtained by use of the EPMA, the presence of divalent and trivalent Ni together in these minerals could not be determined, so this issue remains uncertain. To gain certainty about this, Mössbauer spectroscopy is suggested to obtain the required information. If the presence of divalent as well as trivalent Ni can be confirmed then unknown #1b is a new mineral species. In this case, unknown #1c would be the ferroan variety of unknown #1b. If the presence of divalent and trivalent Ni cannot be confirmed then the analyses could be incorrect. With the presence of unknown #1c and #1b in the assumed centre of the deposit it appears likely that unknown #1a might have also occurred there. As the Bon Accord deposit is completely mined out since the 1960s it is impossible to start a new and detailed sampling campaign for clarification.

Unknown #2 (figure 5.2) has the mineral formula $Ni_3(As,Sb)$, with As and Sb substituting for each other (figure 4.34). This substitution indicates that unknown #2 is a mixed crystal with the expected end members Ni_3As and Ni_3Sb. Given that unknown #2 is an autonomous species, it is a new mineral. If this mineral does not consist of intermediate members, then all analyses of unknown #2 could be allocated to Ni_3As. This needs to be investigated by synthesizing Ni_3As and Ni_3Sb, including the investigation of their XRD powder patterns and those of unknown #2 (not produced in the scope of the present study). If unknown #2 would belong to Ni_3As, it needs to be compared with the powder patterns of nickelskutterudite, which is the synonym for the discredited species dienerite (Ni_3As). If the powder patterns do not fit with nickelskutterudite, it is a new mineral species.

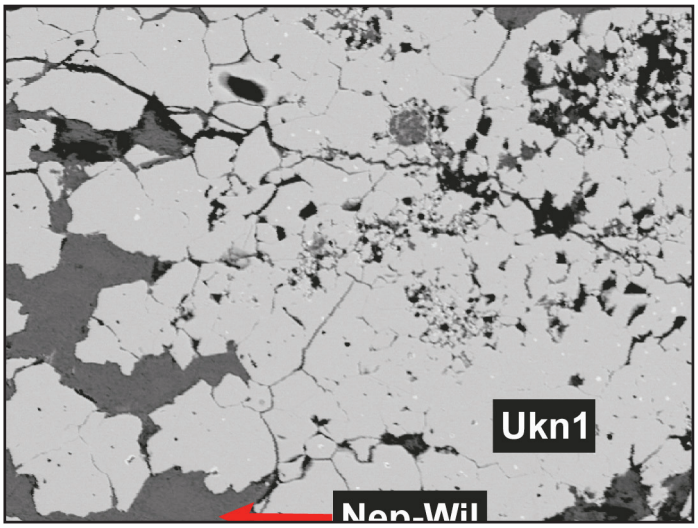

Figure 5.1 Backscatter image of unknown #1 (light grey) together with the népouite-willemseite assemblage (dark grey), obtained by use of the EPMA.

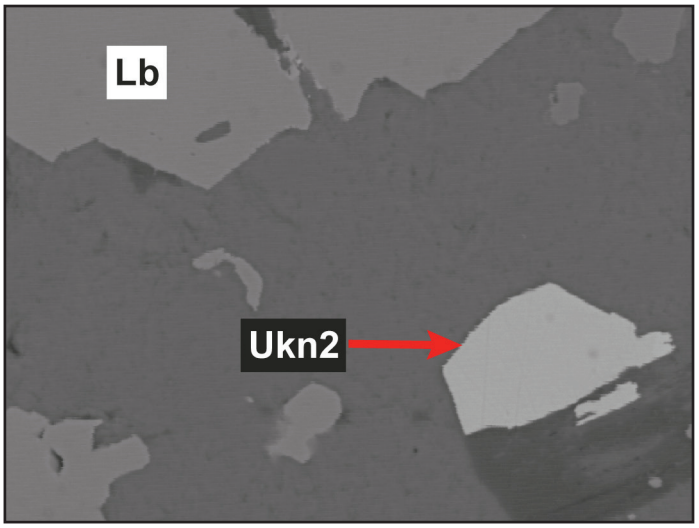

Figure 5.2 Backscatter image of unknown #2 (light grey) together with liebenbergite (grey) and the népouite-willemseite assemblage (dark grey), obtained by use of the EPMA.

Unknown #3 (figure 5.3) has the mineral formula Ni_3Sb. Though no IMA-accepted mineral with such a formula is known, it is reported by Laufek *et al.* (2010) from experiments, and by Nixon *et al.* (1990) from the Tulameen mafic-ultramafic complex in British Columbia, Canada, and is therefore regarded as a new mineral

species.

Unknown #4 (figure 5.4) has the mineral formula Ni_3Sb_2. No mineral with such a formula is reported to occur in nature, nor from experiments. Therefore it is regarded as a new mineral species, though just one mineral grain could be analysed.

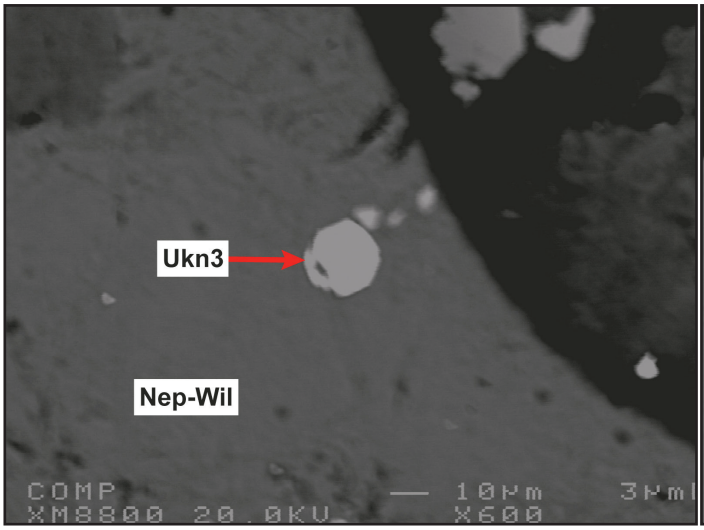

Figure 5.3 Backscatter image of unknown #3 (light grey) together with the népouite-willemseite assemblage (dark grey), close to a mark (black), obtained by use of the EPMA.

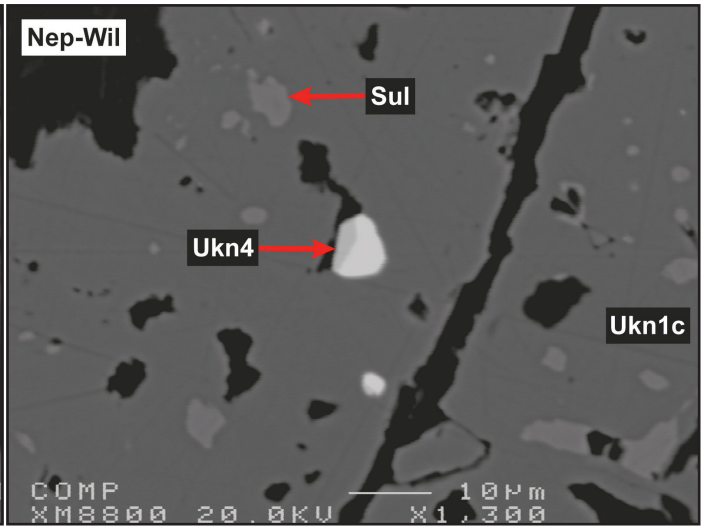

Figure 5.4 Backscatter image of unknown #4 (light grey) in unknown #1c (dark grey) which contains several inclusions of sulphides / sulphosalts (grey), together with the népouite-willemseite assemblage (black), obtained by use of the EPMA.

Unknown #5 (figure 5.5) has the mineral formula $(Ni,Fe)_3As_2$, with Ni and Fe substituting for each other (figure 4.37). Though Sb is too low as to consider it in the mineral formula, it substitutes with Fe, which in turn substitutes also with Ni. These substitutions indicate unknown #5 to be a mixed crystal with the respective end members Ni_3As_2, Fe_3As_2 and Sb_3As_2, which are all never reported to date to occur in nature. If this is the case,

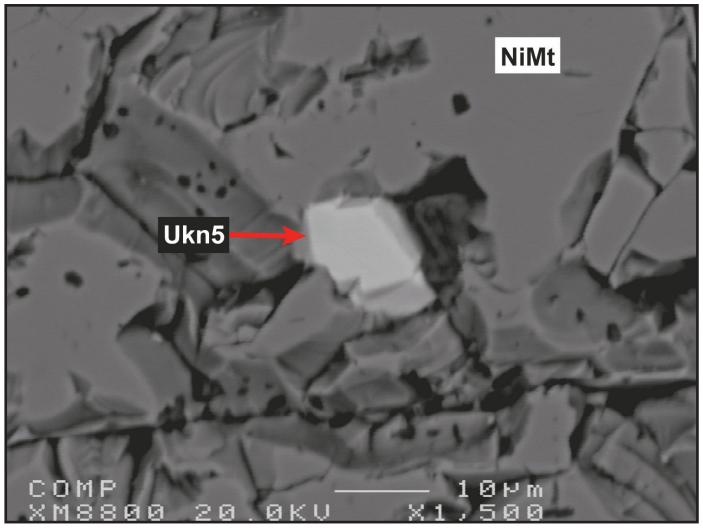

Figure 5.5 Backscatter image of unknown #5 (light grey) in nickeloan magnetite (dark grey) obtained by use of the EPMA.

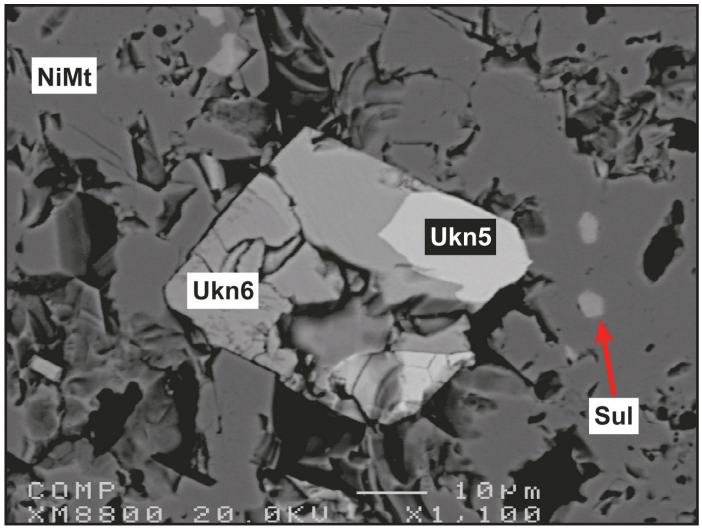

Figure 5.6 Backscatter image of unknown #6 (grey), intergrown with unknown #5 (whitish) in nickeloan magnetite (dark grey) which contains several inclusions of sulphides/ sulphosalts (light grey), obtained by use of the EPMA.

unknown #5 can be allocated to Ni_3As_2. So, unknown #5 can be regarded as a new mineral species, no matter if it is an autonomous species or a mixed crystal.

Unknown #6 (figure 5.6) has the mineral formula Ni_7AsS_5. No mineral with such a formula is reported to occur in nature, nor from experiments. Therefore it is regarded as a new mineral species.

Unknown #7 (figure 5.7) has the mineral formula Co(Ni,Fe), with Ni and Fe substituting for each other (figure 4.40). The expected end members are CoFe, which is wairauite, and CoNi, which is not reported to

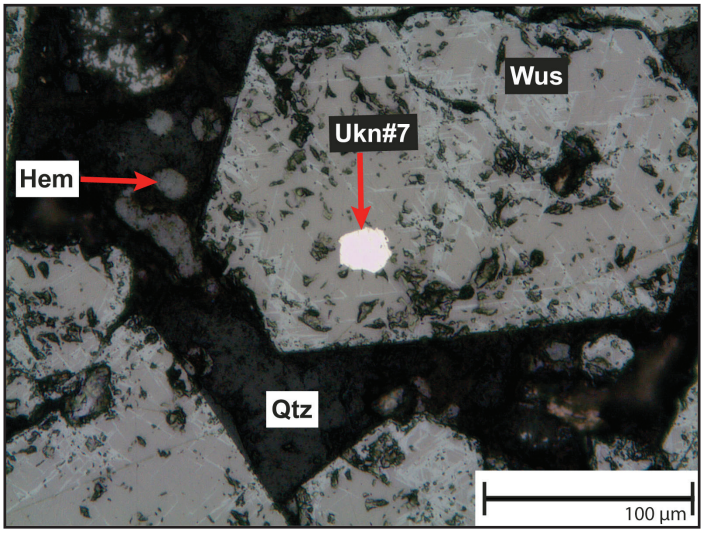

Figure 5.7 Unknown #7 (bright) in martitized wüstite (brownish grey), together with quartz (dark grey) and hematite drops (grey), obtained by the use of optical microscopy.

occur in nature, nor from experiments. If unknown #7 is an autonomous mineral, it is a new species, and if it can be allocated to CoNi, it is a new mineral species as well.

5.3 Mineral formation conditions

5.3.1 Mineral paragenesis and relations amongst the minerals

All in all, the following minerals are observed in the samples of the Bon Accord deposit: bonaccordite, bunsenite, cochromite, cobaltian chromite, liebenbergite, népouite, nimite, trevorite, ferroan trevorite, nickeloan magnetite, willemseite, breithauptite, nickeline, nisbite, orcelite, millerite, heazlewoodite, marcasite, anilite, bornite, chalcocite, digenite, pure antimony, pure copper, unknown #1b, unknown #1c, unknown #2, unknown #3, unknown #4, unknown #5 and unknown #6. Except for marcasite, anilite, bornite, chalcocite, digenite and pure copper, which form all together a minor to accessory part in the modal mineralogy, all the other minerals contain Ni in considerable concentrations. This is a highly unusual feature which supports the suggestion of Tredoux et al. (2010) to regard the Bon Accord Ni-oxide body as a new rock type, called jamestownite. According to the mineral paragenesis and their textural relationships in the samples of Bon Accord, a paragenetic sequence is deduced to gain an understanding of the approximate mineralization time (figure 5.8). The subdivision into Bon Accord A, the contact and Bon Accord B shall point out significant interrelations.

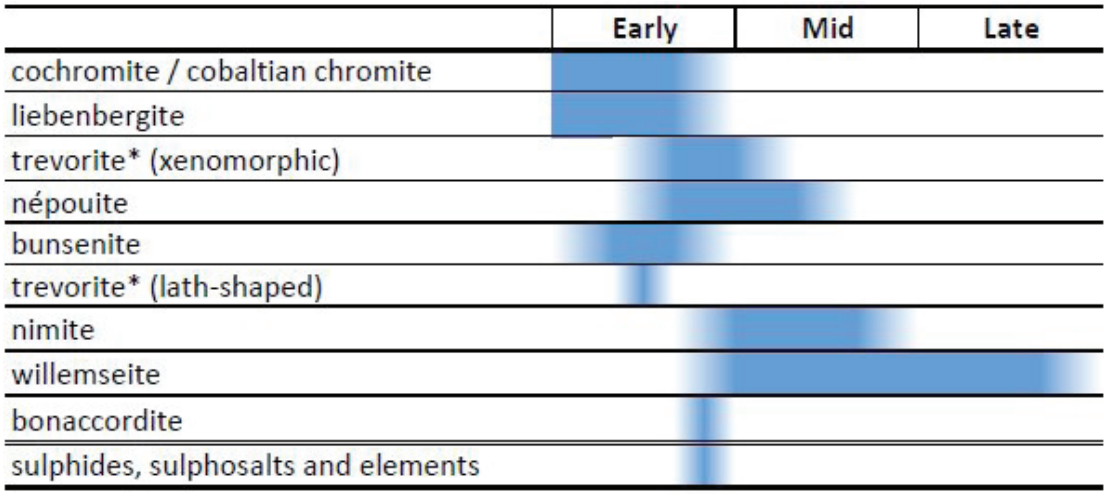

Figure 5.8 Paragenetic sequence about the observed minerals in the Bon Accord deposit. Fading colour marks the unknown start, respectively end of occurrence of a mineral. Early, mid and late indicate possible alteration events which lead to the formation of alteration products. *) unknown #1b, unknown #1c, trevorite, ferroan trevorite, trevorite and nickeloan magnetite are abbreviated with trevorite.

In Bon Accord A the cochromite is in contact with the hypidiomorphic unknown #1b and #1c (figure 3.10). Liebenbergite occurs in contact with népouite, willemseite, the lath-shaped unknown #1b and #1c, containing also inclusions of unknown #1b and #1c. This assemblage is surrounded by xenomorphic unknown #1b and #1c (figure 4.4a). Bunsenite occurs in the népouite-willemseite assemblage and surrounds the xenomorphic unknown #1b and #1c (figure 3.9). Additionally, bunsenite occurs also enveloped by the xenomorphic unknown #1c (figure 3.19). Bonaccordite is present as single bunches within the népouite-willemseite assemblage (figure 3.9) but also intergrown and crosscutting the xenomorphic unknown #1c (figure 3.17). Xenomorphic #1b and #1c contain inclusions of unknown #4, nisbite, millerite and heazlewoodite. These inclusions occur only in the xenomorphic unknown #1b and #1c. Unknown #2, unknown #3, nisbite and pure antimony occur in the népouite-willemseite assemblage.

In the contact, népouite and willemseite are intergrown with each other (figure 3.3) and surrounded by xenomorphic trevorite. Nimite veins crosscut the népouite-willemseite assemblage (figure 3.23). Hypidiomorphic trevorite is in contact with cochromite. Trevorite has inclusions of breithauptite, orcelite and heazlewoodite. These inclusions occur only in the xenomorphic trevorite.

In Bon Accord B népouite and willemseite are interwoven with each other (figure 3.2). Nimite veins crosscut this assemblage. Xenomorphic trevorite / ferroan trevorite / nickeloan magnetite is in contact with cochromite / cobaltian chromite. Single grains of hypidiomorphic and lath-shaped trevorite / ferroan trevorite / nickeloan magnetite occur in the népouite-willemseite assemblage (figure 3.29). Trevorite contains inclusions of breithauptite, orcelite and heazlewoodite. Ferroan trevorite contains inclusions of unknown #5, unknown #6, breithauptite, nickeline, orcelite, millerite, heazlewoodite, bornite, chalcocite and digenite. Nickeloan magnetite contains inclusions of unknown #5, breithauptite, nickeline, orcelite and millerite. These inclusions occur only in the xenomorphic trevorite, ferroan trevorite and nickeloan magnetite. Marcasite, anilite and pure copper occur in the népouite-willemseite assemblage.

The knowledge about this plus the observed textures suggest several processes which are displayed in figure 5.9. For simplification, unknown #1b, unknown #1c, trevorite, ferroan trevorite and nickeloan magnetite are

summarized to trevorite. Cochromite and cobaltian chromite are summarized to cochromite for the same reason. Since those minerals, which are abbreviated with trevorite, occur separate from each other this should

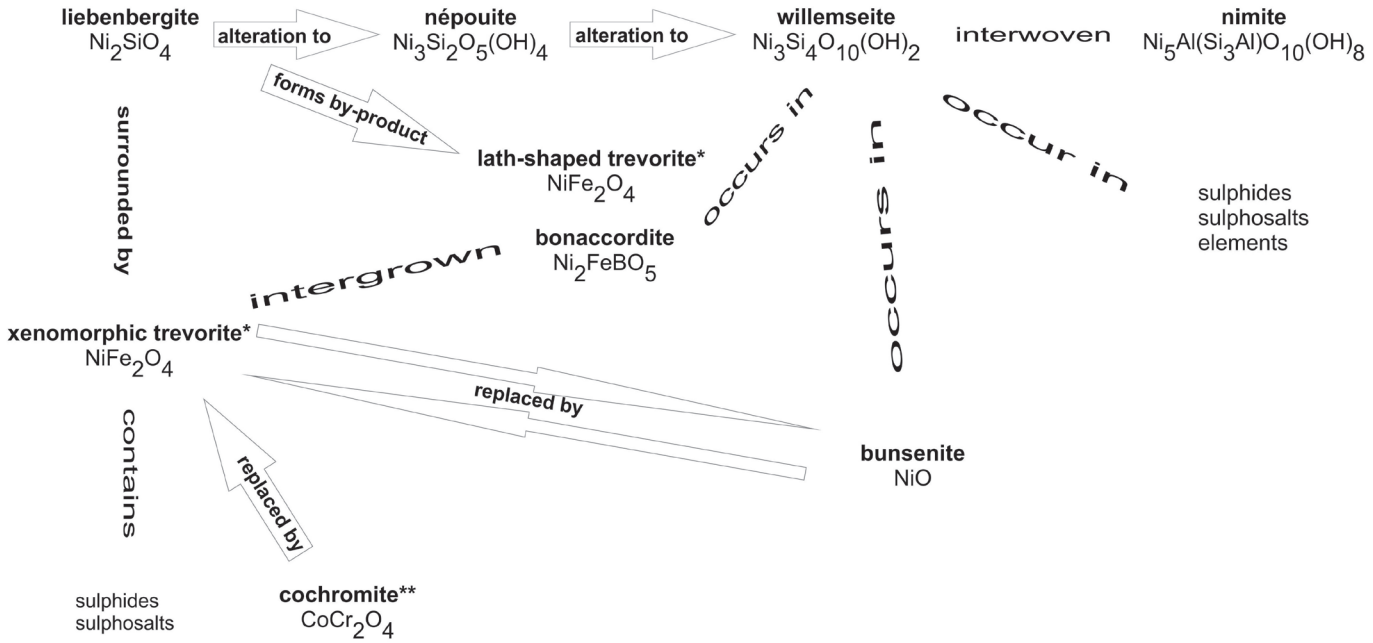

Figure 5.9 Scheme about the relations of the observed minerals. *) unknown #1b, unknown #1c, trevorite, ferroan trevorite and nickeloan magnetite are abbreviated with trevorite. **) cochromite and cobaltian chromite are abbreviated with cochromite. The sulphides, sulphosalts and elements are too many as to list them separately, so they are summarized.

not give a problem. The same applies for the minerals which are summarized as cochromite

Liebenbergite became altered to népouite. During this process, lath-shaped trevorite formed in places (figure 3.18). Since all relic liebenbergites, which occur together in one nodule, extinct at the same time it is likely that each nodule used to be one whole liebenbergite grain which got altered. This supports the formation of the lath-shaped trevorite as a by-product during alteration. Furthermore the népouite altered to willemseite. It is also possible that liebenbergite altered directly to willemseite, since only minor amounts of népouite are observed.

The cochromites are nearly completely replaced by the xenomorphic trevorite (figure 3.10). Due to this they must have formed prior to the xenomorphic trevorite.

Since bunsenite is observed to be replaced by xenomorphic trevorite (figure 3.19), but also to replace the xenomorphic trevorite (figure 3.9), two different generations of bunsenite can be assumed – it is conspicuous that both bunsenite generations do not differ in their mineral chemistry, though De Waal (1979) observed one Fe-enriched and one Fe-depleted bunsenite generation. – So xenomorphic trevorite replaced the first generation of bunsenite, and became itself replaced by a second generation of bunsenite. This means that xenomorphic trevorite has not been present right from the start. That is supported with the intergrowth of xenomorphic trevorite and bonaccordite (figure 3.17), which formed during hydrothermal alteration.

At least two different generations of trevorite can be suggested – the xenomorphic trevorite which is depleted in Ge and a little enriched in Sb, and the lath-shaped trevorite which is enriched in Ge and depleted in Sb (figure 4.4). Obviously they formed independently from each other.

Sulphides and sulphosalts became replaced by the xenomorphic trevorite (e.g. figure 3.25 and 3.26). This

means that they formed prior to the formation of the xenomorphic trevorite or even contemporaneously as latest possibility.

Nimite formed at least contemporaneously with the willemseite, since they are interwoven with each other (figure 3.31).

Népouite, willemseite and nimite are clearly deformed in the contact and Bon Accord B. The lath-shaped trevorites follow there the deformation (figure 3.29), so a deformation event must have happened after the main alteration.

The mineral chemistry of liebenbergite, népouite, willemseite, nimite, cochromite and cobaltian chromite, and the minerals of the magnetite-trevorite series (as well as the new mineral species) has been presented in chapter 4. The conspicuous trend of Ni-depletion and (Mg + Fe)-enrichment in the minerals népouite, willemseite, nimite and the minerals of the magnetite-trevorite series is shown briefly in figure 5.10. Since népouite, willemseite and nimite substitute most Ni with Mg, and the minerals of the magnetite-trevorite series substitute most Ni with Fe, Mg and Fe are added here. Willemseite, nimite and the minerals of the magnetite-trevorite series are all richest in Ni and poorest in (Mg + Fe) in the Bon Accord A samples, and richest in (Mg + Fe) and poorest in Ni in the Bon Accord B samples. The Bon Accord A samples of népouite show the same trend, whereas the népouites of the contact and Bon Accord B show no correlation of Ni towards (Mg + Fe). The alteration of liebenbergite to népouite to willemseite is represented by this, so the Bon Accord A samples contain népouites of the transition liebenbergite to népouite, and the contact and Bon Accord B samples contain népouites of the transition népouite to willemseite. Therewith the népouite is an exception in the Ni-depletion of the minerals. Taken as a whole, the mineral chemical behaviour of these minerals indicates that the Bon Accord Ni-oxide body has been a massive rock that got altered intensely by hydrothermal fluids which carted off the Ni. This confirms the observation of De Waal (1977) that the core of the Bon Accord is richer in Ni than the outer rim.

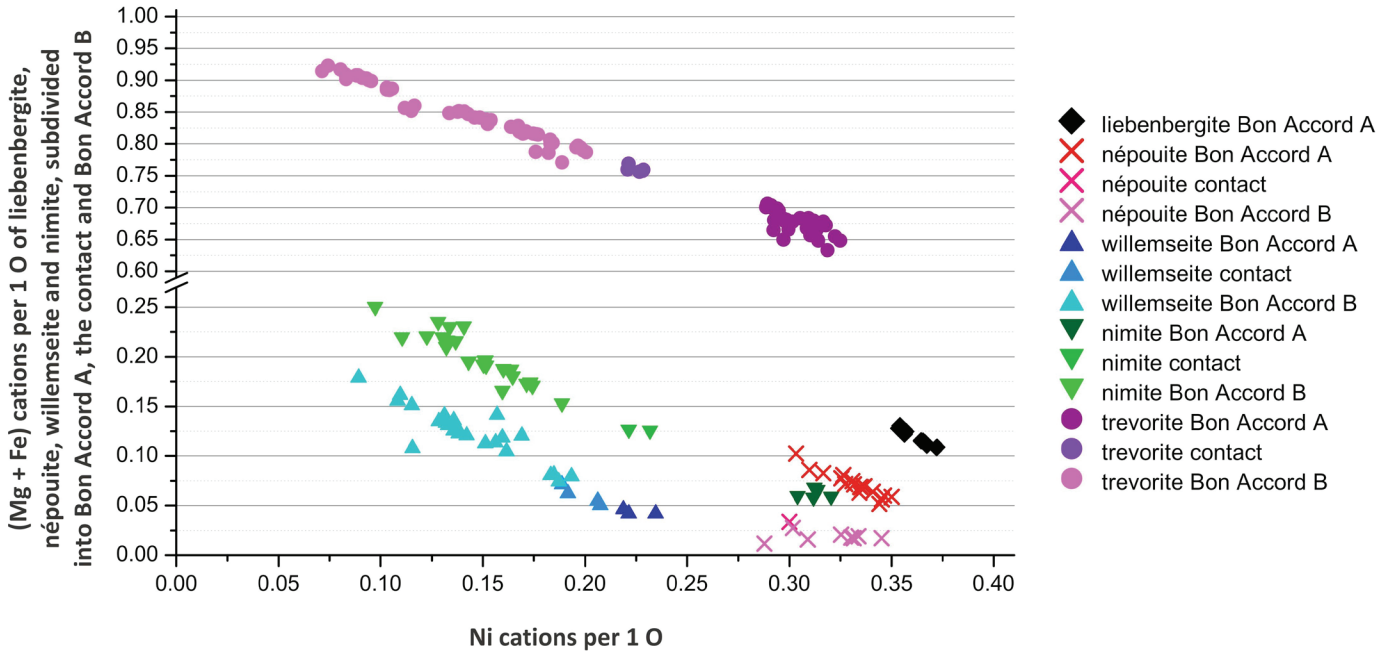

Figure 5.10 Binary plot of Ni vs. (Mg + Fe), showing Ni-depletion in liebenbergite, népouite, willemseite, nimite and the minerals of the magnetite-trevorite series (summarized to trevorite), with subdivision into Bon Accord A, the contact and Bon Accord B. The plotted values are cations per 1 O.

5.3.2 Thermal stabilities of the minerals

For localizing the different processes of mineral formation it is necessary to know the thermodynamic properties of the minerals, but these information are not investigated. Temperature ranges for the mineral formations are published by various authors, but no studies on the thermodynamic properties of this uncommon mineral assemblage have been conducted. So the given temperature ranges for the mineral formations need to be handled with care. Nevertheless these information shall give an impression about the possible thermal environment for the mineral formation in the Bon Accord Ni-oxide body.

Besides experiments, one uncommon occurrence of the paragenesis trevorite-bunsenite-bonaccordite is reported by Sawicki (2008) from fuel crud in pressurized water reactors. There, the temperature is about 345°C on the surface of the fuel rods, where these minerals grow. Obviously trevorite, bunsenite and bonaccordite formed there under hydrothermal conditions. The B source for bonaccordite is definitely and solely the coolant liquid, which contains boric acid.

As it is reported by Hemingway (1990), experimental studies show that bunsenite can be formed also at a temperature of 1000°C. Ziemniak *et al.* (2005) synthesized trevorite powders at a temperature of 950°C and nichromite at 1200°C. Cochromite is reported to be synthesized at 1300°C by Koc and Timucin (2005), as well as at 900°C by Liu and Liang (2000). Bish (1981) synthesized liebenbergite at temperatures of 500°C and 1200°C.

The formation temperature range for népouite is investigated by Korytkova *et al.* (2005). They reported about a required minimum temperature of 250°C and a maximum temperature of 450°C. Carriat *et al.* (1994) synthesized willemseite at 25°C, 150°C, 250°C and 500°C. De Waal (1970a) observed that nimite starts to decompose at a temperature of 710°C.

Since the xenomorphic trevorite and bonaccordite are intergrown with each other, a formation temperature of about 345°C for this process appears likely, and suggests therewith hydrothermal conditions. Liebenbergite and cochromite require a higher formation temperature than trevorite and bonaccordite, so they must have formed prior to them.

Since cochromite can definitely form at temperatures of about 900°C to 1300°C, and liebenbergite from 500°C to 1200°C, an approximate temperature range of 900°C to 1200°C for the formation of both minerals at the same time can be assumed, indicating therewith magmatic conditions.

The allocation of bunsenite is difficult since there are two generations of it. By reason that bunsenite is observed to form at 345°C as well as at 950°C, the formation of the bunsenite, which becomes replaced by the xenomorphic trevorite, is indicated to have happened just after the formation of liebenbergite and cochromite. This is supported by plotting the Ni / (Ni + Fe) molar ratio of bunsenite (table 5.2) in the pseudo-binary phase diagram Fe_2O_3-NiO of Rhamdhani *et al.* (2008) (figure 5.11). Since bunsenite and trevorite coexist, they share the field "S + B" within the red marked part of the field. This indicates a temperature range of about 600°C to 900°C as the formation temperature for bunsenite. The bunsenite, which replaces the xenomorphic trevorite, formed therewith about the same time as the xenomorphic trevorite.

Table 5.2 Ratios of Ni / (Ni+Fe) for the analysed bunsenites

n 1	0.9873
n 2	0.9819
n 3	0.9910
n 4	0.9973
n 5	0.9978
n 6	0.9920

The required temperatures to form népouite and willemseite imply with a maximum of 450°C a hydrothermal fluid that possibly altered the minerals of the Bon Accord. A formation temperature range for nimite is not known. But since it starts to decompose at 710°C (De Waal, 1970a) it formed probably during hydrothermal processes as well.

The formation time of the sulphides, sulphosalts and elements is difficult to evaluate. The Ni-sulphides and sulphosalts might have been present in the primary assemblage, but from textural evidence it appears more likely that they are of hydrothermal origin and formed prior to the xenomorphic trevorite or at least at the same time. Due to the presence of quantities of S in hydrothermal fluids, and Ni in the primary mineral assemblage (for example liebenbergite), it is likely that the Ni-sulphides are a by-product of the hydrothermal alteration of the primary minerals. Since hydrothermal fluids can contain As and Sb as well, the formation of the sulphosalts during the hydrothermal processes is also indicated.

A hydrothermal origin for the Cu-sulphides is indicated as well. The chert samples contain Cu-sulphides and pure nickel, whereas the Bon Accord samples contain Ni-sulphides (amongst others) and pure copper. This indicates a hydrothermal exchange of Cu and Ni.

This can be supported with the interpretation of Ward (1999) and De Waal (1979), that Bon Accord falls well in the metamorphic aureole of the Nelspruit batholith, as well as by Tredoux *et al.* (1989) that Bon Accord falls well in the metamorphic aureole of the Stentor pluton.

These described processes are summarized in figure 5.12, including the identification of minerals as the primary assemblage, as hydrothermal minerals, as alteration products as well as by-products.

Considering only the temperature, the primary assemblage is suggested to have been liebenbergite and cochromite, and possibly the early bunsenite generation.

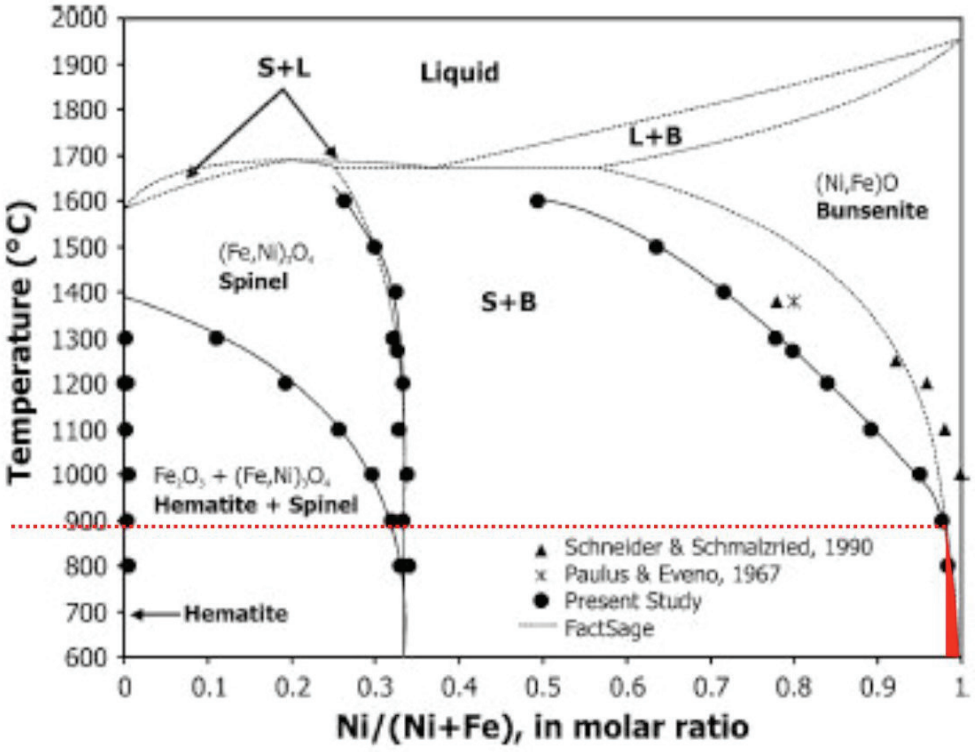

Figure 5.11 Pseudo-binary phase diagram of Fe2O3-NiO in air, modified after Rhamdhani et al. (2008). The red field marks the area of the Ni / (Ni + Fe) molar ratio of the bunsenites of the present study. Since bunsenite coexists with the xenomorphic trevorite, the red field is limited to the boundary of S + B on the right. The red dotted line shows the maximum formation temperature of about 900°C for the bunsenites. S = spinel, B = bunsenite, L = liquid.

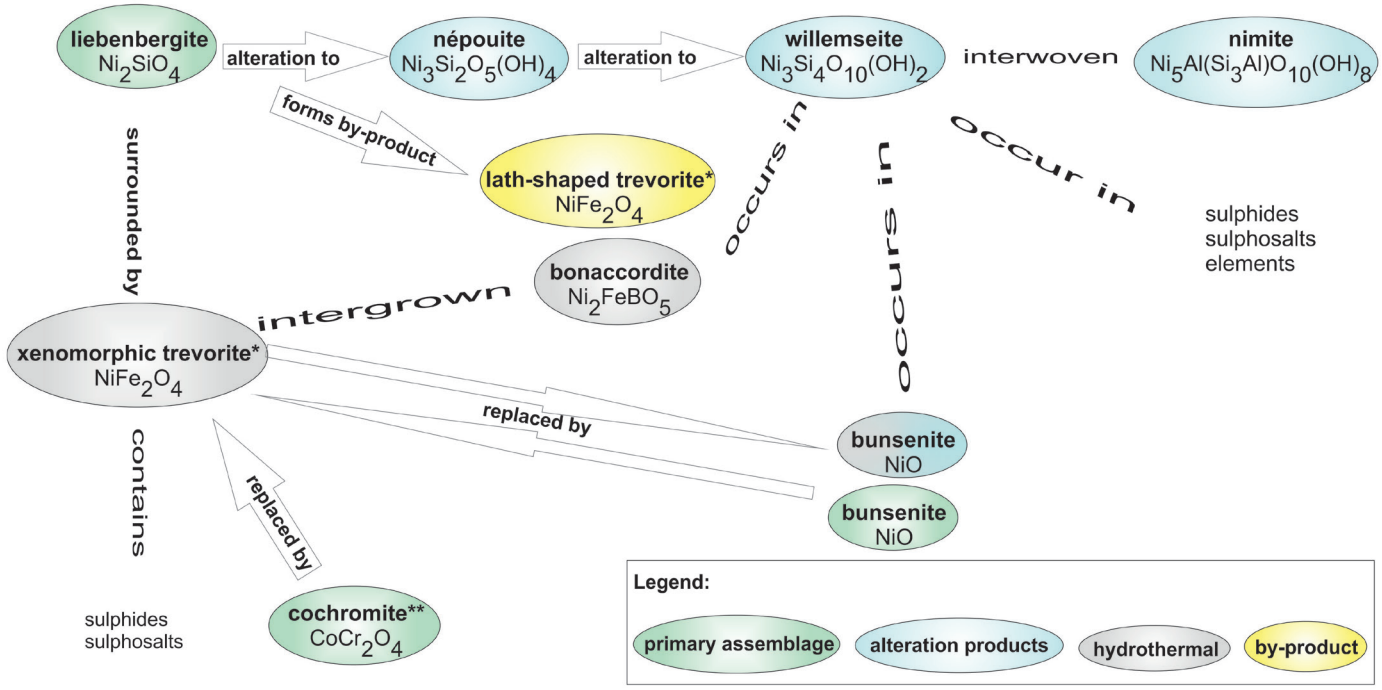

Figure 5.12 Scheme about the relations of the observed minerals, including the formation processes. *) unknown #1b, unknown #1c, trevorite, ferroan trevorite and nickeloan magnetite are abbreviated with trevorite. **) cochromite and cobaltian chromite are abbreviated with cochromite. The sulphides, sulphosalts and elements are too many as to list them separately.

5.3.3 Primary assemblage and parent rock of the Bon Accord Ni-oxide body

To gain an impression, which kind of rock the parent rock could have been, it is essential to consider only the samples of Bon Accord A, which is undeformed and least altered. The original amount of cochromite in the parent rock cannot be estimated since it is nearly completely replaced. Liebenbergite is only present as relics, but adding the percentages of its alteration products népouite, willemseite as well as the percentage of the relic liebenbergite from the modal mineralogy, the amount of liebenbergite prior to alteration is suggested to have been about 50 %. Common rocks which contain about 50 % olivine are peridotites. Those consist also mainly of Al-containing minerals. Since cochromites contain also quite large amounts of Al, this is therewith also the case for the primary assemblage. Due to this the parent rock is suggested to have been a Ni-rich spinel-peridotite.

6. Conclusions

Since the Bon Accord is a highly unusual geological occurrence, several scientists spent their attention to investigate this small-sized ore body. Amongst others, the classification of Bon Accord into different rock types (De Waal, 1977) or zones (Tredoux *et al.*, 1989), its major mineral assemblage (De Waal, 1977), its position within the host rocks, age and REE-patterns (Tredoux *et al.*, 1989) have been investigated in the past; also suggestions of the origin of Bon Accord have been presented by De Waal (1977) and Tredoux *et al.* (1989). However, there are still gaps in the understanding of the mineralogy, relations amongst the minerals, formation processes as well as the origin of the Bon Accord.

Aim of this study was the detailed investigation of the mineralogy, the distribution of the minerals, their composition and variation, as well as detailed investigation of the texture and fabric to gain a better understanding of the ore-forming processes. All in all, the following things can be concluded:

1. The observed Bon Accord mineral assemblage consists of bonaccordite, bunsenite, cochromite, cobaltian chromite, liebenbergite, népouite, nimite, trevorite, ferroan trevorite, nickeloan magnetite, willemseite, breithauptite, nickeline, nisbite, orcelite, millerite, heazlewoodite, marcasite, anilite, bornite, chalcocite, digenite, pure antimony, pure copper, unknown #1b, unknown #1c, unknown #2, unknown #3, unknown #4, unknown #5 and unknown #6. The mineral formula for unknown #1b is $Ni^{2+}(Ni^{3+},Fe^{3+})_2O_4$, for unknown #1c it is $Ni^{2+}(Fe^{3+},Ni^{3+})_2O_4$, for unknown #2 $Ni_3(As,Sb)$, unknown #3 Ni_3Sb, unknown #4 Ni_3Sb_2, unknown #5 $(Ni,Fe)_3As_2$and for unknown #6 it is Ni_7AsS_5. Unknown #2 to #6 do not agree with any IMA-accepted mineral and are therefore regarded as a new mineral species. Unknown #1b and unknown #1c are regarded to be a new mineral species as well, but the presence of trivalent Ni together with divalent Ni needs to be verified. Unknown #1b with its formula $Ni^{2+}(Ni^{3+},Fe^{3+})_2O_4$ is expected to represent the missing link between trevorite ($NiFe_2O_4$) and $NiNi_2O_4$, which is reported from experiments by Barbier et al. (2000) but not known to date to occur in nature; unknown #1c, $Ni^{2+}(Fe^{3+},Ni^{3+})_2O_4$, can therefore be regarded as the ferroan variety of unknown #1b. In that way it is expected that the by De Waal (1969) given ranges for the number of Ni-ions per 32 O can be continued with 8-10 Ni-ions per 32 O for unknown #1c, 10-12 Ni-ions per 32 O for unknown #1b and 12-14 Ni-ions per 32 O for $NiNi_2O_4$ (unknown #1a) which could not be observed, but its presence in the centre of Bon Accord appears likely.

2. The oxide and silicate minerals are in agreement with the documentation by De Waal (1977), but gaspéite and reevesite, which he reported as well, are not observed. Regarding the sulphides and sulphosalts he documented only millerite, breithauptite and heazlewoodite, but also violarite which is not observed in the samples of the present study. Tredoux (2006) reported about a new mineral species with the mineral formula $Ni_7(As,Sb)_3$ which is not observed as well. Nevertheless six new minerals are reported from the Bon Accord deposit in the present study.

3. Furthermore two generations of bunsenite are present. De Waal (1979) already reported about two bunsenite generations, with the first one being Fe-enriched and the second one being Fe-depleted. This is not

in agreement with the bunsenites of the present study – here the two generations are of textural evidence and show no mineral chemical significant difference to each other.

4. From mineral chemistry as well as from petrography also two generations of each unknown #1b, unknown #1c, trevorite, ferroan trevorite and nickeloan magnetite are present – one generation of xenomorphic and another generation of lath-shaped phenotype. The latter generation is Ge-enriched and Sb-depleted, whereas the xenomorphic generation is Ge-depleted and Sb-enriched.

5. The compositional variation of the minerals shows that alteration increases clearly from the samples with the Ni-richest minerals in Bon Accord A to those with the Ni-poorest minerals in Bon Accord B, which is in good accordance to the degree of deformation.

6. Based on the relations of the minerals amongst each other, two formation steps can be observed – a magmatic high-temperature formation and a hydrothermal low-temperature formation. According to De Waal (1977) the primary assemblage consisted of trevorite, liebenbergite, bonaccordite and the Fe-enriched bunsenite, which cannot be confirmed. It is shown that cochromite / nichromite and liebenbergite formed the primary assemblage. If the early generation of bunsenite has been part of this, as Tredoux *et al.* (1989) suggested, remains doubtful. During hydrothermal alteration, liebenbergite became altered to népouite and further to willemseite. The Ge-enriched generation of unknown #1b / unknown #1c / trevorite / ferroan trevorite / nickeloan magnetite formed thereby as by-product. Nimite can be assumed to have formed during these processes. The Ge-depleted generation of unknown #1b / unknown #1c / trevorite / ferroan trevorite / nickeloan magnetite formed under hydrothermal conditions, together with bonaccordite and the second generation of bunsenite. The sulphides, sulphosalts and pure Sb and Cu formed at least during the formation of the Ge-depleted trevorite.

7. Following the primary assemblage liebenbergite-cochromite / nichromite, and considering the approximate ascertainable percentage of liebenbergite prior to alteration, which is calculated to have been 50 %, the parent rock is suggested to have been a Ni-rich spinel-peridotite.

8. Since the Bon Accord Ni-oxide body shows a highly unusual mineralogy in consisting of Ni-rich rock forming minerals, due to its occurrence within the Jamestown ophiolite complex and due to its, by Tredoux *et al.* (1989) suggested deep mantle origin, it is suggested by Tredoux *et al.* (2010) to recognize the Bon Accord as a new rock type and to name it jamestownite. Though the origin of the Ni remains a controversial issue, this suggestion can be supported, due to the assured occurrence within the Jamestown ophiolite complex and since this rock type differs in its mineralogy significantly from any other rock type by consisting of liebenbergite, trevorite, bunsenite etc.

9. This mineralogical study showed no indication that the Bon Accord Ni-oxide body is an altered palaeometeorite as stated by De Waal (1977), or that the Ni is derived from such. It is shown that the Bon Accord deposit is a magmatic formation which is hydrothermally altered. But this study gives no indications

for the source of the high Ni concentrations. The derivation of the Ni from the Earth's core, as Tredoux *et al.* (1989) stated, can neither be negated nor confirmed with this mineralogical study.

Future work should include microanalytic work to investigate the unknown minerals. For unknown #1b and unknown #1c it is required to verify the presence of trivalent together with divalent Ni, for example by the use of Mössbauer spectroscopy. In addition to this, mineral syntheses as well as XRD are suggested to verify if unknown #2 and unknown #5 are intermediate members. Furthermore the registration of these minerals would be a significant contribution to the knowledge of natural minerals.

Since there is a huge gap in the knowledge about the thermodynamic properties of bonaccordite, bunsenite, cochromite and nichromite, gaspéite, liebenbergite, népouite, nimite, reevesite, trevorite, willemseite as well as unknown #1 to unknown #6, it would be important to investigate those. This would allow the creation of a model for the formation conditions of the Bon Accord and contribute to the investigation of the origin of Bon Accord.

Furthermore the detailed investigation of the buried hematite-magnetite body and of the Bon Accord Ni-sulphide body would give information if these two deposits are in any genetic relation to the Bon Accord Ni-oxide body. Also very close meshed mapping and seismic reflection would be a good addition to verify if further ore bodies are present below the Earth's surface, but also to verify if the Bon Accord is rootless or not. Especially the latter would contribute to clarify the origin of the Ni, but to realize this, it is necessary to make the area accessible which is one of the reasons why these things have not been done yet.

The locating of analogue deposits with comparable material and minerals could contribute to the understanding of the origin and formation of such a deposit.

In the scope of this study the mineral paragenesis, chemical variation, texture and fabric as well as the relation amongst the occurring minerals have been detailed investigated. Though several new aspects of the Bon Accord Ni-oxide body could be worked out, open questions remain as for instance the genetic relation of Bon Accord to the host rocks as well as its origin.

7. Acknowledgements

I wish to thank everyone who made this thesis possible by support and guidance during the course of this project. At first I thank Professor Marian Tredoux, who introduced me into exotic mineral deposits. She enabled for me the accomplishment of a study about a highly unusual South African Ni-deposit which included the discovery of seven new mineral species, based on her first observations. In virtually every instance she was my primary point of reference and spent even nights with me to discuss ideas. Thank you for your unceasing efforts regarding the organization of this project, and for your invaluable scientific input. I also want to thank Dr Wojciech Przybylowicz for his dedication and support during the analyzes on the μPIXE at iThemba labs in Cape Town, thanks also to your wife Jolanta and for both your friendship. Furthermore I thank Professor Anthony E. Williams-Jones of the McGill University, Canada, for the use of the microscope and microprobe, as well as scientific input. Many thanks to Professor Robert F. Martin for your valuable support as well as scientific input. Thank you also to Professor Klaus Bente and Professor Gert Klöss for the use of the microscope and microprobe, as well as scientific input. I would like to express my gratitude also to Mrs Rina Immelman for her unfailing support and organizational effort, but also the whole staff of the Department of Geology for all their friendliness.

Very special thanks to my fiancé Sebastian Fuchs, who was always listening to my ideas and always supported me emotional. Also a very special thank you to Konstanze, Hans-Joachim and Ella Fuchs, you were always there for me and supported me emotional and with great food. Thank you as well to my parents Ingrid and Reinhard Wildau and to my brother Michael Wildau, you supported and listened me as well though several km are between us. Many thanks for all your patience with me. Thank you as well to my friends Corinna, Christin, Stefan, Anja, Daniela and Frank for all your patience with me and for your understanding.

8. List of References

Akimoto, S., Matsui, Y., Syono, Y., 1976. High-pressure crystal chemistry of orthosilicates and the formation of the mantle transition zone. Phys. Chem. Miner. Rocks, NATO Adv. Study Inst. "Petrophys.": 327-63.

Akpanika, O.I., Ukpong, E.E., Olade, M.A., 1987. Mineralogy and geochemical dispersion in tropical residual soils overlying a talc deposit in southwestern Nigeria. Chemical Geology, 63(1-2): 109-119.

Allsopp, H.L., Davies, R.D., De Gasparis, A.A.A., Nicolaysen, L.O., 1969. Review of Rb-Sr age measurements from the early Precambrian terrain in the south-eastern Transvaal and Swaziland. Special Publication - Geological Society of South Africa, 2: 433-443.

Andreoli, M.A.G., Ashwal, L.D., Hart, R.J., Huizenga, J.M., 1999. A Ni- and PGE-enriched quartz norite impact melt complex in the late Jurassic Morokweng impact structure, South Africa. Large meteorite impacts and planetary evolution II, special paper 339. Geological Society of America.

Andreoli, M.A.G. et al., 2008. Siderophile minerals in the melt sheet of the Morokweng impact crater, South Africa: Similarities and differences with the Sudbury deposits, Large meteorite impacts and planetary evolution IV, Vredefort Dome, South Africa.

Anhaeusser, C.R., 1964. The geology of the Lily syncline and a portion of the Eureka syncline between Sheba Siding and Louw's Creek Station, Barberton mountain land. M.Sc. thesis (unpubl.), University Witwatersrand, Johannesburg.

Anhaeusser, C.R., 1973. The evolution of the early Precambrian crust of Southern Africa. Philosophical Transactions of the Royal Society of London. Series A, Mathematical and Physical Sciences, 273(1235): 359-388.

Anhaeusser, C.R., 1976. The geology of the Sheba Hills area of the Barberton mountain land, South Africa, with particular reference to the Eureka syncline. Transactions of the Geological Society of South Africa, 79: 253-280.

Annersten, H., Ericsson, T., Filippidis, A., 1982. Cation ordering in Ni-Fe olivines. American Mineralogist, 67(11-1): 1212-1217.

Anthony, J.W., Bideaux, R.A., Bladh, K.W., Nichols, M.C., 1995. Handbook of mineralogy. Silica, Silicates, 2. Mineral Data Publ., Tucson.

Anthony, J.W., Bideaux, R.A., Bladh, K.W., Nichols, M.C., 1997. Handbook of mineralogy. Halides, Hydroxides, Oxides, 3. Mineral Data Publ., Tucson.

Anthony, J.W., Bideaux, R.A., Bladh, K.W., Nichols, M.C., 2003. Handbook of mineralogy. Borates, carbonates, sulfates, 5. Mineral Data Publ., Tucson.

Arai, S., 1994. Characterization of spinel peridotites by olivine spinel compositional relationships - review and interpretation. Chemical Geology, 113(3-4): 191-204.

Barbier, A., Mocuta, C., Renaud, G., 2000. Structure, transformation, and reduction of the polar NiO(111) surface. Physical Review B, 62(23): 16056-16062.

Bird, J.M., Botto, R.I., Morrison, G.H., Weathers, M.S., 1974. Specimens from Earth's core. Transactions-American Geophysical Union, 55(7): 697-697.

Barthelmy, D., 2010. Mineralogy Database. Information downloadable from the official website: www.
webmineral. com.

Bish, D.L., 1981. Cation ordering in synthetic and natural Ni-Mg olivine. American Mineralogist, 66(7-8): 770-776.

Brandl, G., Cloete, M., Anhaeusser, C.R., 2006. Archaean greenstone belts. In: Johnson, M.R., Anhaeusser, C.R., Thomas, R.J. (Eds.), The geology of South Africa. Geological Society of South Africa
Council for Geoscience, Johannesburg, pp. 9-56.

Brindley, G.W., Wan, H.M., 1975. Compositions, structures, and thermal-behavior of nickel-containing minerals in lizardite-nepouite series. American Mineralogist, 60(9-10): 863-871.

Byerly, G.R., Palmer, M.R., 1991. Tourmaline mineralization in the Barberton greenstone belt, South-Africa - Early Archean metasomatism by evaporite-derived boron. Contributions to Mineralogy and Petrology,

107(3): 387-402.
Cameron, E.N., 1966. Ore microscopy. John Wiley & Sons, Inc., New York.
Cameron, E.N., 1977. Chromite in the central sector of the Eastern Bushveld Complex, South Africa. American Mineralogist, 62: 1082-1096.
Carriat, J.Y., Che, M., Kermarec, M., 1994. Influence of order-disorder parameters on the reducibility of Ni- and Cu-containing silicates: application to talc and chrysocolla. Catalysis Letters, 25: 127-140.
Challis, G.A., Long, J.V.P., 1964. Wairauite - a new cobalt-iron mineral, Mineralogical Magazine, pp. 942-948.
Chamberlain, J.A., Delabio, R.N., 1965. Mackinawite and Valleriite in the Muskox intrusion. American Mineralogist, 50(5-6): 682-&.
Chamberlain, J.A., McLeod, C.R., Traill, R.J., Lachance, G.R., 1965. Native metals in the Muskox intrusion. Canadian Journal of Earth Sciences, 2: 188-215.
Cloete, M., 1990. The metamorphic history of the Komati Formation (Barberton, South Africa): a P-T-t path and its tectonic implications. Ext. Abstr., 3rd Int. Archaean Symposium, Perth, pp. 121-123.
Cloete, M., 1991. An overview of metamorphism in the Barberton greenstone belt. In: Ashwal, L.D., Ed., Two Cratons and an Orogen - Excursion guidebook and review articles for a field workshop through selected Archaean terranes of Swaziland, South Africa and Zimbabwe. IGCP Project 280, Johannesburg.
Cloete, M., 1994. Aspects of volcanism and metamorphism of the Onverwacht Group lavas in the south-western portion of the Barberton greenstone belt. Ph.D. (unpublished) Thesis, University of the Witwatersrand, Johannesburg, 419 pp.
Condie, K.C., Macke, J.E., Reimer, T.O., 1970. Petrology and geochemistry of early Precambrian graywackes from Fig Tree Group, South-Africa. Geological Society of America Bulletin, 81(9): 2759-&.
Condie, K.C., Hunter, D.R., 1976. Trace element geochemistry of Archean granitic rocks from the Barberton region, South Africa. Earth and Planetary Science Letters, 29(2): 389-400.
Crosse, A.F., 1921. A rich nickel ore. J. chem. Soc. S. Afr., 21: 126.
Danchin, R.V., 1967. Chromium and nickel in Fig Tree shale from South Africa. Science, 158(3798): 261-&.
De Ronde, C.E.J., 1991. Structural and geochronological relationships and fluid-rock interaction in the central part of the ~3.2-3.5 Ga Barberton greenstone belt, South Africa, University of Toronto, Toronto, Canada, 370 pp.
De Ronde, C.E.J., De Wit, M.J., 1994. Tectonic history of the Barberton greenstone-belt, South-Africa - 490 million years of Archean crustal evolution. Tectonics, 13(4): 983-1005.
De Waal, S.A., 1969. Nickel minerals from Barberton, South Africa -.I. Ferroan Trevorite. American Mineralogist, 54(7-8): 1204-&.
De Waal, S.A., 1970a. Nickel minerals from Barberton, South Africa: II. Nimite, a nickel-rich chlorite. American Mineralogist, 55(1-2): 18-30.
De Waal, S.A., 1970b. Nickel minerals from Barberton, South Africa: III. Willemseite, a nickel-rich talc. American Mineralogist, 55(1-2): 31-42.
De Waal, S.A., Viljoen, E.A., 1971. Nickel minerals from Barberton, South Africa .4. Reevesite, a Member of Hydrotalcite Group. American Mineralogist, 56(5-6): 1077-&.
De Waal, S.A., 1972. Nickel minerals from Barberton, South-Africa .5. Trevorite, Redescribed. American Mineralogist, 57(9-10): 1524-&.
De Waal, S.A., Calk, L.C., 1973. Nickel minerals from Barberton, South-Africa .6. Liebenbergite, a Nickel Olivine. American Mineralogist, 58(7-8): 733-735.
De Waal, S.A., Viljoen, E.A., Calk, L.C., 1974. Nickel minerals from Barberton, South Africa. VII Bonaccordite, the nickel analogue of ludwigite. Transactions of the Geological Society of South Africa, 77: 375.
De Waal, S.A., 1977. The nickel deposit at Bon Accord, Barberton, South Africa - A proposed paleometeorite. Geological Society of South Africa, 4: 87-98.
De Waal, S.A., 1978. Nickel minerals from Barberton, South Africa: VIII. The spinels cochromite and nichromite, and their significance to the origin of the Bon Accord nickel deposit, Bulletin du Bureau de recherches géologiques et minières: géologie des gîtes minéreaux, Paris, pp. 225-230.
De Waal, S.A., 1979. The metamorphism of the Bon Accord nickel deposit by the Nelspruit granite. Transactions

of the Geological Society of South Africa, 82: 335-342.
De Waal, S.A., 1986. The Bon Accord nickel occurrence at Barberton. Mineral Deposits of Southern Africa, I & II. Geological Society of South Africa, Johannesburg, 287-291 pp.
De Wit, M.J., 1982. Gliding and overthrust nappe tectonics in the Barberton-greenstone belt. Journal of Structural Geology, 4(2): 117-&.
De Wit, M.J., Hart, R.A., Hart, R.J., 1987. The Jamestown ophiolite complex, Barberton mountain belt - a section through 3.5 Ga oceanic-crust. Journal of African Earth Sciences, 6(5): 681-730.
De Wit, M.J., 1991. Archean greenstone-belt tectonism and basin development - Some insights from the Barberton and Pietersburg greenstone belts, Kaapvaal craton, South-Africa. Journal of African Earth Sciences, 13(1): 45-63.
De Wit, M.J. et al., 1992. Formation of an Archean continent. Nature, 357(6379): 553-562.
De Wit, M.J., Hart, R.A., 1993. Earth's earliest continental lithosphere, hydrothermal flux and crustal recycling. Lithos, 30(3-4): 309-335.
Dick, H.J.B., 1974. Terrestrial nickel-iron from Josephine peridotite, its geologic occurrence, associations, and origin. Earth and Planetary Science Letters, 24(2): 291-298.
Dziggel, A., Stevens, G., Poujol, M., Anhaeusser, C.R., Armstrong, R.A., 2002. Metamorphism of the granite–greenstone terrane south of the Barberton greenstone belt, South Africa: an insight into the tectono-thermal evolution of the 'lower' portions of the Onverwacht Group. Precambrian Research, 114(3-4): 221-247.
Eggleton, R.A., Fitz Gerald, J., Foster, L., 2011. Chrysoprase from Gumigil, Queensland. Australian Journal of Earth Sciences, 58(7): 767-776.
ETH, 2011. Eidgenössische Technische Hochschule Zürich: Institute of Geochemistry and Petrology. Information downloadable from the official website: www.geopetro.ethz.ch. In: Büchel, C. (Editor). Büchel, C.
Driesner, T., Zürich. EU, 2012. Legal notice, European Commission. Information downloadable from the official website: http://ec.europa.eu
Galí, S. et al., 2009. Stability of "Garnierites" in the Falcondo nickel lateritic deposit, Dominican Republic. Revista de la Sociedad Espanola de Mineralogía, 11: 89-90.
Gray, J., 1921. Discussion - a nickel-rich ore. J. chem. Soc. S. Afr., 21: 158.
Hemingway, B.S., 1990. Thermodynamic properties for bunsenite, NiO, magnetite, Fe3O4, and hematite, Fe2O3, with comments on selected oxygen buffer reactions. American Mineralogist, 75(7-8): 781-790.
Henderson, C.M.B., Redfern, S.A.T., Smith, R.I., Knight, K.S., Charnock, J.M., 2001. Composition and temperature dependence of cation ordering in Ni-Mg olivine solid solutions: a time-of-flight neutron powder diffraction and EXAFS study. American Mineralogist, 86(10): 1170-1187.
Henshaw, J. et al., 2006. A model of chemistry and thermal hydraulics in PWR fuel crud deposits. Journal of Nuclear Materials, 353(1-2): 1-11.
Hofmann, A., Harris, C., 2008. Silica alteration zones in the Barberton greenstone belt: A window into subseafloor processes 3.5-3.3 Ga ago. Chemical Geology, 257(3-4): 224-242.
Hurley, P.M., Pinson Jr, W.H., Nagy, B., Teska, T.M., 1972. Ancient age of the Middle Marker horizon, Onverwacht Group, Swaziland Sequence, South Africa. Earth and Planetary Science Letters, 14(3): 360-366.
Ishimaru, S., Arai, S., 2008. Nickel enrichment in mantle olivine beneath a volcanic front. Contributions to Mineralogy and Petrology, 156(1): 119-131.
Keenan, J., 1986. The Bon Accord nickel sulphide depost, Barberton greenstone belt. Geological Society of South Africa, I: 281-285.
Koc, N., Timucin, M., 2005. Activity–composition relations in MnCr2O4–CoCr2O4 solid solutions and stabilities of MnCr2O4 and CoCr2O4 at 1300°C. Journal of the American Ceramic Society, 88(9): 2578-2585.
Kohler, E.A., 2003. The geology of the Archean granitoid-greenstone terrane in the vicinity of three sisters, Barberton greenstone belt, report on mapping and geological studies between 1990 and 1994. Bulletin of the council for geoscience, pp. VI, 150 p.

Korytkova, E.N. et al., 2005. Synthesis of nanotubular Mg3Si2O5(OH)4-Ni3Si2O5(OH)4 silicates at elevated temperatures and pressures. Inorganic Materials, 41(7): 743-749.

Krivolutskaya, N., Bryanchaninova, N., 2011. Olivines of igneous rocks. Russian Journal of General Chemistry, 81(6): 1302-1314.

Lamb, S.H., 1984. Geology of part of the Archean Barberton greenstone belt, Swaziland, Cambridge University, Cambridge, U.K., 178 pp.

Laufek, F., Drábek, M., Skála, R., 2010. The system Ni-Sb-Te at 400°C. Canadian Mineralogist, 48(5): 1069-1079.

Li, C., Ripley, E.M., Mathez, E.A., 2003. The effect of S on the partitioning of Ni between olivine and silicate melt in MORB. Chemical Geology, 201(3-4): 295-306.

Linkenheld, C., 2010. Kompetenz in Mikroskopie & Imaging. Information downloadable from the official website: www.mikroskopie.de, Speyer.

Liu, P.S., Liang, K.M., 2000. High-temperature oxidation behavior of the co-base superalloy DZ40M in air. Oxidation of Metals, 53(3): 351-360.

Lowe, D.R., 1991. Geology of the Barberton greenstone belt: an overview, 47-58. In: Ashwal, L. D., Ed., Two Cratons and an Orogen - Excursion Guidebook and Review Articles for a Field Workshop Through Selected Archaean Terranes of Swaziland, South Africa and Zimbabwe., Dept. Geol., Univ. Witwatersrand.

Lowe, D.R., 1994. Accretionary history of the Archean Barberton greenstone belt (3.55-3.22 Ga), southern Africa. Geology, 22(12): 1099-1102.

Madala, F., 2009. Mineralogy and major element geochemistry of rocks from the Jamestown ophiolite complex, Barberton greenstone belt, South Africa. unpublished. BSc Hons Thesis, University of the Free State, South Africa.

Maksimovich, Z., 1975. The isomorphous series lizardite-nepouite. International Geology Review, 17(9): 1035-1040.

Manceau, A., Calas, G., Decarreau, A., 1985. Nickel-bearing clay-minerals. 1. optical spectroscopic study of nickel crystal-chemistry. Clay Minerals, 20(3): 367-387.

Manor, B., 2008. Barberton Manor Guest House.

Matsui, Y., Syono, Y., 1968. Unit cell dimensions of some synthetic olivine group solid solutions. Geochemical Journal, 2: 51-59.

McGill, 2011. McGill University. Information downloadable from the official website: www.mcgill.ca, Montreal.

Montoya, J.W., Baur, G.S., 1963. Nickeliferous serpentines, chlorites, and related minerals found in 2 lateritic ores. American Mineralogist, 48(11-2): 1227-&.

Nixon, G.T., Cabri, L.J., LaFlamme, J.H.G., 1990. Platinum-group-element mineralization in lode and placer deposits associated with the tulameen Alaskan-type complex, British Columbia. Canadian Mineralogist, 28: 503-535.

Nwe, Y.Y., 1976. Electron-probe studies of aarlier pyroxenes and olivines from Skaergaard Intrusion, East Greenland. Contributions to Mineralogy and Petrology, 55(1): 105-126.

Oosthuyzen, E.J., 1970. The geochronology of a suite of rocks from the granitic terrain surrounding the Barberton Mountain Land. Ph.D. Thesis, University of the Witwatersrand, Johannesburg, unpublished.

Pandey, S.K., Shrivastava, J.P., Roonwal, G.S., 2008. Occurrence of ferroan trevorite within olivine megacrysts of the MORB from Southern East Pacific Rise. Current Science, 95(10): 1468-1473.

Paris, I., Stanistreet, I.G., Hughes, M.J., 1985. Cherts of the Barberton greenstone-belt interpreted as products of submarine exhalative activity. Journal of Geology, 93(2): 111-129.

Poujol, M., Robb, L.J., Anhaeusser, C.R., Gericke, B., 2003. A review of the geochronological constraints on the evolution of the Kaapvaal Craton, South Africa. Precambrian Research, 127(1-3): 181-213.

Press, F., Siever, R., 1995. Allgemeine Geologie. Spektrum, Akad. Verl., Berlin; Heidelberg.

Rankama, K., Sahama, T.G., 1968. Geochemistry. Univ. of Chicago Press, Chicago, Ill.

Rhamdhani, M.A., Hayes, P.C., Jak, E., 2008. Subsolidus phase equilibria of the Fe-Ni-O system. Metallurgical

and Materials Transactions B-Process Metallurgy and Materials Processing Science, 39(5): 690-701.
Sack, R.O., Ghiorso, M.S., 1991. Chromite as a petrogenetic indicator. Reviews in Mineralogy and Geochemistry, 25(1): 323-354.
SACS, 2006. The South African Committee for Stratigraphy, based at the Council for Geoscience, Pretoria, South Africa. Information downloadable from the Council's official website: http://www.geoscience.org.za.
Sawicki, J.A., 2008. Evidence of Ni2FeBO5 and m-ZrO2 precipitates in fuel rod deposits in AOA-affected high boiling duty PWR core. Journal of Nuclear Materials, 374(1-2): 248-269.
SERC, 2011. Science Education Resource Center at Carleton College. Information downloadable from the official website: http://serc.carleton.edu. Science Education Resource Center, Northfield, Minnesota.
Song, Y., Moon, H.S., Chon, H.T., 1995. New occurrence and characterization of Ni-serpentines in the Kwangcheon area, Korea. Clay Minerals, 30(3): 211-224.
Tredoux, M. et al., 1989. Platinum group elements in a 3.5 Ga nickel-iron occurrence - Possible evidence of a deep mantle origin. Journal of Geophysical Research-Solid Earth and Planets, 94(B1): 795-813.
Tredoux, M., Garuti, G., Zaccarini, F., Cloete, M., 2006. Sub-microscopic phases in the bon accord Ni ore body, Barberton, South Africa, Goldschmidt Conference, Melbourne, Australia, pp. 656.
Tredoux, M. et al., 2010. Jamestownite: a new PGE-rich rock type from the Barberton greenstone belt, South Africa. In: Árkai, P. et al. (Editors), 20th general meeting of the International Mineralogical Association. Department of Mineralogy, Geochemistry and Petrology, University of Szeged, Budapest, pp. 266.
Trevor, T.G., 1920. Nickel: Notes on the occurrence in the Barberton district. South African Journal of Industrial Engineering, 3: 532-533.
UFS, 2011. Natural and Agricultural Sciences Faculty, Centre for Microscopy of the University of the Free State. Information downloadable from the official website: http://natagri.ufs.ac.za/. University of the Free State, Bloemfontein.
Villanova-de-Benavent, C., Proenza, J.A., Galí, S., Tauler, E., 2011. Talc- and serpentine-like "garnierites" in the Falcondo Ni-laterite deposit, Dominican Republic, SGA, Antofagasta, Chile.
Ward, J.H.W., 1999. The metallogeny of the Barberton greenstone belt, South Africa and Swaziland.
Westraat, J., Kisters, A.M., Poujol, M., Stevens, G., 2005. Transcurrent shearing, granite sheeting and the incremental construction of the tabular 3.1 Ga Mpuluzi batholith, Barberton granite greenstone terrane, South Africa. Journal of the Geological Society, 162(2): 373-388.
Winefordner, J.D. (Ed.), 1995. Chemical Analysis - a series of monographs on analytical chemistry and its applications. Particle-Induced X-Ray Emission Spectrometry (PIXE), New York.
Xin, H., Eisenhour, D.D., Buseck, P.R., 1995. Cobalt-rich, nickel-poor metal (wairauite) in the Ningqiang carbonaceous chondrite. Meteoritics, 30(1): 106-109.
Zhan, W., Guggenheim, S., 1995. The dehydroxylation of chlorite and the formation of topotactic product phases. Clays and Clay Minerals, 43(5): 622-629.
Ziemniak, S.E., Gaddipati, A.R., Sander, P.C., 2005. Immiscibility in the NiFe2O4-NiCr2O4 spinel binary. Journal of Physics and Chemistry of Solids, 66: 1112-1121.